Scalable Nanowire Networks: Growth and Functionality

Martin George FRIEDL

We can only see a short distance ahead, but we can see plenty there that needs to be done.

— Alan Turing

To my family,
and my teachers…

Acknowledgements

As I turn the page on this chapter in my life, I am grateful for the opportunity to thank the ones who helped make my PhD work possible. At the same time, I would like to acknowledge those that have made my time in Lausanne during the PhD so enjoyable. I am afraid I will not be able to do everyone justice in this condensed text, but I will do my absolute best.

First, I would like to extend my deepest gratitude to **Anna Fontcuberta i Morral** for everything she has offered me, both on a personal and professional level. She is a supervisor with seemingly superhuman levels of compassion, kindness and selflessness. Her venerable qualities make her a great source of both professional and academic inspiration. I appreciate that, despite her busy agenda, she always makes time for her students and I greatly valued being able to discuss with her nearly every day. This human element is a big part of what made working at LMSC such a pleasure. Though, more than a just a boss, her friendship is something I will cherish for the rest of my life. Thank you, Anna.

I would like to thank **Yves Leterrier**, **Lincoln J. Lauhon**, **Nicolas Grandjean** and **Philippe Caroff** for taking time out of their busy schedules and agreeing to be on my PhD defense committee. I feel very humbled to have such a highly-qualified panel of experts and very much look forward to the discussion.

I would like to also thank a few of my collaborators. Specifically, thank you to **Dominik Zumbühl** at Uni Basel for our close collaboration throughout my PhD. Thank you for having consistent faith in the project, for devoting a significant amount of your lab's resources to the collaboration and for inviting me to Basel to see how the magnetotransport measurements are done. **Kris Cerveny**, I am very thankful that we got the chance to work together. I appreciated being able to discuss all things quantum with you and I appreciate the patience you showed during those times where you stuck it out with the difficult samples and managed to get some very nice measurements out of them. I additionally appreciated our conversations about everything from longevity to meditation. I would further like to acknowledge **Pirmin Weigele** for his collaborative work and our discussions. A very warm thank you to **Vladimir Dubrovskii** for our fruitful collaborations and his fundamental insights into crystal growth. Equally-important were the collaborations with **Andrés Raya**, **Sara Martí Sánchez** and **Chunyi Huang** so thank you to them; much of this work would not have been possible without their tireless efforts.

Acknowledgements

A very large contribution to life in the lab was my beloved colleagues. My first experience at LMSC was during my first four months of the Master's, having just arrived in Switzerland and feeling a bit overwhelmed with it all. I did a semester project with **Francesca Amaduzzi** on Raman Spectroscopy of InAs nanowires. This was my first dive into the nanowire world and opened my eyes to LMSC as a group which stuck with me. So, thank you **Francesca** and **Esther Alarcón Lladó** for taking me under your wing and opening my eyes up to the field. After this, I came back for the Master's Thesis at LMSC with **Heidi Potts** performing electrical measurements on InAs nanowires. Thank you, **Heidi**, I learned a great deal from you during this time. Your ability to hit a perfect work/life balance is commendable and something I hope to be able to achieve myself one day.

Then came the start of the PhD, a change of topic from nanowires to nanomembranes and along with it my introduction to the world of MBE growth. Thank you to the growers at the time **Gözde Tütüncüoglu**, **Heidi Potts**, **Federico Matteini** and **Jelena Vukajlovic Plestina** for helping me learn the ropes of the big complicated machine that is the MBE. **Gözde**, thank you for patiently passing on to me your process for nanomembrane growth, helping debug my failed growths and the life you brought to every party. **Heidi**, being the only other InAs grower in the group I appreciated your insight and experience on InAs nanowire growth when I was looking to do the same on the nanomembranes. Your enthusiasm when it came skiing, hiking and sailing was refreshing and helped break up the work discussions. Thank you for the fond memories, be it travelling for conferences or during dinners with you, Patrick and Irene. **Federico**, I was always intrigued by our discussions which often strayed from nanowires towards entrepreneurship and technology. Whether you know it or not, you were one of the people that sparked my interest in business and start-ups. For this, I am grateful as I keep my eyes open for the next opportunity. **Jelena**, I am thankful for your helpful advice in cleanroom fabrication which benefited me several times. I am equally grateful for your company at the many conferences, including in St Petersburg, and am very grateful for the family dinners/lunches we've shared. **Daniel Rüffer**, you left already before I began my PhD so I never had the chance to work with you, nevertheless, I learned a great deal from the scripts you left behind. Going through your old codes was like doing digital archaeology on long-lost artefacts of coding wizardry. It pushed me to become a better python coder and I kept discovering useful features you had implemented to control various lab setups. This culminated in being able to use your cryostat scripts for the temperature-dependent Hall measurements which saved me an immense amount of time. For this alone, I owe you a big "thank you!".

Bridging the gap between the old and the new generation of PhD students were the two last graduates, **Dmitry Mikulik** and **Luca Francaviglia**. **Dmitry**, though our research topics didn't have many commonalities, I still appreciated being able to discuss aspects of the cleanroom processes with you and always appreciated the unique perspective you brought to many discussion topics. **Luca**, we shared many things during our time at LMSC, including many hotel rooms, an office and a house. Your calm demeanour and sense of humour always made the time we spent very pleasant, both at the office and otherwise. I have particularly fond

memories of exploring Japan with you during our conference, thank you for this.

In recent years there has been a shift change in the group with the latest batch of fresh PhD recruits coming on-board. Thanks to the new-age III-V MBE crew: **Akshay Balgarkashi**, **Didem Dede**, **Lucas Guniat**, **Nick Morgan** and **Wonjong Kim**. **Akshay**, in our growths, we are often both playing the same game of "where will the indium go?" and I valued having someone to discuss this with to improve my understanding. I have also enjoyed the perspective you bring to other, more spiritual, aspects of my life including discussions of meditation and Buddhism. **Didem**, thank you above all for your patience in taking over the project, my long rambling explanations and also for putting your faith in my past work. Your contagious enthusiasm and inquisitive nature keep me energized and on my toes, perfect preparation for my upcoming defense! **Lucas**, I am very thankful for having worked with you because you bravely walk the fine line of serious intellectual discussion and light-hearted jokes which you (usually) pull off perfectly. I always appreciated your input on growth results as well as discussions about cleanroom fabrication. Though I quickly learned to not tempt you on the subjects of Swiss watches, keyboards or Japanese coffee-making contraptions out of fear of having to postpone my graduation by another year. In all seriousness, I value your friendship and time spent together both in and out of the office. **Nick**, ever since your Master's with Heidi, I was secretly hoping you would stay so you could bring your industrial experience, and love of Tex-Mex to the lab. I think the lab is much richer now that you did and I value very much having been able to discuss all aspects of nanomembrane growth with you. I admire your fortitude and systematic approach in the face of difficult problems, such as nanomembrane growth on silicon. Though, equally-important has been your friendship even outside of work and someone in the lab who can relate with me on my love of peanut butter, among other (often unhealthy) American foods. **Wonjong**, thanks also to you for the shared insight into your fabrication process. Given the sensitivity of your process to any small variation and your ability to get fantastic, reproducible nanowire arrays, I feel like I have learned a lot from you on the fabrication side. Outside of the lab, you've been a fantastic friend and memories of our dinners are something I will always cherish. **Jean-Baptiste Leran**, you're the leader of both MBE crews and you've been here the whole time, steadfast and dependable. I greatly value everything you have done for the whole lab when it comes to keeping the MBE running. Whether there was water pouring into the control electronics or a power cut so bad that it crashed everything in the whole MBE lab, you always had a no-nonsense approach to get the machine back online ASAP. I also appreciated our dinners at your chalet and your generosity when it came to bringing delicious croissants, oysters, fondue and crêpes to the office for us to enjoy.

Then there are the (current) office mates, thank you all for the company and the discussions, academic or otherwise. **Elias Stutz**, thank you for the collaboration on the Zn_3P_2 nanomembranes, without you I don't think my first six months of measurements during the PhD would have ever been published as I moved on to the nanomembrane growth! **Mahdi Zamani**, back when you were doing III-V MBE growth we would often discuss nanowire polarity which

Acknowledgements

Abstract

With the rise of quantum computing and recent experiments into topological quantum computers come exciting new opportunities for III-V semiconductor quantum nanostructures. In this thesis, we explore the scalable fabrication of patterned arrays and branched networks of horizontally-oriented III-V nanowires with potential applications in the highly-relevant fields of topological quantum computing and infrared photodetection. We approach this challenge through the use of selective-area epitaxy applied to the technique of molecular beam epitaxy. The first part of this thesis serves to introduce the reader to the relevant topics of quantum computing and epitaxial crystal growth in the context of molecular beam epitaxy. It continues by touching on the applied topics related to electrical transport in nanostructures and transmission electron microscopy.

The second part of this thesis begins with the main result which is the growth of In(Ga)As nanowires through the use of selective-area GaAs nanomembranes as templates on GaAs $(1\,1\,1)$B substrates. Here, we find that the deposition of InAs on a GaAs nanomembrane favours the growth of an intermixed InGaAs nanowire at the top of the GaAs. We build upon this by also demonstrating the growth of branched wires by patterning branched slits into the SiO_2 mask. Electrical transport is then demonstrated by adding extrinsic dopants that are shown by atom probe tomography measurements to segregate to the top of the wire. Magnetotransport measurements on these wires show diffusive transport and weak localization with coherence lengths on the order of $100\,nm$. In a follow-up publication, we then explore the remote-doping of InGaAs nanowires to improve their electrical properties and achieve quasi-1D transport. We start by optimization of the growth parameters to increase In content in the wires. This is followed by growing a remote-doped structure with which we can to improve the electron mean free path by roughly two orders of magnitude to $250\,nm$. With this, magnetoconductance measurements now show transport in the weak anti-localization regime. At the same time, remote-doped test structures analysed by atom probe tomography uncover a dopant segregation effect taking place during the GaAs nanomembrane growth.

Rounding out the growth on GaAs substrates, the third part of the thesis switches the platform to GaAs $(1\,0\,0)$. Here we find that the GaAs nanomembranes do not grow very much in the vertical direction and as a result, the nanowires grow very close to the substrate. We observe a significant reduction in intermixing between InAs and GaAs which allows for the growth of pure InAs wires. We then describe initial promising results on field-effect transport measurements performed on these nanowires.

The fourth and final section of this thesis addresses the integration of GaAs nanomembranes

on the silicon platform, starting with Si (1 1 1). Here, it is found that different surface treatments before the start of GaAs growth allow for preferential orientation of GaAs nanomembranes. We further discuss the effects of a polynucleated growth regime on the formation of defects, including anti-phase boundaries, and suggest an approach to reduce such defects by encouraging mononucleated growth.

Finally, the thesis is concluded with some closing remarks, an outlook and appendices including everything from extra experiments to a summary of technical lab contributions and paper supplementaries.

Keywords: nanowires · nanoscale membranes · III-V semiconductors · template-assisted growth · selective-area epitaxy · molecular beam epitaxy · heteroepitaxy · transmission electron microscopy · electrical properties · quantum transport

Résumé

Avec l'essor des ordinateurs quantiques et les récents développements dans le domaine des ordinateurs quantiques topologiques, de nouvelles opportunités s'offrent aux nanostructures quantiques semi-conductrices III-V. Dans cette thèse, nous explorons la fabrication évolutive de maillages et réseaux ramifiés de nanofils orientés horizontalement sur un substrat. Celles-ci ont des applications potentielles dans le domaine des ordinateurs quantiques topologiques et des photodétecteurs infrarouges. Nous abordons ce défi en utilisant l'épitaxie par zones sélectives appliquée à la technique de l'épitaxie par jets moléculaires.

La première partie de cette thèse sert à présenter au lecteur les thèmes pertinents sur les ordinateurs quantiques et de la croissance de cristaux épitaxiaux dans le contexte de l'épitaxie par jet moléculaire. Elle continue en abordant des sujets appliqués liés au transport électrique des nanostructures et à la microscopie électronique à transmission.

La deuxième partie de cette thèse commence par le résultat principal qui est la croissance de nanofils In(Ga)As sur des nanomembranes GaAs fabriquées par épitaxie à zones sélectives comme support des substrat de GaAs (1 1 1)B. Nous observons ici que le dépôt d'InAs sur une nanomembrane de GaAs favorise la croissance d'un nanofil InGaAs mixte au sommet du GaAs. Nous nous appuyons sur cela pour démontrer également la croissance de fils connectés en gravant des ouvertures ramifiées dans le masque de SiO_2. Le transport électrique est ensuite démontré en ajoutant des dopants extrinsèques. Des mesures tomographiques à sonde atomique ont montré leur ségrégation au sommet du fil. Les mesures de magnétotransport effectuées sur ces fils montrent un transport diffusif en mode de faible localisation avec des longueurs de cohérence d'environ 100 nm. Dans une publication ultérieure, nous explorons le dopage à distance de nanofils InGaAs pour améliorer leurs propriétés électriques et réaliser un transport quasi-1D. Nous commençons par une optimisation des paramètres de croissance pour augmenter la concentration d'indium dans les nanofils. Ceci est suivi par la croissance d'une nanostructure dopée à distance avec laquelle nous observons une amélioration du libre parcours moyen des électrons d'environ deux ordres de grandeur à 250 nm. Simultanément, des structures de test dopées à distance analysées par tomographie à sonde atomique révèlent un effet de ségrégation des dopants se produisant pendant la croissance des nanomembranes GaAs.

Pour compléter la section sur la croissance sur des substrats en GaAs, la troisième partie de la thèse traite des croissances sur des substrat de GaAs (100). Nous constatons ici que les nanomembranes de GaAs ne croissent pas beaucoup dans la direction verticale et que, par conséquent, les nanofils se développent très près du substrat. Nous observons une réduction

significative du mélange entre InAs et GaAs, ce qui permet la croissance de fils InAs purs. Nous décrivons ensuite les premiers résultats prometteurs des mesures de transport à effet de champ effectuées sur ces nanofils.

La quatrième et dernière section de cette thèse traite de l'intégration des nanomembranes de GaAs sur la plateforme silicium, en commençant par la croissance sur du Si (1 1 1). Ici, on constate que différents traitements de surface avant le début de la croissance de GaAs permettent une orientation préférentielle des nanomembranes de GaAs. Nous discutons en outre des effets d'un régime de croissance polynucléé sur la formation de défauts, y compris les limites d'antiphase, et proposons une approche permettant de réduire ces défauts en encourageant la croissance mononucléée.

Enfin, la thèse se termine par quelques remarques finales, une perspective et des annexes-contenant des expériences supplémentaires, un résumé des contributions techniques et les compléments aux articles scientifiques.

Mots-clés : nanofils · membranes nanométriques · semiconducteurs III-V · croissance assistée par modèle · épitaxie à zone sélective · épitaxie par jet moléculaire · hétéroépitaxie · microscopie à transmission d'électrons · propriétés électriques · transport quantique

Contents

Contents

Contents

List of publications

First-Authored Publications

1 <u>M. Friedl</u>, K. Cerveny, P. Weigele, G. Tütüncüoglu, S. Martí-Sánchez, C. Huang, T. Patlatiuk, H. Potts, Z. Sun, M. O. Hill, L. Güniat, W. Kim, M. Zamani, V. G. Dubrovskii, J. Arbiol, L. J. Lauhon, D. M. Zumbühl and A. Fontcuberta i Morral. Template-Assisted Scalable Nanowire Networks. *Nano Letters* **18**, 2666 (2018)

2 E. Z. Stutz*, <u>M. Friedl</u>*, T. Burgess, H. H. Tan, P. Caroff, C. Jagadish and A. Fontcuberta i Morral. Nanosails Showcasing Zn_3As_2 as an Optoelectronic-Grade Earth Abundant Semiconductor. *Phys. Status Solidi RRL* **13**, 1900084 (2019) *equal contribution

3 A. M. Raya*, <u>M. Friedl</u>*, S. Martí-Sánchez*, V. G. Dubrovskii, L. Francaviglia, B. Alén, N. Morgan, G. Tütüncüoglu, Q. M. Ramasse, D. Fuster, J. M. Llorens, J. Arbiol and A. Fontcuberta i Morral. GaAs Nanoscale Membranes: Prospects for Seamless Integration of III-Vs on Silicon. *Nanoscale* (under review) *equal contribution

4 <u>M. Friedl</u>*, K. Cerveny*, C. Huang, D. Dede, M. Samani, M. O. Hill, W. Kim, L. Güniat, T. Patlatiuk, J. Segura-Ruiz, L. J. Lauhon, D. M. Zumbühl and A. Fontcuberta i Morral. Dopant Segregation and Weak Anti-localization in Remote-Doped Nanowire Y-Branches. (in preparation) *equal contribution

Co-Authored Publications

1 H. Potts, <u>M. Friedl</u>, F. Amaduzzi, K. Tang, G. Tütüncüoglu, F. Matteini, P. C. McIntyre and A. Fontcuberta i Morral. From Twinning to Pure Zincblende Catalyst-Free InAs(Sb) Nanowires. *Nano Letters* **16**, 637 (2016)

2 H. Potts, Y. van Hees, G. Tütüncüoglu, <u>M. Friedl</u>, J.-B. Leran and A. Fontcuberta i Morral. Tilting catalyst-free InAs nanowires by 3D- twinning and unusual growth directions. *Crystal Growth & Design* **17**, 3596 (2017)

3 H. Potts, N. P. Morgan, G. Tütüncüoglu, <u>M. Friedl</u> and A. Fontcuberta i Morral. Tuning growth direction of catalyst-free InAs(Sb) nanowires with indium droplets. *Nanotechnology* **28**, 054001 (2017)

4 J. Vukajlovic-Plestina, W. Kim, V. G. Dubrovski, G. Tütüncüoglu, M. Lagier, H. Potts,

Contents

1 Motivation & Context

Following several decades of Moore's Law scaling, further increases in field-effect transistor (FET) densities are becoming increasingly difficult and expensive to realise in general [1]. This can be seen by the delay in releasing new technology nodes, for example, Intel's 10 nm Cannon Lake processors were planned for release at the end of 2016, though due to production issues, the release had to be pushed back to 2018. While certain manufacturers are dealing with density scaling issues better than others, the challenge of making smaller transistors is only going to get increasingly difficult as feature sizes approach atomic length scales. Putting things into perspective, current commercial FinFETs at the 10 nm node are only about 7 nm wide which corresponds to only ~26 Si atomic planes!

Below the 10 nm node, quantum effects begin to play an important role as tunnelling currents and short channel effects make it very difficult to keep the transistors in the off state. Consequently, maintaining low static power dissipation is a significant obstacle. This is being combatted by moving to structures with increased electrostatic control over the channel, such as FinFETs and eventually wrap-gate nanowire (NW) geometries. This effectively increases the barrier height when the transistor is off, thus reducing the tunnelling current and static power dissipation. Nevertheless, process variability, specifically in the transistor threshold voltage, is another significant challenge [2]. With channel widths below 10 nm fabricated using a self-aligned quadruple patterning (SAQP) approach [3, 4] even slight etching variability over a single wafer can broaden the distribution of threshold voltages of transistors, resulting in yield problems. Furthermore, in such scaled structures, differences in the electrostatic environment around a channel due to trapped charges and process variations can also significantly broaden the distribution of transistor threshold voltages [5].

Still, many ideas are being proposed to continue the Moore's Law trend using traditional complementary metal-oxide-semiconductor (CMOS) technologies, including moving to vertically-integrated gate-all-around NW transistors [6–8]. While this may temporarily alleviate the physical scaling constraints, the challenges of static power dissipation and increased sensitivity to process variation will only make it increasingly difficult to scale down further. Thus, many so-called "More than Moore" approaches are being devised to achieve better perfor-

mance at the same physical scales [9]. The development of these beyond-CMOS ranges from using tunnel field-effect transistors (TFETs) with the promise of low sub-threshold swings [7, 10, 11] to using high-mobility materials to increase transistor speeds [12–14]. In all cases, research into new materials that can be integrated with silicon is a significant part of the research effort.

Apart from "re-engineering" the transistor, entirely new computing paradigms are also being explored for their possible benefits in solving practical problems. Magnetic computing schemes for example, have the advantage of not having any current flow and therefore a computation could theoretically only consume close to the minimum thermodynamic energy needed to perform a calculation [15]. Other approaches explore ultra-parallelized approaches such as DNA computing which use millions of DNA strands to solve specific problems by highly-parallelized chemical interactions [16–18]. While for DNA computing a universal computational architecture for solving many problems is quite a challenge to implement, the approach of quantum computing is one that promises to combine a highly-parallelized approach with the practicality of universal computation.

1.1 Quantum Computing

The concept of quantum computing was first introduced by Richard Feynman in 1981 during his famous lecture "Simulating physics with computers" [19]. Feynman proposed that the optimal way to simulate the quantum world would be by using a quantum simulator which could take the form of a quantum computer. In such a quantum simulator, whole quantum systems could be simulated through the controlled interactions of many quantum particles. Indeed still today, quantum simulation is one of the most promising applications of quantum computers because the simulation of quantum systems is extremely computationally expensive for classical computers [20, 21]. Currently, due to the exponential scaling of quantum states with the number of qubits, classical simulations of quantum systems are limited to ~50 qubits [22]. To, therefore, prove that quantum computers are superior to classical ones (for certain problems), also given the controversial name "quantum supremacy", a minimum of around 50 qubits is needed [23]. Due to the enormous complexity involved in building and, more importantly, reliably operating these machines, arriving at the ~50 qubit number and proving that quantum computers do have an advantage over classical computers is proving very challenging. The latest reports, however, look promising and suggest this may have recently been achieved by Google [24].

1.1.1 Complexity Theory

An important question to ask oneself before venturing into the endeavour of building a quantum computer is: "Once we have a quantum computer, what do we do with it?" To understand where quantum computers stand compared to classical computers when solving various kinds of problems, we need to delve into computational complexity theory.

Computers today are highly-refined computing machines with billions of transistors in every central processing unit (CPU). Nevertheless, each transistor computes part of a solution to a given calculation. To have a faster CPU and perform many calculations, more transistors are simply condensed on a single chip to all work in parallel. The problem arises once the density cannot be scaled any further due to previously-mentioned scaling constraints. For computationally-expensive problems, such as determining the prime factors of a large number, the solution can take a long time to compute even with billions of transistors working towards the solution.

The complexity of a given problem can be classified by how the computing time scales with the number of inputs. Visual representation of the categories associated with complexity theory is given in Figure 1.1. Polynomial (P) time problems are problems that classical computers can solve in polynomially increasing timescales. This means that as the algorithm input size n is increased, the computation time scales as n^x where $x > 1$. These are generally considered problems that are not difficult for classical computers to solve. The difficulties arise with non-deterministic polynomial (NP) time problems. These consist of a more difficult class of problems that are classically solvable in longer-than-polynomial time but are still verifiable in polynomial time. Our society depends heavily on problems in this category for encryption schemes. In one of the first encryption schemes, Rivest–Shamir–Adleman (RSA) encryption, the security lies in the fact that factoring the product of two large prime numbers is not feasible in a reasonable (polynomial) amount of time on a classical computer [25]. On the other hand, if one of the secret prime factors is known, it is easy to verify that it is, in fact, the correct solution.
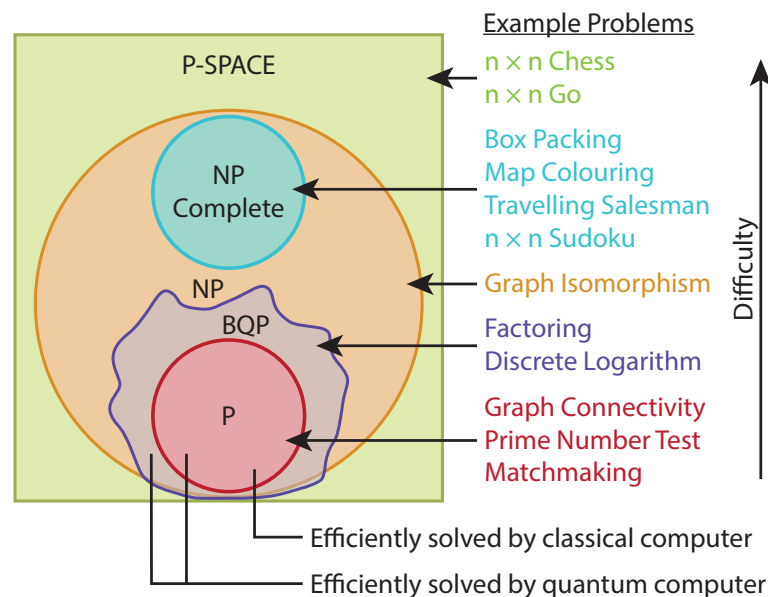
Figure 1.1 – Diagram showing the various types of problems classified based on their complexity. Figure heavily inspired by Aaronson [26].

It is in these certain kinds of problems where quantum computers promise to have a large advantage over classical computers. Qualitatively, in a universal quantum computer with N quantum bits, the bits exist in a coherent state that is a quantum superposition of 2^N possible classical solutions. Through successive gate operations on the coherent state, it is possible to manipulate it in such a way that the measurement probability of the solution is enhanced through constructive interference while the wrong solution destructively interfere. Thus, once the state is ultimately measured, it yields the solution to the problem with a high probability. Because an extremely large (2^N) number of classical states can be represented by a relatively small number of N qubits, in a sense, quantum computers perform the equivalent of a highly parallelized computation on many classical states simultaneously.

Due to the nature of quantum information systems, writing algorithms for quantum computers requires a drastic shift from conventional programming with a good understanding of quantum information theory. Though the learning curve can be steep, many resources exist to learn about quantum algorithms one of the most comprehensive of which is by Vogel [27], for those that are interested. Many quantum computing algorithms have already been developed, many of them offering the previously-mentioned speed-up over classical computers [28–30] while future applications that are being researched include quantum machine learning [31]. Also worth mentioning is that the development of quantum algorithms has even led to the improvement of certain classical algorithms [32]. Especially in the noisy intermediate-scale quantum (NISQ) era that we are about to enter [33], as qubits are scarce, quantum algorithms must continue to be streamlined since lack of hardware scalability can be compensated to some degree by more efficient algorithms.

1.1.2 Decoherence

In any real-world quantum computer, the qubits cannot be fully isolated from the environment. Because of this, there will be some minimal environmental interaction, whether it be through phonons, electric fields, etc. When these interaction occurs, the carefully-prepared coherent qubit state becomes entangled with the many degrees of freedom that exist in the environment. Consequently, the desirable quantum interference effects upon which quantum computing relies on get suppressed, introducing errors into the computation [34]. When this happens for small, quick calculations they can simply by restarted. The problem arises when an algorithm with many sequential gate operations takes longer to complete than the coherence time of the qubits. This is exacerbated when scaling up to larger numbers of qubits because the probability of having a qubit decohere during the calculation approaches one. Furthermore, for larger calculations with many steps simply restarting the whole calculation is not possible. Instead, quantum error correction (QEC) hardware/code is used to add redundancy and to correct for any errors that occur during the calculation. In fact, the amount of QEC that has to be constantly performed to correct for errors will be so great that it is believed that the large majority of future quantum computer's resources will be spent on performing QEC [35].

As any useful quantum computing algorithms will likely have to have (at least) hundreds of logical qubits employing multiple orders of magnitude more sequential gate operations, there has been an immense effort put into developing theoretical QEC schemes. One of the most error-resistant class of QEC are so-called surface codes. Surface codes are a promising type of QEC as they have been theorized to work even at relatively high error rates of up to 3% [36]. The disadvantage of these is that the number of physical qubits providing the error correction can be very large, around 104 physical qubits per single logical qubit, with even more physical qubits required for higher error rates [37].

1.1.3 Current State of Quantum Computing

Today, many competing quantum computer architectures are being supported to various degrees by different research groups and industry players. Table 1.1 shows a summary and comparison of some of the different kinds of quantum computing architectures that currently exist.

Architecture	Dephasing Time (T_2^*)	Gate Operation Time	# of Qubits	Single Qubit Gate Error
SC Qubits	100 μs [38]	~10-100 ns [38, 39]	19 [40]	<0.1% [41]
QD Qubits	100 μs [42]	~100 ns [42]	4 [43–45]	<0.1% [42]
Ion Qubits	>10 min [46]	~1 μs [47]	7 [48]	<0.1% [49]
Topo. Qubits	>1 min est. [50]	10-100 ns est. [51]	0	-

Table 1.1 – Comparison of state-of-the-art qubit architectures.

Gate fidelity, the percentage of time that a gate operation is successful, is equally, if not more important than the coherence time of the qubits. Conversely, the gate error rate describes the portion of gate operations with introduce errors into the calculations.

While there are many specific ways to reduce decoherence and gate-induced errors, industry has polarized into two general approaches for one day reaching a practical quantum computer. The first approach is that of using very large numbers of qubits and deal with errors by performing QEC. This is being undertaken by most companies, including Google, IBM, and Rigetti working on SC qubits, but also by newer companies employing trapped ion systems such as IonQ and AQT. This method uses unprotected, relatively short-lived but easy-to-build qubits in large numbers. Their large numbers (eventually in the millions/billions of physical qubits), combined with QEC schemes, would make up for their short coherence times to enable universal quantum computation using a few thousand logical qubits.

On the other hand, the approach employed by Microsoft is slightly different in that they are developing topological qubits with, theoretically, much longer coherence times and lower error rates [50, 52]. The advantage of this approach is that they would need to perform much less QEC and they could therefore have orders of magnitude less physical qubits to make an

equally powerful quantum computer. However, the disadvantage of this approach is that, unlike SC qubits that have been extensively studied in many groups all over the world, a working topological qubit (to the best of our knowledge) has never been demonstrated. It is thus a higher-risk approach but one that holds a greater reward if it does work.

1.2 Majorana Fermions

Topological qubits have become a very important topic in the field of quantum computing. This is because topological qubits have been predicted to have exceptionally long coherence times due to their inherent topological protection. Various kinds of quasi-particles and systems have been proposed, though Majorana fermions (MFs) seem to be the most experimentally-accessible. As such, there has recently been a surge of research predicting their behaviour, gathering experimental proof of their existence and architectures for using them as qubits in a topological quantum computer.

These quasi-particles were first proposed to exist by Italian physicist Ettore Majorana in 1937 [53]. He theorized that, in contrast to common Dirac fermions (all fermions in the standard model, except possibly neutrinos), other non-Dirac fermions may exist which have non-abelian properties. This means that exchanging these particles changes their wave-function in some non-trivial way and can for example introduce a phase offset.

For decades, it was not apparent in which sort of physical systems it would be possible to observe these exotic quasi-particles. The first mention of MFs in a physical system were suggested in an important work by Read and Green [54] in 1997 where they showed that in a 2D p-wave superconductor, vortices could bind Majorana zero modes (MZMs). A few years later, Kitaev [55] took this to 1D and proposed his seminal chain model with which he described the existence of MZMs at the ends of a 1D p-wave superconductor. He theoretically described how within a 1D p-wave superconductor so-called Majorana operator pairing (and annihilation) occurs between adjacent cooper pairs such that at each end of the 1D wire a single unpaired Majorana bound state is left, as illustrated in Figure 1.2.
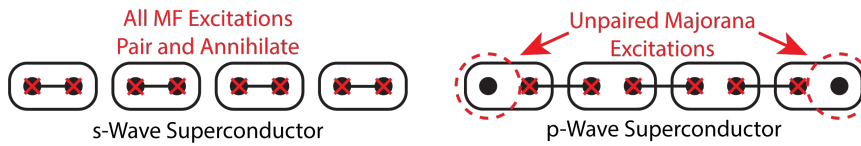
Figure 1.2 – Illustration of the Kitaev chain model describing two possible scenarios for Majorana pairing. Only scenario on the right leads to unpaired Majorana particles at the ends of the 1D chain.

Despite the fact that p-wave superconductors do not readily exist in nature, later works proposed ways to circumvent this by producing "effective" p-wave superconductors by combining existing materials. Using a theoretical approach, Fu and Kane [56] first looked at the superconducting proximity effect between an s-wave superconductor and a topological insulator. They

found that the resulting material had effectively the same properties as p-wave superconductor and could support MZMs. In 2010, other theoretical reports showed that the same could be obtained using a high spin-orbit semiconductor in a strong magnetic field [57, 58]. Thus, taking a common s-wave superconductor and putting it in close proximity to a semiconductor NW allows for cooper pairs to tunnel into the NW. If then Zeeman splitting is induced by applying a strong magnetic field and the NW material has a high enough spin-orbit coupling, one creates an effective p-wave superconductor with a Hamiltonian similar to the one proposed by Kitaev. Such a system could, in theory, be able to host MZMs.

1.2.1 Recipe for Majorana Fermions

Experimentalists have proposed a list of ingredients that would be needed for the experimental demonstration of MFs. This can be summarized by the following recipe: Starting with a normal 1D semiconducting NW, the conduction band of both spin up and spin down electrons are degenerate, as shown in Figure 1.3a. If instead we use a semiconductor NW with high spin-orbit coupling, the conduction bands of each spin shift in opposite directions, breaking the spin degeneracy within the wire (Figure 1.3b). If a magnetic field is then applied to the nanowire, it induces a Zeeman splitting, E_z (Figure 1.3c). Finally, the last required ingredient is to create a superconducting gap, which is done by inducing superconductivity in the NW from a nearby s-wave superconductor (Figure 1.3d).

(a) Regular semiconductor.

(b) Add high spin-orbit coupling.

(c) Magnetic field causing Zeeman splitting.

(d) Proximitize with superconductor.
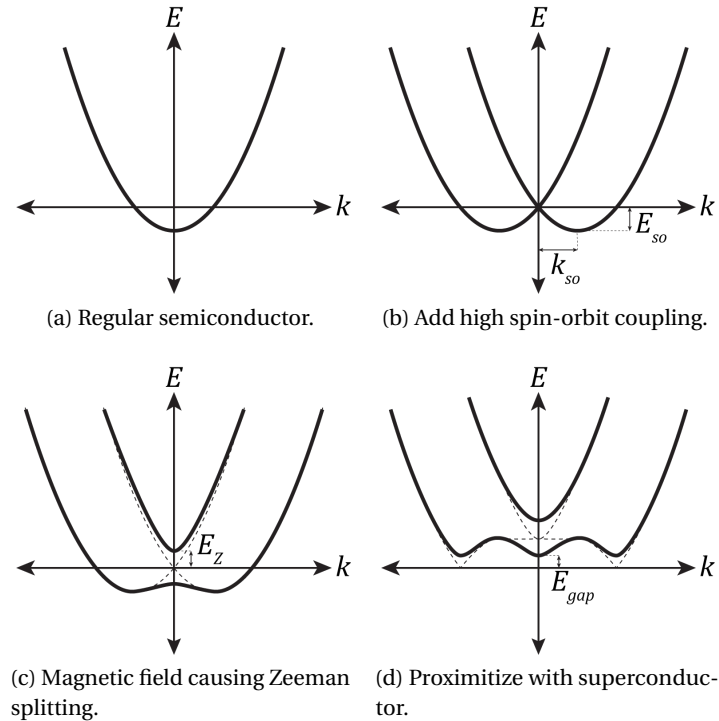
Figure 1.3 – Recipe for Majorana Fermions.

1.2.2 MF-Based Quantum Computing

The non-abelian characteristics of MFs lead to very interesting possibilities for quantum computing. Proposed approaches for building qubits based on MFs involve encoding quantum information into a minimum of four MFs hosted on two superconducting NWs islands [52, 59, 60].

The method by which gate operations are achieved on MF-based qubits can be broadly divided into two categories: physical manipulation of MFs and measurement-based approaches. The exchange of non-abelian particles creates a non-trivial change in the state of the quantum system. Exploiting this, multiple exchanges of MFs in a network of Y-junctions can thus be used to manipulate a topological qubit and implement gate operations [61–68].

More recently, measurement-based approaches have been proposed in which, instead of physically braiding the MFs, the computation is performed by successive parity measurements on groups of MFs [52, 59, 67, 69, 70]. Such so-called projective parity measurements have the same effect as adiabatic braiding of MFs without having to physically move them. This approach has the advantage of simplifying the device fabrication, as branched NW geometries for physical braiding of MFs are no longer required. At the same time, these kinds of schemes still benefit from topological protection.

However, one of the drawbacks of topological quantum computation with MFs is the fundamental problem that the available gates only make up a Clifford-complete set which is a only subset of what is needed for a universal quantum computation [62, 71]. Luckily, a Clifford-complete set of gates can be combined with a single non-Clifford gate in order to achieve universal quantum computation. This however means that at least part of the computation will not benefit from topological protection. Many designs have been proposed to augment MF-based architectures with other kinds of qubits in order to get to a universal set of gates [52, 68].

There has been increasing interest specifically in combining gate-defined quantum dots with MFs in order to perform quantum computation without physical braiding of MF excitations [52, 59, 69, 70, 72]. In such approaches, gate-defined quantum dots in between MFs can be tuned to allow adjacent MFs to interact and/or perform readout operations. An example of such an architecture is given in Figure 1.4.

Finally it should also be noted that while the significant challenges associated with realizing a MF-based qubit are slowing down the experimentalists, theorists continue to forge ahead with exciting new architectures and proposals involving even more exotic quasiparticles. Two examples include Fibonacci anyons which hold the promise of fully topologically-protected universal quantum computation [73, 74], and parafermions which have been suggested to allowing topological quantum computation either without strong magnetic fields [75] or without the need of a superconductor [76].
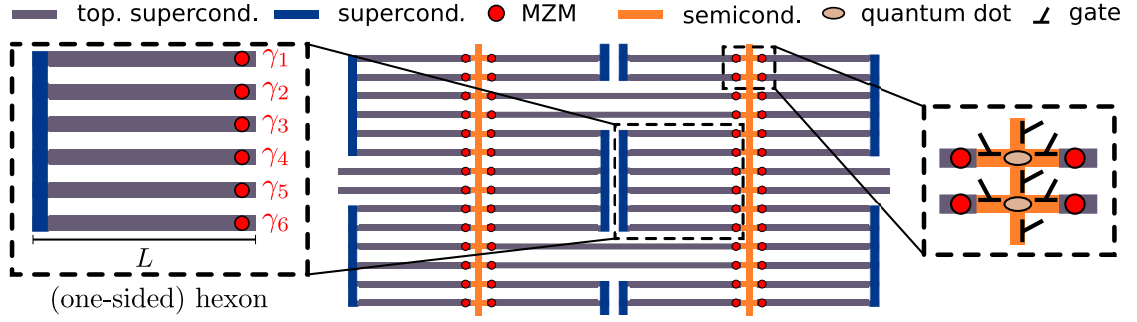
Figure 1.4 – Illustration of a proposed scalable MF-based quantum computing architecture based on semiconductor nanowire networks proximitized by a superconductor. Reproduced from Karzig *et al.* [52] with permission from the American Physical Society.

1.2.3 Dephasing Time Limitations of Topological Qubits

A challenge in achieving long-lifetime topological qubits was described in 2012 by Rainis and Loss [77] where they identified that a likely limitation to the coherence of a proximitized topological qubit would be the tunnelling of a free electron from the environment into the superconducting NW. Known as quasi-particle poisoning, this has the effect of changing the parity of the bound state and thus causing decoherence of the quantum state. They went on to estimate the timescales at which poisoning events occur using quantitative results from experiments and concluded that such Majorana qubit lifetimes likely would range from 10 ns to 100 µs. This was cause for some concern as 100 µs is roughly the same dephasing time achieved by current SC qubits and thus such MF-based qubits would offer no advantage over SC qubits.

In 2015, Higginbotham *et al.* [78] measured the quasi-particle poisoning time and estimated that the parity lifetime of the bound state was ~10 ms. This was an encouraging result, suggesting that a MF-based qubit would in fact be able to achieve long coherence times. To further increase the coherence times of topological qubits, architectures that protect against quasiparticle poisoning (QPP) are being proposed. Most of these approaches involve "charge protecting" the superconducting island by making it large enough that its Coulomb charging energy is large enough so as to make it energetically unfavourable for a free electron to tunnel into the island from the environment [52, 59]. Current estimates of the coherence times in such charge-protected qubits have been estimated by Knapp *et al.* [50] to be on the order of minutes.

1.2.4 Experimental Systems for the Observing MFs

Since the first experimental signatures of MFs in 2012 in vertically-grown III-V NWs [79–81], both incremental improvements to these systems as well as the investigations of new systems have been performed in order to further understand these phenomena. The III-V material systems in which MFs are being actively investigated can be broken down into three main

categories: vertically-grown NWs, gated two-dimensional electron gas (2DEG) systems and in-plane selective-area growth (SAG) NWs. A good review of the progress in the field was given last year by Lutchyn *et al.* [82].

For many reasons, vertically-grown NWs were the initial system in which MF signatures were observed. These types of wires have been around for a long time [83] and as a result, a deep level of understanding has been achieved in the field. This level of understanding includes a large degree of control over the crystal structure during growth [84–89] and has been augmented by an equally-good understanding of their electrical transport properties [90–94]. Since the first experiments, groups have focused on improving the fabrication of MF devices using such wires by implementing cutting-edge growth techniques. One of the most impressive growth advances in this field has been the achievement of growing an epitaxial aluminium superconducting layer on the side of a InAs NWs [95]. Though this method isn't without its critics [96], it has been shown to greatly reduce the number of interfacial traps and was shown to give a hard superconducting gap [97]. Other notable advancements in the field include the growth of NW crosses or junctions where the direction and position of the NWs has been controlled to yield intersecting NW structures for future MF braiding experiments [98–101].

The second category of systems that are being investigated for MFs are those based on 2DEGs. This approach leverages the in-depth knowledge of the 2DEG growth community to create high-mobility InAs/GaAs 2DEGs which, similarly to vertically-grown NWs, can then be prox-imitized with a superconducting epitaxial aluminium layer for MF experiments [102]. The elegant aspect of this approach is that the aluminium can be patterned and acts as a gate to electrically-define the NW in the 2DEG while at the same time inducing superconductivity in it. The result is a very clean, hard-gapped system in which subtle transport features in the topological regime can be observed due to the lack of disorder caused by semiconductor surfaces [103–105]. These detailed investigations into the subtle behaviour of Majorana-like features have provided further evidence to suggest the existence of MFs predicted by theory.

The last category is that of SAG NW systems and is the approach described in this thesis. This is an approach in which NWs are now grown in-plane by selective-area epitaxy (SAE) (described in Section 2.3), yielding several advantages of vertical NW growth. The first reports using this relatively new approach with potential applications to MF investigations only appeared in the last few years [106–109] with the most recent reports even implementing epitaxial aluminium superconducting contacts [110–113]. The advantage of this method over vertical NW growth is the improved the scalability granted by the patternable SAE mask. This allows for a finer degree of control over NW position and growth direction while also enabling the growth of highly-branched structures in a scalable way.

2 Theoretical & Experimental Foundations

This chapter is meant to serve as an introduction to the concepts and techniques that one should generally be familiar with to understand the experimental results discussed in the following chapters. I first introduce the basic concepts of general 2D crystal growth (independent of growth technique), before moving on to the specific case of adding a growth mask to obtain SAE. Here, I tried to again start with general SAE before moving towards specific cases, finishing with SAE for NW growth and a comparison between various NW growth techniques. Electrical transport is then also introduced in the following section, beginning with classical concepts before touching on relevant key topics in quantum transport. Lastly, in addition to concepts, I felt that it is essential to also describe some of the experimental tools and methods used extensively throughout this thesis. Given the number of processes used in the cleanroom, this could have been a very long section! I, therefore, decided to focus on a few key techniques, namely molecular beam epitaxy (MBE): for growth, transmission electron microscopy (TEM): for high-resolution analysis of grown samples and lamella lift-out by focused ion beam (FIB): for preparing thin samples to image by TEM.

2.1 Epitaxial Growth

Epitaxy refers to the ordered arrangement (Greek: *taxis*) of atoms on top (Greek: *epi*) of a another crystal. The term was first coined roughly 100 years ago and today is used regularly to describe an approach to produce or "grow" semiconductor crystals through an inherently bottom-up approach. When atoms are sent on a substrate surface at a high enough temperature, they diffuse until they find a lattice site which minimizes the total system's energy. The grown crystal structure thus matches that of the substrate with no discontinuity meaning that the grown crystal has what is called an epitaxial relationship with the substrate. If the atoms are not able to find an appropriate lattice site due to too-low growth temperature, incompatible substrate or because the high growth flux causes them to get covered first, this can lead to island formation and polycrystalline/amorphous growth which in this research is undesirable.

The term bottom-up refers to the method by which complex structures are created through material deposition and self-assembly (ex: epitaxial growth). It is often used in contrast with top-down approaches, meaning fabrication of complex structures by subtraction of material (ex: photolithography + etching). The tools in the toolbox of a top-down process engineer generally involve various approaches for large-area deposition, patterning and selective removal. On the other hand, when performing bottom-up growth of structures one must instead take into careful consideration the thermodynamic and kinetic effects as these are the forces that drive the formation of nanostructures during their growth. Often these two approaches can be combined, as top-down approaches are widely-used technologies while the bottom-up offers very fine control over interfaces and dimensions while being able to overcome material mismatch [114] and utilizing smaller amounts of expensive materials. SAE is a great example of an epitaxial growth method that utilizes aspects of both top-down fabrication and bottom-up epitaxial growth.

2.1.1 Driving Force for Epitaxial Growth

Epitaxial growth is fundamentally a crystallization process, involving a phase change from a liquid or gas to a solid. As with all phase changes, thermodynamics will dictate whether or not it will occur. The driving force behind crystallization is known as the Gibbs free energy. The term Gibbs free energy can be summarized as the reversible work (energy) that can be extracted from a closed system at constant temperature and pressure. This is very elegantly described in more detail by other sources, such as Refs [115, 116], I, therefore, refer the reader there for a more rigorous explanation. Though, for understanding epitaxial growth, it is sufficient to know that a system tends to evolve by minimising its Gibbs free energy. Furthermore, once the system has reached its minimum energy, it is said to have reached its thermodynamic equilibrium.

In a system such as an MBE growth chamber, this means that the atomic growth species will self-assemble into a crystal only if their solid form is energetically favourable, meaning the system can decrease its Gibbs free energy by crystallizing into a solid. This decrease in Gibbs free energy is thus the driving force behind the growth of the crystal. Gibbs free energy is composed of both interface and bulk contributions. Therefore, the growth will tend to proceed in a way that minimizes interface energy which is already enough to be able to explain the fundamental processes involved in epitaxial crystal growth.

2.1.2 2D Growth Modes

The most basic case of epitaxial growth is simple 2D layer growth. The description of how crystal epitaxy proceeds in the 2D case is a very good precursor to describe growth within a constrained area, as in SAE.

Starting with the substrate, epitaxial growth is highly dependent on the substrate that is used

as this serves as a platform upon which the deposited atoms (given enough thermal energy) will arrange themselves. Ideally, the atoms in the grown material a continuation of the same crystal structure of the substrate without any defects. This is relatively straightforward then the substrate and the grown material are the same, a case known as homoepitaxy. However, when the substrate and grown materials differ, this is called heteroepitaxy. Heteroepitaxy is typically more challenging as the two materials have a different lattice constant, thermal expansion coefficient and sometimes even crystal structure. As a result, strain accumulation and/or defect formation (described in Section 2.2) in the grown material can occur. Despite the challenges, the rich number of material combinations make heteroepitaxy a very interesting and active area of research. A significant portion of the work in this thesis can be boiled down to trying everything possible to get around the difficulties associated with heteroepitaxial growth.

To understand the method by which these defects are formed I will begin by describing the physical effects that play a role in epitaxial growth. One can imagine atoms impinging on a surface made of the same material (homoepitaxy) as shown in Figure 2.1. Note that the method by which the atoms arrive (adsorb) on the surface is defined by the growth method (MBE, MOCVD, etc.), however, once the atoms are on the surface, the surface physics is, to a first approximation, common across different growth methods. In Figure 2.1 we can see the basic processes involved in 2D epitaxial crystal growth. First, the incoming flux supplies atoms that become adsorbed on the surface, thus becoming adatoms. At sufficiently high temperatures, these weakly-bonded adatoms have enough energy to diffuse on the surface of the crystal. They have some temperature-dependent chance of desorbing from the surface and being lost. Alternatively, there is also a probability that the adatoms on the surface spontaneously begin to nucleate a monolayer or crystal. Though, due to the low nucleation probability and long adatom diffusion lengths at high temperatures, step-flow growth is the most likely mechanism through which a monolayer grows. In this case, the monolayer is randomly nucleated and this island grows progressively larger, as almost all incoming adatoms find their way to the growth front because it is highly energetically favourable (minimizes energy due to dangling bonds at the surface). As a result, the monolayer grows quickly. All of these stochastic processes happen simultaneously on the surface with different probabilities and as a whole, they contribute to the macroscopic growth of the layer.

We turn now to the heteroepitaxial case, where it is necessary to begin to look at the energy contribution of the interfaces to describe the growth. Before we begin, it is important to note that, in reality, subtleties such as surface reconstructions and bonding configurations need to be considered. Here, however, the treatment has been boiled down to the fundamentals to help explain the general concepts. Let us define γ_s as the surface energy density of the substrate, γ_d as the surface energy density of the deposited layer and γ_i as the interface energy density between the substrate and the deposited layer. The growth will depend on the relationship between γ_s and $(\gamma_d + \gamma_i)$. If $\gamma_s \geq (\gamma_d + \gamma_i)$ then the growth of the layer is energetically favoured and it will grow layer by layer in the Frank-van der Merwe growth mode shown in Figure 2.2a. This is also the case for homoepitaxy because $\gamma_s == \gamma_d$ while γ_i is very small because the
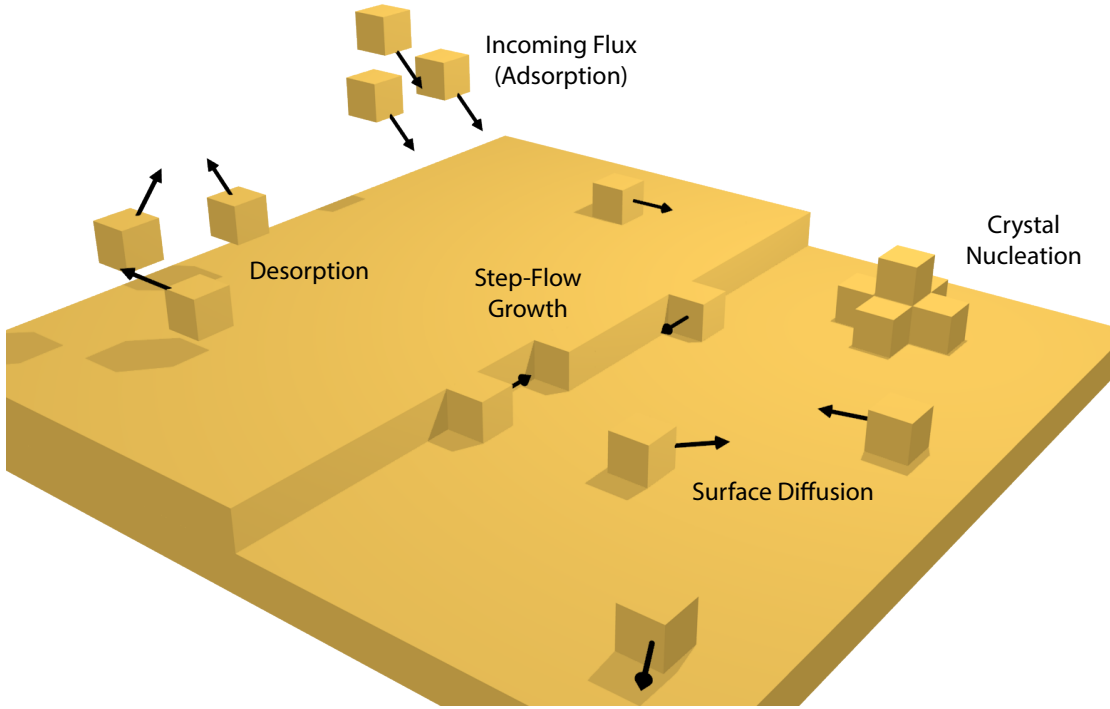
Figure 2.1 – Figure depicting various processes taking place at the atomic scale during 2D layer growth.

substrate and grown materials are the same. If instead $\gamma_s \ll (\gamma_d + \gamma_i)$ then the system will tend to leave as much of the substrate uncovered as possible, despite the deposited material. This highly 3D form of growth is referred to as Volmer-Weber growth and is depicted in Figure 2.2b. Finally, there exists an intermediate regime where $\gamma_s < (\gamma_d + \gamma_i)$ called Stransky-Krastanov growth, depicted in Figure 2.2c. Here, the layer begins to grow in the Frank-van der Merwe, but beyond a certain thickness (called the critical thickness) the layer is so highly strained that it switches to the 3D Volmer-Weber growth mode.

(a) Frank-van der Merwe   (b) Volmer-Weber   (c) Stransky-Karastanov
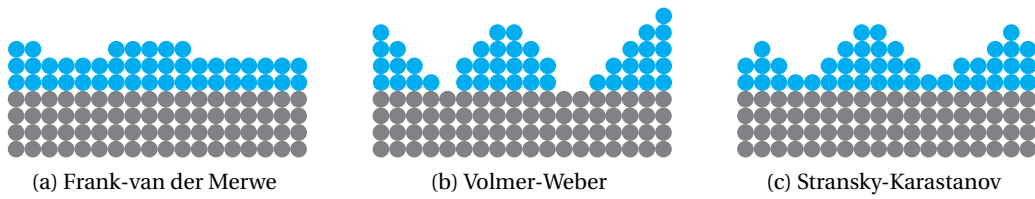
Figure 2.2 – 2D crystal growth modes.

The desired growth mode depends on the ultimate goal of the grower. For 2DEG growth, for example, Frank-van der Merwe growth is desirable because it will lead to the lowest disorder and highest mobility devices. Instead, a 3D growth regime can also be used to engineer a desired structure. A classic example of this is using the large lattice mismatch between InAs and GaAs to form InAs QD on GaAs by the Stransky-Krastanov growth mode [117, 118].

2.1.3 Wulff Construction

Extending the previous concepts to 3D crystal growth, in this case, there is a much richer array of crystallographic planes that need to be considered when determining the lowest-energy arrangement of the crystal, known as the equilibrium crystal shape (ECS). Each family of crystallographic planes has a different density of dangling bonds, this leads to different surface energy contribution for each facet. For example, high-index facets with many dangling bonds will have a high energy density and they will not appear in a given crystal's ECS as low-index facets with lower energies will be favoured instead. Even the surface reconstruction, meaning the arrangement of atoms on the surface of the facet, will affect the surface energy and thus the ECS. The surface reconstruction can also be influenced by extrinsic factors such as temperature and pressure [119–121] this is one of the ways by which the grower can control which facets are expressed in the grown crystal [122, 123].

As shown in Equation (2.1), we can express the surface contribution G_s of a crystal's Gibbs free energy as a sum over the crystal's facets i where we multiply each facet's area A_i by its surface energy density γ_i.

$$G_s = \sum_i \gamma_i A_i \tag{2.1}$$

Gibbs postulated that for a given ECS, the free surface energy of the crystal must be at a minimum. Consequently, the ECS will tend to suppress high-surface-energy facets in favour of lower-surface-energy facets which will have the largest area. In 1901, Wulff hypothesized that in a given crystal at thermodynamic equilibrium, the surface energy density of a facet is proportional to the distance of this facet from the centre of the crystal [124]. This was later coined the Gibbs-Wulff theorem and it was only in 1953 that this was formally proven by Herring [125].

If we know the surface energy density of all possible facets of a given crystal, the Gibbs-Wulff theorem provides one of the most useful ways of visualizing the ECS: the Wulff construction. In 2D, this approach consists of drawing a polar plot with coordinates (r, ϕ) where the length of the vector (r) represents the surface energy of a given crystallographic plane and the direction of the vector (ϕ) is the normal of the given plane. The centre of this polar plot is called the Wulff point. Once the surface energy plot has been obtained, tangent lines can be drawn in at the nodes to represent the most favourable crystal planes that will make up the ECS. Figure 2.3 shows an example of a Wulff construction where the surface energy density is plotted in blue while the crystal itself is plotted in black. We see how $r_1 < r_2$ which tells us that the facet corresponding to r_1 has a lower surface energy density. This is reflected in the final shape because the r_1 facet is much larger than the r_2 facet.
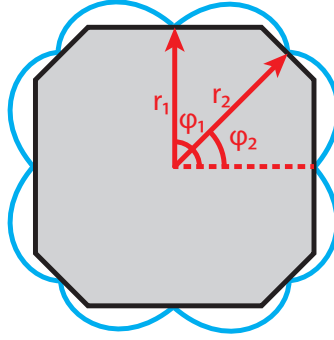
Figure 2.3 – Example of a Wulff construction. The polar plot is shown in blue, with the resulting crystal shown in black.

2.1.4 Winterbottom Construction

Most epitaxial growth does not happen in free space but rather on a growth substrate. This changes the energetics of the system and needs to be taken into account. The equilibrium crystal shape of a crystal attached to a flat substrate was first introduced by Winterbottom [126] and is therefore called the Winterbottom construction. The difference between the Wolff shape and the Winterbottom construction is that now there is a crystal-substrate interface energy γ_{CS} that has to be taken into consideration. As the system will always try to minimize its total energy, if the solid-solid interface energy is much smaller than the substrate-vapour interface energy γ_{SV}, then the crystal will favour a larger interface with the substrate, also known as a higher "wetting" of the substrate.

The general approach to drawing the Winterbottom construction is to take the Wulff shape and draw the substrate at a distance of $\gamma_{CS} - \gamma_{SV}$ below the Wulff point, as shown in Figure 2.4a. The case where the crystal-substrate interface energy is larger than the substrate-vapour interface energy is shown in Figure 2.4b. The opposite case is then shown in Figure 2.4b.

(a) Relaxed (b) $\gamma_{CS} > \gamma_{SV}$ (c) $\gamma_{CS} < \gamma_{SV}$
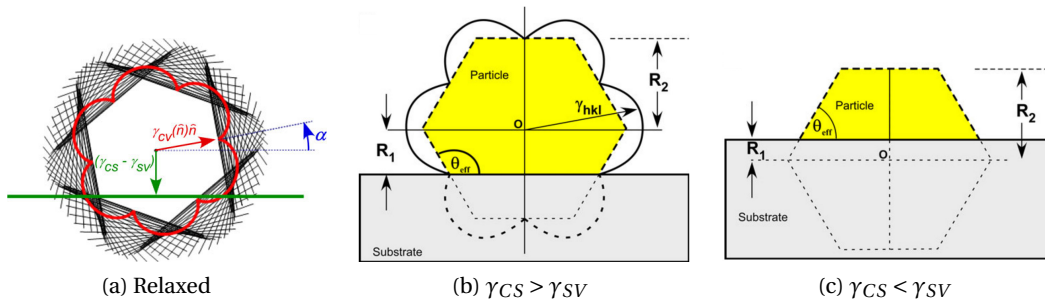
Figure 2.4 – Description of the Winterbottom approach for drawing the ECS of a crystal in contact with a flat substrate. Reproduced from Kaplan *et al.* [127] under the Creative Commons Attribution License

2.1.5 Kinetic Considerations

Although the Wulff and Winterbottom constructions provide an intuitive way to imagine the lowest energy shape of a crystal, they only apply to systems at thermodynamic equilibrium. In reality, during crystal growth, the system is not at thermodynamic equilibrium due to the constant flux of growth species arriving on the substrate. Kinetic considerations, including facet-dependent fluxes (due to inclination), relative facet growth rates, diffusion of adatoms between facets and facet-dependent adatom diffusion lengths, will define a so-called kinetic crystal shape (KCS) which is the kinetic equivalent of the ECS. In other words, the KCS is the steady-state crystal shape that is reached after an infinitely-long growth and is purely dictated by the growth kinetics in the absence of thermodynamic considerations. As summarised in Figure 2.5, in reality, the final crystal shape is the result of a competition between the ECS and KCS [128]. The degree to which each is expressed is dependent on the growth conditions.

The material deposition rate plays an important role in determining to which degree kinetic effects will play a role in the growth. For example, very low deposition rates will result in the system being very close to equilibrium conditions and therefore one can expect shapes close to those predicted by the Wulff/Winterbottom construction predictions. On the other hand, high deposition rates can force the shape to expresses thermodynamically-unfavourable (high-index) facets due to kinetic effects [128–130]. Figure 2.6 shows the theoretical prediction of nanomembrane (NM) growth by SAE when only thermodynamics are considered compared to when kinetic effects are also taken into account. Finally, growth catalysts further complicate matters as they can increase the growth rate of certain facets significantly leading to non-Wulff-like crystal shapes, such as in vapour–liquid–solid (VLS) nanowire growth where the (111)B facet grows significantly faster due to the presence of the metal catalyst droplet [131].
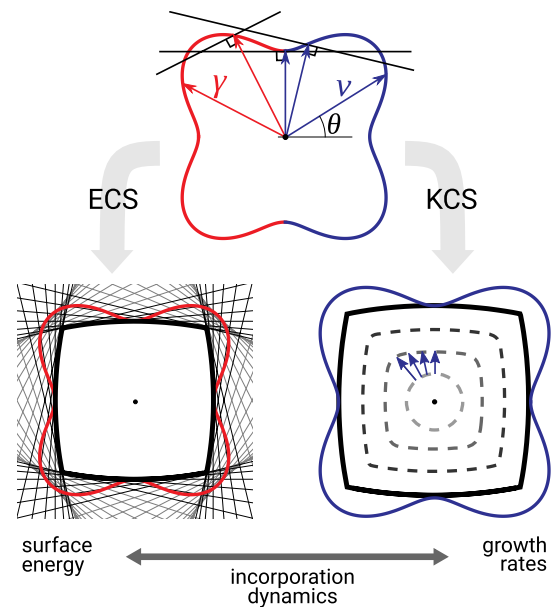
Figure 2.5 – Diagram depicting the competition that occurs between the ECS and the KCS during crystal growth. Reproduced from Albani *et al.* [128] with permission from John Wiley & Sons, Inc.

Phase-Field Approach

Simulating kinetic effects using atomistic approaches becomes too computationally-expensive at the scales required to observe faceting, even at the nanoscale. Thus, a promising alternative for modelling crystal growth while taking kinetic effects into account is by using a so-called
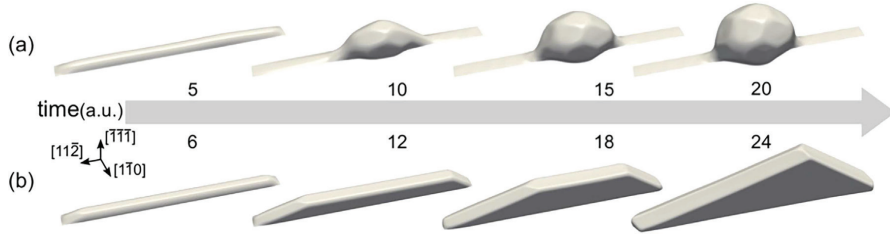
Figure 2.6 – Comparison of growth models for SAE of a GaAs NM using a purely thermodynamic regime (a) and including kinetic effects (b). Notice the model only gives realistic predictions when accounting for kinetic effects. Reproduced from Albani *et al.* [128] with permission from John Wiley & Sons, Inc.

phase-field approach [128, 130, 132, 133]. This approach models the facets of a crystal as diffuse/continuous interface defined by the value of a phase-field function ϕ. This function is defined over the whole simulation space, in 2D or 3D. The function takes on the value of $\phi = 1$ inside the crystal and $\phi = 0$ outside of the crystal. Since the function is continuous everywhere, the surface of the crystal is defined as the line/surface where $\phi = 0.5$ as it transitions between 0 and 1. The time-evolution of the phase-field function can then be expressed as a function of various terms that represent physical (kinetic) aspects of growth. An example given by Albani *et al.* [130] is:

$$\frac{\partial \phi}{\partial t} = F(\hat{n})|\nabla \phi| + \nabla \cdot \left[M(\phi) \nabla \phi \right]$$

Here, the first term accounts for the incoming material and $F(\hat{n})$ represents flux which depends on the surface normal $\hat{n} = -\nabla \phi / |\nabla \phi|$. The second term accounts for surface diffusion of adatoms between facets with some mobility coefficient $M(\phi)$. The surface adatom diffusion is further expressed in terms of the difference in chemical potential between facets which drives the diffusion from one facet to another. The final parameter included in the model is a facet-dependent adatom lifetime term which takes into account the growth rate of various facets. The reader is encouraged to look at references [128, 130] for more details on these equations.

The facet-dependent adatom lifetime can also be thought of as the growth rate of various crystal facets. This value needs to be defined from experiment, making this a semi-empirical model. After the facet growth rates have been defined, typically by performing a time series of MBE growths, the time evolution of the phase-field function can be solved numerically using a finite element approach. After proper calibration of the facet growth rates, this phase-field approach becomes a powerful method for predicting the time evolution of kinetically-driven crystal growth. It is important to note that this approach is flexible enough to also be applied even when the growth surface is masked by an oxide, as is the case in SAE [130]. Lastly, recently it has also been shown that the phase-field approach is flexible enough to also be extended to take thermodynamic considerations into account allowing for the modelling of crystal

growth that falls somewhere in between the two extremes of purely-thermodynamic and purely-kinetic growth [128].

2.2 Defects in Heteroepitaxial Growth

Heteroepitaxial growth of crystals can often result in the formation of defects. In this section, I would like to touch on the two major reasons for defect formation which are relevant in the context of this thesis, namely lattice mismatch and polarity mismatch.

2.2.1 Lattice Mismatch

The lattice mismatch ϵ is defined in terms of the lattice constants of the substrate and deposited material, a_s and a_d, respectively. The lattice mismatch can be expressed as $\epsilon = (a_d - a_s)/(a_s)$. The larger the lattice mismatch, the larger the interface energy between the two materials and the harder it is to grow one material on top of the other without forming defects. Figure 2.7 shows a comparison between different semiconductor materials and their lattice constants.
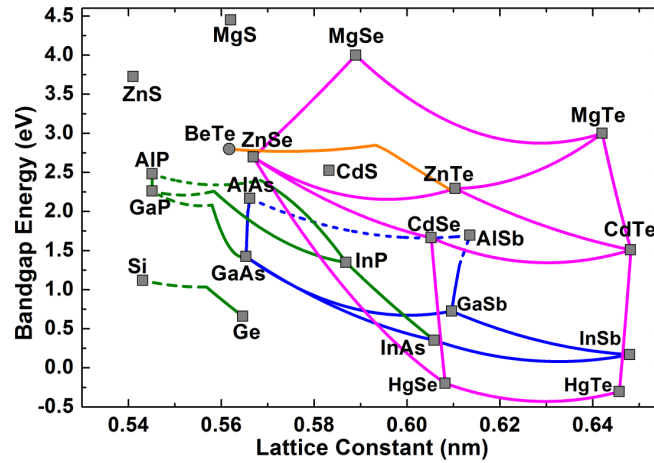
Figure 2.7 – Graph of lattice constant vs. bandgap of various semiconductor materials. The epitaxial growth of a material on a substrate with a different lattice constant leads to a lattice mismatch and potentially the formation of defects. Reproduced without modifications from Smith *et al.* [134] under the Creative Commons Attribution 3.0 license.

When performing heteroepitaxy with lattice-mismatched materials, the mismatch can be accommodated by elastic and/or plastic relaxation. As depicted in Figure 2.8a, elastic strain relaxation is the reversible deformation of the unit cell of a material under compressive or tensile stress which acts to accommodate the lattice mismatch and the deposited material eventually regains its relaxed lattice constant. The limitation of this growth mode is that in a 2D film, the unit cell is unable to expand laterally and instead expands in the vertical direction to accommodate for the reduced lattice constant in the horizontal direction. This is very energetically-expensive and beyond a certain critical thickness, the material will switch to a

plastic relaxation mode and begin to form defects. However, it has been shown that for vertical NW growth the critical thickness is inversely proportional to the NW diameter [114]. As such, sufficiently thin NWs can overcome very large lattice mismatches due to elastic relaxation and lateral expansion/contraction at the base of the wires.

Plastic relaxation is when a defect is formed in the crystal which accommodates some of the lattice mismatch. A defect with its Burgers vector located in-plane with the substrate will act to relax the strain, as depicted by the formation of a perfect misfit dislocation at the interface between the two materials shown in Figure 2.8c. Techniques such as the growth of a periodic interfacial misfit array have been developed to overcome large lattice mismatches and regain a smooth growth regime when growing highly mismatched materials [135–158].

(a) Relaxed   (b) Elastic strain relaxation   (c) Plastic strain relaxation
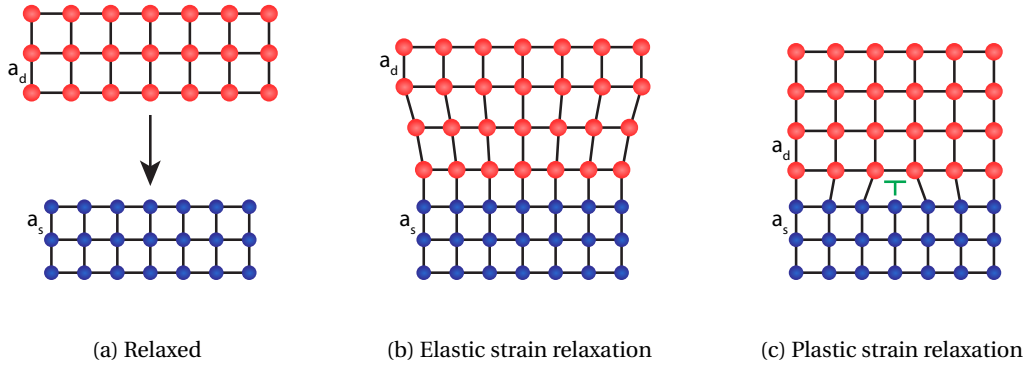
Figure 2.8 – Ways of accommodating for lattice mismatch.

2.2.2 Polarity Mismatch

Polarity mismatch is the second major cause of defects in heteroepitaxial growth. This kind of mismatch becomes a concern when a polar material (such as a compound III-V semiconductor) is grown on top of a non-polar substrate (such as silicon), as shown in Figure 2.9. When a polar crystal forms on a non-polar substrate, since the substrate has no polarity, the polarity of the crystal can be either A-polar (group III atom on top) or B-polar (group V atom on top). When two nuclei with different polarities merge, they will form anti-phase boundaries (APBs) at their interface which are characterized by, for example, Ga-Ga and As-As bonds in GaAs shown in Figure 2.9a [159]. Therefore, it is crucial to control the initial stages of crystal growth to ensure that all nuclei start to grow with the same atomic species so their all nuclei have the same polarity and merge without forming defects. However, as displayed in Figure 2.9b, even if we carefully control that the first layer is composed of the same atomic species (in this case Ga), mono-atomic steps on the substrate can also lead to the formation of APBs. Therefore, to avoid polarity mismatch it is very important that both initial layers of all nuclei are composed of a single atomic species and that the substrate is atomically smooth. Alternatively, if one can grow the nanostructure from a single nucleus, this is also an approach to reduce APB

formation. This is the topic of Chapter 5.

(a) Flat substrate.   (b) Mono-stepped substrate.
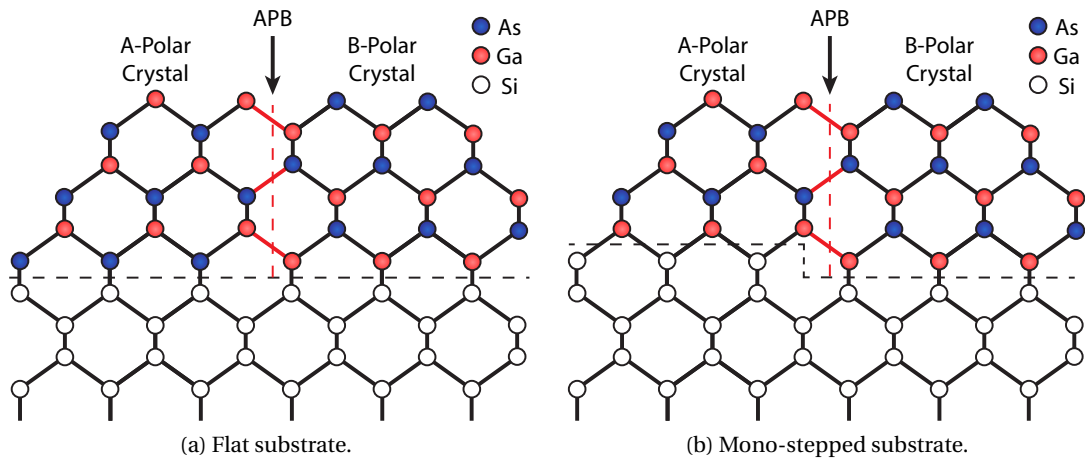
Figure 2.9 – Example of different ways of forming APBs due to polarity mismatch when growing GaAs on Si. a) Two crystals are nucleated with different polarities leading to an APB due to different atomic species in their first monolayer. b) Two crystals are nucleated with different polarities leading to an APB this time due to a mono-step in the substrate, despite having the same atomic species in their first monolayers.

2.3 Selective Area Epitaxy

Selective-area epitaxy, also called selective-area growth, is a specific approach used in epitaxial growth that is particularly useful for the growth of nanostructures. It consists of using a high-surface-energy material, typically an oxide or nitride, to cover most of the substrate and limiting the growth within small patterned openings. At sufficiently high temperatures, adatoms arriving on the mask see a high-energy surface that is not energetically favourable to nucleate on and so they tend to diffuse on the surface and/or eventually desorb. This leaves the mask portion typically free of deposited material. At the same time, within the patterned holes the cost to nucleate solid material is significantly smaller and, as a result, growth happens exclusively within the openings in the mask.

This type of growth is interesting for the growth of nanostructures as the openings in the mask can be patterned on the scale of tens of nanometres, giving rise to nanostructured crystal semiconductors. Patterned semiconductor NW arrays, for example, have been grown both by MBE and by metalorganic chemical vapour deposition (MOCVD) using this approach. The disadvantage of SAG is that a sufficiently high growth temperature is required to prevent the growth of material on the oxide mask to get a high selectivity [160]. Achieving high selectivity means that the material only grows within the patterned openings rather than on the oxide mask.

One of the first reports of selective area growth was described in 1962 by Joyce and Baldrey

[161] working a Texas Instruments where they reported on the growth of Si within openings in SiO_2. This was followed by Tausch and Lapierre [162] in 1965 and Shaw [163] in 1966 who took a similar approach to grow GaAs using a selective-area epitaxy within openings in a SiO_2 mask. While Tausch and Lapierre saw significant lateral overgrowth onto their SiO_2 masks, Shaw reported well-defined faceting of the grown GaAs crystals. Coincidentally, this work coincided roughly with the discovery of the VLS mechanism for vertical NW growth which was reported by Wagner *et al.* [83]. Though SAE was not used for NW growth for some time, many groups focused on using it for two-dimensional (2D) device fabrication by epitaxial lateral overgrowth (ELO) processes, also known as microchannel epitaxy (MCE) [164, 165]. Fukui and colleagues published a series of papers describing the fabrication of quantum wires grown by SAE using MOCVD [166–168] as shown in Figure 2.10.

| (a) Fukui and Ando [167] | (b) Fukui *et al.* [168] |
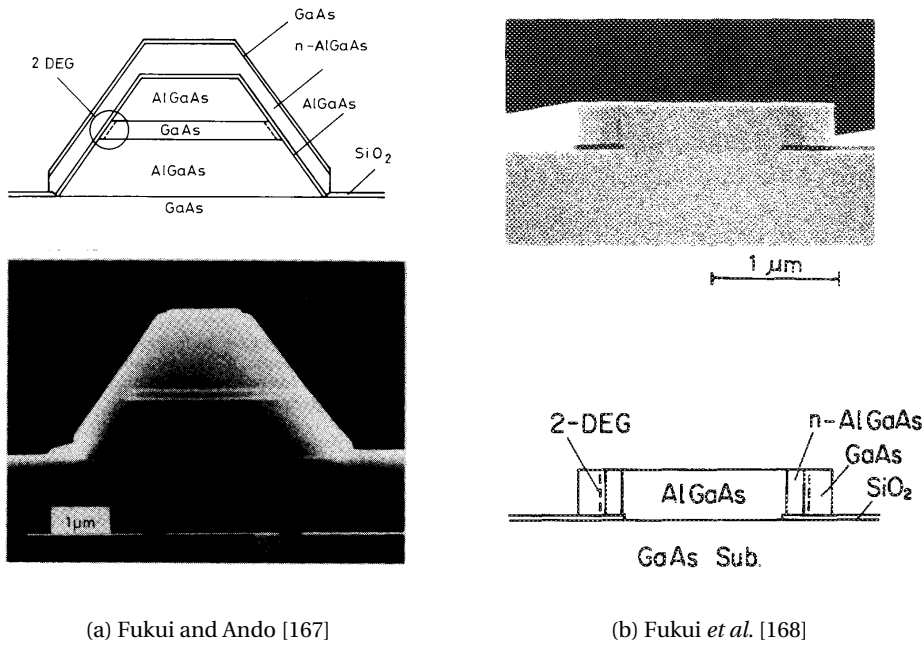
Figure 2.10 – Images from first SAE quantum wires grown by Fukui and colleagues by MOCVD. Reproduced by permission of the Institution of Engineering & Technology and AIP Publishing, respectively.

Around this time, SAE by MBE was being attempted for the first time by many Japanese groups. Okamoto and Ohata [169] noted that relatively high growth temperatures were necessary in order to achieve selectivity by conventional MBE [169]. This led to further investigations using SAE combined with several exotic flavours of MBE including electron-cyclotron resonance plasma-excited molecular beam epitaxy (ECR-MBE) [170], migration-enhanced epitaxy (MEE) [171] and hydrogen-assisted molecular beam epitaxy (H-MBE) [172, 173]. All of these studies were attempting to achieve selectivity at lower growth temperatures to improve the crystal quality of the resulting structures.

Since then, SAE has been used extensively to grow a multitude of semiconductor geometries

and materials. A non-exhaustive summary of the publications utilizing SAE for nanostructure growth has been compiled in Table 2.1. Given the number of reports on using SAE for vertical NW growth [174], a separate table, Table 2.2, has been dedicated to the use of SAE applied to vertical NW growth.

	MBE	MOCVD
GaAs	[175–178]	[179–181]
GaSb	[106, 107]	-
GaN	-	[182–184]
InP	[185–187]	[129, 188–191]
InAs	[106, 107, 192]	[113, 188, 193]
InSb	[109]	-

Table 2.1 – Table of references for SAE of nanostructures (not including vertical NWs).

	MBE	MOCVD
GaAs	[160, 194, 195]	[196–203]
GaSb	-	-
GaN	-	[204]
InP	-	[205, 206]
InAs	[194, 207, 208]	[6, 197, 209, 210]
InSb	-	-

Table 2.2 – Table of references for SAE of vertical NWs.

2.3.1 SAE Growth Dynamics During GaAs Growth by MBE

To interpret growth results, it is important to have a clear picture of what is happening on the sample. Previously, the growth dynamics of single species crystals were described generally. Now, moving to the description of growing a binary compound such as GaAs, an extra layer of complexity is added as both atoms have to be present for the material to form into the desired crystal phase. To complicate matters further, both growth species behave very differently from one another during growth, and it is important to understand the behaviour of each species separately to explain a certain growth outcome.

Figure 2.11a gives a visual representation of the four main processes that play a major role during the growth of crystals by SAE. Many of the same processes from planar 2D crystal growth are at play in SAE, however, there are some subtle differences due to the presence of the SiO_2 mask. The presence of the mask results in the appearance of secondary fluxes that can also contribute to crystal growth, as shown in Figure 2.11b.

The Group III species, depicted as Ga atoms in red, arrive on the substrate as single atoms. They adsorb to the substrate, which is mostly covered by the SiO_2 mask, and due to the high growth temperatures they can diffuse on the surface up to several microns [120, 211, 212]. This means that under certain conditions, the indirect group III flux that is collected from diffusion around the base of the nanostructure can contribute substantially to nanostructure growth [213]. SAE nanostructures can thus grow at much higher growth rates compared to the nominal 2D layer growth rate.

The Group V species, depicted in blue, arrive on the substrate as As_2 or As_4 molecules depending on the cracker temperature of the As cell (see Section 2.5.1). The cracker in this work was kept at a relatively low temperature of 600 °C, resulting in mostly As_4 arriving on the sample. As_4 flux has been shown to result in longer Ga diffusion lengths which is advantageous for vertical NW growth [214]. It has been simulated by density functional theory (DFT) on GaAs (100) that As_4 molecules split into two As_2 dimers, one of which gets adsorbed while the other desorbs [120]. Furthermore, in contrast to Ga atoms, these As molecules are much more weakly bonded to the surface and as a result, tend to desorb much more easily than Ga while also not being mobile on the surface [120]. Therefore, the typical method by which As indirectly contributes to the growth is through (multiple) adsorption/desorption processes from neighbouring sites.

(a) MBE Processes   (b) MBE Fluxes
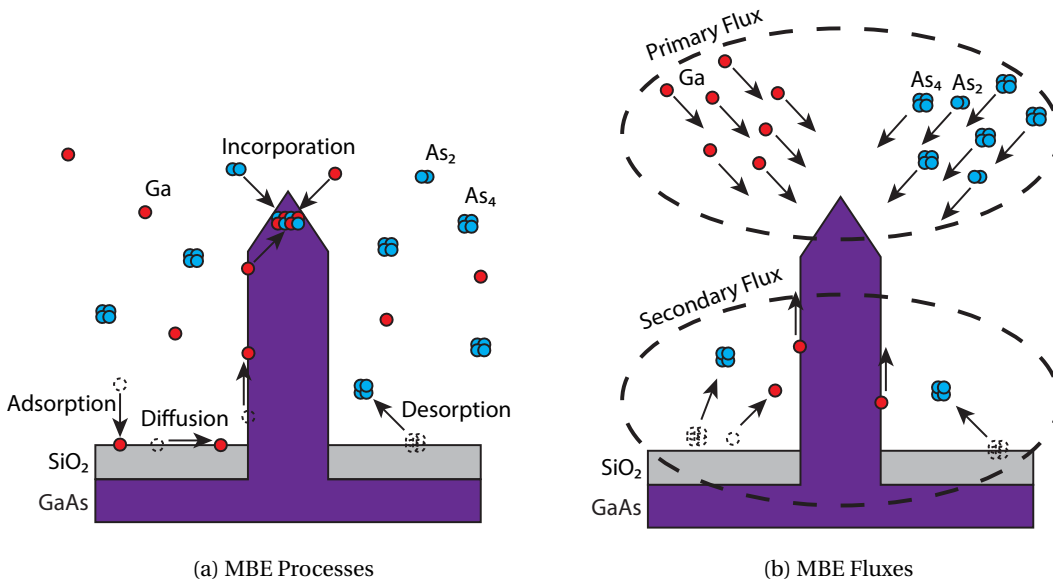
Figure 2.11 – a) Summary of the different processes that occur during MBE growth b) Comparison of primary growth flux compared to secondary growth flux.

2.3.2 Comparison of NW Growth Methods

Shown in Table 2.3 is a comparison of three methods used to grow NWs in a position and direction-controlled manner. All of these methods are quite different, each with their advantages and disadvantages which I would like to highlight here.

Technique	Growth Direction	Max NW Length	Large-Scale NW Networks?	On Si?
SA-VLS	Vertical/Tilted	>20 µm	No	Yes
TASE [215–217]	Any	<10 µm	No	Yes
SAE	In-Plane	>1 mm	Yes	No

Table 2.3 – Comparison of patternable NW growth approaches.

SA-VLS is a method for nanowire growth similar to SAE where an oxide mask is patterned with holes exposing the substrate beneath. However, the first step in the growth is the deposition of a catalyst droplet such as Ga into these holes before growing NWs via the standard VLS approach. Note, vertical SA NWs can also be grown without a liquid catalyst using a vapour-solid approach, however, they have very similar characteristics to VLS NWs and have therefore been omitted from the comparison in Table 2.3. This technique is useful for growing NWs in the $\langle 111 \rangle$ direction [218] which can also be used to grow tilted wires on (100) substrates [219]. The NW length by VLS is theoretically unlimited and it has the advantage that this approach works well for growing NWs on silicon substrates. The drawback of this approach is that horizontally-oriented wires are quite difficult to grow, as are reliable intersections between NWs. As such, it is not a viable approach for growing large-scale NW networks.

TASE is an approach that can be described as SAE extended into the third dimension. Instead of a 2D oxide mask, TASE, uses patterned silicon on insulator substrates, oxidation and selective Si etching to create a three-dimensional growth template of SiO_2 [215, 216]. This template is then used to constrain the growth of III-V crystals to create complex nanostructure geometries with favourable electrical properties [217]. Due to the very low surface diffusion length of elemental As_2 and As_4, TASE is only possible when using metal-organic As precursors with large diffusion lengths on SiO_2, such as in MOCVD. In this case, the precursors diffuse along the SiO_2 template walls until they reach the Si substrate where they finally dissociate, depositing their elemental growth constituents and thus nucleating crystal growth. Due to this necessity of having precursor diffusion down to the Si surface, TASE NWs grow at a rate of about 1 µm/h and their maximum length is fundamentally limited by the diffusion length of the precursors which is generally on the order of a few microns [216]. Large-scale TASE NW networks have thus far not been demonstrated but it is worth mentioning that TASE networks may be challenging to realize due to formation of APBs during the merging of NWs.

In comparison to these two methods, SAE NWs offer certain benefits with few drawbacks. The

growth direction is not as flexible as TASE, however, following certain specific crystallographic directions, NWs can typically be grown in at least three directions on the substrate [108–113]. This, combined with no limitation on the maximum NW length makes it an ideal approach for growing NW networks. Though, the greatest disadvantage of this approach is that so far integration on Si remains very difficult and has not been demonstrated. The integration of SAE NMs on silicon is the topic of Chapter 5.

2.4 Electrical Transport

Due to the electrical nature of computers, including those of the quantum variety, knowledge of the behaviour of electrons and holes within the materials used is essential to the understanding and optimization of their operation. This section serves to remind the reader of the most important concepts that are relevant to the understanding of the research goals and direction of this thesis. I begin with the basic concepts of classical semiconductor transport before touching on a few topics which become important when size reduction gives rise to tangible quantum effects.

2.4.1 Classical Transport in a Semiconductor

The discussion of classical transport in a semiconductor in this thesis will assume some basic prior exposure to the concepts of semiconductor band structure, doping and carrier mobility. There are several textbooks [220, 221] that have been written on the subject and the reader is encouraged to refer to these for a more in-depth approach to the topic.

As a recap, the concept of an electrical band diagram consists of a low-energy valence band that represents the nominally-occupied electron states while the higher-energy conduction band represents all of the nominally-unoccupied electron states. At the lowest possible energy of the system (ie: temperature of absolute zero), all states in the valence band are filled while all states in the conduction band are empty. The degree to which the valence band and conduction band differ in energy is called the bandgap. The bandgap changes according to material and this difference is what classifies the material as a conductor, insulator or semiconductor.

In a conductor (such as a metal) the valence electrons are weakly bound to the nuclei in the crystal lattice and as such, it is not very energetically-expensive to hop to empty neighbouring lattice sites and consequently, the bandgap in the material is considered to be zero. If a voltage is applied to the material, the drift and diffusion of mobile carriers in the material give rise to a measurable electrical current.

In the case of an insulating material, the electrons are strongly-bonded to each nucleus and/or there are no neighbouring lattice sites to which it is energetically favourable to hop. This is represented in the band structure as a large bandgap (~4eV or greater). In these materials, an applied voltage does not cause a significant current to flow and thus they are called insulators.

In between these two extremes are semiconductors. These are considered to be materials that are insulating at absolute zero but at higher temperatures, thermal energy is enough to overcome the bandgap and make them conductive. By convention, these types of material are considered to have bandgaps in the range of 0 to ~4eV.

Conductivity

Conductivity is arguably the most important concept in semiconductor transport as it is the most easily electrically-measurable property of a material. This means that in many experiments, as well as practical applications, it is the change in conductivity that is fundamentally at the centre of measuring the presence of some phenomenon or that is responsible for an operation in a CPU.

Conductivity in a semiconductor is a function of both the free carrier concentration (number of charges) and the mobility of those carriers (roughly the speed at which they travel in the material). In a semiconductor, we can have two types of carriers, electrons and holes. Holes are simply an empty lattice site in a sea of electrons which has a net positive charge. Similarly to electrons, this pseudo-particle can travel and behaves as if it were its own positively-charged particle. By analogy, we refer to holes in the same way we refer to bubbles underwater, despite them being simply voids in a medium.

The total conductivity σ in a material is thus composed of the contribution from both electrons and holes, taking into considering the concentrations (n and p, respectively) and mobilities of both (μ_n and μ_p, respectively), as described by Equation (2.2), where q is simply the fundamental charge constant.

$$\sigma = nq\mu_e + pq\mu_h \tag{2.2}$$

Doping

Extrinsic doping is the method by which carriers are added to the conduction band or valence bands by adding impurities to the material. This is a method used to change the carrier concentration (and by extension the conductivity) in a semiconductor by adding impurities. By adding dopant impurities with extra valence electrons (n-type) or with fewer valence electrons (p-type), we can add electrons to the conduction band or holes to the valence band, thus influencing the free carrier concentration. It is also important to note that if both n and p-type dopants are added to a material, the resulting holes and electrons recombine with each other forming a compensation-doped material with a net free carrier concentration that is lower than either of the added dopant concentrations.

In silicon (group IV), a common n-type dopant is phosphorus (group V) while a common p-type dopant is boron (group III). For compound (III-V) semiconductors such as GaAs, group IV materials such as silicon and carbon can be used as dopants [222]. What complicates matters is that depending on which lattice site (Ga or As) the impurities go to, the effect of doping can be p-type and n-type [223, 224]. Furthermore, at high doping concentrations, the dopants become less efficient due to the formation of defects so the overall carrier concentration of the material does not increase much beyond this point [225].

Mobility

Along with carrier concentration, mobility is the second important contribution to the conductivity in a material. As discussed previously, when a voltage is a applied to a material it creates an electric field and causes the charge carriers to drift. Formally, mobility is defined as the constant of proportionality between the carrier drift velocity v_d and electric field E in the material, as described by Equation (2.3).

$$v_d = \mu E \tag{2.3}$$

In a diffusive medium, the carriers are accelerated by the electric field but at the same time, they are also slowed down due to scattering processes. The average velocity of these carriers, taking into account the scattering, is the drift velocity. Various kinds of scattering processes exist, including phonon scattering [226–229], ionized impurity scattering [230, 231] and interface scattering [232–234], all of which negatively affect the mobility of the material. As described by Matthiessen's rule in Equation (2.4), the overall mobility in a material can be calculated as the reciprocal sum of all individual scattering-limited mobility components. Each mobility component corresponds to the mobility of carriers in the presence of only a single particular scattering mode.

$$\frac{1}{\mu_T} = \frac{1}{\mu_1} + \frac{1}{\mu_2} + ... \tag{2.4}$$

Furthermore, these scattering mechanisms are temperature-dependent, as shown in Figure 2.12. For example, phonon scattering is dominant at high temperatures while at low temperatures lattice phonons are suppressed, reducing this form of scattering while other scattering mechanisms, such as impurity scattering, become dominant.
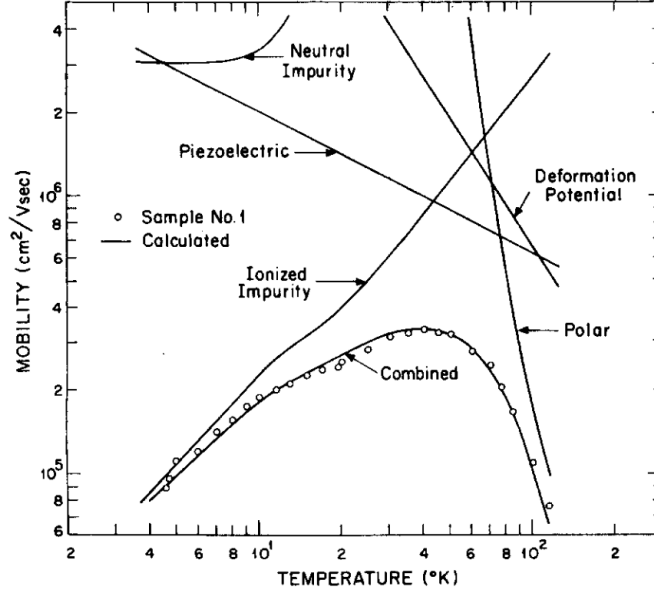
Figure 2.12 – Temperature-dependence of mobility in a GaAs sample, showing the temperature dependence of various scattering mechanisms. Reproduced from Wolfe *et al.* [229] with permission from AIP Publishing.

2.4.2   Figures of Merit

When optimizing any system, quantitative (and measurable) performance metrics, also known as figures of merit, are essential. These serve as a point of comparison between iterations to reach an optimal result. In the current work, the goal was to build a NW structure to host MFs in future experiments. Therefore, the performance metrics, in this case, were low disorder, measured as long elastic mean free path and coherence length, combined with a high spin-orbit interaction (SOI) in the material, measured by a short spin-orbit length. These figures of merit are broken down in more detail in the following subsections.

Elastic Scattering Length, l_e

The first figure of merit to consider is the elastic scattering length l_e, also called the electron mean free path. This quantity describes the average distance an electron travels before it is scattered by one of many possible scattering processes. To conserve the properties of the electrons, we try to make l_e as long as possible. Scattering processes can be either elastic (energy and phase conserving) or inelastic (changing energy, adding phase error). l_e does not distinguish between these two types of scattering events, so an increase in the frequency of either one will result in a lower l_e.

Phase Coherence Length, l_ϕ

The phase coherence length l_ϕ is a figure of merit describes the distance that a carrier travels on average before its wave function has accumulated enough phase error (through inelastic scattering events) that any information encoded in the phase is lost. The significance of this value is that in a quantum computer, all quantum states must remain coherent throughout a calculation for quantum interference effects to take place and produce the desired result. Therefore, l_ϕ should be made as long as possible to minimize disruption to the quantum information in the system.

Spin-orbit Length, l_{SO}

A last important semiconductor property for the chance of observing MFs is having a material with large SOI. SOI coupling is a material property that describes how closely the spin of the electrons couple to their orbital angular momentum around the nucleus. Heavier materials, such as InAs and InSb have higher spin-orbit coupling as they have more positively-charged protons in their nuclei which couple more strongly to the electron spin. The effect of SOI is that as electrons move through the material, they feel a relativistic effective magnetic field which causes their spin to precess due to Larmor precession.

To experimentally measure the SOI, we can measure the spin-orbit length l_{SO}. This value represents the average length that an electron with a well-defined spin travels on average before its spin is fully randomized due to spin-dephasing scattering events [235]. Each scattering event causes the electron to change momentum, thus changing its position in k-space and experiencing a different effective magnetic field due to SOI. The result is that after each scattering event, the electron spin precesses around a different axis, and multiple scattering events eventually cause the spin to become fully randomized. The stronger the SOI, the faster this happens and as a result, l_{SO} is inversely proportional to SOI strength.

As a final note, in diffusive mesoscopic systems, the relationship between l_{SO} and l_ϕ is important as it defines whether or not quantum backscattering in the material will be enhanced or reduced. This effect is described in more detail in Section 2.4.4.

2.4.3 1D Transport

Up until now, I have been describing the basics of electrical transport in the classical case, however, the picture changes significantly when we begin to enter the mesoscopic regime between macroscopic and nanoscopic systems. The dimensionality of a mesoscopic system is defined by comparing its size to l_ϕ [235]. Starting from a 3D system, a dimension is removed for each dimension in which l_ϕ is smaller than the size of the system. For example, a 2DEG is a 2D system because it is only confined in the vertical direction. Similarly, a nanowire can be considered a 1D system because it is confined in two dimensions while a quantum dot is an example of a 0D system. From now on I will only discuss transport in 1D systems as they are

the only relevant system to this thesis work.

Therefore, a 1D mesoscopic system will have $l_\phi > W$ and $l_\phi < L$. Where W is the width of the NW and L is the length of the NW. This feature of having a long l_ϕ compared to the NW width is what differentiates quantum transport from classical transport due to the effects of quantum interference, something that is not visible in classical systems. Based on the size of the electron mean free path, 1D mesoscopic transport can be broken down into three regimes: diffusive, quasi-ballistic and ballistic transport. These three regimes are summarized in Figure 2.13.
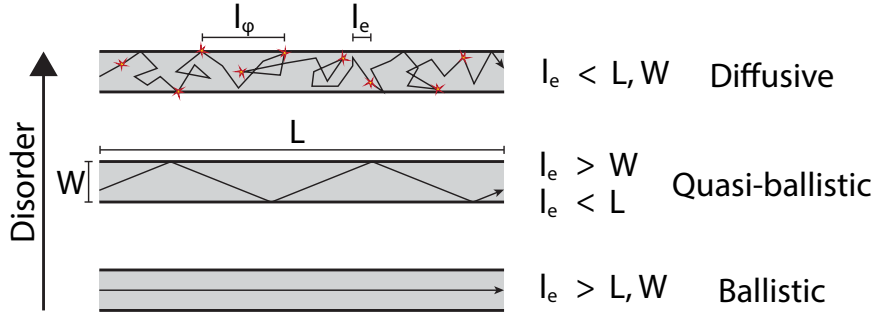
Figure 2.13 – Description of different transport regimes, depending on the mean free path in the material.

Diffusive Transport

Diffusive transport occurs in systems with high scattering rates. In such systems, the electron mean free path is shorter than both the width and length of the NW. Although the electron mean free path is shorter than the width, the phase coherence length can be much longer, thus quantum effects still need to be considered in such systems to fully describe their electrical transport properties. An example of diffusive transport will be discussed later in this thesis in the case of Si-doped InGaAs NWs in Section 3.1.

Ballistic Transport

In systems with very little scattering, the mean free path can be much longer than both the width and length of the NW. Thus, most electrons can travel on a straight (ballistic) path through the NW. This second type of transport is called ballistic transport and has the interesting feature that the resistance becomes independent of NW length in this regime. A further feature of ballistic transport is the quantization of conductance which takes place as a function of applied gate voltage. This effect appears due to charge quantization under reduced dimensions which results in a finite number of conductance channels conducting in the NW at any given time. A nice example of ballistic transport across InAs NW junctions was recently shown by [217].

Quasi-ballistic Transport

Finally, in between the diffusive and ballistic transport regime, we have the quasi-ballistic regime. In general, we can consider the quasi-ballistic regime to encompass the case where electron mean free path is longer than the NW width but not as long as the NW length.

2.4.4 Magnetoconductive Effects

Magnetoconductance refers to the change in a material's conductance as a function of an applied magnetic field. Along with applying an electric field, applying a magnetic field is one of the few ways through which the carriers in a material can be manipulated by macroscopic means. Furthermore, magnetic fields have the important effect of influencing the trajectory of electrons in the material by the Lorentz force, thereby also affecting their quantum properties. Thus, the magnetoconductive properties of a mesoscopic system offer insight into the quantum behaviour of electrons in the material from which quantum figures of merit such as l_e, l_ϕ and l_{SO} can then be deduced. In this subsection, the phenomena of weak localization (WL) and weak anti-localization (WAL) will be summarised due to their relevance in the electrical characterization of the NWs studied in this thesis. If the reader is interested, references for a more mathematically rigorous treatment of these phenomena are given here [236–238].

Coherent Backscattering

In a classical system, knowing the initial conditions and classical equations of motion, it is possible to deterministically calculate the trajectory of a particle through a medium. As such, there is only one possible path for the particle to take given a set of initial conditions. In a quantum system with sufficiently long coherence length, this is not the case as there is a probabilistic distribution of infinitely-many possible paths that must be considered. Thus, to calculate the conductivity of the material in the quantum regime, all possible paths and their probabilities must be considered in a superposition. Because of this quantum treatment, there is the possibility of quantum interference between electrons paths resulting in a conductivity that is not explained classically. Quantitatively, a system will exhibit WL when $l_{SO} > l_\phi > l_e$ while $l_\phi > l_{SO} > l_e$ will lead to WAL [235].

The path which makes the difference in the quantum correction to conductivity, in the case of WL and WAL, is the backscattered path. This means any path in which the electron follows a loop, changing momentum by multiple elastic scattering events and eventually returning to its original position. Figure 2.14 shows the behaviour of an electron (and its spin) in a diffusive system as it scatters around a closed path. The red path represents the time-reversed path of the electron around the loop. In the absence of strong SOI, the electron spin is unaffected by the elastic scattering events around the path and so the spin does not precess. When looking at the probability of obtaining the state containing these two time-reversed paths, it is observed that the interference terms between the two possible paths add up to increase the overall

probability of the backscattered path. As such, coherent backscattering is enhanced by a factor of two above the classical case which does not take into account the quantum interference terms. This leads to a decrease in conductivity G at zero magnetic field. When a magnetic field is applied, the Lorentz force on the electrons causes their trajectories to curve, thus breaking time-reversal symmetry and destroying the quantum interference between the two paths [237]. At high fields, the conductance values return to that of the classical prediction.
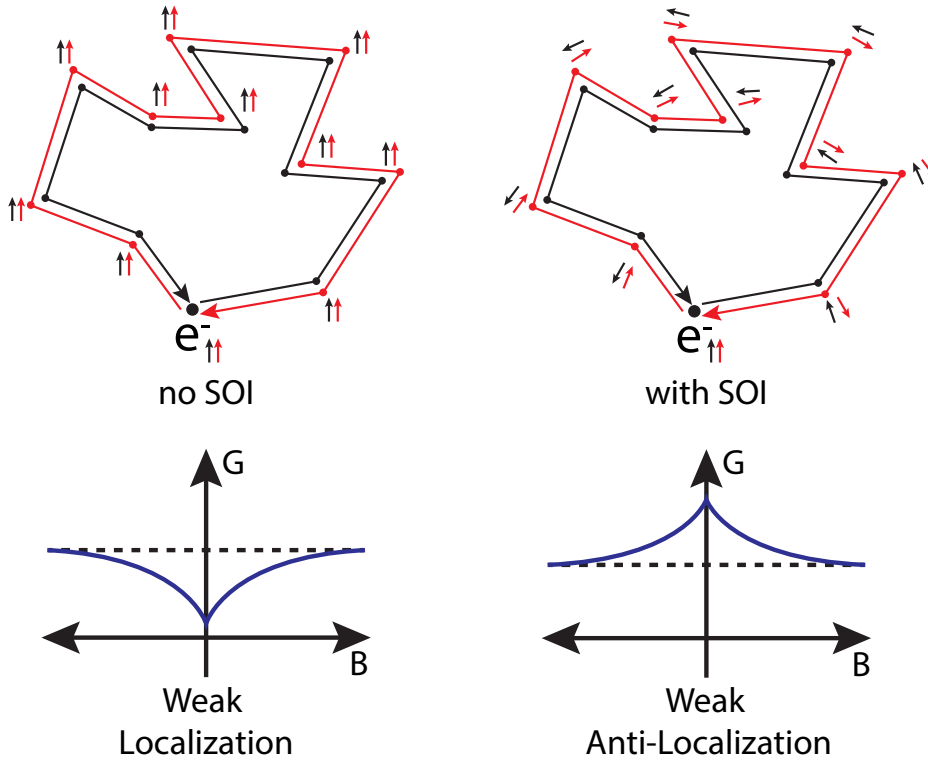
Figure 2.14 – Depiction of a possible electron scattering path (black) and the time-reversed path (red) both with and without SOI with electron spins shown as arrows.

With strong SOI, the electron spin precesses in the SOI-induced magnetic field due to Larmor precession. Each scattering event slightly modifies the axis around which the spin is precessing and over time the spin is modified. In the mathematical treatment, again calculating the probability of the two time-reversed paths, this time taking into account the spin precession, it is observed that the interferences terms this time reduce the probability of observing the backscattered paths to one half of the classical value. This then leads to an increase in conductivity G at zero magnetic field which again approaches the classical value at high magnetic fields due to breaking of time-reversal symmetry.

Lastly, it has been reported that the conductance regime can be tuned. There are two components that make up the total SOI in zincblende crystals: so-called Dresselhaus SOI arising from atomic crystal inversion asymmetry and Rashba SOI arising from structural/geometrical

inversion asymmetry such as the presence of an interface [239–241]. Reports have shown that the degree of Rashba SOI can be tuned in a semiconductor by inducing asymmetry either structurally [242, 243] or by applying an electric field [244, 245] resulting in a transition between WL and WAL regimes.

2.4.5 Surface States and Fermi Level Pinning

In nanostructures with higher surface-to-volume ratios, the surface states contribute greatly to the overall electrical properties. On any crystal surface, the atoms naturally rearrange into the most energetically favourable position, creating a certain surface reconstruction that differs from the bulk crystal, as mentioned in Section 2.1.3 in the context of epitaxial growth. The surface reconstruction also has implications for the electrical properties of the crystal because it defines which kinds of surface states are formed. Both intrinsic (ex: dangling bonds) and extrinsic (ex: dopants) surface states are important in determining the resulting the band structure at the surface of the crystal. The effect of ionized surface states is the appearance of a surface charge density which causes surface band bending. This band bending fixes the Fermi level at a certain potential at the surface and is referred to as Fermi level pinning. The potential at which the Fermi level is pinned is entirely dependent on the types of surface states that are present. The band bending at the surface of various semiconductors is compared in Figure 2.15.

(a) Si   (b) GaAs   (c) InAs
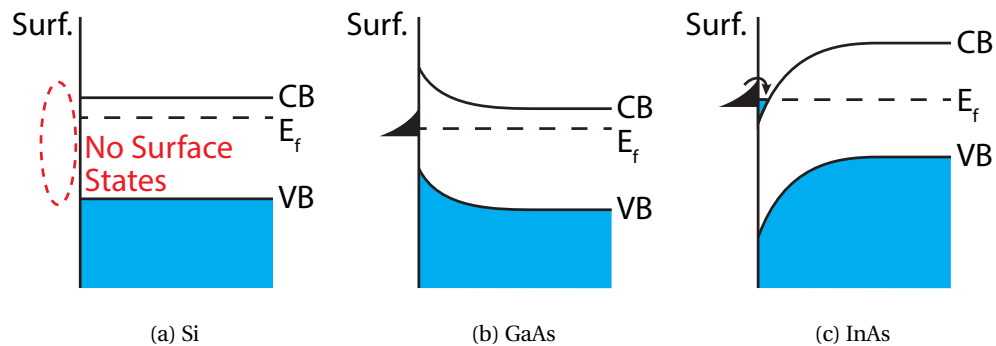
Figure 2.15 – Diagrams of how surface Fermi level pinning affects different semiconductors. a) Si surfaces passivated by SiO_2 are not pinned due to the perfect passivation and lack of surface states. b) GaAs surfaces with a native oxide are pinned in the middle of the band-gap. c) InAs surfaces with a native oxide are pinned in the conduction band. (Note: energies are not to scale)

In the case of Si (1 1 1), in vacuum the surface states cause the Fermi level to be pinned in the mid-gap [246], however upon exposure to oxygen, the surface states were entirely passivated and led to the unpinning of the Fermi level at the surface [247]. The availability of this nicely-behaved oxide on silicon is one of the main reasons for its widespread use in the semiconductor industry. On the other hand, in III-V materials the oxides are not as well-behaved and generally

do not passivate the surface well. Pristine GaAs (1 1 0) in vacuum, for example, does not have its Fermi level pinned due to lack of surface states with energies within the bandgap [248]. However, the addition of oxygen to the surface causes strain and break-up of the chemical bonds at the GaAs surface. This leads to defects which pin the Fermi level in the mid-gap even with just 3% oxide surface coverage for both n-type and p-type samples [249].

On InAs (1 1 0) surfaces however, it has been widely reported that the Fermi level gets pinned in the conduction band due to a surface electron charge density on the order of $1 \times 10^{12} \, \text{cm}^{-2}$ [250–254]. Though in certain cases, namely on InAs (1 1 0) non-polar surfaces just after cleaving, flat-band conditions were reported as in GaAs [255, 256]. However, after a certain time, even in ultra-high vacuum (UHV) conditions, surface states begin to appear due to adsorption of hydrogen atoms [257, 258]. Adsorbates and oxidation have also been reported to lead to surface accumulation on InAs (1 1 0) surfaces [259–263].

In an bulk undoped semiconductor, the Fermi level falls approximately in the middle of the bandgap (the exact value depends on the density of states in the conduction and valence bands). In nanostructures with a large surface-to-volume ratio, the effect of surface states plays a very important role in the properties of the material. If the surface of a semiconductor were perfectly passivated, the Fermi level would be that of the bulk. However, this is rarely found to be the case in III-V materials due to the presence of surface states. Tersoff [264] suggested that the relevant gap to consider is the indirect gap rather than the direct gap in the Γ-valley because the indirect gap spans a larger region in k-space and is more representative of the overall conduction band properties. In Figure 2.16 we can see qualitatively how the indirect mid-gap energy E_B can predict why the Fermi level is pinned close to the direct mid-gap $E_g/2$ in AlAs and GaAs, while pinning the Fermi level in the conduction band of InAs. The arrows represent how changing the group III and group V element affects the conduction band minimum (CBM) and valence band maximum (VBM), respectively. Heavier group III elements cause the CBM to decrease in energy, while lighter group V elements cause the VBM to decrease in energy.
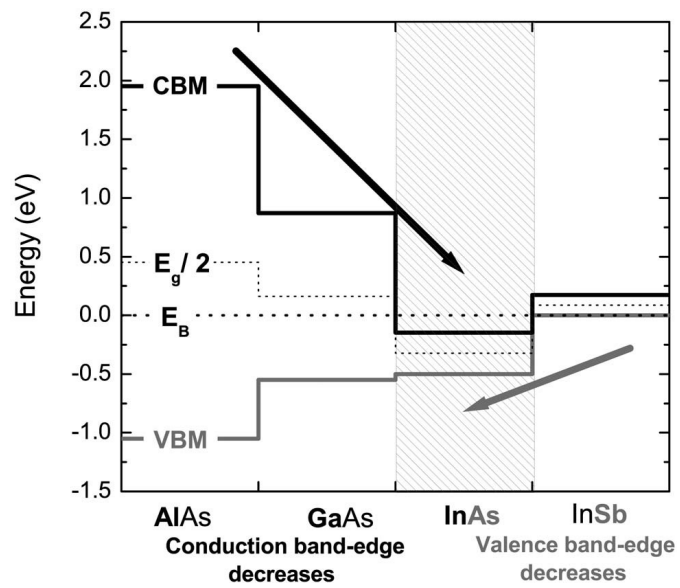
Figure 2.16 – Schematic of band alignment in various III-V semiconductor materials showing the branch-point energy close to which the Fermi level is pinned. Adapted from Piper *et al.* [265] with permission from the American Physical Society.

2.5   Experimental Methods

This section serves to elucidate the techniques employed to obtain the results in this thesis. The important experimental techniques in this thesis can be divided into two categories: growth and characterization. First, I will discuss the details of MBE growth from an experimentalist perspective. Second, I will move to the optical characterization of samples, including sample preparation by FIB followed by TEM imaging and energy-dispersive x-ray spectroscopy (EDS) for obtaining elemental maps. It is worth mentioning that although scanning electron microscopy (SEM) was used extensively throughout this work to characterize all MBE-grown samples, it will not be described here because it is has become such a mainstream technique that the reader can read up on if they wish outside of the context of this thesis [266].

2.5.1   MBE

Since the 1960s, where much of the growth was performed by chemical vapour deposition (CVD) at high pressures and high temperatures, there was significant push to develop growth techniques at lower temperatures and lower pressures. The motivation for this was to decrease both solid-state diffusion of layers as well as the presence of unwanted dopants in the final materials [267]. In this direction, the first report of SAG of GaAs by MBE was in 1975 from Bell labs where Cho and Ballamy grew samples at very low pressures in comparison to CVD methods [268]. They used growth temperatures between $530\,°C$ and $670\,°C$ and growth pressures of around 1×10^{-7} Torr. The resulting films were monocrystalline within the openings in the SiO_2 but polycrystalline and insulating on top of the SiO_2 mask. Their very low selectivity was possibly due to the quality of their CVD oxide mask.

MBE is an approach used to grow high-quality crystals of various materials, including Si, III-V and some oxide-based semiconductors. The advantages of the technique are that the growth is performed under ultra-high vacuum conditions using ultra-pure (99.9999%) source materials, which means that the resulting material is also extremely chemically pure. At the same time, the growth can be performed in a large range of substrate temperatures from $0\,°C$ up to $800\,°C$ (in our system) while purpose-built high-temperature MBE chambers can go as high as $1850\,°C$ [269]. At the other end of the scale, certain MBEs can reach temperatures below $-30\,°C$ for the epitaxial growth aluminium superconductors on InAs [95]. The high growth temperatures allow for high crystal-phase purity in the materials that are grown. As a result, both the high chemical and phase purity means that MBE growth can produce a material with figures of merit close to the material's theoretical limits. For example, researchers working on state-of-the-art GaAs/AlGaAs 2DEG devices can consistently produce devices with low-temperature electron mobilities exceeding 1×10^7 cm^2/Vs [270, 271].

In the next sections, I will describe in detail the MBE system used for this work, including the features of the growth chamber itself, followed by the capabilities of the cluster as a whole.

Growth Chamber

A schematic diagram of our MBE growth chamber is shown in Figure 2.17. The chamber is composed of a rotating substrate holder, referred to as the manipulator, which rotates at 7 rpm with infrared heating of the sample from the top (back of sample). A thermocouple is located on the manipulator allowing for temperature feedback, taking into account that, around the growth temperature, the sample surface is generally about 120 °C colder than the thermocouple reading (depending on holder and sample).
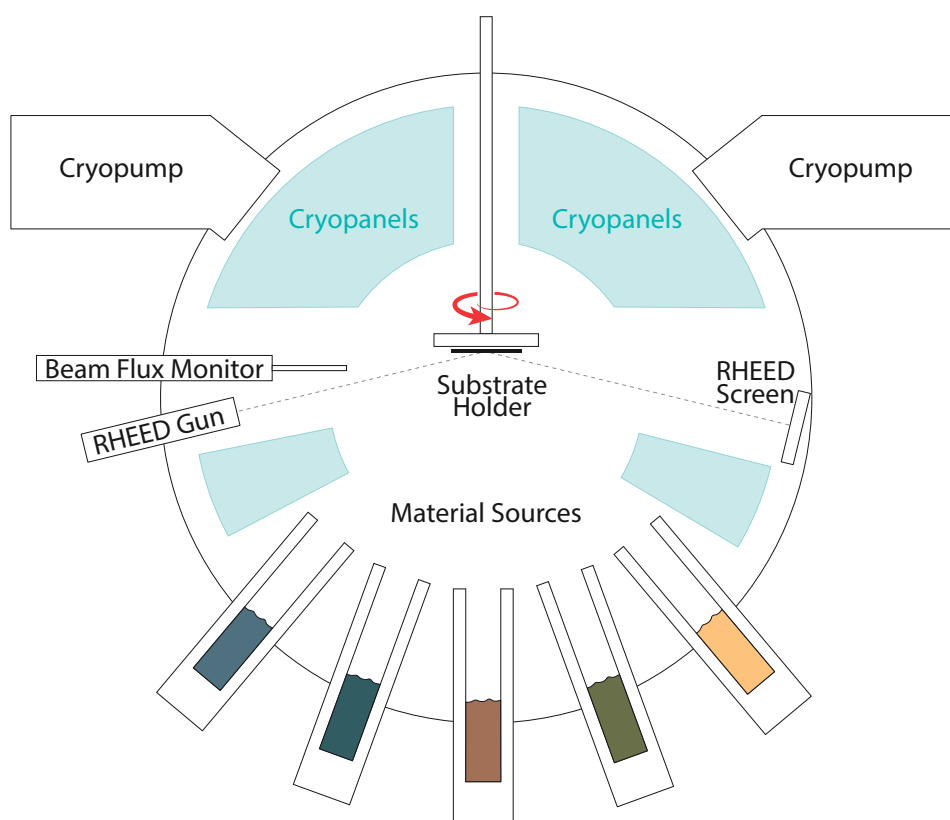
Figure 2.17 – Diagram of the internals of our MBE system.

The sample is loaded facing downwards, with the material sources located in the bottom part of the chamber. Each cell is loaded in one of the ten ports and has a pneumatically-actuated shutter (not shown) in front of it to achieve binary control over the fluxes. As shown in Table 2.4, there are three main kinds of cells used in our MBE which will be described in more detail. All cells, regardless of type, are water-cooled by an open-circuit cooling water line, preventing the rest of the chamber from heating up significantly during cell operation.

The group III materials (Ga, In, Al) were supplied to the substrate using solid-source effusion cells. In these cells, the material is melted in a crucible and heated to the point where its vapour pressure exceeds the pressure in the growth chamber($\sim 1 \times 10^{-10}$ Torr). At this point,

Material	Cell Type	Standby	Operation
Gallium	Effusion	550 °C	900-1000 °C
Indium	Effusion	515 °C	760-850 °C
Aluminium	Effusion	750 °C	1000-1120 °C
Arsenic	Valved Cracker	374 °C	374 °C
Antimony	Valved Cracker	380 °C	450 °C
Silicon (Dopant)	Sublimation	10 A	20-40 A
Carbon (Dopant)	Sublimation	10 A	20-40 A

Table 2.4 – Summary of growth materials loaded in our solid-source MBE, including cell types and rough operating parameters.

atoms begin to be ejected from the crucible and travel towards the growth substrate along a straight (ballistic) trajectory due to the high vacuum in the chamber. The flux is then controlled by the cell temperature and higher deposition rates are achieved simply by heating the cells to higher temperatures.

Due to their high vapour pressure in the solid phase, the group V materials (As, Sb) were supplied by solid-source valved cracker cells. In this type of cell (depicted in Figure 2.18), the bulk of the material is kept at a constant temperature (in the solid form) while the growth flux is controlled by a needle valve. This also allows for greater flux stability and reproducibility as the material is generally not ramped up or down like effusion cells. However, the Sb cell in our system still has to be ramped during operation for two reasons. First, its needle valve cannot be fully closed, leading to a small leak into the chamber on the order of 1×10^{-9} Torr even at 0% valve opening when the bulk is hot. Second, its location directly underneath the ion gauge means that the measured chamber pressure will never reach transfer conditions needed for sample removal unless the Sb bulk is ramped down to ~380 °C.

For doping, the chamber is equipped with two solid wire sublimation cells (Si, C). These are operated by running a current through them causing them to heat up to ~1000 °C and begin emitting an atomic flux suitable for doping. These cells were not proportional–integral–derivative (PID)-controlled but rather current-controlled with higher currents corresponding to higher dopant fluxes.

The UHV conditions are achieved in part by the dual cryopumps (CTI Cryo-Torr 10 and CTI Cryo-Torr 8) located on either side of the growth chamber fed by a closed-loop helium circuit. The helium is supplied by compressors located outside of the lab. The cryopumps are assisted by two cryopanels fed by a liquid nitrogen supply line and vented outside (open-loop). With this configuration, the nominal base pressure achieved by the system is ~1×10^{-10} Torr.

Pressures are measured using a standard ion gauge equipped with dual filaments for redundancy. A second ion gauge is mounted on a retractable arm and is referred to as the beam flux monitor (BFM). This filament is used exclusively for flux calibration of the cells when it is

inserted into the middle of the chamber, below the sample. Here, in the path of the material fluxes, it can measure the beam equivalent pressure (BEP) which is related to the rate of atoms arriving on the substrate.

The BFM calibrations are combined with reflectance high-energy electron diffraction (RHEED) calibrations which are more time-consuming to perform, though more accurate as they directly measure the monolayer growth-rate of the III-V semiconductors. RHEED was performed using a 12 keV electron gun shooting electrons at a grazing angle of a few degrees towards the sample. Opposite the RHEED gun is a phosphorescent screen for visualising the RHEED patterns combined with a leaded viewport to block any x-rays. The RHEED growth rate can be related to the measured BEP allowing for more frequent, quick calibrations by BFM. In general, RHEED calibrations were performed once a year with BFM calibrations performed every 2-3 months, depending on flux stability and frequency of growths.

For monitoring temperature reproducibility, the chamber is equipped with a pyrometer. Recently, this has been augmented with the installation of an infrared-transparent ZnSe viewport and a high-definition infrared camera allowing us to obtain detailed images of the temperature distribution on the sample during growth.

As_2 vs As_4 Flux

Due to the majority of our growths being III-As compounds, the most important cell in our MBE is the As cell. The As cell used in the growth of these structures is a Veeco valved cracker cell, a diagram of which is shown in Figure 2.18. It functions differently than the standard effusion cells used for the Group III materials in both its containment and release of the growth material. The area of the cell that contains the bulk As material is a separate chamber, called the As tank. It is maintained in the range of 350-400 °C (depending on how full it is) and is kept at a constant temperature throughout a growth. At these temperatures and pressures, the solid As sublimates into mostly As_4 molecules which are released through a needle valve controlled by a stepper motor to create a finely-adjustable flux. The As_4 molecules then travel down a heated tube called the cracking zone which, depending on its set temperature, can be used to crack the As_4 molecules into smaller As_2 molecules.

Depending on if As_2 or As_4 is used during growth, different growth results can be observed. Typically in our group, for NW growth, the cracker is set to a relatively low temperature of 600 °C and produces mostly As_4. The As_4 flux gives Ga atoms a longer diffusion length on the substrate [214], and as a result, As_4 is more desirable for vertical NW growth where the Ga diffusion up the NW sidewalls is a significant source of Ga feeding the growth [272].
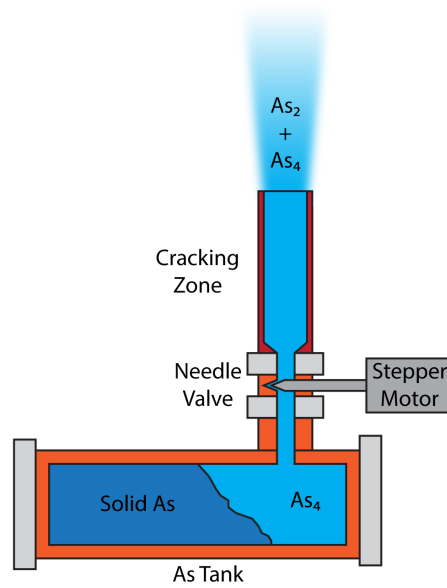
Figure 2.18 – As cracker cell diagram.

MBE Cluster

The MBE growth chamber makes up only part of the whole vacuum system. A drawing of the overall MBE cluster built by DCA is shown in Figure 2.19. The system of UHV chambers takes on a planetary configuration around a single central chamber. What makes this system particularly user-friendly and compact (but at times also a headache to maintain) is the robotic manipulator arm located in the central distribution chamber. From the moment the cassette of eight samples is loaded into the load-lock, until the moment they are unloaded, the robot arm performs all of the sample manipulations between various chambers. As a result, the whole degassing and growth process can be performed remotely from the office.

When the time comes to perform a growth, samples are loaded in the load-lock cassette and the load-lock chamber is pumped down. Halogen lamps heat the load-lock to 150 °C for 2 h to get to UHV conditions. At which point, the samples are transferred into the storage chamber one at a time. From here, the samples are transferred from the storage chamber to the degassing chamber and degassed one at a time for 2 h at 400 °C or 600 °C for GaAs or Si substrates, respectively. After degassing, samples can be transferred into one of the growth chambers for MBE growth. After growth, the samples are again transferred to the load-lock cassette and unloaded. In this thesis, the hydrogen chamber and #2 growth chamber were not used.
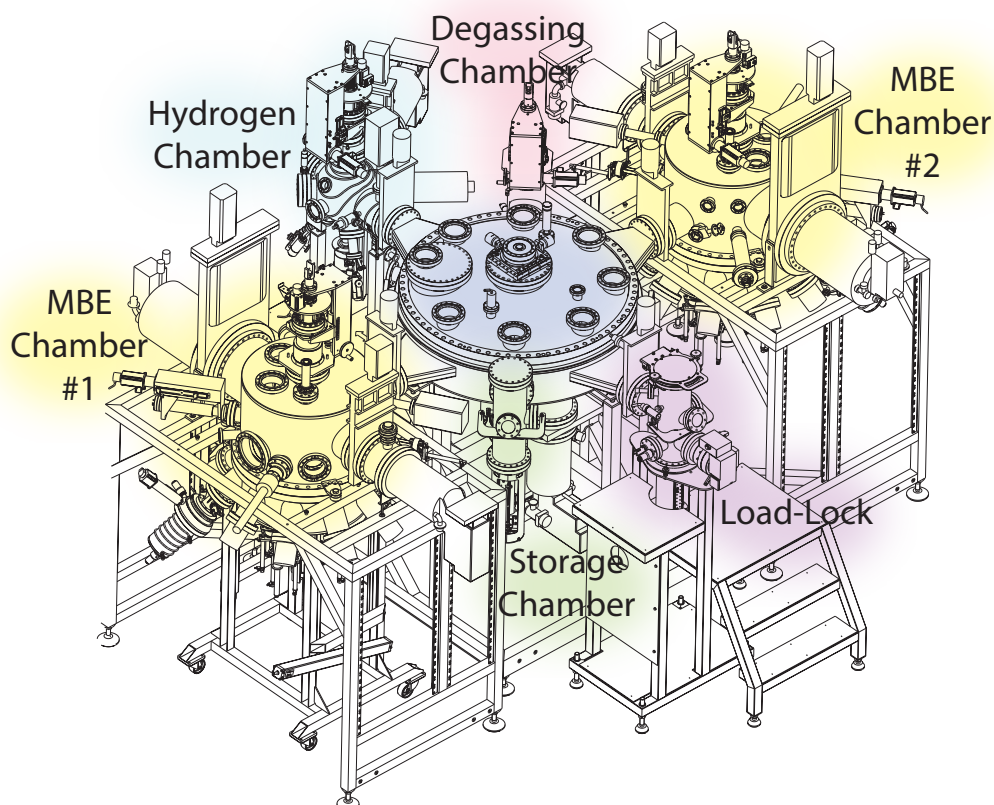
Figure 2.19 – Diagram of MBE cluster.

2.5.2 TEM

The samples grown in the context of this PhD thesis were characterized in various ways. Structural characterization of the growths made up the majority of the analysis, with only select samples being further characterized electrically or by more advanced characterization methods such as atom probe tomography (APT). All samples were imaged by SEM to get an initial idea of the growth quality by looking at NM uniformity and faceting. The resolution of SEM is orders of magnitude better than optical microscopy, however, the minimum practical resolution of about 5 nm is still too large for imaging crystal defects. Furthermore, high-resolution chemical contrast was also desired. Therefore, further analysis of a selection of membranes was then performed by various TEM techniques to shed light on the crystal quality and elemental distribution in the NWs.

TEM can be broadly described as a collection of techniques in which high-energy electrons passing through a sample are imaged to gain information about it. Theoretically, one benefit of TEM, compared to the other popular imaging technique, SEM, is due to the high electron energies used. The de Broglie wavelength of a 3 keV electron typically used in SEM is about 410 pm whereas for a 200 keV electron typically used in TEM the de Broglie wavelength is

only 6 pm. This means that the diffraction-limited resolution of a TEM is substantially higher. Though, in practice, unlike optical microscopy, factors such as magnetic lens aberrations and electron interactions with the sample generally limit the resolution before the diffraction limit is reached.

A diagram of the typical internals of a TEM microscope is shown in Figure 2.20. The TEM microscope used throughout this PhD was an FEI Tecnai Osiris microscope, installed at EPFL in 2011. It consists of a high-brightness 80-200 keV field emission gun (FEG), a pole piece with four EDS silicon drift detectors (SDDs) for x-ray analysis and has a scanning transmission electron microscopy (STEM) resolution of 0.18 nm. Furthermore, this microscope is equipped with a bright-field (BF), two annular dark-field (ADF) and a high-angle annular dark-field (HAADF) detector for STEM imaging. A double-tilt sample holder was used to align the sample along the desired zone axis.
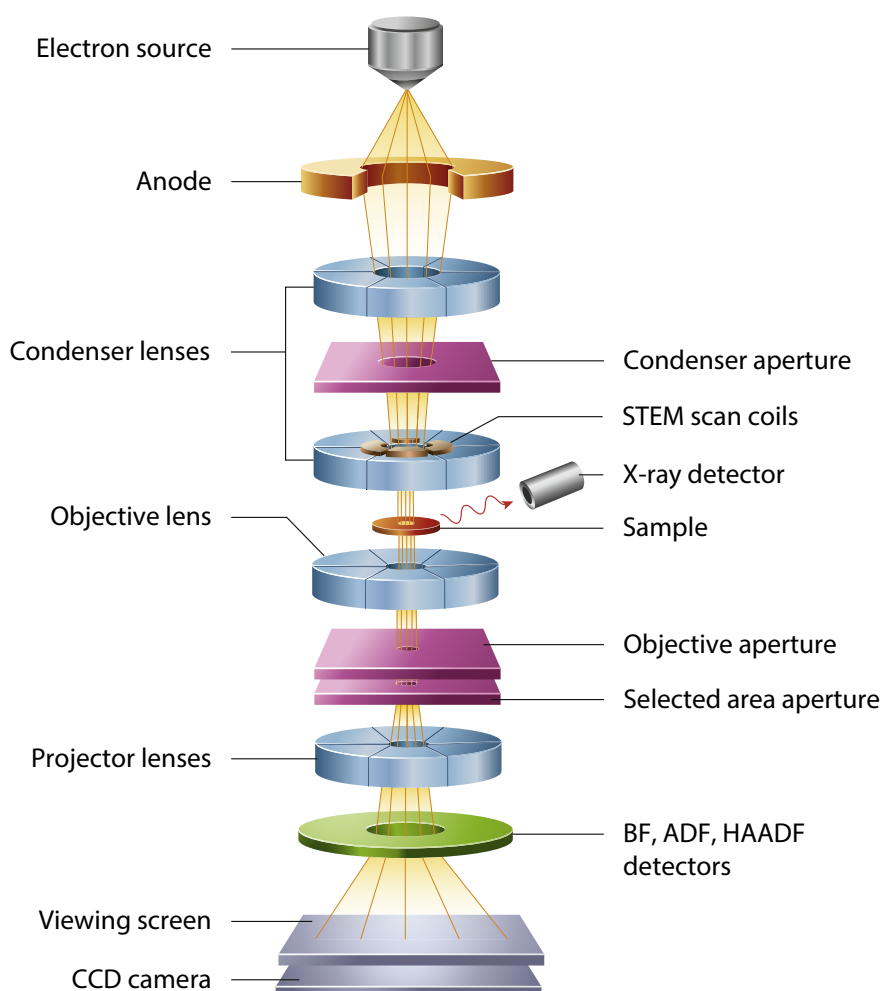
Figure 2.20 – Diagram of modern TEM column, similar to the FEI Tecnai Osiris microscope used in this thesis. Adapted from [273] with permission from Elsevier.

To help describe the electron path during TEM mode operation, Figure 2.21 has been included here. In traditional TEM mode, the condenser lenses are set such that the sample is illuminated by a large, parallel beam of electrons. The electrons diffract within the sample and exit the other side. The objective lens then serves the purpose of focusing the electrons into what is known as the back focal plane, in line with the objective aperture. Here a reciprocal-space image is formed and is where a diffraction pattern would be observed for a crystalline substrate. The objective aperture can be used to select a single diffraction spot to perform dark-field TEM. Below this, an intermediate image of the sample is formed at the level of the selective-area diffraction aperture. Similarly, an aperture can be inserted here and a smaller portion of the sample can be selected to get a diffraction pattern from only this region. Finally, the adjustable intermediate and projector lenses work together to project either the reciprocal space image or the real space image onto the charge-coupled device (CCD) camera below. By adjusting the current in the bottom two lenses, the user can thus switch at will between imaging and diffraction modes.
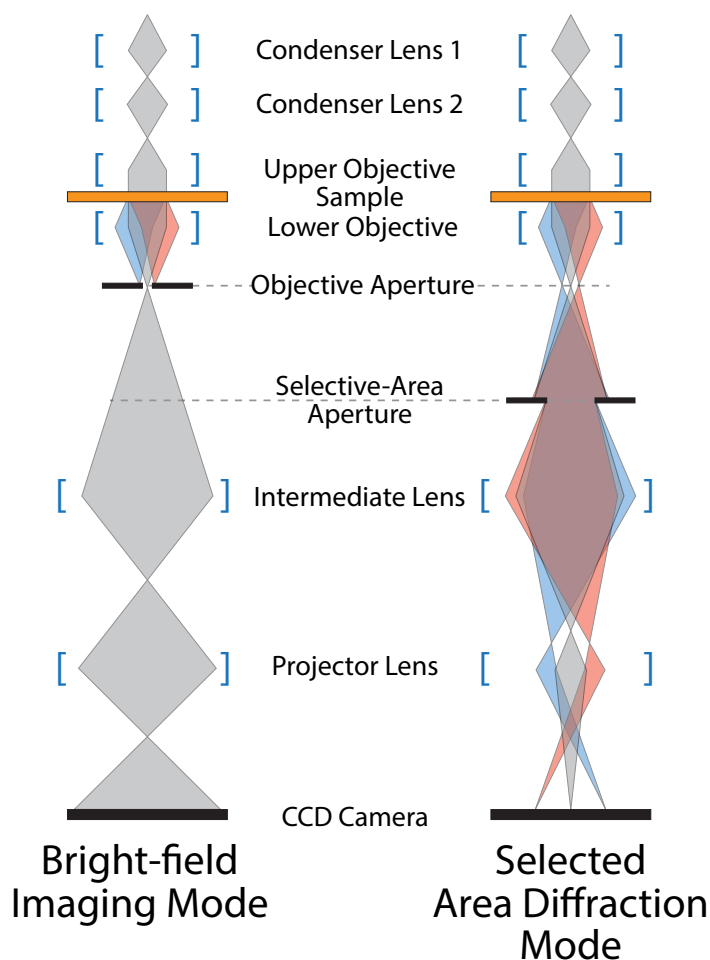
Figure 2.21 – Diagram showing electron path for bright-field TEM imaging vs. diffraction mode imaging.

STEM

STEM is a flavour of TEM where the incident beam is converged to a sub-nanometre spot and rastered across the sample, similar to SEM. Unlike conventional TEM where the scattered electrons are directly imaged on a single CCD detector, in STEM multiple annular CCD detectors are used.

The consideration of electron interactions with the sample, as shown in Figure 2.22, is an important consideration for understanding the resolution advantages of STEM compared to SEM. In both cases, the electron beam penetrates the sample, spreading as it does so. In SEM, relatively low-energy secondary electrons can only escape relatively close to the surface while elastically backscattered electrons have more energy and thus can be emitted from deeper within the sample. Finally, for chemical mapping, x-rays interact very little with the substrate and thus are emitted from a large volume under the beam, resulting in a very low resolution for chemical mapping in SEM.
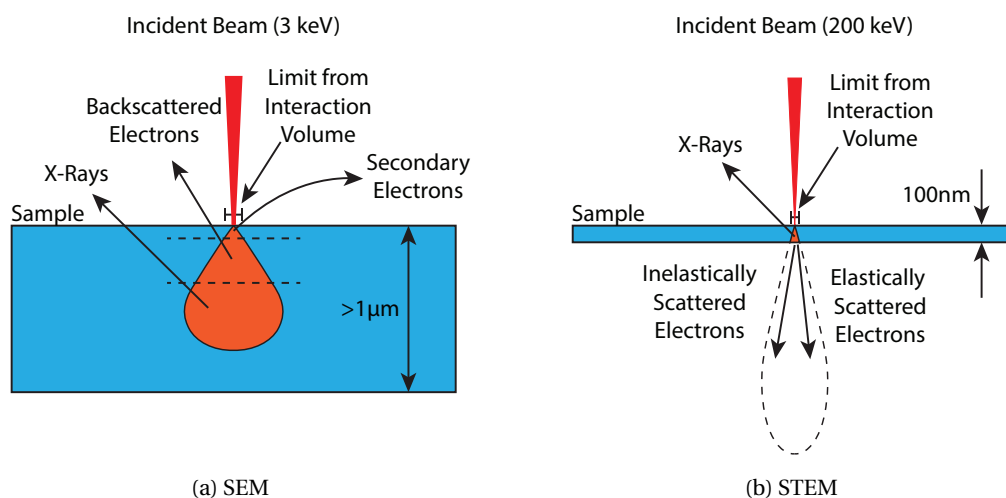
Figure 2.22 – Comparison of resolution limits due to interaction volumes in SEM vs STEM.

A significant advantage of TEM over SEM is the fact that the higher-energy 200 keV beam does not spread as quickly as the 3 keV beam when it travels through the sample. The second advantage in TEM stems from the fact that the sample is much thinner, thus the beam does not spread very much before it exits the sample, resulting in a significantly smaller interaction volume. This smaller interaction volume is also a significant advantage for chemical mapping by x-ray spectroscopy techniques because in STEM, due to the small sample thickness, the resolution of EDS is significantly better.

EDS

EDS is an approach used both in SEM [274] and STEM [275–277] which enables elemental mapping of a sample by measuring the x-ray signal emitted from the sample. Over the years, advancements in aberration correction, x-ray spectrometry and computational speed have made it possible to perform chemical mapping down to the atomic limit [278]. Today, this option is available in many high-end aberration-corrected commercial microscopes.

Figure 2.23a shows the process by which x-rays are produced from the atoms of the sample. Inner electrons close to the nucleus get scattered by the high-energy electron beam. An outer-shell electron then jumps down to fill the vacancy and releases its surplus energy in the form of an x-ray photon when doing so. The resulting photon energy is in the range of a few to several keV. Each element has multiple such transitions that can occur, depending on which electron is scattered and which electron takes its place. This is summarized in Figure 2.23b showing the different transitions in a single atom and their corresponding names.

(a) EDS   (b) Atomic tansitions
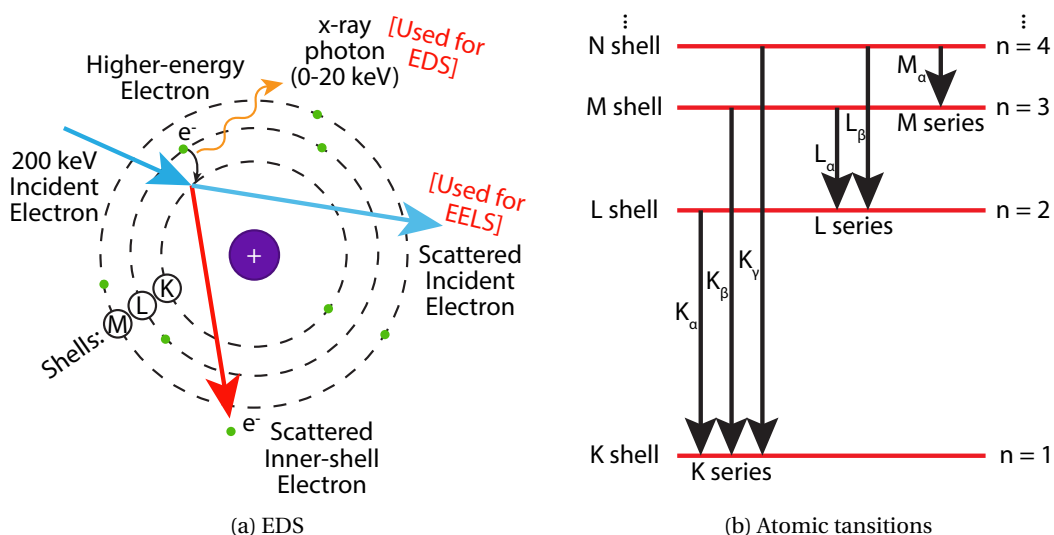
Figure 2.23 – Depiction of how x-rays used in EDS are produced in the TEM column.

The key point which makes EDS such a powerful tool is that for each element these transitions all have different energies, and thus each element has an x-ray fingerprint by which it can be uniquely identified. In practice, however, with multiple elements in a single sample, this becomes more challenging due to overlapping x-ray peaks. Going a step further, by taking into account sample geometry and absorption effects, elemental quantification becomes possible to within a few percent error. This was, therefore, an essential tool in quantifying the material purity of samples grown in this thesis, specifically when looking at the In concentration in InGaAs NWs, as well as when looking at intermixing between InAs and GaAs.

The FEI Tecnai Osiris microscope used in this thesis was specially-equipped for high-speed and

high-sensitivity EDS spectroscopy thanks to its four Super-X SDD x-ray detectors built into the pole piece, just above where the sample sits in the column. These four liquid nitrogen cooled detectors integrate the x-ray signal from an exceptionally large area and as a result, offer a larger signal to noise ratio over conventional single or double detector setups. Additionally, a low-profile double-tilt sample holder based on beryllium components and specifically designed for minimizing x-ray absorption and background x-ray signal was used in all investigations.

2.5.3   TEM Sample Preparation

Proper sample preparation for TEM analysis was critical to obtain good images and was often even more time-consuming than the imaging itself. Here I explain the three methods that were explored to prepare TEM samples. A summary of the pros and cons of these methods is shown in Table 2.5.

Technique	Dry Transfer	Ultramicrotomy	FIB Lamella
Time/Cost	Low (10 min)	Med. (2 h)	High (4 h)
Difficulty	Easy	Med.	Hard
Yield (NMs)	High (>100)	Med. (>10)	Low (<10)
Selectivity	Low	Med.	High
Cross-section?	No	Yes	Yes
Min. NM Height	~200 nm	~500 nm	0 nm
Min. Achievable Thickness	Sample thickness	~50 nm	~20 nm

Table 2.5 – Comparison of TEM preparation techniques.

From this comparison, we see that dry transfer is the easiest approach, while FIB is the most arduous. However, the difficulty, cost and low yield of FIB are offset by the fact that this technique offers unparalleled selectivity without a restriction on minimum NM height because it does not rely on the mechanical scraping/peeling to remove the nanostructures from the substrate. Ultramicrotomy was also tried as a compromise between the two previously-mentioned techniques because it offered the ability to prepare cross-section samples without the use of FIB. However, the peeling of NMs from the substrate by epoxy embedding means the NMs need to be at least about 500 nm tall or they will not be removed reliably. Due to this limitation, this approach was abandoned after the first few samples, as typical NMs grown in this thesis were about 300 nm tall. The technique, however, is still included in the comparison for completeness.

Dry Transfer

Dry transferring of grown samples onto a copper carbon TEM grid was the simplest TEM sample preparation approach used in this work. Due to its speed, ease of implementation, low-cost and large yield, it is by far the most common sample preparation technique for analysing MBE-grown nanostructures in our lab. The technique consists of mechanically transferring nanostructures from a growth substrate onto an electron-transparent substrate used for TEM.

The transfer can be performed in several ways, including directly touching the TEM grid to the growth substrate to break off the nanostructures, some of which then stick to the grid. This was later refined by using a razor blade to first remove the nanostructures followed by gently dispersing them with the help of an eyelash over the delicate carbon grid to avoid damaging it.

Dry transferring has the advantage that in one transfer hundreds of nanostructures can be deposited on the grid allowing for the imaging of many structures. All nanostructures, however, land flat on their sides and therefore only side-view TEM images are obtainable. Also, nanostructures can agglomerate and overlap on the grid which results in a lower yield of nanostructures that are suitable for imaging. Another disadvantage for large nanostructures such as NMs is that the mechanical transfer method inevitably leads to breakage resulting in the loss of information regarding the nanostructure's relationship with the substrate. Lastly, if the nanostructures are thicker than about 150 nm then they will absorb too much of the incident electron beam for high-resolution transmission electron microscopy (HR-TEM) imaging. Therefore this technique is not suitable for thick nanostructures.

FIB Lamella Lift-Out

Despite its large time investment, FIB lamella lift-out was the technique that yielded the most useful insight into how the NWs were growing on top of the NMs. The main tool that enables this type of TEM sample preparation is the FIB microscope, a schematic of which is shown in Figure 2.24.
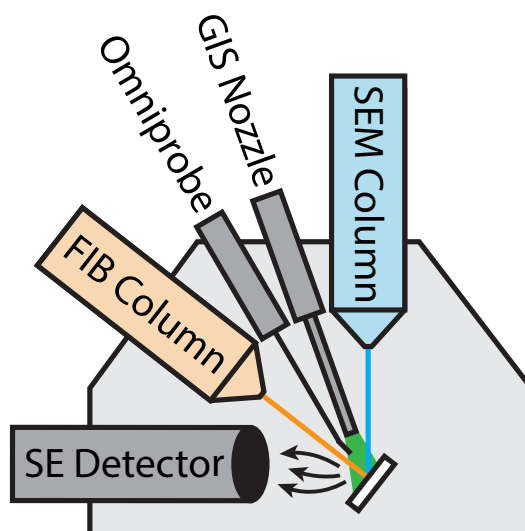
Figure 2.24 – Diagram of a dual-column FIB tool used to cut and lift out lamellas for TEM analysis.

The dual-beam microscope can be thought of as a regular 5 keV SEM column including a secondary electron detector, combined with a second column tilted at 52 ° to the main electron column. Instead of an electron source, the second column uses a 30 keV ionized Ga atom source. The Ga atoms have a much higher kinetic energy than the electrons and can sputter away material from the sample surface. By controlling the sweeping pattern and ion beam current, complex shapes can thus be patterned into the substrate using the ion beam.

The ion beam enables the selective removal of material, however, a second important feature of the FIB microscope is the ability to selectively add material to the substrate. This is achieved using the gas injection system (GIS) nozzle. The GIS nozzle consists of a very small-diameter tube from which a metal-organic precursor gas is injected into the chamber. When hit by either electron or ion beams, this precursor decomposes into solid carbon-rich platinum that is deposited on the sample. The amount of carbon is higher when the electron beam is used, while when the ion beam is used there is much less carbon deposited as the precursor is almost entirely decomposed by the beam. This ability for selective Pt deposition is very useful because it allows for the sticking of lamellas to TEM grids.

The final important feature of the FIB microscope is the Omniprobe AutoProbe. This consists of a very small-diameter Tungsten needle which can be inserted into the chamber. It is mounted on a 3-axis piezo stage for very precise movements down to 100 nm increments. The AutoProbe is what is used to perform the physical manipulation of the lamella, enabling the transfer of the lamella from the substrate to the TEM grid.

The process of preparing a sample by FIB consists of many steps which are outlined here. First, the area of interest is prepared by depositing a 15 μm long, 2 μm wide and 4 μm thick

layer of protective platinum. Next, the areas to either side of the platinum are removed with the ion beam. The sample is tilted to 45° to the ion column and the lamella is released from the bottom and on one side. Next, the tungsten Omniprobe AutoProbe needle is approached to the sample until it makes contact with the lamella. The final approach is done in 100 nm increments to avoid breaking the lamella. It is then stuck in place using a combination of ion and electron beam-assisted Pt deposition. Next, the lamella is cut away from the substrate on the remaining side and the substrate is retracted to leave the lamella stuck to the Omniprobe tip.

The lamella is then approached to an M-shaped post on a copper lift-out TEM grid. Unlike standard carbon film grids, this special type of TEM grid is made specifically with posts where lamellas can be attached. The grids used in this thesis had three posts, two M-shaped posts and a single I-shaped post in the centre. The M-shaped posts were used for all samples in this thesis, this is because they offer more stability to the final lamella as they allow for sticking the lamella with Pt on both sides as opposed to just one side. This reduces the chances that the lamella warps/curls during the thinning process, something that had been observed in the first lamellas made. Additionally, the M-shaped post provides a bit of extra protection for the lamella in the event of loading mishaps when performing TEM.

Upon contact of the lamella with the M-shaped post, the two bottom corners of the lamella were stuck to the post with Pt. This was followed by the cutting off of the AutoProbe tip to release it from the sample and retracting it. The lamella was then thinned. Thinning was performed by successively smaller beam currents of 1000 nA, 500 nA and 100 nA at successively shallower grazing incidence angles. After the last thinning step, the lamella is somewhere between 100-150 nm thick. Though this is still somewhat too thick for optimal atomic-resolution HR-TEM, the extra thickness gives more signal in STEM EDS which was given priority in this case.

Peel-off Ultramicrotomy

Ultramicrotomy was briefly tested as an easier alternative to FIB lamella preparation. This technique consists of pouring an epoxy resin on an area of interest on the growth sample. The epoxy cures around the high aspect-ratio nanostructures which become embedded within it. The epoxy resin is then peeled from the substrate, taking the nanostructures with it. The epoxy piece is then cut down to size using a diamond wire saw. Finally, the step of ultramicrotomy consists of taking the remaining epoxy piece with nanostructures embedded within it and cutting very thin slices from it, as thin as 50 nm if desired. The thin slices are then transferred onto a traditional carbon TEM grid for imaging. See Ref [279] for more details about how this method is applied for vertical NWs.

The advantage of this approach compared to FIB is that many consecutive slices can be cut from a single sample, allowing for many more cross-sections to look at in TEM. Furthermore, basic depth profiling into the sample can be performed by looking at every Nth slice cut by

the ultramicrotome. The disadvantages of this method were that the NMs had to be quite tall to be properly peeled by the epoxy resin and that the ultramicrotomy often led to cracking of the NMs cross sections, as shown in Figure 2.25.
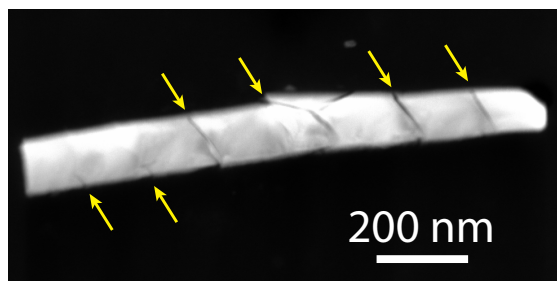
Figure 2.25 – HAADF STEM image of a GaAs NM cross-section obtained by peel-off ultra-microtomy showing large cracks that develop likely through the process of diamond knife cutting.

3 Template-Assisted NW Growth on GaAs (111)B

The results of lateral NW growth on top of GaAs NMs grown on GaAs (111)B substrates will be presented in this chapter. Our initial publication on the topic of template-assisted In(Ga)As NW growth is first presented in Section 3.1. Then, Section 3.2 explores the follow-up to this initial work in which we looked at modulation-doping these wires with silicon in order to improve their electrical properties.

3.1 Template-Assisted Scalable Nanowire Networks

M. Friedl, K. Cerveny, P. Weigele, G. Tütüncüoglu, S. Martí-Sánchez, C. Huang, T. Patlatiuk, H. Potts, Z. Sun, M. O. Hill, L. Güniat, W. Kim, M. Zamani, V. G. Dubrovskii, J. Arbiol, L. J. Lauhon, D. M. Zumbühl and A. Fontcuberta i Morral. Template-Assisted Scalable Nanowire Networks. *Nano Letters* **18**, 2666 (2018)

The content of this paper has been reformatted to match that of this thesis with references combined with those at the end of this thesis. The content and figures have been reproduced here without modification with the permission of the American Chemical Society.

My contribution to this work consisted of growing and imaging all samples, including all growth campaigns leading up to obtaining NWs on top of the NMs. This was rounded out with finite element simulations of the strain relaxation in the grown samples and direct measurement of the strain by Raman spectroscopy (both included in the supplementary information (SI) in Appendix C.1.5, Appendix C.1.4).

This work represents a substantial portion of work performed over the course of my PhD. This work was the result of a large collaboration between five groups and it took about two years to go from the initial results until the publication of the paper. Initial attempts at growing InAs on GaAs NMs were promising and it was confirmed by TEM that the NW was fairly pure. However, NW uniformity along the length of the NW was somewhat lacking for good electrical measurements likely due to the large lattice mismatch. The growth parameter space was explored we believed that if we reduced the dimensions of the NW we might be able to achieve

better uniformity. Indeed we saw that it was possible to make the NWs more uniform by depositing less InAs but what we didn't know at the time was that by reducing the amount of InAs deposited, we were increasing the relative fraction of intermixed Ga, thus yielding InGaAs NWs. The resulting NWs, therefore, had very high resistances (measured in Basel), despite the better uniformity observed by SEM. This was surprising because it was expected that an InAs NW would have its Fermi level pinned in the conduction band at the surface and the NW would thus be highly-conductive.

In order to some conduction, the decision was made to add Si dopants to the NWs. When this was done, the NWs began to conduct many orders of magnitude better than before and it was possible then to perform magnetotransport measurements in Basel. The results of these magnetoconductance measurements gave WL behaviour which was perplexing because it was expected that an InAs NW would, in fact, exhibit WAL due to the high SOI. The extracted figures of merit were promising. The short electron mean free path of on the order of a few nanometres was expected due to the high doping concentration while the phase coherence length of greater than 100 nm was also promising.

At the same time, at Northwestern they were able to perform APT to image the wire along with the dopants in the wire which were undetectable to us by other methods such as TEM or nano-secondary ion mass spectrometry (SIMS). There were three important results that came out of the APT analysis: first, the In content in the wire was only about 17%, second, what we expected to be a single NW was, in reality, two small NW each sitting on the {113} facets of the NM, and third, the dopants had all accumulated at the top of the structure rather than being uniformly incorporated in the NW.

Despite the surprises, the result of these investigations showed us that it was possible to use GaAs NMs as templates for the growth of in-plane NWs and even use the templates to create branched NW structures. The quantum electrical transport properties of the NWs, however, had some room for improvement, and this was largely the goal of our next paper (described in Section 3.2) where the figures of merit of the NWs were increased significantly.

3.1.1 Abstract

Topological qubits based on Majorana Fermions have the potential to revolutionize the emerging field of quantum computing by making information processing significantly more robust to decoherence. Nanowires are a promising medium for hosting these kinds of qubits, though branched nanowires are needed to perform qubit manipulations. Here we report a gold-free templated growth of III-V nanowires by molecular beam epitaxy using an approach that enables patternable and highly regular branched nanowire arrays on a far greater scale than what has been reported thus far. Our approach relies on the lattice-mismatched growth of InAs on top of defect-free GaAs nanomembranes yielding laterally oriented, low-defect InAs and InGaAs nanowires whose shapes are determined by surface and strain energy minimization. By controlling nanomembrane width and growth time, we demonstrate the formation of

compositionally graded nanowires with cross-sections less than 50 nm. Scaling the nanowires below 20 nm leads to the formation of homogeneous InGaAs nanowires, which exhibit phase-coherent, quasi-one-dimensional (1D) quantum transport as shown by magnetoconductance measurements. These results are an important advance toward scalable topological quantum computing.

3.1.2 Introduction

In the past few years, much progress has been made toward fabricating and scaling up qubit density to build universal quantum computing systems that can outperform classical computers by quantum schemes [38, 280–283]. The ideal qubit should combine long coherence times, fast qubit manipulation, and small size, while maintaining scalability to many-qubit systems. Long coherence times are fundamentally challenging to achieve in various qubit systems due to the presence of numerous forms of environmental noise, requiring operating temperatures in the range of a hundred millikelvin [284, 285]. A system, which has been proposed to be much more robust against such perturbations, is the topological qubit [286, 287]. This type of qubit, for example, composed of Majorana fermions (MFs) [55, 286] or Majorana parafermions (MPFs) [75, 76], would have the inherent property of being topologically protected and would thus exhibit exceptionally long coherence times. Signatures of MF states have been observed experimentally in, among other systems, III-V semiconductor nanowires (NWs) in close proximity to an s-wave superconductor [79, 80, 288], while a few other groups have reported anomalous MF signatures in similar systems [81, 289, 290]. In general, these studies have focused on using III-V materials, such as InAs and InSb, due to their high-spin-orbit coupling strength and g-factor [291]. Current efforts are focused on performing the first manipulations of MFs to further verify theoretical predictions, for which low-disorder, connected 1D branches are required [62]. Gold-free and defect-free NW branches made of a high-purity, high-spin-orbit III-V material would be an ideal platform for manipulating MFs. Excellent progress has been made toward this goal with reports on the growth of monocrystalline gold-assisted InSb NW branches, which display a weak anti-localization due to the large spin-orbit interaction of the material, as well as a hard superconducting gap [98, 100]. Scalability is another important aspect of any future computational system, and on this front, the Riel group has recently demonstrated patternable ballistic InAs NW crosses through template-assisted growth on silicon [217].

Despite recent progress, a few challenges still exist with current methods to produce branched structures. The fabrication of NW networks and intersections has been explored for many years for classical computing by overlapping individual wires [292–294]. For MF applications, the stringent requirement of maintaining coherent transport across the intersection means that, currently, the most popular NW cross structures rely on the intersection of two gold-catalysed NWs grown along two different ⟨1 1 1⟩B directions leading to an interface-free junction [99, 219, 295–297]. After growth, free-standing crosses are obtained, which then need to be transferred onto a separate substrate for further device fabrication, limiting the ultimate scalability. A

scalable scheme would instead enable the NW growth and intersections to be realized directly on the final device substrate. At the same time, for future device integration, the use of gold seeds poses a problem for compatibility with complementary metal-oxide-semiconductor (CMOS) technologies [298]. Here, we demonstrate a new approach to grow gold-free branched In(Ga)As NWs at the wafer scale by using GaAs nanomembranes (NMs) as templates.

Defect-free GaAs NMs of exceptional quality constitute the ideal templates for further In(Ga)As NW growth [177, 299]. Such structures have been successfully grown by both metalorganic chemical vapour deposition (MOCVD) and molecular beam epitaxy (MBE) using a gold-free selective area approach [177, 300]. The NMs are patternable at the wafer scale and can additionally be fabricated in the form of Y-shaped structures by growing them along the three $\langle 11\bar{2} \rangle$ directions on GaAs (111)B substrates [300]. When the growth of these GaAs NMs is followed by InAs, the InAs accumulates at the top of the NMs, forming In(Ga)As NWs along the NM vertex, as depicted schematically in Figure 3.1a. Shown in Figure 3.1b is the progression of the NW growth, which initiates as InGaAs and then evolves to pure InAs for longer growth times. By varying the deposition times and growth conditions, the size and composition of the NWs can be changed. Combining the concepts of patterning NMs into Y-branches and performing In(Ga)As NW growth on top of GaAs NMs, Y-shaped In(Ga)As NW junctions can be obtained, as shown in Figure 3.1c,d. Our approach thereby enables the growth of gold-free branched NWs at the wafer scale.
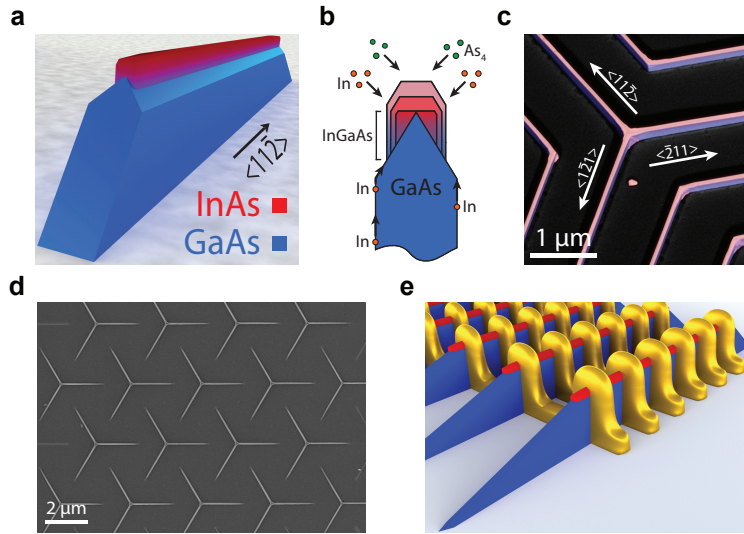
Figure 3.1 – Growth of NWs on NMs. (a) Model of a single GaAs/InAs NM/NW structure. (b) Diagram showing NW growth progression. (c) A 30° tilted scanning electron microscopy (SEM) image of a branched NM/NW structure taken with an energy-selective backscattered electron detector for z-contrast. The image is false-coloured for visibility and annotated with relevant substrate directions. (d) SEM image of branched NW structures grown in a regular array. (e) Model of an array of contacted linear NM/NW structures used in magnetotransport measurements.

In this Letter, as the first step toward building MF devices based on this approach, we demon-

strate the growth of low-defect linear In(Ga)As NWs based on GaAs NMs. Magnetotransport measurements (depicted schematically in Figure 3.1e) demonstrate weak localization in the diffusive regime suggesting quasi-1D quantum transport. This makes such NWs ideal candidates for future quantum computing schemes.

3.1.3   Nanomembranes as a Platform

Membranes with top ridges parallel to the substrate were grown as described previously [177]. The InAs NWs were then grown for 200 s at an As_4 flux of 8×10^{-6} Torr, an In rate of 0.2 Å/s and a substrate temperature of 540 °C. This optimized substrate temperature yielded continuous InAs growth on top of the NMs. The details can be found in the supplementary information (SI) (Appendix C.1). A Si dopant flux of $\sim 10 \times 10^{13}$ cm^{-1} s^{-2} was also introduced to increase the conductivity of the NWs.

The NW morphology, composition, and structural quality were extensively characterized by correlated analysis using various electron microscopy techniques. These included electron energy loss spectroscopy (EELS) and atomic resolution aberration-corrected high-angle annular dark-field (HAADF) scanning transmission electron microscopy (STEM). The results were then coupled with geometrical phase analysis (GPA) to give strain information [301, 302], which in turn was fed into a semi-empirical model to understand the formation of the NWs from a theoretical standpoint.

Analysis of focused ion beam (FIB) lamellas prepared perpendicular to the NW axis by HAADF STEM and correlated EELS (Figure 3.2a-c) show that ~50 nm diameter InAs NWs form on the 250 nm tall GaAs NMs. The InAs material preferentially accumulates along the top ridge of the GaAs NM, forming the NW, which is primarily InAs with a ~20 nm thick intermixed InGaAs region at its base. (See the SI, Appendix C.1, for details.) This InGaAs region likely occurs due to strain-mediated intermixing with the GaAs NM below as has been observed in InAs quantum dots on GaAs [303]. It is important to note that we observe no In signal from the NMs; the faint signal seen in the EELS map is believed to be created during the FIB cutting by a combination of redeposition of the TiO_x protective layer and surface diffusion of the highly mobile In adatoms. Looking instead at the NW facets, as seen in Figure 3.2d, the resulting InAs NW structures are terminated by two (110) facets on the sides and have a single flat (111) top facet. The appearance of this (111) facet, instead of the two {113} facets as in the GaAs NMs, can be explained by the higher As_4 flux used in the InAs NW growth [304, 305]. No defects were observed when viewing this transverse lamella in atomic-resolution HAADF STEM mode. As strain along the NW axis was predicted to be more difficult to relax than in the transverse direction, a second FIB lamella was prepared parallel to the axis of the NW and also imaged using atomic resolution HAADF STEM. Here, a few misfit dislocations were observed near the InAs/GaAs interface, with an estimated density of approximately 100 μm^{-1}, as described in the SI (Appendix C.1). This constitutes a 40% reduction in dislocation density with respect to the equivalent two-dimensional (2D) growth of InAs on GaAs and at least three

times improvement with respect to the twin density typically observed in self-catalysed InAs NWs [89, 306, 307].

Turning now to explaining the morphology of the structures, an analytical model shows that the surface and strain energy minimization play the most important role in driving the NW to adopt the observed shape (see the SI in Appendix C.1). By taking advantage of the atomic resolution offered by HAADF STEM images, GPA was performed on the initial FIB lamella cut perpendicular to the NW axis. Looking specifically at the (111) plane spacing, a substantial 2-3% residual compressive strain is observed within the NW, as shown in Figure 3.2e, with the corresponding line scan given in Figure 3.2f. Using this strain value, a semi-quantitative model was developed to describe the NW formation energy, taking into account the InAs/GaAs surface energies and the InAs elastic strain energy. The total energy of the system was then minimized with respect to the NW aspect ratio. Interestingly, the experimentally observed aspect ratio coincides with that of the theoretical minimum energy shape, suggesting that the NW shape is simply driven by energy minimization. (See the SI in Appendix C.1 for details.)

3.1.4 Electrical Transport in the Mesoscopic Regime

To bring the NWs into the 1D electrical transport regime, they were downscaled to ~20 nm diameters by narrowing the GaAs NMs by using smaller SiO_2 openings and shorter growth times for less lateral growth. The resulting NWs were smaller both laterally and vertically, resulting in intermixed InGaAs NWs, as depicted for small diameter NWs in the growth progression diagram in Figure 3.1b. These results were confirmed by performing APT, which additionally yielded information about the Si dopant distribution. The APT analysis confirmed the presence of an InGaAs NW, while also uncovering signs of dopant rejection during crystal growth, causing an accumulation of Si atoms at the NW surface. Figure 3.2g shows a typical APT map of the In mole fraction and Si dopant distribution. A quantitative composition profile of the NW surface was extracted in the proximity histogram (proxigram) shown in Figure 3.2h. In this sample, the NW group III mole fractions are ~17% In and ~83% Ga. (Additional maps are given in the SI in Appendix C.1)

Analysis of different InGaAs samples by APT tomography under similar conditions shows a slight tendency toward preferential In evaporation. In addition, a GaAs capping layer was deposited on the APT sample after the NW growth, which may have enhanced the Ga intermixing [308]. For these reasons, we consider the In mole fraction in this NW as a lower bound. Although a Si flux was present during InAs NW growth, the Si atoms are not homogeneously distributed throughout the NW (Figure 3.2g). The Si atoms instead appear to accumulate preferentially at the (111) growth interface, resulting in a quasi-remotely doped structure.

The electrical properties of the NWs were explored through multi-contact resistance measurements on an array of NWs, for which an example device is shown in Figure 3.3a. An array of 34 NWs, comparable to those on which APT was performed, was used for these tests as a way to obtain the average response from many devices. Standard four-point measure-
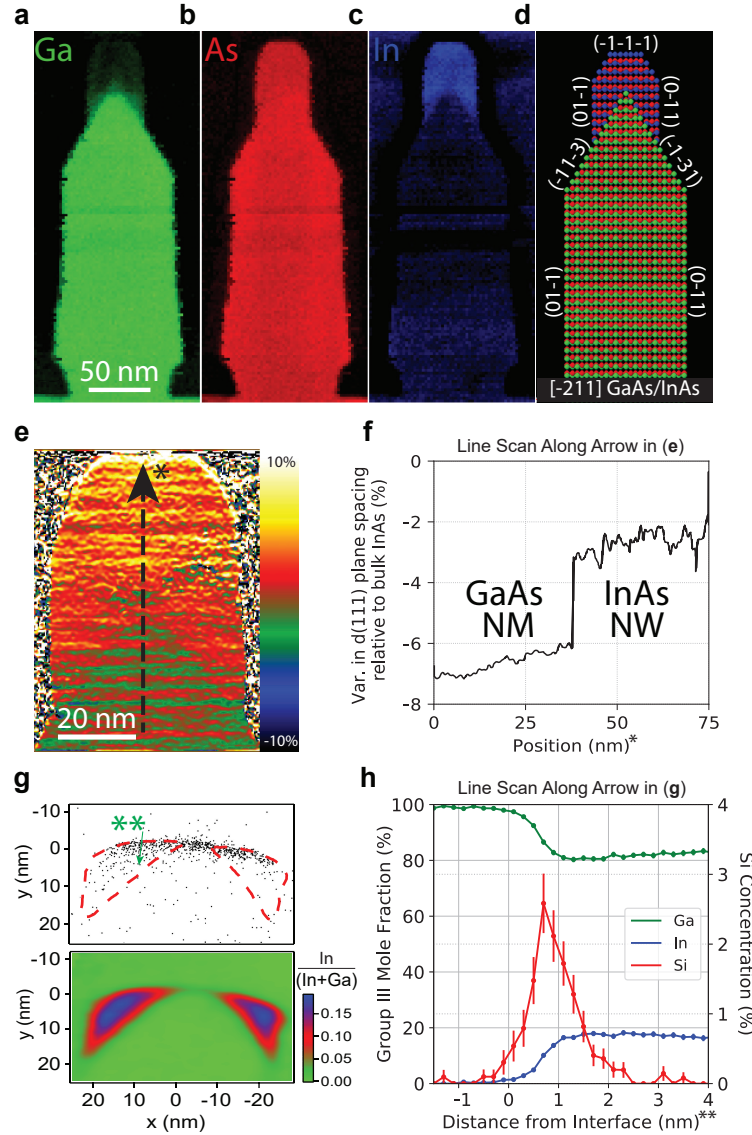
Figure 3.2 – Transmission electron microscopy (TEM) and atom probe tomography (APT) analysis. (a-c) EELS maps with elemental contrast of a NM/NW cross-section. Note that the overlap of the In EELS signal with the Ti signal from the TiO_x capping layer has caused an anomalous background of In within the NM, which is not physical. (d) Atomic model showing faceting of the NM/NW heterostructure. (e) GPA map of the InAs NW region. (f) Line scan along arrow in panel (e). (g) APT map of scaled-down NWs used in electrical measurements showing In concentration (lower map) and accumulation of Si dopant atoms (black dots) at the surface of the NW with In isoconcentration lines as a guide to the eye (upper map). Note that, since the NWs were capped with GaAs for APT analysis, the measured In concentration can be considered as a lower bound for the uncapped structures. (h) Proxigram line scan along the dashed arrow in panel (g) showing Si accumulation on the NW top facet and In concentration within the NW.

ments were then carried out at room and low temperatures before moving to low-temperature magnetoconductance transport experiments.
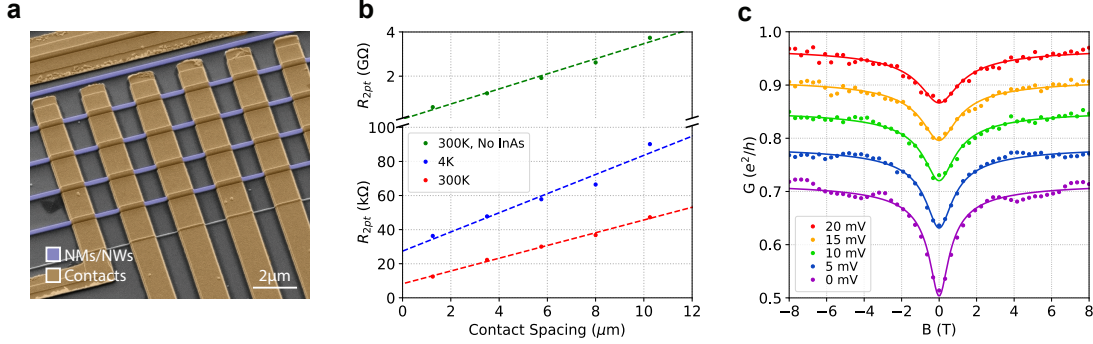
Figure 3.3 – Magnetotransport measurements. (a) False-coloured SEM image of four InAs/-GaAs NMs/NWs contacted in parallel. (b) Transmission line measurement to extract contact resistance and resistivity (per NM) at 4 K and 300 K, in comparison with NMs without the InAs deposition step. (c) Average differential conductance per NW as a function of magnetic field perpendicular to the NMs for a range of bias voltages measured at 1.5 K for a 1.25 μm-long NW segment. The traces for biases above 0 mV are offset for clarity.

Room-temperature transmission line measurements, shown in Figure 3.3b, gave linearly scaling and repeatable resistances, suggesting that a good-quality contact was achieved. A control sample without InAs NWs (as shown in green in Figure 3.3b) shows a 5 orders of magnitude increase in resistance, directly proving that the observed conduction occurs due to the InAs deposition. Device behaviour remained linear and ohmic down to 4.2 K, albeit with an increased contact resistance. Magnetoconductance measurements at 1.5 K revealed a zero-field minimum of conductance consistent with a weak localization (WL) behaviour, as shown in Figure 3.3c [309]. The conductance of the devices was measured under constant bias, while the magnetic field was applied perpendicular to the substrate and was swept from -8 T to 8 T. This analysis indicates conduction in the quasi-1D transport regime and elucidates important quantum figures of merit such as coherence length and spin-orbit length, as described below. A coherence length l_ϕ of 130 nm and a lower bound on the spin-orbit length l_{so} of 280 nm were obtained by fitting the experimental data. The system was assumed to be in the diffusive regime with the electron mean free path $l_e << W$, with W being the width of the conducting channel, estimated from the APT results to be about 20 nm. In this regime, l_e is thus constrained to be a few nanometres due to the large amount of dopant and surface scattering. A simple quasi-1D model for the quantum corrections to the conductivity in the diffusive limit (details in) gives an excellent agreement with the data and yields $l_\phi \approx 130 \pm 4$ nm near zero bias, as shown in the solid traces in Figure 3.3c. In the absence of weak anti-localization, and adding spin-orbit coupling to the model, a lower bound for l_{so} of 280 nm is estimated. Some small variations in the conductance at large magnetic fields are noticeable, presumably signatures of conductance fluctuations, which are strongly suppressed due to averaging from the parallel NW arrangement as well as the relatively short coherence length. These initial results show that the electron confinement at the top of NWs

grown on NMs is sufficient to produce quasi-1D conduction. These NWs could therefore be viable hosts for Majorana bound states provided that two potential obstacles are addressed. First, a NW made of a higher spin-orbit material such as pure or nearly pure InAs or InSb will be required; i.e.,intermixing should be reduced or eliminated. This will be apparent by the observation of weak anti-localization instead of weak localization. Second, impurity, interface, and alloy scattering need to be reduced such that l_e transitions from the diffusive to the ballistic transport regime.

3.1.5 Conclusion and Outlook

The fast-growing field of quantum computing and the promise of robust, topologically protected qubits with III-V NWs drives the pursuit of scalable approaches to branched NW networks. We have described a path forward using GaAs NMs as templates for the In(Ga)As NW growth. By exploiting strain in the highly mismatched InAs/GaAs system, continuous, low-defect NWs were formed. We have further observed weak localization, demonstrating that such NWs can provide sufficient confinement to achieve quasi-1D conduction. Our gold-free wafer-scale approach to branched NWs serves as a platform for future investigations into 1D transport and quantum computation with III-V NW networks with many exciting possibilities. From the MBE growth perspective, using GaSb NMs already described by other groups to grow InSb NWs would be interesting due to the higher g-factor of InSb [106, 291]. Alternatively, suitable plastic strain relaxation, for example, by interfacial misfit array formation [310], may enable GaAs NMs to be viable templates for InSb NW growth. At the same time, the growth of new kinds of structures with additional functionalities is another avenue to explore, including, for example, research into parafermion devices by stacking multiple NWs on top of each other [75]. The wealth of intriguing new possibilities and approaches offered by template-assisted III-V NW growth makes this method an important step toward realizing a scalable quantum computing scheme based on NW topological qubits.

Methods

Substrate Preparation. Undoped GaAs (111)B substrates were prepared by first depositing 25 nm of SiO_2 by plasma-enhanced chemical vapour deposition (PEVCD). This was followed by e-beam lithography using ZEP resist and low-temperature development to achieve low line edge roughness [311]. Subsequent dry etching with fluorine chemistry was used to etch the SiO_2 down to the GaAs surface, and a final wet etch in a dilute buffered HF solution helped remove any remaining oxide. This yielded openings varying from 30-100 nm in width and 10-20 μm in length, depending on the e-beam pattern.

Growth. The nanostructures were grown in a DCA P600 solid-source MBE. The optimal growth of the GaAs/ InAs NM/NW heterostructures was found to be at a temperature of 630 °C/540 °C (as measured by the pyrometer), As flux of 4×10^{-6} Torr/8×10^{-6} Torr and Ga/In deposition rates of 1 Å/s/0.2 Å/s, respectively. The NMs were typically grown for 30 min (180 nm nominal

2D thickness), while the InAs NWs were grown for 200 s (4 nm nominal 2D thickness).

(S)TEM. The NMs cross-sections were prepared by FIB milling normal to the substrate surface and investigated by atomic-resolution aberration-corrected HAADF STEM in a probe corrected FEI Titan 60-300 keV microscope operated at 300 keV. The elemental maps were obtained by using EELS coupled to a Tecnai F20 microscope.

Contacting. Contacts were patterned by e-beam lithography followed by dual-angle evaporation of 14 nm/80 nm of Cr/Au for good side-wall coverage. Before metallization, an O_2 plasma clean and a 6 min ammonium polysulphide etch at 40 °C were used to ensure a clean, oxide-free contact [312].

Quantum Transport Model. The conductance of the NW is described as:

$$\Delta G = -\frac{2e^2}{hL}\left(\frac{1}{l_\phi^2} + \frac{1}{l_B^2}\right)^{-1/2}$$

where L is the spacing between the contacts and l_B is the magnetic dephasing length given by $l_B = D\tau B$, with D as the diffusion constant ($D_{1D} = vFl_e$ for 1D diffusion). In this limit, the magnetic dephasing time τ_B is given by $\tau_B = 3l_m4/W2D$, where $l_m = \hbar/eB$ is the magnetic length [309, 313, 314].

GaAs Capping. After the growth of the NW/NM heterostructures, a ~30 nm GaAs cap was deposited in situ by MBEs at 400 °C. In the middle of this GaAs cap, the In shutter was opened for 10 s, making a few-monolayer insertion of $In_{0.16}Ga_{0.84}As$, indicating the midpoint of the GaAs cap. The NW/NM heterostructures were then coated with a ~110 nm GaAs layer [315] using ion-beam sputtering at 9 kV and 7.5 mA for 1 h. The capping layer protected the sample from damage caused by the ion beam during FIB.

APT. A standard lift-out method [315, 316] was performed in a FEI Helios dual-beam FIB microscope with a micromanipulator, and the as-prepared wedge-shaped samples were welded onto Si microposts. Finally, the needle-shaped APT specimens were obtained by ion-beam annular milling. APT was performed with a local-electrode atom-probe (LEAP) 4000X Si tomograph (Cameca, Madison, WI) at a sample temperature of 40 °C and a background pressure of 3×10^{-11} Torr. An ultraviolet focused laser with a wavelength of 355 nm was used to evaporate the sample atoms into ions, at a pulse rate of 250 kHz and detection rate of 0.7%. The pulse energy was gradually changed from 1.2 pJ to 0.8 pJ during the evaporation process. The data was reconstructed using IVAS 3.8.1 to provide a 3D composition profile. SEM images of the nanotips taken in the FIB were used to guide the choices of the reconstruction parameters.

Supporting Information

InAs growth studies, Raman spectroscopy, strain analysis, growth model, change in free energy of formation with aspect ratio, NW composition, InAs crystal quality, defect density, magnetotransport model, conductivity map, and APT mass spectra. Available in Appendix C.3.

Acknowledgements

3.2 Dopant Segregation and Weak Anti-localization in Remote-Doped Nanowire Y-Branches

M. Friedl*, K. Cerveny*, C. Huang, D. Dede, M. Samani, M. O. Hill, W. Kim, L. Güniat, T. Patlatiuk, J. Segura-Ruiz, L. J. Lauhon, D. M. Zumbühl and A. Fontcuberta i Morral. Dopant Segregation and Weak Anti-localization in Remote-Doped Nanowire Y-Branches. (in preparation) *equal contribution

The content of this paper has been reformatted to match that of this thesis with references combined with those at the end of this thesis. Although this paper has not been submitted for publication due to some final measurements which are pending, it has been brought as close as possible to the final version using the currently-available data.

My contribution to this work consisted of growing all samples and imaging them in SEM. This included the electrically-measured samples and those measured by APT. I also performed all of the FIB lamella preparation and TEM imaging on the samples presented in this work. Finally, I contributed to writing a large fraction of the manuscript and the making of the figures.

3.2.1 Abstract

Modulation-doping of semiconductors is a common technique used in semiconductor devices to obtain extremely high carrier mobilities. Recently, nanowires grown by selective-area epitaxy have been gaining much attention due to their high crystal quality, scalability and applicability for making branched nanowire networks. They have immense potential for exciting applications in the fields of topological quantum computing and infrared photodetection. In these wires, the convenient placement of a high-bandgap template below the nanowire lends itself extremely for being used in a remote-doped geometry. In this report, we demonstrate the modulation doping of InGaAs nanowires grown on GaAs templates. After imaging the Si dopants added to the GaAs templates grown on GaAs (111)B, we observe an interesting dopant segregation effect. Finally, performing low-temperature magnetotransport measurements we observe weak localization and a mean free path of >200 nm across a nanowire Y-junction. This work serves as a blueprint for applying this technique in similar systems for achieving long-range coherent transport.

3.2.2 Introduction

Over the years, modulation-doping has proven to be a staple technique in many applications employing high-performance semiconductor heterostructures. This technique allows for the creation of two-dimensional electron gases (2DEGs) with high carrier concentration combined with extremely high mobilities. From Nobel Prizes [317–319] to research into in topological qubits [102–105] and high-power applications using high electron mobility transistors (HEMTs) [320, 321], a wide range of fields have benefited and are continuing to benefit from remotely-

doped 2DEGs heterostructures. With current knowledge and modern epitaxy techniques, state-of-the-art 2DEGs devices can achieve mobilities regularly exceeding 1×10^7 cm^2/Vs [270, 322].

The field of semiconductor nanowires (NWs) has also been gaining attention in recent years due to exciting new prospects and applications of semiconductor NWs. These applications include photovoltaics [323–327], photodetectors [328–331], lasers [332–336], single-photon emitters [337, 338], and research into topological quantum computing [95, 98–101].

It has generally been reported that the large surface-to-volume ratio and increased surface scattering in NWs result in their mobilities being significantly lower than those measured in bulk. This is exacerbated in InAs NW by the surface Fermi level pinning resulting in most of the conduction occurring at the surface [254]. Room-temperature electrically-measured mobilities for undoped, vertically-grown InAs NWs thus fall in the range of ~20-3000 cm^2/Vs [6, 89, 339–341]. Non-contact measurement techniques yield slightly higher mobilities due to the smaller length scale of the interactions and possible selection-bias (higher mobility regions contributing more to the signal). Values for these types of measurements fall in the range of ~4000-6000 cm^2/Vs [89, 342, 343]. In both cases, mobilities are significantly lower than the bulk value of around 30 000 cm^2/Vs [344]. Similarly to bulk, direct doping of NWs significantly reduces carrier mobilities due to ionized dopant scattering. Also in vertically-grown GaAs NWs remote-doping has been reported as a viable approach to adding carriers without negatively affecting carrier mobility [345, 346]. In some cases, it has even been reported that modulation-doped NW mobilities can significantly exceed those of undoped NWs [347, 348].

Recently, similar selective-area epitaxy (SAE) approaches for growing lateral III-V NWs have been gaining popularity due to the high NW crystal quality and scalability of this growth approach which is unmatched by any other bottom-up NW growth method. Furthermore, the ability of SAE NW to be grown into NWs networks [108] and the relative ease with which they can be further processed directly on the growth substrate makes them extremely attractive for use in experiments exploring topological quantum phenomena [110–113]. The growth of SAE NWs on top of a higher-bandgap buffer material makes these types of wires great candidates for remote-doping by placing dopants under the NWs in the buffer layer. Modulation-doped NWs growing using an SAE approach were first reported by Fukui and colleagues in micrometre-scale AlGaAs/GaAs heterostructures in the late 80s [166, 168]. However, in the most recent reports on In(Ga)As SAE NWs grown on the ten-of-nanometres-scale, remote-doping has not been reported.

In this work, we demonstrate the growth of quasi-1D InGaAs NW heterostructures hosting coherent transport by combining remote-doping with SAE. We report on the incorporation behaviour of In into the InGaAs NWs as a function of growth conditions which allowed us to then grow optimized remote-doped NWs. These were then analysed by atom probe tomography (APT) where we observed an interesting dopant segregation effect. Our analysis is rounded out by low-temperature electrical transport measurements across InGaAs NW Y-branches demon-

strating the high NW crystal quality across the junction. This research lays the groundwork for the fabrication of enhanced-mobility In(Ga)As SAE NWs by means of remote-doping. Such devices are an asset to the topological quantum computing community where long coherence lengths and carrier densities are prerequisites for good device performance.

3.2.3 Growth

Remote-doped InGaAs NWs were grown on top of GaAs buffers using an SAE approach, as depicted in Figure 3.4 (a). A GaAs substrate was covered by a SiO_2 mask to achieve high growth selectivity. The SiO_2 mask was then patterned with stripes along the three equivalent $\langle 11\bar{2}\rangle$ directions on the substrate using e-beam lithography and reactive ion etching. The resist was stripped with an O_2 plasma and the substrate was etched in a dilute buffered HF solution before being loaded into the molecular beam epitaxy (MBE) cluster for growth.

Figure 3.4 (b) shows the desired structure that was targeted during MBE growth. Silicon dopants are introduced inside the GaAs buffer underneath the NWs such that the carriers fall into the lower-bandgap NW. As a result, the NWs benefit from an increased carrier concentration due to the extrinsic dopants while ionized impurity scattering is limited due to the spatial separation of carriers and ionized dopants.

The samples were degassed for 2 h at a temperature of 400 °C before being loaded into the growth chamber. Prior to growth, a final high-temperature degassing step was performed at 630 °C in order to remove the native oxide on the GaAs substrate. The GaAs buffers were then grown at a temperature of 630 °C at an equivalent 2D GaAs growth rate of 1 Å/s with an arsenic beam equivalent pressure (BEP) of 4×10^{-6} Torr. GaAs buffers were grown to an equivalent 2D thickness of 100 nm, resulting in structures with a height of ~300 nm. Towards the end of the buffer growth, Si dopants were introduced for a short duration via a Si sublimation cell at a rate of ~10×10^{13} cm^{-2} s^{-1} to achieve the desired doping profile. After GaAs growth, the substrate temperature was decreased to 540 °C, while the As BEP was increased to 8×10^{-6} Torr for InAs deposition. The In was sent on the substrate at an InAs equivalent growth rate of 0.1 Å/s, and was closed after the 2D equivalent of 60 nm of InAs was deposited on the substrate.

Figure 3.4 (c) shows a representative scanning electron image of the remotely-doped NW structures after growth. We see that a high degree of uniformity in both the buffers and the NWs is achievable. Similarly, as shown in Figure 3.4 (d), Y-branched structures can be made as a result of merging three equivalent $\langle 11\bar{2}\rangle$ directions on the substrate, as has been reported previously [108]. These branched structures can similarly be made to exhibit a high degree of NW uniformity throughout the structure, including at the intersection, as was further confirmed by x-ray fluorescence (XRF) measurements performed at European Synchrotron Radiation Facility (ESRF) included in Appendix C.2.

A growth series was performed for exploring the effects of the growth conditions on the In concentration in the NWs. Four samples were grown while varying the In deposition rate and

As BEP. Focused ion beam lamellas were then prepared and analysed by scanning transmission electron microscopy (STEM) energy-dispersive x-ray spectroscopy (EDS) to obtain elemental maps of the NW cross-sections. The resulting In concentration maps are shown in Figure 3.4 (e-h). Here, the atomic concentration of In is calculated as $C_{In}/(C_{In} + C_{Ga} + C_{As})$ with the maximum possible concentration being 50% for pure InAs.

Even though the total thickness of InAs deposited on each sample was kept the same, we see that a higher In flux yields an increased In concentration in the NW. The InAs growth temperatures are relatively low for solid-phase diffusion which is typically only observed above 750 °C [349–351]. The Ga intermixing is instead believed to be mediated by surface adatom diffusion during growth. This thermodynamically-driven effect can thus be suppressed by higher deposition rates which bring the system away from the thermodynamic regime and push it towards the kinetic regime [128].

The effect of the V/III ratio is less well-understood. In Figure 3.4 (e), at high V/III ratios and low growth rates, InGaAs grows to form a flat (1 1 1)B top facet, after which NW growth stops. This suggests that desorption of In species from this flat top facet under these conditions may be high. However, if the In rate is increased, as in Figure 3.4 (h), then NW growth is re-established which can be explained by the fact that the increased incoming flux becomes greater than the desorbing flux, thus continuing NW growth. Similarly, if the V/III ratio is decreased, as in Figure 3.4 (f), a similar effect is achieved the reason for which is still under discussion, investigation.

Shown in Figure 3.4 (g), the highest In concentration in this growth series was about 25%, corresponding to $In_{0.5}Ga_{0.5}As$. This was achieved using a higher In flux and lower V/III ratio which indicated that higher In rates and lower V/III ratios should be pursued to reduce Ga intermixing in the NW. This result is at least partially-supported by recent reports on (1 0 0) GaAs substrates where very low V/III ratios are used to grow pure InAs NWs on top of GaAs(Sb) buffers [110].
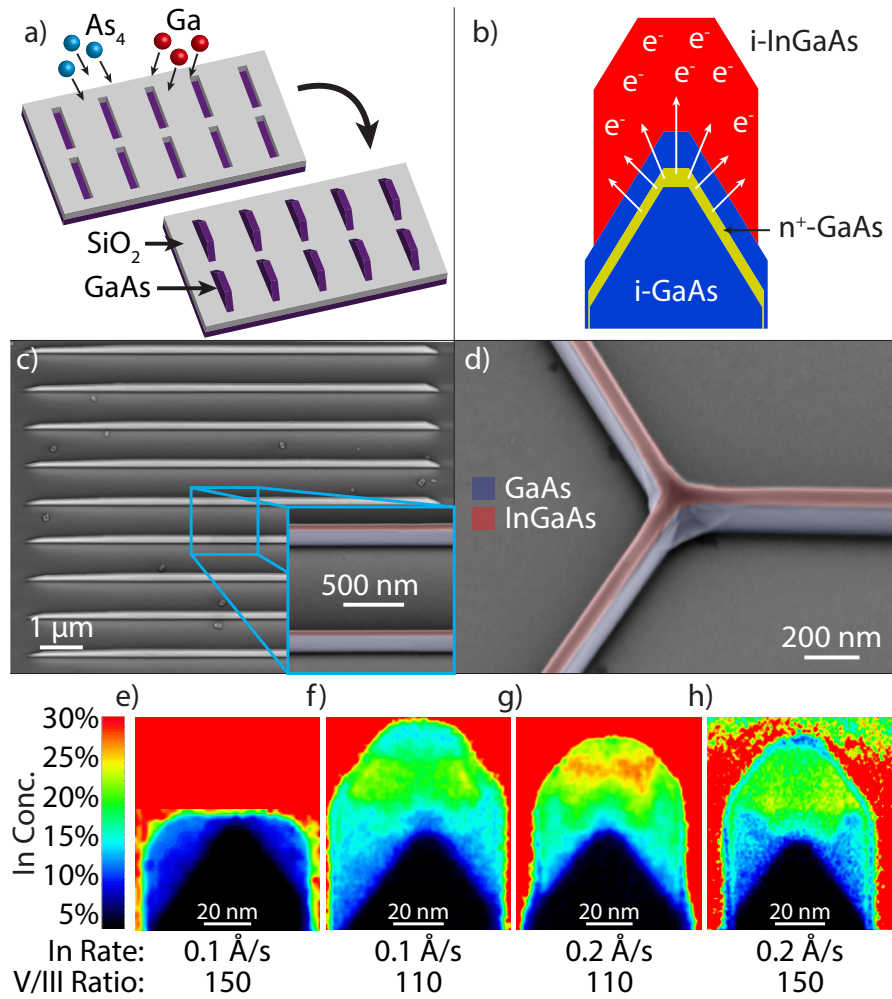
Figure 3.4 – a) Illustration of the SAE growth process. b) Diagram showing the desired doping profile for remote-doped InGaAs NWs on GaAs nanomembranes (NMs). c) Tilted scanning electron microscopy (SEM) image of an array of NWs after MBE growth. d) Close-up tilted SEM image of a Y-junction showing uniform coalescence of InGaAs NWs. e-h) Elemental maps of In concentration taken with STEM EDS on NW cross-sections showing the dependence of growth conditions on NW composition.

3.2.4 Atom Probe Tomography

As the silicon dopant concentration was well below the detection limits of STEM EDS, APT was used as a technique to image the distribution of the dopants in the GaAs templates. For the best accuracy, a hybrid strategy for imaging the structure was devised by combining STEM EDS and APT with STEM used as a reference for the APT reconstruction which in turn offered the high sensitivity required for imaging dopant concentrations and as well as a 3D representation of the sample not accessible by STEM.

An In-free growth structure, shown in Figure 3.5 (a) was devised to gain a good understanding

of dopant incorporation. The growth consisted of two main parts. First, a high-temperature growth was performed at the usual GaAs buffer growth temperature of 630 °C. Close to the top of the structure, a small amount (~10%) of Al was added as a marker (shown in red). This was followed by the introduction of the Si dopants about 5 nm after. Finally, a second Al marker was added just after the Si dopants. Thus, the Si dopants were introduced at the mid-point between the two Al markers.

After the second aluminium marker, a capping layer was grown over the whole structure. The capping layer conditions were achieved by reducing the substrate temperature to 450 °C and increasing the V/III ratio to 200. This reduced the Ga diffusion length on the surface and led to a more conformal shell growth, yielding the proper aspect ratio for APT analysis. After 1/3 of the shell had been grown, the Al shutter was opened again and after having reached 2/3 of the shell growth time the Al shutter was closed. This left a thick shell with a third marker in it that could be used to tune the APT evaporation settings during the initial stage of analysis. Prior to APT, to confirm that the structure and layers were within the requirements, a focused ion beam (FIB) cross-section was performed, followed by STEM EDS, as shown in Figure 3.5 (b).

In Figure 3.5 (c) and (d) we see the APT reconstruction of the structure shown as projected 2D density maps of Al^+ and $Si^+ + Si^{++}$, respectively. The Al signal follows closely the one seen in Figure 3.5 (b) where the two high-temperature markers are clearly visible and the Al concentration is comparable to that measured by STEM EDS. On the other hand, looking at the Si signal, relatively little Si is observed where it was introduced into the structure, in between the two Al markers. Instead, there is a strong Si peak close to the top of the structure.

Looking at the line scan shown in Figure 3.5 (e), the effect is even more clear. Here we see a line scan from the top to the bottom of the structure, following the arrow in Figure 3.5 (c). We see two very sharp Al peaks around 30 nm and 75 nm corresponding to the Al markers. Though we expected the Si concentration to peak between the two Al peaks, instead we observe a large Si concentration above the upper Al marker around 25 nm. The Si concentration at this point is also much higher than was expected. The nominal expected concentration, based on the Si dopant flux and GaAs growth rate, is about 1.6×10^{19} cm^{-3}, as indicated by the horizontal dashed line.

These results suggest possible facet-dependent incorporation of the Si atoms during the growth of the GaAs buffer crystal. There appears to be a substantial amount of Si atoms that accumulate on the surface during growth, with only a relatively small amount getting incorporated into the structure during the high-temperature growth. After this, the temperature is dropped by several hundred degrees and all the dopants get incorporated at a single point on the small (111)B facet on to of the NM. Not only are these results from a fundamental growth perspective, but they may also be used as a method to achieve very highly delta-doped structures in the future.

As this structure has no InGaAs NW in it, in the NW structure, it is impossible to tell whether or not the Si dopants incorporate below the InGaAs NW as they did with the APT shell or if

they could also get displaced during InGaAs NW growth. The growth temperature also gives no indication because InGaAs NW growth is performed at 540 °C, exactly in between the two regimes used in the APT study. To understand exactly where the Si atoms are going, a follow-up APT analysis must be performed which is currently underway. Nevertheless, promising electrical measurements have been performed which are suggestive of a low-disorder NW.
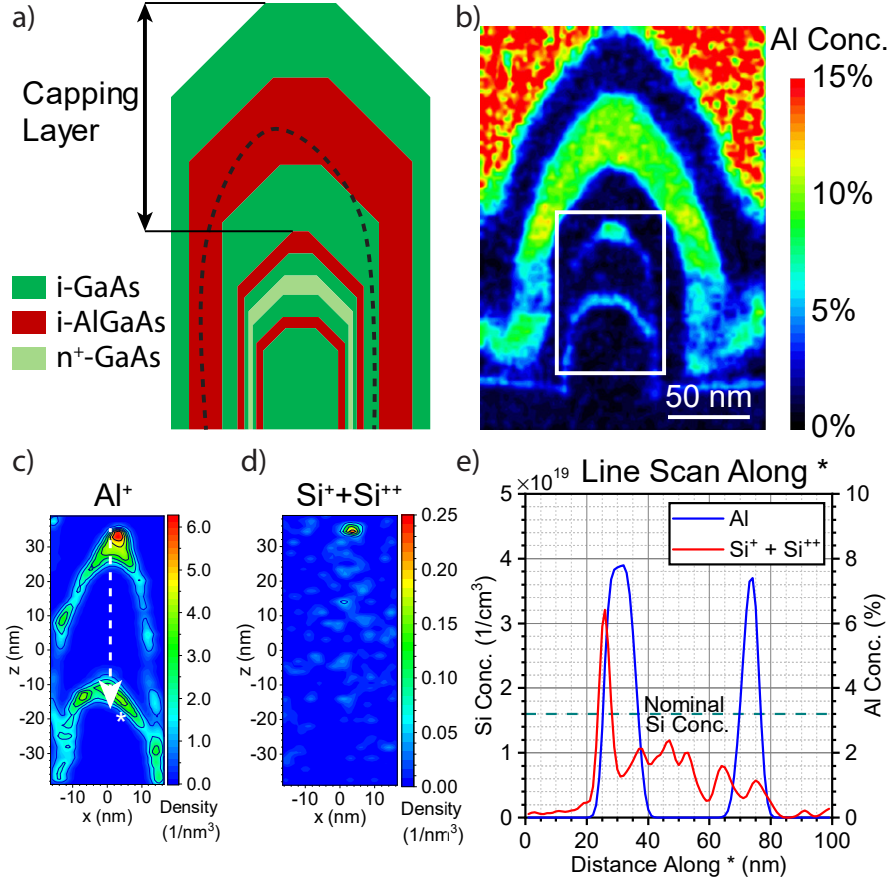
Figure 3.5 – a) Diagram of the structure analysed by APT with the imaged area denoted by the dashed line. b) Cross-sectional STEM EDS elemental map of the Al concentration in the structure showing the location of the reference markers for determining where the Si dopants were deposited. c-d) Elemental maps obtained by APT showing the Al concentration (c) and the Si concentration (d) in the structure. e) Line scan along the arrow in (c) showing the atomic concentration of Al and Si as a function of depth into the sample.

3.2.5 Magnetotransport

As-grown samples were electrically contacted near the Y-junctions (see Experimental section), passivated by a 40 nm-thick HfO$_2$ gate oxide, and a top gate was evaporated on top. An SEM image of an electrical device is shown in Figure 3.6 (a). A false-coloured cross-sectional FIB STEM image is shown in Figure 3.6 (b) showing the different layers of the device. Note

that dual-angle evaporation of all metal contacts was performed to ensure continuity of the contacts over the high aspect-ratio structures.
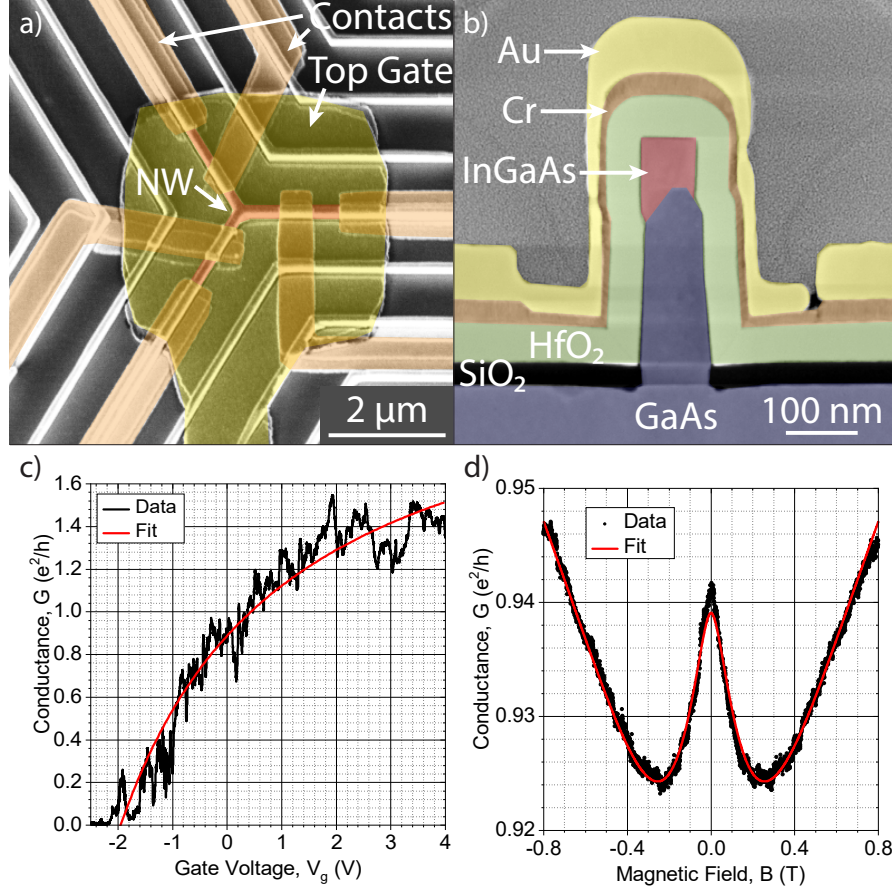
Figure 3.6 – a) SEM image of a fabricated electrical device showing three pairs of four-point contacts and a global top gate b) False-coloured cross-sectional STEM high-angle annular dark-field (HAADF) image showing the layers in a fabricated electrical device. c) Graph showing the NW conductance as a function of top gate voltage from which field-effect mobility was extracted d) Graph of the magnetoconductance response of the NW exhibiting a clear weak anti-localization (WAL) peak

The samples were then cooled down and electrically characterized at 10 K, 4 K and 1.7 K. The conductance as a function of top gate voltage was investigated, as shown in Figure 3.6 (c) and a field-effect mobility of around 500 cm^2/Vs was extracted. Field-effect mobility was modelled in the manner of Gül *et al.* [295], shown in Equation (3.1).

$$G(V_g) = \left(R_s + \frac{L^2}{\mu C(V_g - V_{th})}\right)^{-1} \qquad (3.1)$$

with $L = 600$ nm (length of channel), R_s a series contact resistance, V_g the applied gate voltage,

V_{th} the threshold voltage for pinch-off, $\epsilon_0 = 8.854 \times 10^{-12}$ F/m, $\epsilon_{\text{HfO}_2} = 6.5$ [110], and C the gate capacitance. The gate capacitance was estimated numerically using a finite element simulation in COMSOL, though similar values were calculated analytically using a coaxial cable or parallel plate capacitor models.

The magnetoconductance of the devices was then probed, and displayed weak anti-localization behaviour, as shown in Figure 3.6 (d). Weak anti-localization is an effect exhibited in diffusive systems with spin-orbit interaction, which manifests as a negative quantum correction to the magnetoconductance away from $B = 0$. This is a result of the intrinsic breaking of time-reversal symmetry of the carriers due to the effective magnetic field the electrons experience due to spin-orbit interaction. Quantitatively [94, 309, 313, 314]:

$$\Delta G = \frac{e^2}{h} \frac{1}{L} \left[3 \left(\frac{1}{l_\phi^2} + \frac{4}{3 l_{so}^2} + \frac{1}{l_B^2} \right)^{-1/2} - \left(\frac{1}{l_\phi^2} + \frac{1}{l_B^2} \right)^{-1/2} \right.$$
$$\left. - 3 \left(\frac{1}{l_\phi^2} + \frac{1}{l_e^2} + \frac{4}{3 l_{so}^2} + \frac{1}{l_B^2} \right)^{-1/2} + \left(\frac{1}{l_\phi^2} + \frac{1}{l_e^2} + \frac{1}{l_B^2} \right)^{-1/2} \right] \tag{3.2}$$

Here L is the spacing between the contacts, e is the electron charge, h is the Planck constant, l_ϕ is the phase coherence length, l_{so} is the spin-orbit length, l_e is the mean free path, and l_B is the magnetic dephasing length, given by $l_B = \sqrt{D \tau_B}$, with $D = v_F l_e$ as the 1D diffusion constant. The magnetic dephasing length squared l_B^2 in the pure limit is given by:

$$l_B^2 = \frac{C_1 l_e l_m^4}{W^3} + \frac{C_2 l_e^2 l_m^2}{W^2} \tag{3.3}$$

where $l_m = \hbar/eB$ is the magnetic length, W is the channel width, and $C_{1,2}$ are constants dependent on the type of boundary scattering in the system. This formalism allows for the extraction of the coherence length ($l_\phi \sim 388$ nm), spin-orbit length ($l_{so} \sim 405$ nm), and mean free path ($l_e \sim 250$ nm) at 1.7 K. Here we note good agreement in the extracted values for l_e from the field-effect mobility and magnetoconductance measurements independently. The coherence length is a measure for how far an electron will travel on average before having its phase randomised due to inelastic scattering events. The spin-orbit length is the length that an electron travels before undergoing a rotation of 1 rad in spin, and is a measure for the strength of the spin-orbit interaction in the material. The mean free path is the average length that a carrier travels without any scattering event.

The device's magnetoconductance was probed at different gate voltages to determine the evolution of the length parameters in the presence of an electric field. The expected spin-orbit interaction in such a system is of Rashba type, which manifests as a result of an electric field gradient. Such a gradient is often an intrinsic property of the system at an interface. It can

additionally be tuned through the extrinsic application of electric fields via electrostatic gates [352]. Recently, the Dresselhaus spin-orbit interaction of such a system has been investigated theoretically [353], which suggests that the spin-orbit interaction we encounter may not be solely due to a Rashba-type interaction. Though a thorough investigation of this requires a gate configuration allowing for independent tuning of the density without moving the position of the wave function, currently unavailable in our system due to lack of a back-gate. Nevertheless, the data show the system evolving from a pure weak anti-localization with large positive gate voltage, through an intermediate regime with no applied gate voltage, and to a purely weak localization regime before pinch-off.

3.2.6 Conclusion

In this work, we have shown that the remote-doping of InGaAs nanostructures is a promising approach to improving their quantum transport properties. We first explored how to augment the In concentration in template-assisted InGaAs NWs grown by SAE by tuning the MBE growth conditions. We found that increasing In deposition rate to go deeper into the kinetic growth regime and a low V/III ratio favours higher In concentrations in the NWs, as confirmed by STEM EDS measurements. We then analysed the dopant distribution in test structures by APT. Here we found the interesting effect of dopant segregation at the top of the structure with a very small amount of silicon dopant incorporation into the structure during growth. This dopant segregation effect will thus need to be studied in further detail to elucidate at which temperatures it can be circumvented. Furthermore, it may even be possible to use this dopant segregation effect as a method to make even sharper delta-doped layers. Despite the dopant segregation, we observe weak anti-localisation behaviour and are able to extract a mean free path of about 250 nm. This corresponds to a two-orders-of-magnitude improvement over our previous traditionally-doped InGaAs NWs and is now comparable with values observed by other groups working with similar systems. It is important to note that all electrical measurements were performed across a Y-branch junction which serves as proof of the quality of the crystal across this junction.

3.2.7 Experimental

Growth. MBE growth was performed in a DCA P600 solid-source MBE chamber. 25 nm of SiO_2 was deposited on GaAs (111)B substrates by plasma-enhanced chemical vapour deposition (PEVCD). These were patterned by e-beam lithography using 35 nm of ZEP resist and etching in an SPTS APS dielectric etching tool employing SF_6 and CHF_3 chemistry. After resist stripping in an O_2 plasma, the samples were etched for 10 s in a highly dilute buffered HF solution to remove ~5 nm of SiO_2 everywhere and smooth the mask. Samples were then loaded and annealed at 400 °C for 2 h in a degassing chamber followed by 630 °C for 30 min in the growth chamber immediately prior to growth.

STEM. Cross-sections of the samples were prepared first in an FEI Nova 600 Nanolab dual-

beam SEM/FIB tool before being loaded into an FEI Tecnai Osiris microscope operating at 200 keV in STEM mode. Elemental contrast was obtained by EDS thanks to four cryo-cooled Super-X silicon drift detector (SDD) x-ray detectors.

Contacts. The devices were cleaned and the contacts were patterned with standard electron beam lithography, followed by an O_2 plasma cleaning. Before metallization, the samples were then exposed to an ammonium polysulfide (NH_4S_x) solution for 150 s in order to remove the native oxide [312]. Cr/Au contacts were deposited via dual-angle evaporation (7+7 nm/25+25 nm) in order to achieve suitable side-wall coverage. Next, 40 nm of HfO_2 was applied via atomic layer deposition. Then another round of e beam lithography to pattern the top gates and another metallization step was carried out before the sample was bonded into a chip carrier and measured.

4 Template-Assisted NW Growth on GaAs (100)

In addition to NW growth on (111) substrates, this section will present some preliminary, unpublished work that has been performed on the growth of InAs NWs on GaAs (100) substrates. Following the promising reports by various groups of selective-area growth (SAG) NWs on (100) substrates [106, 107, 109–113], some of my recent experiments also included the growth on (100) substrates.

4.1   Growth and Structural Analysis

Figure 4.1 shows an example of InAs NWs grown on a GaAs (100) with the growth conditions shown in Table 4.1. Apart from the use of a different substrate, the fabrication process is identical to that described previously in Section 3.1. It was found that NWs seemed to favour growth along either $\langle 110 \rangle$ directions or $\langle 100 \rangle$ directions.

(a) NWs along $\langle 011 \rangle$.

(b) NWs along $\langle 010 \rangle$.
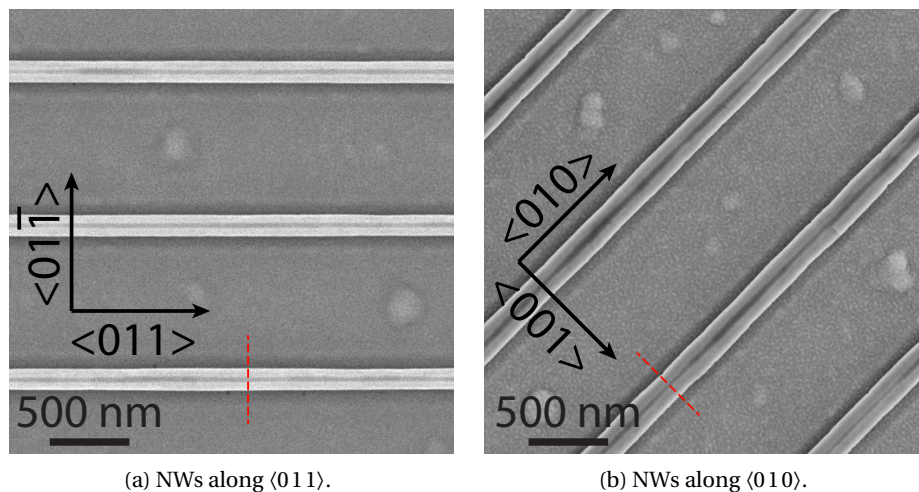
Figure 4.1 – SEM images of InAs NWs grown on (100) GaAs substrates along two different directions.

Material	T_{subs}	Rate	V/III Ratio	Thickness
Ga	630 °C	0.3 Å/s	80	100 nm
In	540 °C	0.3 Å/s	10	63 nm

Table 4.1 – Growth conditions used for initial InAs NW growth on (100) GaAs substrates.

Cross-sectional FIB lamellas were prepared from these wires, cut along the red lines in the SEM images in Figure 4.1. Then, STEM EDS analysis was performed on them to check for elemental purity and degree of intermixing. The resulting EDS maps are shown in Figure 4.2. Analysis of NWs grown in both thinner and thicker oxide openings was performed for each of the two directions.
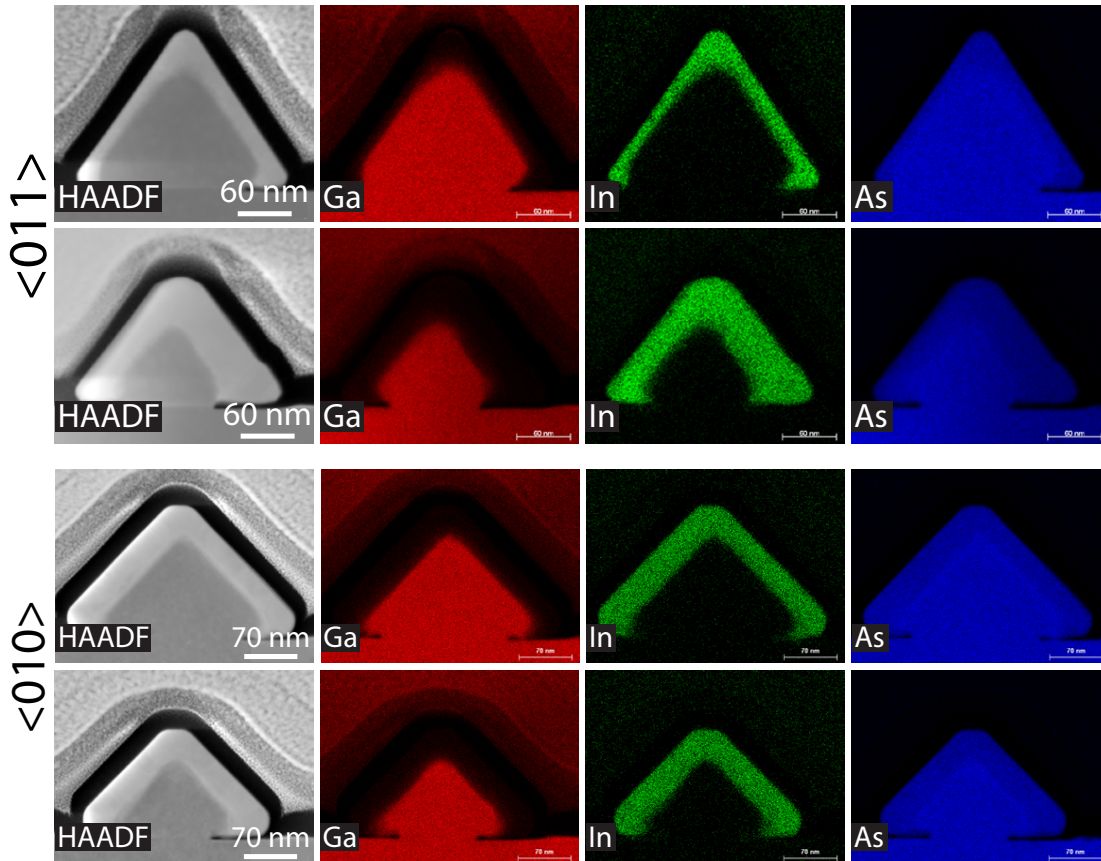
Figure 4.2 – EDS elemental maps of four NWs grown on (100) GaAs.

From the EDS analysis, it is apparent that the degree of intermixing between the InAs and the GaAs is significantly reduced on (100) substrates compared to what is seen on (111)B substrates which form InGaAs NWs. The reason for this is attributed to the presence of more thermodynamically-stable facets in the (100) NWs. These are faceted with {110} facets for wires in the ⟨100⟩ direction and {111} facets for wires grown in the ⟨110⟩ direction.

In this initial growth, it was apparent that too much GaAs was deposited as the buffers had a triangular cross-section and the InAs was beginning to overgrow on top of the SiO_2 mask. In a follow-up growth, the overall deposited thickness of GaAs was reduced from 100 nm down to 50 nm and similarly, the deposition rate was decreased from 0.3 Å/s down to 0.15 Å/s to try and create a smoother (1 0 0) top facet. The resulting STEM EDS maps are shown as a function of slit width in Figure 4.3.
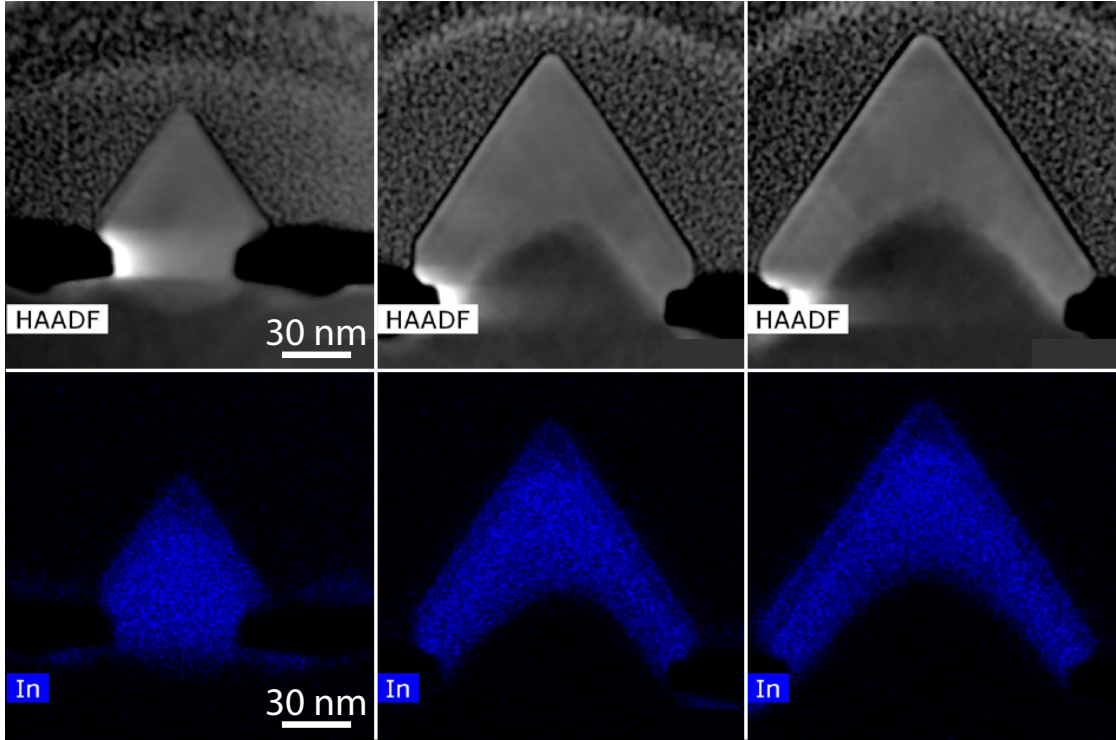
Figure 4.3 – Influence of slit size on InAs NW morphology. Notice that for small slits, the InAs completely fills the slits with seemingly no GaAs buffer growth.

Here it is seen that the smaller volume of deposited GaAs led to a more favourable geometry for InAs NW formation. Interestingly, for the smallest slits it appears that the desorption rate of Ga is higher than the incident flux, resulting in very little GaAs buffer growth. In this case, the InAs fully fills the slit. The exact reason for the lower growth rate of the GaAs buffer in smaller slits is not yet well understood and is currently being investigated.

4.2 Electrical Measurements

Low-temperature field-effect transistor (FET) measurements were performed at EPFL on (1 0 0) NWs, similar to those analysed in Figure 4.2. Electrical contacts were fabricated on arrays of ten NWs in parallel using a combination of e-beam lithography and sputtering of Cr/Au. In-situ Ar milling was used to remove the native oxide, as in Refs [89, 354], and an etching

series here determined that the optimal Ar milling time was 5 s. This was followed by an atomic layer deposition (ALD) process to deposit 20 nm of Al_2O_3. At the start of the ALD process, 50 pulses of TEMAH at the process temperature of 200 °C were used to remove the native oxide and passivate the NW surface [355, 356]. A second e-beam step followed by sputtering of a Cr/Au top gate was then performed. Samples were then wire-bonded and loaded into a liquid-helium cryostat for testing. A device is shown in Figure 4.4a along with a typical FET measurement shown in Figure 4.4b.
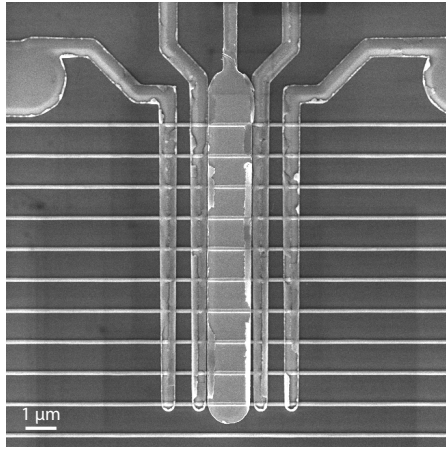
(a) Top-gated NW device.
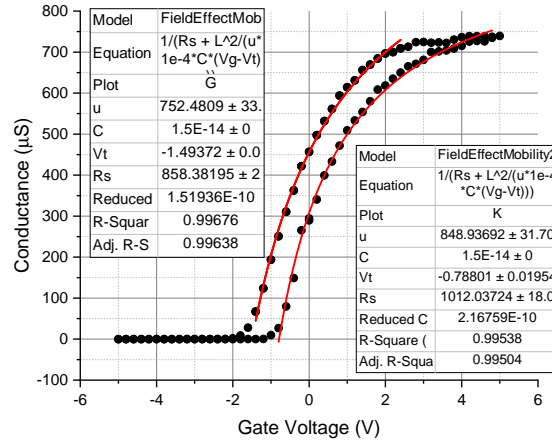
(b) FET measurement.

Figure 4.4 – a) SEM image of a top-gated FET device. b)FET measurement on an array of ten parallel InAs NWs performed at 4 K.

The traces in Figure 4.4b were fit using the model from Gül *et al.* [295]. Capacitance was estimated using a finite element model in COMSOL and an ideal dielectric constant of $\epsilon_r = 8$ was assumed. Using this, the field-effect mobility of the NW was measured to be around 750-850 cm^2/Vs. This is only slightly lower than what has been reported in vertically-grown InAs NWs grown in our group, before taking into account semiconductor capacitance [89]. Still, this is lower than recent publications on SAG NWs: Lee *et al.* [113] report 1170 cm^2/Vs from Hall measurements while Krizek *et al.* [110] report 5600 cm^2/Vs from top-gated FET measurements. One reason for this difference is likely the InAs/GaAs interface which is rough and probably disordered, leading to a large amount of interface scattering. Since these were some of the first growths, the ribbon-like InAs layer is not optimal and results in enhanced interface scattering compared to a more rounded NW cross-section. The lack of a passivation layer on top of the NWs also leads to significant interface scattering which would justify passivating the NW surface with a higher-bandgap material in the future.

4.3 Branches and Intersections

As on the (1 1 1)B GaAs wafers, branched geometries were also explored on (1 0 0) wafers. Much like on the previous substrate, the NWs were observed to maintain their uniform shape across the intersection suggesting that it does not contain a significant number of defects.

One interesting feature which was observed was the difference in NW growth rates for NWs grown at 90° angles to each other along equivalent ⟨1 1 0⟩ directions. An example of an intersection between two such wires is given in Figure 4.5.
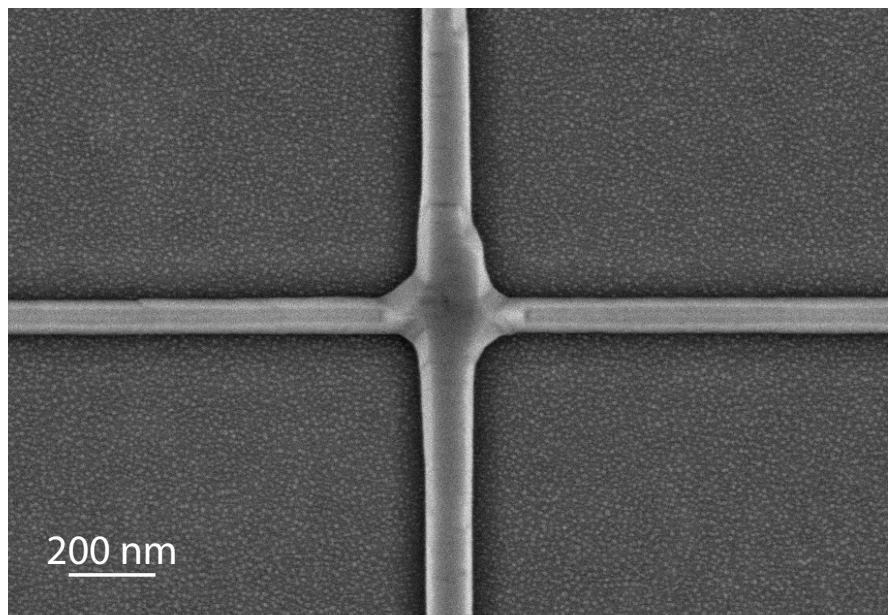
Figure 4.5 – Intersection of two InAs NWs growing along ⟨1 1 0⟩ directions on a GaAs (1 0 0) substrate.

Here, the NWs oriented left to right in the SEM image is terminated by two (1 1 1)A facets and a flat (1 0 0) top facet. On the other hand, the top-to-bottom oriented NW appears to have accumulated much more material and is, therefore, larger with less clear faceting. This is in agreement with what has been reported by Krizek *et al.* [110] and is likely related to the fast growth rate in the ⟨1 1 1⟩B direction which is what allows for such high aspect ratio NMs on (1 1 1)B substrates.

It was noted however that NWs terminated by (1 1 0) and (1 1 1)A facets had similar growth rates. Therefore, to make uniform intersections, we focused on intersecting these orientations of NWs. When avoiding the (1 1 1)B-faceted NWs, very uniform intersections can be obtained, as shown in Figure 4.6.

(a)

(b)
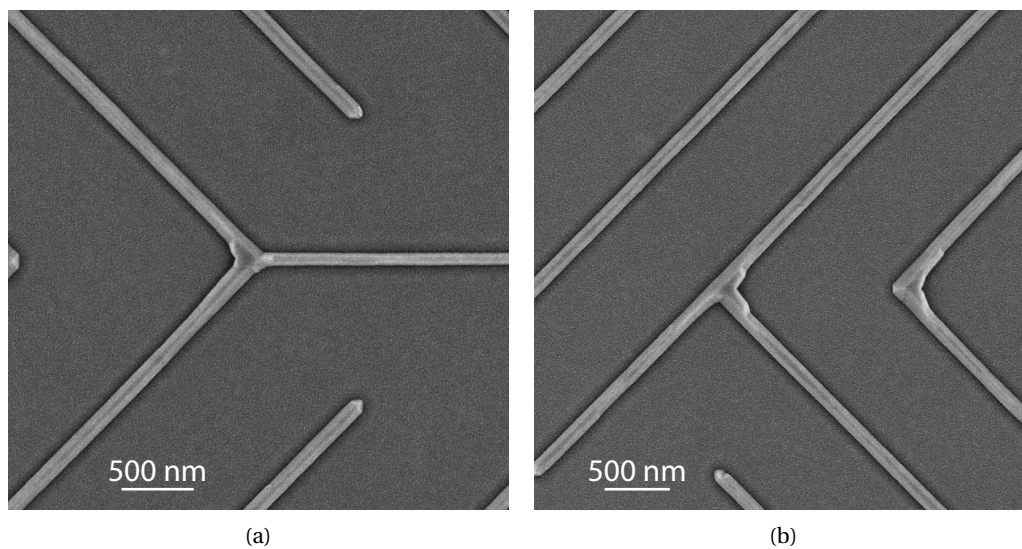
Figure 4.6 – Two SEM images of branched NW geometries showing uniform merging of InAs NWs grown on a GaAs (100) substrate.

5 GaAs Nanomembrane Growth on Si (111)

While the growth of template-assisted NWs on GaAs substrates exhibits the many exciting possibilities offered by this approach, the use of the non-CMOS-compatible GaAs substrate makes prospects of large-scale integration of such structures on conventional CMOS very unlikely. The goal of the research presented in this chapter was, therefore, to gain understanding into the growth mode of GaAs NMs on silicon (1 1 1) to work towards a reliable approach for eventually growing template-assisted NWs on a complementary metal-oxide-semiconductor (CMOS)-compatible substrate.

5.1 GaAs Nanoscale Membranes: Prospects for Seamless Integration of III-Vs on Silicon

A. M. Raya*, <u>M. Friedl</u>*, S. Martí-Sánchez*, V. G. Dubrovskii, L. Francaviglia, B. Alén, N. Morgan, G. Tütüncüoglu, Q. M. Ramasse, D. Fuster, J. M. Llorens, J. Arbiol and A. Fontcuberta i Morral. GaAs Nanoscale Membranes: Prospects for Seamless Integration of III-Vs on Silicon. *Nanoscale* (under review) *equal contribution

My contribution to this work consisted of assisting with sample fabrication, coordinating the growths, growth analysis and discussion of the theoretical growth model. I also contributed to writing a large fraction of the manuscript as well as making the figures.

5.1.1 Abstract

The growth of compound semiconductors on silicon has been widely sought after for decades, but reliable methods for defect-free integration of these materials have remained elusive. Recently, interconnected GaAs nanoscale membranes have been used as templates for the scalable integration of nanowire networks on III-V substrates. Here, we demonstrate how GaAs nanoscale membranes can be seamlessly integrated on silicon by controlling the density of nuclei in the initial stages of growth. We also correlate the absence or presence of defects with the

existence of a single or multiple nucleation regime for the single membranes. Certain defects exhibit well-differentiated spectroscopic features that we identify with cathodoluminescence and micro-photoluminescence techniques. Overall, this work presents a new approach for the seamless integration of compound semiconductors on silicon.

5.2 Introduction

III-V nanostructures have gained increasing attention over the last years due to their prospects in a wide range of applications such as high-speed electronics [357], optoelectronics [358–360], thermoelectrics [361], and photovoltaics [325, 362]. Their small dimensions and tailored shapes can be used to modify the inherent semiconductor properties, thus extending their range of application. Yet, high substrate and processing costs mean that III-V devices are generally only cost-effective in specific, high-performance applications. The synthesis of III-V materials on Si substrates, however, could be a cost-competitive way to integrate cutting-edge optoelectronic and high-speed electronic devices with existing silicon technology [363].

Taking GaAs as an example, two important factors make the growth of GaAs on Si substrates a challenge. First, the 4.2% lattice mismatch between Si and GaAs makes the defect-free growth of GaAs very difficult. Nonetheless, recent work suggests that such large lattice mismatches can be overcome through the appropriate interface engineering to form a periodic misfit array that plastically relaxes the mismatch strain [106, 110, 145]. The second challenge is the formation of anti-phase boundaries (APBs) [363]. When a binary compound semiconductor (such as GaAs) is deposited on top of a monoatomic semiconductor (such as Si), both A-polar and B-polar GaAs islands can nucleate. In the mononuclear regime, where each GaAs monolayer is nucleated at a single point, the whole grown crystal will have the same polarity. However, in the polynuclear regime, where many islands nucleate and coalesce to form the final crystal, the polarity mismatch between islands creates APBs [159, 364]. These APBs manifest as regions of As-As or Ga-Ga bonds. An additional source for such APBs, as will be discussed, is through multiple twinning processes [365]. These APBs are shown to be optically and electrically detrimental [366] and thus their formation must be suppressed.

To overcome these challenges, many approaches have been explored both for III-V thin-film and nanostructure growth on silicon. III-V thin films on silicon have been achieved through strained superlattice growth [367], buffer growth [368, 369], thermal annealing [364, 370, 371], and substrate patterning [372, 373]. Additionally, III-V nanostructure growth on silicon [374, 375] has also been explored with the growth of vertical nanowires (NWs) on silicon [374–376] or in-plane NWs and ridges [176, 373]. Several studies have also explored the use of aspect-ratio trapping to reduce the vertical propagation of defects formed at the substrate interface [364, 377–379].

One particularly interesting approach, which has been used successfully to overcome challenging substrate/nanostructure mismatch conditions in the past, is selective-area epitaxy (SAE) or selective-area growth (SAG). SAE and SAG have proven to be effective techniques for the

synthesis of III-V nanostructures such as NWs [174, 380], tripods [381], and V-shaped nanofins [192, 382]. SAE is carried out on nanopatterned substrates at high temperature in such a way that the sticking coefficient of the adatoms is zero on the mask and non-zero in the etched openings [112]. The growth of GaAs nanomembranes (NMs) on GaAs (1 1 1)B substrates has been achieved by etching long slits along the $\langle 1\,1\,\bar{2} \rangle$ family of directions, as reported for both metalorganic chemical vapour deposition (MOCVD) [300] and molecular beam epitaxy (MBE) [177]. The shape of these NMs is primarily driven by the growth kinetics [130]. They exhibit a defect-free crystal structure which leads to a high homogeneity in the optical properties of NM ensembles [299]. Their high aspect-ratio geometry combined with their pristine crystal quality enables their use as templates for growing highly mismatched materials [108], extending their functionality and design opportunities [383].

In the present study, our particular interest is in exploring how GaAs NMs can be used to address some of the major challenges associated with integrating III-Vs on silicon substrates. We demonstrate the growth of GaAs NMs on Si (111) by selective-area MBE in both majority-mononuclear and majority-polynuclear regimes by varying slit length. It is demonstrated that the growth of largely defect-free, single-crystal NMs is possible for openings shorter than one micrometre. For SAE openings longer than one micrometre, poly-nucleation and the consequent APB formation significantly limits the growth of defect-free NMs. We study the influence of different growth conditions on the crystal structure of these NMs and develop a growth model that explains the data. We then analyse the optical properties of the NMs by cathodoluminescence (CL) and μ-photoluminescence (PL) and directly correlate them with localized defects identified by scanning transmission electron microscopy (STEM).

5.3 Results and discussion

GaAs NMs were grown by MBE on patterned Si (111) substrates with 30 nm of thermally grown oxide. Stripes were patterned with widths in the range of 60-80 nm, and lengths of up to several microns. A scheme of the substrate before and after growth is depicted in Figure 5.1 (a) and (b), respectively. Figure 5.1 (c) and (d) show a tilted scanning electron microscopy (SEM) image of a typical GaAs NM array obtained after 60 min of growth in long and short slits, respectively. We observe that GaAs grows only in the longitudinal openings in the SiO_2 mask with a high degree of selectivity, as reported for GaAs substrates [112, 160, 177]. Compared to the growth on GaAs substrates [177], the NMs grown on Si do not fill the openings for longer slits, as seen in Figure 5.1 (c). Instead, we observe several separate NMs merging. This merging often forms visible defects whose shape in SEM resembles APBs in GaAs thin films on Si [159]. While the defect density remains constant, the total number of defects per NM is greatly reduced for shorter slits. We deduce that for shorter slits the growth moves towards the mononuclear regime where the merging of multiple polarity-mismatched nuclei is strongly reduced.

To increase the crystalline quality of the NMs, we experimented with various substrate treatments before growth. To foster a single polarity in the seeds, growths were preceded by a

soaking period in Ga or As$_4$ flux followed by an annealing step. The percentage of preferentially-aligned nuclei was calculated with the help of SEM imaging in a region with short, 180 nm-long slits, as shown in Figure 5.1 (e). Here, the NM growth was preceded by a 30 s gallium exposure followed by a 5 min anneal and shows a clear enhancement of the left-pointing NMs, marked in blue. The table shown in Figure 5.1 (f) summarizes the effect of various substrate treatments that were performed and the resulting percentage of aligned NMs. The preferential alignment is given by the number of NMs whose long axis points towards the $\langle 11\bar{2}\rangle$ direction, divided by the total number of NMs considered for the analysis. A minimum of 100 NMs per sample were checked for the quantification to ensure a large enough sample size.

From the table in Figure 5.1 (f) we see that without any pre-treatment the NMs are randomly orientated, split about 50/50 between the two directions. Preferential alignment increases with Ga pre-deposition time and is further enhanced by adding an annealing step after pre-deposition. Interestingly, it was observed that As$_4$ pre-deposition also led to preferential alignment. However, due to the vastly different surface dynamics of the two growth species, as well as the large body of scientific literature about Ga-catalysed nanostructure growth from the NW community, in this report, we will focus on the gallium exposure strategy with the As pre-deposition approach to be addressed in a separate paper.

We further explored if the gallium droplets formed on the surface could drive the nucleation down to the mononuclear growth regime (as in the case of self-catalysed NW growth) [376], thus avoiding APB formation. SEM micrographs of samples on which a 30 s gallium pre-deposition was performed followed by 2 min and 15 min of GaAs growth are shown in Figure 5.1 (g) and (h), respectively. Before GaAs growth, it was observed that the slits seem mostly empty except for a few nanoscale droplets around the edges, in contact with the SiO$_2$. After 2 min of GaAs growth, multiple GaAs crystals with an average diameter of about 50 nm begin to nucleate in the same area. The nucleation of many islands during the early stages of growth is consistent with the polynuclear growth regime. Such a regime has also been observed in the homoepitaxial growth of NMs on (111) GaAs substrates [384].

We observe that GaAs islands nucleate preferentially at the interface with the SiO$_2$. It suggests that this corner offers the lowest-energy position for crystal nucleation, which is also the case for NWs [376]. This is in contrast to the growth on GaAs substrates where the nucleation occurs inside the slits, rather than at their edges [384]. This confirms that the heteroepitaxial interface has much higher energy than the homoepitaxial interface and drives nucleation to favour the corners at the edges of the slit. The corner nucleation occurs despite the formation of a relatively high-energy GaAs/SiO$_2$ interface, which is not favoured when growing on GaAs substrates.
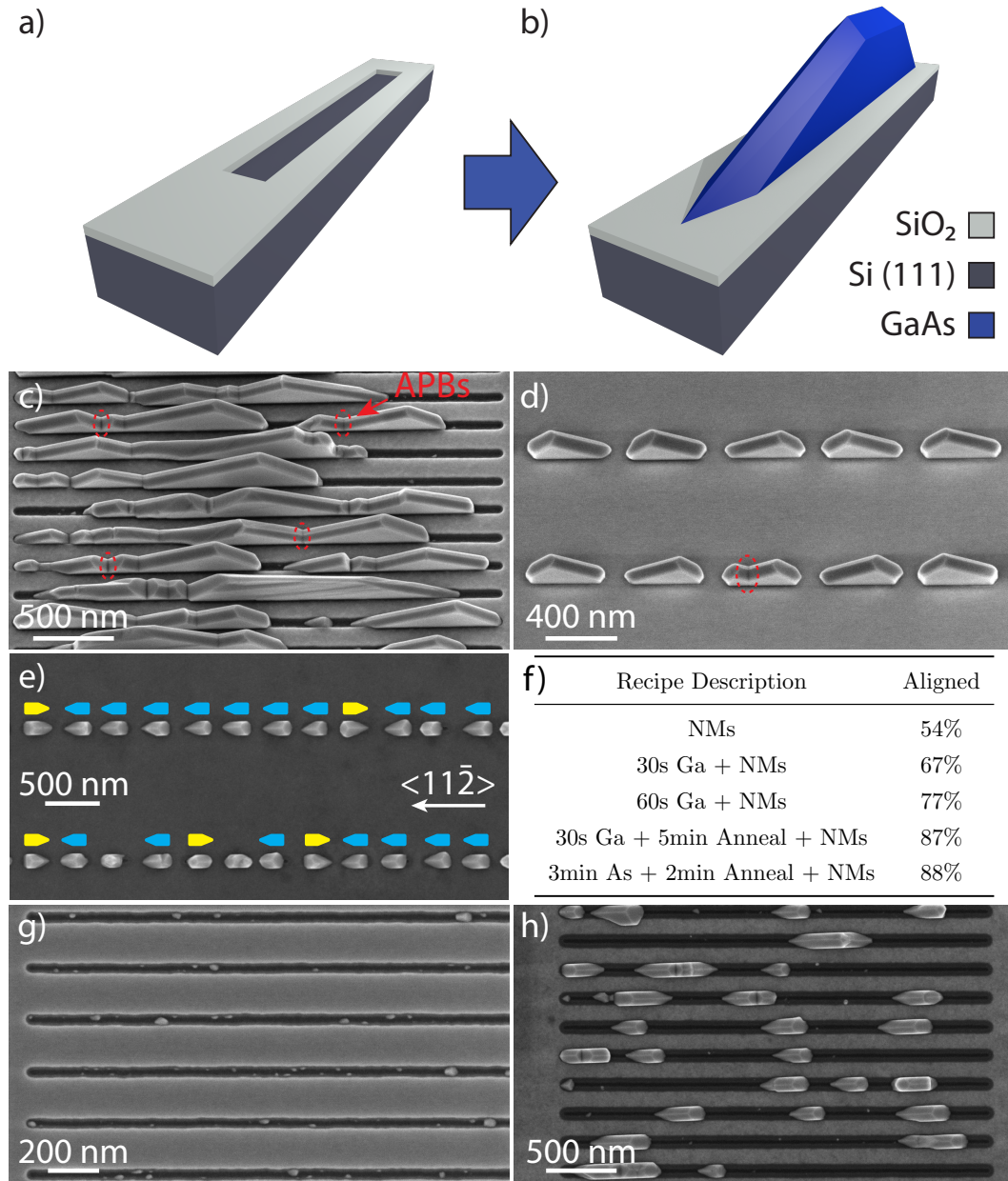
Figure 5.1 – a) Schematic of a patterned SiO$_2$/Si substrate ready for MBE growth. b) Schematic of the SAE growth of NMs. c-d) Tilted SEM images after 60 min of GaAs NM growth without gallium pre-deposition on Si (111) for long slits (c) and short slits (d), with APBs circled in red. e) Top-view SEM image of NMs grown by 30 s Ga pre-deposition + 5 min anneal + NM growth showing preferential crystal orientation. f) Summary of different growth recipes and the resulting percentage of aligned crystals. g-h) Top-view SEM images after 30 s of gallium pre-deposition, followed by 2 min and 15 min of GaAs growth, respectively.

Furthermore, as the gallium droplets observed before growth also seem to favour the edges of the slits, therefore, GaAs islands may nucleate within the gallium droplets. These crystal

nuclei then grow relatively quickly, forming small tetrahedra with their long axis aligned either along the $[11\bar{2}]$ or $[\bar{1}\bar{1}2]$ direction after only a few minutes of growth. The orientation of the first layers of the crystal can be affected by the formation of twins which results in these two possible tetrahedral orientations [196, 385]. In the absence of twins, the orientation of these tetrahedra is directly related to the crystal structure of the substrate. Once the tetrahedra reach the edges of the openings, they grow upwards, developing vertical (110) side facets [130, 300]. The formation of such vertical facets starts to be clear after 15 min of growth, as seen in Figure 5.1 (h). Eventually, the crystals merge yielding a single, continuous NM in the slit. As mentioned previously, the coalescence of oppositely-oriented structures, due to the presence of polynucleated islands, is what causes the formation of kinks such as those circled in red in Figure 5.1 (c) and (d).

We now provide a model that explains some important features of nucleation and growth of GaAs NMs on Si with gallium pre-deposition. This process consists of two steps, the nucleation of gallium droplets and subsequent growth (with continued nucleation) of GaAs NMs starting from these droplets. We first consider the nucleation of gallium droplets in Si/SiO_2 slits during the gallium pre-deposition step. The number of gallium atoms arriving per unit length of the slit per unit time equals IW with $I = 0.664 \, \text{nm}^2/\text{s}$ as the atomic flux of gallium (equivalent to the growth rate of $0.3 \, \text{Å}/\text{s}$), and W as the slit width (60-80 nm). In principle, the I value can also include the indirect gallium flux originating from the adatom diffusion on the oxide, without changing the model equations and conclusions. However, due to the high substrate temperature of $630 \, °\text{C}$, the indirect flux is estimated to be only about 10% of the direct flux and has thus been neglected in the numerical estimates [160]. Taking into account the rotation of the sample, one side of the slit receives the incoming flux during half of the rotation period. We can thus say that one-half of the incoming flux arrives at each side of the slit and then diffuses along the side. The coalescence of these diffusing adatoms leads to the nucleation of gallium droplets, as shown in Figure 5.2 (a). Assuming that the gallium adatoms have a concentration n_1 per unit length at a distance λ from the droplet surface (at $x = r + \lambda$) and zero concentration at the droplet surface (at $x = r$) with r as the radius of the droplet base, the adatom concentration at the borders of the slit should equal $n(x) = (n_1/\lambda)(x - r)$. Here, x is the coordinate along the slit and λ plays the role of the effective diffusion length of gallium adatoms at the Si/SiO_2 edge. The growth rate of the droplet equals $D \, dn/dx|_{x=r} = D n_1/\lambda$, with D as the diffusion coefficient of gallium adatoms near the Si/SiO_2 corner. The adatom concentration changes with time t according to $dn_1/dt \cong (IW/2 - D n_1 N/\lambda) \rightarrow 0$, with N the droplet density per unit length of the slit. The n_1 must tend to zero for long enough t due to the balance of the arrival rate and growth of gallium droplets [386]. On the other hand, the droplet density changes with time according to $dN/dt = D n_1^2/\lambda$ that their nucleation rate equals the growth rate times the adatom concentration [386, 387].

Solving this equation, we obtain the droplet density (per unit length of the slit) in the form:

$$N = \left(\frac{IW}{2}\right)^{2/3} \left(\frac{3\lambda(1+\delta)}{D}\right)^{1/3} t^{1/3} \tag{5.1}$$

Here, δ accounts for the fraction of GaAs crystals that form without droplets, with a different effective distance between the emerging islands. This δ should be minimized to yield a more mononuclear growth regime. This problem requires a separate study which is beyond the scope of this work. Within our model, N increases with the gallium pre-deposition time and becomes smaller for lower deposition flux, narrower slit and higher diffusivity of gallium adatoms, which is reasonable. Mononucleation of a single gallium droplet in each slit would be reached when the average distance between the droplets becomes equal to the slit length. In particular, statistical analysis of the droplet size distribution after 30 s of gallium pre-deposition reveals the average droplet density $N = 0.375\,\mu m^{-1}$. Using Equation (5.1), this gives an estimate $D/[\lambda(1+\delta)] = 5\,cm/s$.
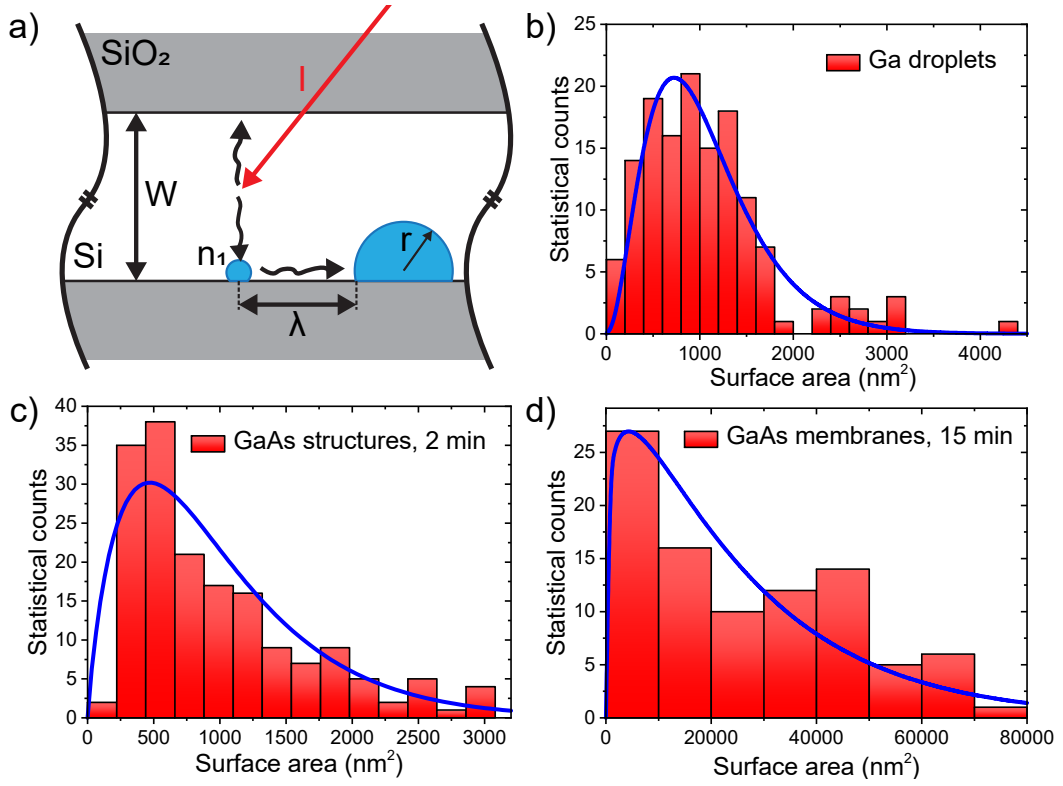
Figure 5.2 – a) Illustration of the model for nucleation of gallium droplets in the slits; b–d) Experimental size distributions of gallium droplets, all GaAs structures after 2 min of growth and GaAs NMs after 15 min of growth (histograms), fitted by Equation (5.2) (blue curves)

Size distributions of gallium droplets after 30 s of gallium pre-deposition, GaAs structures after 2 min of GaAs growth, and GaAs NMs after 15 min of GaAs growth over the slit area are shown in Figure 5.2 (b) to (d). This data was obtained by statistical analysis of SEM images and it shows that the droplets exhibit a large size inhomogeneity in all cases. To understand this feature, we note that, at least for GaAs crystals emerging from gallium droplets, the volume of the crystals increases due to direct impingement of As_4 onto the droplet surface. Hence, the number of GaAs pairs in the crystals increases with their size as $(a + s)$, where $s = i^{2/3}$ is the appropriately normalized dimensionless surface area and a is the dimensionless nucleation

probability of GaAs crystals at $s = 0$. We can equivalently present the growth rate in terms of s in the form $ds/dt = (a + s)/\tau$, with τ as a characteristic growth time. According to Refs [388–390] such a size-linear growth rate leads to the Polya-like distribution over the surface area of the structures S.

$$f(S, \langle S \rangle) = C \frac{a^a}{\Gamma(a)} \frac{1}{\langle S \rangle} \left(\frac{S}{\langle S \rangle} \right)^{a-1} \exp\left(-a \frac{S}{\langle S \rangle} \right) \tag{5.2}$$

where $\langle S \rangle$ is the average surface area occupied by the crystals in a given sample and C is a constant.

The measured average surface area of gallium droplets after 30 s of gallium pre-deposition is 1053 nm^2. The average surface area of the GaAs nanocrystals emerging from these droplets decreases to 992 nm^2 after 2 min of GaAs growth, showing that the aspect ratio of the nanocrystals, including NMs, is higher than for spherical cap droplets. It increases to 25 585 nm^2 after 15 min of GaAs growth, where all nanocrystals acquire the energetically preferred shapes of elongated NMs. Blue curves in Figure 5.2 (c) and (d) show the fits to the size histograms of GaAs nanocrystals and NMs by Equation (5.2), with $a = 1.9$ for $t = 2$ min and $a = 1.2$ for $t = 15$ min. The blue curve in Figure 5.2 (b) shows that Equation (5.2) can also be used for fitting the size distribution of the initial gallium droplets, with the best fit obtained at $a = 3.2$. All these values of a are on the order of unity, corresponding to the size distribution maxima at small surface areas and long right tails of the distributions. Overall, our growth model reveals the kinetic mechanisms that lead to the formation of GaAs NMs in the Si/SiO$_2$ slits. It properly describes the nucleation of droplets at the slit edges, As-controlled crystallization of GaAs crystals from these droplets, their further evolution to the elongated NMs and the broad size distributions of all objects. According to our Equation (5.1), the number of nuclei in each slit can be reduced by growing in thinner slits (smaller W), increasing the gallium diffusion coefficient D by increasing the growth temperature and depositing gallium for shorter time t. More complex scenarios can also be considered, such as two-step growth with higher temperature for nucleation of gallium droplets and lower temperature for growing GaAs. Outcomes of Equation (5.1) thus reveal approaches that can be used in the future for minimization of crystallographic defects resulting from the coalescence of the NMs.

We now turn to the description of correlated CL, μ-PL and STEM measurements used to gain insight into the properties of GaAs NMs, specifically focusing on the effects of defects that arise due to their growth on non-polar Si substrates. Two side-by-side AlGaAs passivated nanostructures were selected due to their structural dissimilarity, as observed by SEM, shown in Figure 5.3 (b). NM A was chosen as it represents the majority of the NMs that are believed to grow in the mononuclear regime and appear defect-free. In contrast, NM B was chosen specifically due to the presence of a kinked surface suggesting the presence of defects which we interpret to be due to a statistically unlikely polynucleated growth. The comparison between their luminescence and structural properties provide insight into the behaviour of such defects in GaAs nanostructures grown on Si.
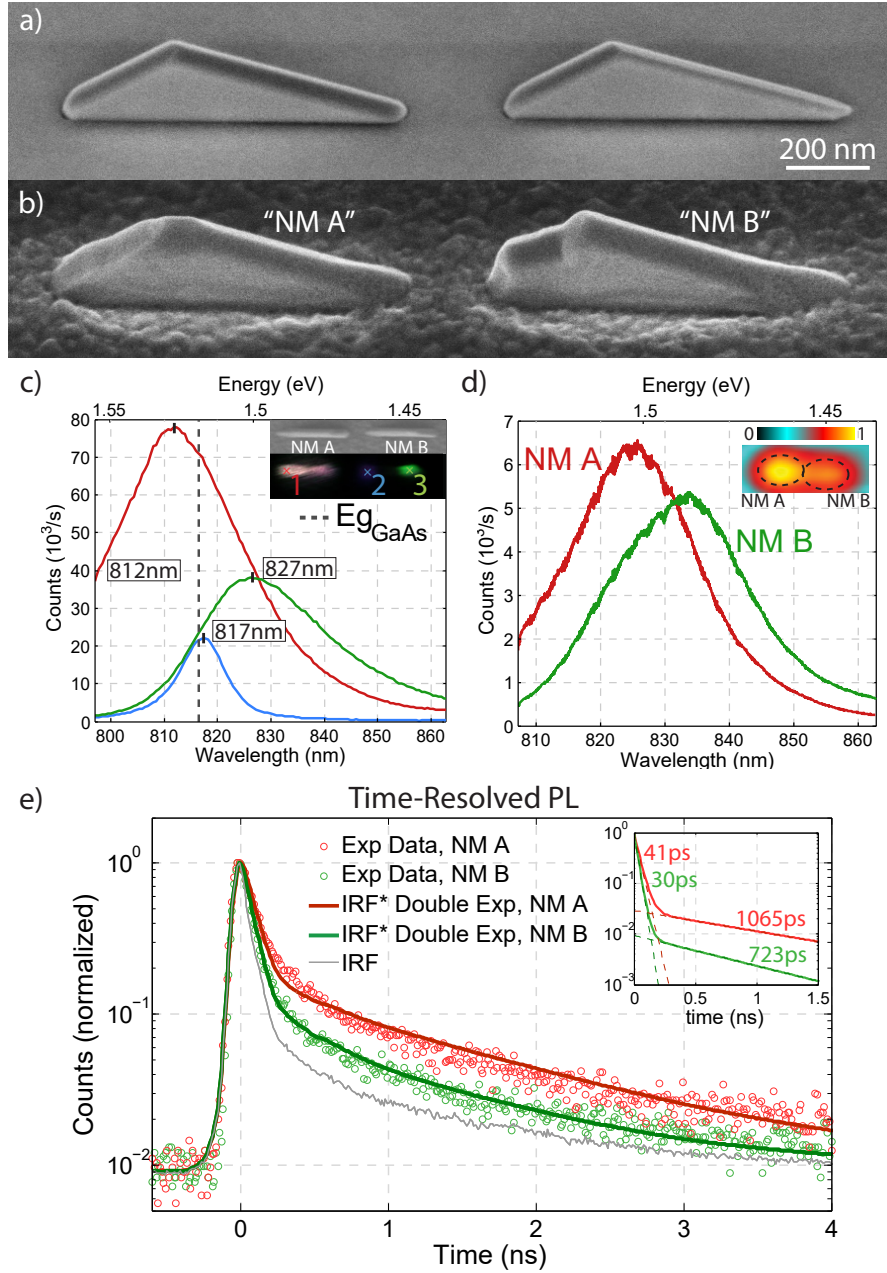
Figure 5.3 – a) Tilted SEM image of GaAs NMs after growth in 800 nm-long slits b) Tilted SEM image of NMs A and B which were passivated with an AlGaAs shell for CL/PL analysis c) CL spectra corresponding to different positions on NMs A and B. The inset shows an SEM image of the investigated region and its CL map. The value of the GaAs bandgap at 12 K is marked by the vertical dashed line. d) μ-PL spectra obtained at the point of each NM where the intensity was strongest. PL map of the intensity distribution is shown in the inset. e) TRPL measurements of NM A and B revealing two distinguishable lifetime components. The points represent the experimental data while the solid curves show the fits to the data obtained by the convolution of the instrument response function with the double exponential functions plotted in the inset.

To increase the luminescence yield of the NMs, their surface was passivated with a 41 nm $Al_{0.3}Ga_{0.7}As$ shell. The shell growth was performed at 440 °C under a high As_4 flux similar to Heigoldt *et al.* [391]. Figure 5.3 (a) and (b) show SEM micrographs of the structures before and after AlGaAs shell growth, respectively. Interestingly, a new (111)B facet appears at the top of one of the NMs, with two small {1 1 3} inclined facets on either side of it. A rough AlGaAs layer covers the whole mask surface as it was deposited at a low temperature for which mask selectivity is lost [160].

Low-temperature CL and μ-PL spectroscopy were performed to characterize their optical properties. Figure 5.3 (c) shows CL spectra obtained at different positions on the two NMs. A SEM image of the analysed region is shown in the inset along with a CL map of the same area, where the emission intensity at each point is correlated with its position in the SEM image. Each colour in the map represents the relative intensity detected at the selected emission wavelengths. Red, green and blue colours correspond to the intensity measured at 812 nm, 817 nm and 827 nm, respectively.

The emission from NM A [red curve in Figure 5.3 (c)] is uniform along the whole structure. The spectrum is centred at 812 nm. This is slightly blue-shifted with respect to the band edge emission of GaAs at 820 nm (dashed line in Figure 5.3 (c)), most probably due to the highly excited regime of CL which leads to band filling [392]. In contrast, the emission from NM B [green and blue curves in Figure 5.3 (c)] exhibits both wavelength and intensity variation along its length. Two spatially-resolved and spectrally-distinct emission regions are present on each side of the NM and are separated by a weaker region at its centre: one side of NM B emits at 817 nm and the other at 827 nm, with emission energy below the band edge. The asymmetric shape of the green curve reveals the presence of a weaker component at lower energies. Both signals from NM B are weaker and shifted towards longer wavelengths with respect to NM A. This could be attributed to a defect-mediated mechanism [393–395].

Figure 5.3 (d) shows the μ-PL spectra corresponding to the maximum PL intensity of each NM, acquired at 6 K. In our μ-PL setup, the spot size of the excitation laser is comparable to the size of the NMs. Consequently, although μ-PL can spatially resolve the signal from the two NMs, each μ-PL spectrum is the convolution of the total emission from each NM. In NM A, the emission is centred at 824 nm, with a full width at half maximum (FWHM) of 25 nm. The emission energy here is consistent with the band edge emission of GaAs at low temperatures. The FWHM is quite broad, especially compared to the values obtained in homoepitaxial GaAs NMs, which is narrower by approximately one order of magnitude [177, 299]. This broadening is attributed to the presence of twinning defects, as confirmed by transmission electron microscopy (TEM) measurements.

The emission of NM B is centred at 833 nm. This spectrum can be fitted by three different Gaussian contributions: a central peak at 836.0 ± 0.5 nm, surrounded by another at 826 ± 2 nm and a less intense one at 851 ± 3 nm. The μ-PL emission is consistent with the sum of the two CL signals. The highly excited regime of the CL leads to band filling effects which are seen here

as a blue shift of the CL emission with respect to that of the PL [392].

Time-resolved photoluminescence (TRPL) measurements from each NM are shown in Figure 5.3 (e), revealing two different lifetime components. This can be seen more clearly when plotting the time evolution on a logarithmic scale, as shown in the inset. The longer-lived components have lifetimes of about 1065 ps for NM A and 723 ps for NM B, while the shorter ones have lifetimes of 41 ps and 30 ps, respectively. Details on the fitting procedure and the effective lifetime calculation are given in Appendix C.3. The short-lifetime pathway contributes much more to the PL decay in NM B than in NM A. This indicates a more defective structure in NM B and is consistent with its previously discussed red-shifted multi-component luminescence.

We turn now to the structural characterization of NMs A and B. After the optical characterization, a focused ion beam (FIB) cross-section containing both NMs was prepared. The NMs were then analysed by high-resolution transmission electron microscopy (HR-TEM) and STEM. The results of these analyses are summarized in Figure 5.4. The top of the figure shows general view HR-TEM micrographs. Atomically resolved high-resolution high-angle annular dark-field (HAADF) STEM image details are shown in the lower part of the figure.

Figure 5.4 (a) and (b) show low-magnification HR-TEM micrographs of NM A and NM B, respectively. It is immediately seen that NM B has a larger number of both in-plane and out-of-plane defects. NM A exhibits a much better crystal quality, with relatively few twinning defects parallel and close to the substrate interface. The density of these twins is about one twin every 2.5 nm. The twinned region extends 52 nm above the interface [Figure 5.4 (c)], after which NM A has a defect-free zincblende (ZB) crystal structure. This is also revealed in the fast Fourier transform (FFT) presented in Figure 5.4 (a) where a pure $\langle 1\,1\,0 \rangle$ ZB pattern is present without any extra diffraction spots. Figure 5.4 (g) shows the atomically resolved image of this defect-free region, with the corresponding intensity profile given in Figure 5.4 (h). The difference in the intensity values arises from changes in Z-contrast given by the HAADF detector ($I \sim Z^2$) and reveals B-polar (As-polar) growth [396]. This is expected when the first nucleated layer of atoms is Ga (a possible consequence of the gallium pre-treatment).

In NM A, an additional set of twins parallel to the $(\bar{1}\,\bar{1}\,\bar{1})$ substrate is found in a 25 nm-thick layer close to the top facet within the AlGaAs shell. Twinning defects following another (inclined) {1 1 1} plane are found only at the far-right side of the NM. Importantly, they do not propagate from the substrate but rather appear after a few nanometres of GaAs and extend to the NM top. Their origin may be related to the overgrowth of GaAs extending on top of the mask, as observed by Tutuncuoglu *et al.* [177]. However, the density of these defects is very low (three twins along the whole NM, located close to the vertex between the base and the long edge of the NM).

In contrast to NM A, NM B presents a relatively high density of defects. Starting from the bottom, the NM exhibits a succession of two $(\bar{3}\,1\,1)$ and $(1\,\bar{3}\,1)$ facets, followed by two $(\bar{1}\,0\,\bar{1})$' and $(0\,\bar{1}\,\bar{1})$' inclined facets, and lastly a $(\bar{1}\,\bar{1}\,0)$ facet, where the "prime" symbol refers to the system of planes obtained after a rotational twin. Several twins along different {1 1 1} planes

are detected in the whole body of the NM. This is consistent with the FFT in Figure 5.4 (b), where we can see multiple out-of-plane rotations of the ZB structure caused by multi-twinning. When two twins around different directions merge, only one of them propagates further. In the case of non-planar polar semiconductor nanostructures the growth front tends to follow the {1 1 1} planes [397]. In the presence of an APB, the growth front evolves along different angles on both sides of the boundary, which explains the formation of kinks at the surface of the nanostructure. The presence of complex APBs at the merging point between polar crystals has been also observed in complex nanostructures such as V-shape nanofins [397], vertical nanospades [178], and close to the nucleation seed of A-polar GaAs NWs [398]. In addition, the complex defects appearing in this region also accumulate strain around them (medium-angle annular dark-field (MAADF) images revealing the accumulation of strain are shown in Appendix C.3). Figure 5.4 (e) and (f) are atomic resolution HAADF-STEM images showing the defects marked in Figure 5.4 (b).

To get more information on this low-angle grain boundary, atomically resolved electron energy loss spectroscopy (EELS) gallium elemental mapping was performed. The polarity of the dumbbells was identified by overlapping the integrated intensity of the gallium $L_{2,3}$ edge with a HAADF micrograph of the area. According to the colour compositional map shown in Figure 5.4 (i), gallium atoms are located on top of the dumbbell at both sides of the boundary. Consequently, Ga-Ga pairs form at the border between the A' and A'' regions, as detailed in the structural map presented in Figure 5.4 (j). At least one other defect involving a polarity inversion is present in a different region of this NM (shown in Appendix C.3).

The distribution of defects in NM B could explain the inhomogeneous CL emission. From TEM analysis, an APB is observed separating the two regions of CL emission. APBs have been reported to act as potential barriers for carriers [396, 397]. Therefore, the APB blocks the diffusion of excitons, creating two spatially separated regions of CL emission. APBs have also been shown to act as recombination centres [366]. Recombination results in the emission quenching close to the APB and leads to a decrease in intensity between the two regions of emission in the CL map. Similarly, the integrated PL intensity is significantly lower in NM B than in NM A, which had no APBs.
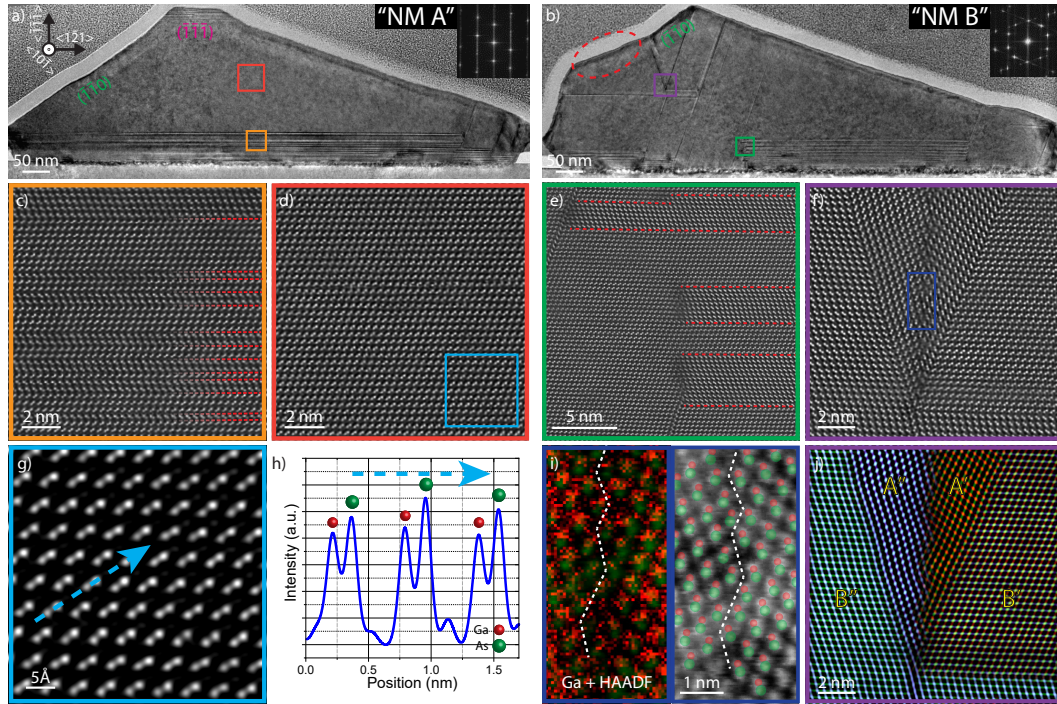
Figure 5.4 – Microstructural characterization of NMs A and B. a,b) Low-magnification HR-TEM micrographs revealing the overall defect distribution in both NMs. The insets show the FFTs corresponding to the regions marked by the red and violet squares, respectively. Aberration-corrected atomically resolved HAADF-STEM micrographs obtained on NM A showing: c) twinned layer (twins marked in red), d) defect-free area, g) zoom from (d) and h) intensity profile obtained along the blue arrow marked in (g) for polarity determination. For NM B: e) twinned layer in contact with the twin-free region, f) defective area near the top of the NM, i) zoomed image from (f) with superimposed gallium signal obtained by EELS (red) and HAADF (green); schematic showing dumbbell composition in the defect. j) Coloured structural map showing different crystal orientations with polarities indicated. A and B refers to the polarities in the vertical direction (A=cation on top and B=anion on top).

The twinned region of NM B is not continuous along its base. Some sections are defect-free while others contain multiple twins. The discontinuity in twining reveals that the growth started from multiple nucleation sites. The example of a region between the twinned and twin-free parts of the NM is shown in Figure 5.4 (e). Here, the left part of the image is defect-free, while the right side contains multiple rotational twins, marked as dashed red lines. When going from left to right, the crystal structure is only preserved for one orientation of the twin. In addition, we observe vertical defects between the defect-free and the twinned region. This is due to the change of polarity in the horizontal direction and is quite similar to what is observed in vertical nanospades [178].

The presence of this highly defective structure at the base of NM B is in stark contrast to the relatively defect-free region observed in NM A. The existence of these two very different crystal

structures in NMs grown side-by-side underline the importance of controlling the phase and coalescence of nucleated islands to achieve defect-free crystal growth of III-Vs on Si.

Overall, correlating the features of the representative TEM-measured samples by observation of NM faceting observed in SEM, we find two distinct types of NMs on Si (111). The first type of NMs present uniform faceting and shape, similar to NM A. These NMs contain a region with twins close to the interface, similar to a buffer layer, oriented in the $(\bar{1}\,\bar{1}\,\bar{1})$ plane. The second type of NMs, presenting irregular faceting and non-uniform shape, contain APBs and other complex defects, similar to NM B. Close to the Si interface, regions both with and without twins exist suggesting that the growth of NM B was mediated by a polynuclear regime. So far, no APBs were observed to originate from the Si-GaAs interface though APBs were found within the bulk of the NM. These APBs are a consequence of the polynuclear growth combined with independent multi-twinning processes in each domain, as was shown by the TEM analysis. This is further supported by the fact that these APBs were not found in NM A, consistent with a structure originating from a single nucleation event.

We have also found that the emission intensity and the energy of the emission of defected NMs are lower than in the single crystalline case. Similarly, the effective lifetime of minority carriers is significantly shorter in the defected structures. We thus suggest that the presence of APBs and other complex defects deteriorates the optical properties of the NMs. This is supported by the fact that the CL signal is very weak in the region where these defects are located.

It is thus clear that the formation of APBs should be minimized for electronic and optoelectronic applications of GaAs NMs on silicon. According to our theoretical model, growth parameter tuning allows for majority mononuclear growth for NMs grown in short slits, and hence the absence of APBs originating from twins. However, polynucleation may be unavoidable for longer NMs (from several to tens of microns). In this case, a different approach is required, one that ensures that all nuclei have the same polarity to avoid APB formation. We saw that a pre-growth treatment consisting of exposing the substrate to gallium or As$_4$ before growth resulted in the preferential orientation of the NMs. More detailed investigations into such pre-treatments are necessary to understand the mechanism by which they can drive the preferential orientation of polar NMs on a non-polar substrate. Equally-interesting is the fact that the preferential orientation of the NMs occurs despite the presence of a large number of rotational twins at the base of both NMs that were investigated. One might expect that a large twinning probability during growth would lead to a randomized distribution of the NMs orientation which is not the case here.

5.4 Conclusions

We have investigated the SAE growth of GaAs NMs on Si(111) substrates by MBE. In contrast to homoepitaxial growth, we have observed a higher heterogeneity in the nuclei formed in the initial stages of growth. We have found that a substrate pre-treatment with gallium or arsenic before growth can greatly reduce defect formation and can thus be an important

element in the defect-free integration of the NMs on Si. We propose a growth model that fits the experimental data and reveals the parameters for growth in the mononuclear regime, that is, one nucleus per slit. TEM analysis on an APB-free NM has shown the presence of in-plane twin defects close to the GaAs-Si interface while crystal continuity along the base of the NM suggests that it grew in the mononuclear regime which is statistically favoured for slit lengths less than about 1 µm. Finally, CL and PL analyses on a NM whose crystal structure is consistent with a polynucleated growth regime suggest that the presence of APBs and other complex defects deteriorate the optical properties of AlGaAs-passivated NMs, as evidenced by lower measured minority carrier lifetimes. Overall, the results presented in this work pave the way for monolithic integration of GaAs NMs and related nanostructures on Si substrates.

Experimental

Substrate preparation. Samples were prepared by starting with an undoped Si(111) wafer on which a 30 nm thick thermal oxide was grown. The wafer was patterned using e-beam lithography in a Raith EBPG-5000+ with ZEP resist. After developing in n-amyl acetate and isopropyl alcohol (1 min each), the wafer was dry etched in an SPTS APS dielectric etching tool using CHF_3/SF_6 chemistry. O_2 plasma stripping of the resist was performed before dipping the wafer briefly into a buffered HF solution and quickly loading it into the MBE chamber to prevent oxidation of the silicon surface.

MBE Growth. Each sample was loaded into a DCA P600 solid-source MBE chamber and degassed at 400 °C for 2 h under ultra-high vacuum. The sample was then loaded into the growth chamber and annealed at 750 °C for another 30 min before launching the growth recipe. NM growth was performed at a substrate temperature of 630 °C under a gallium flux yielding a GaAs equivalent growth rate of 0.3 Å/s and an arsenic beam equivalent pressure (BEP) of 5.5×10^{-6} Torr. AlGaAs-capped samples were capped at a substrate temperature of 440 °C with 41 nm of $Al_{0.3}Ga_{0.7}As$ followed by 7 nm of GaAs to prevent oxidation. Here, the AlAs and GaAs equivalent growth rates were 0.5 Å/s and 1.0 Å/s, respectively, with an arsenic BEP of 1.1×10^{-6} Torr.

CL. CL measurements were performed at 12 K in a closed cycle Attolight Rosa cryostat, using an electron-beam energy of 2.5 keV and current of about 1 nA. The CL signal is collected by a reflective objective (numerical aperture (NA) 0.71) and sent through a 32 cm focal-length spectrometer onto a Peltier-cooled Si charge-coupled device (CCD) after spectral dispersion by a diffraction grating.

µ-PL. Spatially resolved µ-PL characterization was performed at 6 K using a diffraction-limited confocal microscope inserted into a low-vibration, cryogen-free cryostat (Attocube Attodry 1000). A 780 nm pulsed laser was used to excite the sample whose PL signal was dispersed by a 750 mm focal length spectrometer at a resolution of ~30 µeV and detected with a cooled Si CCD. Scanning µ-PL maps were recorded using an XY piezo scanner.

TRPL. TRPL spectra were acquired by the so-called time correlated single photon counting (TCSPC) technique. For this, an avalanche photodiode (APD) with a time resolution of ~25 ps was used.

Cross-sectional STEM. A cross-sectional lamella was cut out of selected NMs using FIB. TEM characterization, including HR-TEM, HAADF STEM and EELS imaging (see Appendix C.3 for details) were performed using a TECNAI F20 field emission gun microscope operated at 200 kV with a point-to-point resolution of 0.14 nm, coupled to a GATAN Quantum EELS spectrometer. Atomically resolved HAADF-STEM images were acquired on a probe-corrected FEI Titan 60-300, equipped with a high-brightness field emission gun (XFEG) and a CETCOR corrector from CEOS to produce a probe size below 1 Å. The microscope was operated at 300 kV, with a convergence angle of 25 mrad and an inner collection angle of the detector of 58 mrad. Atomically resolved aberration corrected HAADF-STEM was used to determine with high accuracy the atomic column positions, allowing the detailed study of polarity [396] as well as the final strain analysis by means of geometrical phase analysis (GPA) [301, 399]. The HAADF-STEM images were treated with a Wiener filter and beam deconvolution for clarity. Atomically resolved EELS mapping to determine the crystal polarity was performed using a Nion UltraSTEMTM 100MC 'HERMES' operated at 60 kV [400].

6 Conclusion & Outlook

In this thesis, we focused on exploring the new possibilities offered by template-assisted nanowire (NW) growth by molecular beam epitaxy (MBE). This promising approach gives the ability to grow wafer-scale arrays and networks of III-V NWs with unprecedented control of NW position and direction while achieving superb crystal quality and functionality. These positive aspects make this growth approach very appealing in the fields of topological quantum computing and infrared photodetectors, both of which have been getting significant attention recently. Specifically, we explored the growth of In(Ga)As NWs on two varieties of GaAs substrates and also investigated the growth of GaAs nanomembranes (NMs) on Si (111) substrates.

First, the growth of In(Ga)As NWs on top of GaAs NMs was demonstrated on GaAs (1 1 1)B substrates. InAs was shown to collect at the top of GaAs NMs to minimize energy, however, the unstable {1 1 3} top facets of the GaAs and large lattice mismatch resulted in highly-intermixed InGaAs NWs. As a result, the NWs had a low conductivity, so extrinsic dopants were introduced to perform electrical measurements. Atom probe tomography (APT) measurements were performed on the extrinsically-doped NWs and it was found that dopants had trouble getting incorporated into the In(Ga)As NW and most of the dopants remained on top the of NW structure. Magnetotransport measurements yielded results indicative of quasi-1D transport and weak localization (WL) behaviour in the diffusive regime while fits gave an electron coherence length of >100 nm.

The following study explored dopant incorporation into this material system to achieve a remotely-doped structure. First, the In concentration of the NWs was shown to increase through lower V/III ratios and higher In fluxes, allowing for the growth of $In_{0.5}Ga_{0.5}As$ NWs. When combined on top of a remotely-doped GaAs NM structure, these NWs exhibited very good transport characteristics compared to the previous extrinsically-doped NWs. Magneto-transport measurements showed weak anti-localization (WAL) behaviour this time and fits indicated that electron mean free paths had increased from on the order of a few nanometres to >200 nm. APT measurements were similarly performed to image the dopant incorporation and it was observed that the dopants also have difficulty getting incorporated during GaAs

growth and instead float to the top of the structure. This interesting effect will, therefore, be the topic of a future study.

Results on the growth of pure InAs NWs on GaAs buffers were then demonstrated on GaAs (100) substrates. Switching to the (100) substrate resulted in a significant decrease in the intermixing of Ga into the InAs NW, likely due to the more stable facets formed on this surface as compared to the faceting in GaAs NMs grown in GaAs (111)B. Low-temperature field-effect transistor (FET) measurements yielded mobilities close to what has been observed in vertically-grown InAs NW in our group, which is very promising considering the relatively large amount of scattering surfaces in these NWs.

Future work on template-assisted InAs NWs can be divided into two categories: improving quantum transport and coupling 1D wires to superconductors. Interface scattering from the NW surface and the GaAs interface is likely the greatest limitation of NW mobility and electron mean free paths. Therefore, current work is focusing on improving these interfaces through various approaches such as with the use of surfactants like Sb, which have been reported to yield smoother buffer layers [401]. Surface passivation with a higher bandgap material is another approach to improve mean free paths of electrons by reducing their interaction with the surface. This would have the additional effect of removing the Fermi level pinning at the surface of the InAs NW, though the resulting lack of carriers could be compensated by remote-doping also on (100) substrates. In the second category, the coupling of 1D wires to superconductors would be the next step towards enabling experiments with Majorana zero modes (MZMs). The superconductor material and deposition method would be two very important parameters for these experiments. Epitaxial aluminium could be attempted, though at least initially, more traditional sputtered deposition of NbTiN (for example) may be a better starting point. If sputtering were used, arsenic capping would have to be employed to protect the surface from oxygen during transfer into the sputtering chamber. In terms of transport, an example of an interesting experiment might include depositing a tunnel barrier between the NW and the superconducting circuit (SC) and observing the metallization of the NW as a function of tunnel barrier thickness (coupling strength) [96].

Other material systems can also be considered such as the growth of InSb NWs, which are thought to be the holy grail for topological quantum computation applications due to their incredibly large g-factor and strong spin-orbit interaction (SOI) [82]. This would, however, be a significant undertaking due to the even larger lattice constant resulting in a larger lattice mismatch when growing on GaAs substrates. Nevertheless, plastic strain relaxation through interfacial misfit (IMF) array formation appears to be a promising approach to achieve this [109, 112]. Further inspiration may be gained from the field of 2D growth in the form of low-temperature AlSb interfacial layers to help with IMF array formation [402]. Low growth temperatures required for switching to antimonide growth, on the other hand, will likely be a problem for maintaining selectivity on the SiO_2 mask. Ways to combat this include hydrogen-assisted molecular beam epitaxy (H-MBE), migration-enhanced epitaxy (MEE) or a two-part growth where 2D growth is performed to switch over to a 6.1 Å lattice constant, followed by

mask fabrication and a subsequent InSb growth step.

On the topic of selective-area epitaxy (SAE) nanostructure growth, many fundamental aspects are left to be understood. At the most fundamental level, the effects of slit width and pitch on NM/NW growth rates have still not been fully modelled. An example of a result that we currently have trouble explaining was given in Figure 4.3 where the smallest slit shows no GaAs growth. A similar effect has also been observed for increasing pitches of slits. Therefore, the next steps will certainly involve many growth series and theoretical modelling to fully understand these phenomena.

The dopant segregation effect that was observed in Chapter 3 is also a very good candidate for future studies. Next steps on this topic would include performing more in-depth growth studies in close collaboration with APT investigations to determine at which temperatures the dopants begin to get incorporated into the GaAs structure. Theoretical modelling, either through atomistic simulations or otherwise, might also help elucidate the nature of the dopant segregation effect. Once this effect is understood, it may be used to achieve very sharp delta-doped nanostructures by accumulating dopants at the surface and dropping the temperature to incorporate them all at once. Naturally, further investigations into remote-doping on (100) substrates also seems like an interesting avenue to explore.

Finally, the growth of GaAs NMs on non-polar Si (111) substrates was the last major topic that was presented. We found that the formation of anti-phase boundaries (APBs) is a significant challenge to growing defect-free NMs in slits longer than about 1 µm. Promising results were achieved by trying various surface pre-treatments to favour nucleation of a certain GaAs polarity. Subsequent cathodoluminescence (CL) and high-angle annular dark-field (HAADF)-scanning transmission electron microscopy (STEM) measurements showed that APBs are indeed electrically-active defects that form at the interface of two mismatched growth nuclei. Future work includes a more careful look at the growth mode and merging of individual nuclei, possibly by adding short growth markers or by performing a time series. This would also shed some light on the origin of the twins observed at the base of the nanostructures which are currently not well understood. One theory is that the twins form after a certain critical thickness to relax accumulated mismatch strain. Though there was an attempt to control polarity by surface treatments before growth, an additional factor to explore is the effect of surface roughness. Anisotropic etching of the surface with KOH would help make the surface atomically flat and possibly further help reduce APB formation by the mono-atomic step mode described in Figure 2.9b. Finally, the effects of miscut substrates could further be explored as a double-stepped surface has been reported to reduce APB formation [403, 404].

This work opens up many interesting new research directions in the field if semiconductor NW growth. Applied to NW growth, SAE is a highly-scalable growth technique that has a bright future ahead and a multitude of interesting applications. These currently include demanding, high-performance applications such as in topological quantum computing but may also one day include integrating III-V materials on silicon to help reduce the cost of

infrared photodetectors, for example.

As the scientific community forges ahead at break-neck pace with advanced growth techniques and an ever-deeper understanding of how these systems behave, I for one am very excited to see what the future holds for nanowire-based topological quantum computers. Though the future is anything but certain, some certainty lies in the fact that there is much left to be understood, even more left to be done and many surprises that we will learn from along the way. At the same time, I truly hope that the quantum computing community as a whole will remain as open as possible by encouraging the sharing of information and scientific discourse to bring the maximum benefit to society.

A Extra Experiments

As is the nature of scientific research, there are always new things to investigate and avenues to explore. During this thesis, there have been many side-projects and parallel collaborations that did not make it into the main text of this thesis. Nevertheless, there are a few which I believe are still worth including as they either yielded an interesting result and/or involved a lot of work (though usually both).

A.1 Nanosails Showcasing Zn_3As_2 as an Optoelectronic-Grade Earth Abundant Semiconductor

E. Z. Stutz*, M. Friedl*, T. Burgess, H. H. Tan, P. Caroff, C. Jagadish and A. Fontcuberta i Morral. Nanosails Showcasing Zn_3As_2 as an Optoelectronic-Grade Earth Abundant Semiconductor. *Phys. Status Solidi RRL* **13**, 1900084 (2019) *equal contribution

The content of this paper has been reformatted to match that of this thesis with references combined with those at the end of this thesis. The content and figures has been reproduced here without modification with the permission of John Wiley and Sons.

My contributions to this paper were the design and execution of the electrical transport measurements. This included contact fabrication and optimization with subsequent measurement in our liquid helium cryostat for temperature-dependent Hall and Van der Pauw measurements. I also contributed to preparing the electrical transport figures and writing a part of the manuscript.

Though this work is not directly related to the theme of the rest of my PhD thesis, the time spent on these measurements combined with the nice results led me to include it here in the appendix. The electrical measurements in this paper were performed in the first six months of my PhD during a maintenance period for the MBE. The temperature-dependent measurements posed quite a fun engineering challenge because they required some innovative thinking to implement a programmable switch box for the measurement signals. I also

included the design details of this equipment in Appendix B.1. The results of the measurements were quite pleasing, as they showed quite clearly that the semiconductor was degenerately p-doped. However, soon after the measurements were complete, I switched to MBE growth of III-V materials and so the results were never published. I am very grateful that Elias came along and was able to combine his Raman measurements with my electrical transport measurements into what turned out to be quite a nice paper in the end!

A.1.1 Abstract

Zn_3As_2 is a promising earth-abundant semiconductor material. Its bandgap, around 1 eV, can be tuned across the infrared by alloying and makes this material suited for applications in optoelectronics. Here, we report the crystalline structure and electrical properties of strain-free Zn_3As_2 nanosails, grown by metal-organic vapour phase epitaxy (MOVPE). We demonstrate that the crystalline structure is consistent with the $P4_2/nmc$ (D_{4h}^{15}) α"-Zn_3As_2 metastable phase. Temperature dependent Hall effect measurements indicate that the material is degenerately p-doped with a hole mobility close to 1×10^3 cm^2/Vs. Our results display the potential of Zn_3As_2 nanostructures for next generation energy harvesting and optoelectronic devices.

A.1.2 Introduction

The increasing production of high-performance electronic devices and the push towards generating energy in a sustainable manner leads to sustainability challenges for optoelectronic and photovoltaic (PV) technologies. Particularly affected are devices using atomic elements of scarce abundance in the earth's crust, which prevents their widespread deployment. In this context, highly functional materials made of earth-abundant elements are being sought for both PV and optoelectronic applications. The second most abundant element in the earth's crust, silicon, is a semiconductor very successfully deployed in the PV market. It suffers nonetheless from its indirect bandgap and the consequently high purity required for the production of efficient solar cells. Both characteristics increase the energy needs for silicon PV device production. The so-called 'second generation' solar cells, built with much thinner, direct bandgap active layers, could in principle solve these two issues. Still, these thin film solar cells exhibit either a long energy payback time (amorphous silicon) or they use scarce and expensive elements (ex: copper, indium, gallium, selenium, cadmium, tellurium).

Direct bandgap semiconductors employing earth-abundant elements could combine the advantages of all these material families. They would enable efficient light collection in a thin film of easily available materials. copper zinc tin sulfide (CZTS) and zinc phosphide (Zn_3P_2) have received increasing attention as materials satisfying these criteria for efficient and sustainable light conversion discussed so far. Belonging to the same family, zinc arsenide (Zn_3As_2) is a p-type semiconductor structurally similar to Zn_3P_2. It exhibits a band gap around 1 eV[405] and potentially high hole mobilities [406]. The stoichiometry of this material can be transformed continuously into Cd_3As_2[407] or Zn_3P_2[408] by appropriate atomic substitutions,

shifting its bandgap energy towards1.5 eV and 0 eV, respectively. $(Zn_{1-x}Cd_x)_3As_2$ transforms from a semiconductor to a three-dimensional Dirac semimetal as x reaches 0.62[409]. The ability to tune its direct bandgap energy makes this material system very attractive for long-wavelength optoelectronics and as a constituent in multi-junction solar cells.

$M_3^{II} X_2^{V}$ compounds crystallize in a structure akin to the anti-fluorite structure, with the difference being that 25% of the cation sites are empty. In turn, this causes a slight tetragonal distortion. Barring the minute deformation, their anion sub-lattice is face-centered cubic. Historically, the progress in the use of II-V materials has been hindered by a lack of suitable substrates matched in terms of their lattice constants and large coefficient of thermal expansion (CTE). InP and GaAs have shown to be the most suited substrates for the growth of Zn$_3$As$_2$, with lattice mismatches of 0.35% and 4% at 300 K, respectively[410]. One should note here however that using InP and GaAs defies the purpose of achieving a sustainable technology with earth abundant elements. Epitaxial thin films of Zn$_3$As$_2$ have been obtained by MOVPE[411], molecular beam epitaxy (MBE)[410] and liquid phase epitaxy[412]. In all these reports, misfit dislocations and cracks at the interface of thin films seem to be unavoidable [413]. The resulting interface defects drastically impair the electrical properties of the heterostructures.

One solution to both the lattice mismatch and CTE difference problems constitutes the use of freestanding nanostructures rather than thin films. In this case, the nanoscale contact area with the substrate allows for very efficient elastic strain relaxation[114]. Examples of heterogeneous integration of materials in the form of nanoparticles or nanowires are numerous[27, 414–416]. Until now there are only a few publications demonstrating synthesis of Zn$_3$As$_2$ and Zn$_3$P$_2$ nanostructures [406, 417–419], including simple device demonstration such as field-effect transistors and photodetectors [406].

Other kinds of free-standing structures include two-dimensional nanoscale objects such as nanosails or nanoscale membranes [177, 179, 192, 302]. Thanks to their potentially equally efficient relaxation of mismatch strain, they provide a perfect platform for the study of two-dimensional structures which are free from any dislocations or cracks. They thus provide information on the intrinsic properties of the material and a path for their realistic use in applications.

A.1.3 Materials and Methods

The Zn$_3$As$_2$ nanosails were grown by horizontal flow gold-catalysed MOVPE on a GaAs (111)B substrate by the vapour–liquid–solid (VLS) method, as in Ref [419]. The growth time was 10 min. Details of the growth are described in Appendix C.4. The morphological properties of the nanosails were characterized by scanning electron microscopy (SEM) and by atomic force microscopy (AFM). Figure A.1 shows a typical SEM picture of the as-grown sample.
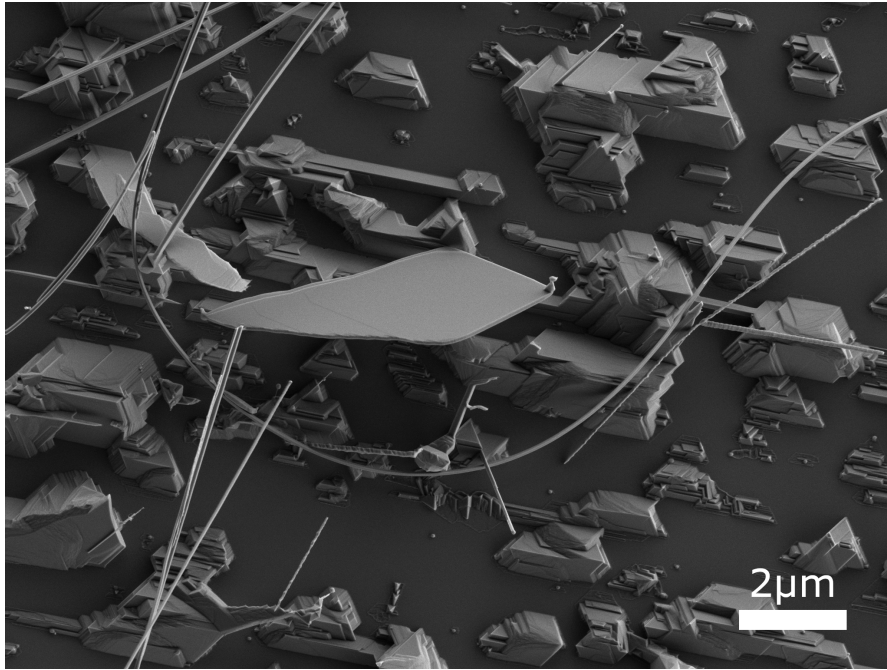
Figure A.1 – Typical top-view scanning electron microscopy image of the surface of a sample grown in the conditions described in the text. Nanosails, nanowires and gold nanoparticles can be seen.

Micro-Raman scattering measurements were performed on individual nanosails at 12 K with a single-frequency optically pumped semiconductor laser at 532 nm wavelength as an excitation source. The laser, with a power of 140 μW at the sample surface, was focused on the sample with a microscope objective ($NA = 0.75$). The polarization of the incident laser was controlled by a linear polariser. The scattered light was collected in backscattering geometry through the same objective and recorded by a TriVista triple spectrometer with gratings of 900 lines/mm, 900 lines/mm and 1800 lines/mm, respectively, and a Princeton Instruments liquid nitrogen cooled multichannel charge-coupled device (CCD) PyLoN camera.

For the device fabrication, the nanosails were detached from the growth substrate by sonication in isopropanol and drop cast onto a thermally oxidized silicon wafer. The contacts were then patterned with aligned e-beam lithography [420] followed by wet etching in a buffered hydrogen fluoride solution with one chip additionally being Ar milled in-situ before metal deposition (see Appendix C.4 for details). The contacts were then deposited by sputtering 20 nm of Cr and 150 nm of Au. The conductivity of the nanosails was measured by applying the van der Pauw method[421] while the thickness of the nanostructures was determined by AFM. The Hall mobility of the nanostructures was measured employing the same four contacts while sweeping a perpendicular magnetic field from −5-5 T.

A.1.4 Results and Discussion

Structural Properties

We start by reporting the structural properties of the nanosails. In bulk form, pure Zn$_3$As$_2$ exists in three different polymorphs named , α' and β [422]. This material can also be found in a fourth crystalline structure when 2-4% of zinc or arsenic atoms are substituted with cadmium [422] or phosphorus [423], respectively. Table A.1 lists the four polymorphs along with their characteristics in terms of symmetry, stability and number of atoms in the unit cell.

Name	Space Group	Stability in Bulk	# of atoms
α	I41cd	Stable: ~300 K	160
α'	P42/nbc	Stable: 457-945 K	160
β	Fm3m	Stable: >945 K	10
α''	P42/nmc	Metastable	40

Table A.1 – The different observed phases of Zn$_3$As$_2$, their space group, stability in the bulk and number of atoms in the unit cell.

The thermodynamically stable Zn$_3$As$_2$ phase at room temperature is the so-called α phase. At temperatures between 457 K and 945 K, typically used for growth, the α' phase with a different symmetry becomes stable. At higher temperatures, the β phase becomes stable. The loss of order of the cations increases the symmetry of this phase and makes it face-centred cubic. Pangilinan *et al.* [424] have observed a strained phase whose symmetry could not be matched with any known pure phase of Zn$_3$As$_2$. They have not identified it as such at that time but given that the symmetry of their phase matches that of the α" phase, this is the first observation of stoichiometrically pure α"-Zn$_3$As$_2$. To the best of our knowledge, this phase has otherwise never been synthesized and identified before.

Raman spectroscopy is a non-destructive technique that provides information not only on the structure, but also on the orientation and symmetry of the material. Figure A.2 shows a representative Raman spectrum of a Zn$_3$As$_2$ nanosail. The spectrum exhibits a dozen peaks separated in two sets: one at low energy ascribed to bending vibrations of the X-Zn-X systems (X = As, P) and the other at high energy, attributed to fundamental stretching vibrations of the Zn-X bonds[425]. The exact position of the deconvoluted stretching mode peaks along with their symmetry are reported in Table A.2. The bending mode peaks acquired under our measurement conditions overlap too much to be reliably deconvoluted. One peak (*) could be the reportedly anomalous peak also observed by Pangilinan *et al.* [424]. A similar Raman

spectrum to the one presented here is observed in α or α" Zn_3P_2 [426], another compound of the α"-$(Zn_{1-x}Cd_x)_3(P_{1-y}As_y)_2$ quaternary phase. This structure of the Raman spectrum is not observed in a lower symmetry phase of Zn_3As_2 such as α [427]. The Raman shift of the peaks identified in that article are listed in Table C.5 in Appendix C.4 for comparison.

In a previous study, Burgess *et al.* [419] assigned the α' phase of Zn_3As_2 to the nanosails obtained in extremely similar conditions (400 °C on GaAs(110)). The crystal structure was assigned by comparing electron diffraction patterns to simulated diffraction patterns of the α- and α'-Zn_3As_2 structures, and the latter seemed to be the most suitable. We simulated the diffraction pattern of α"-Zn_3As_2 in equivalent zone axes to compare with their experimental diffraction patterns. The zinc ordering in the α" phase does not match the crystalline structure of their nanostructures. Details of the simulation are shown in Figure C.20 of Appendix C.4.

Prior to the growth described here, the MOVPE system had been used to grow zinc phosphide on indium phosphide substrates. It is possible that there was some residual phosphorus originating from the precursor or from the substrate in the growth chamber which could have been incorporated in the nanosails. Slight phosphorous contamination is possible in MOVPE, if the system is used both for phosphides and arsenides or if the substrate contains phosphorus. This would explain the growth of the α" phase [423].

Further evidence indicating that our nanosails belong to this phase is that its crystal structure exhibits a relatively small unit cell with 40 atoms, four times less than the α and α' phases. This is consistent with the reduced number of observed first-order phonons in our structures. In conclusion, Raman spectra indicate are consistent with the crystalline phase of the nanosails being α"-Zn_3As_2.
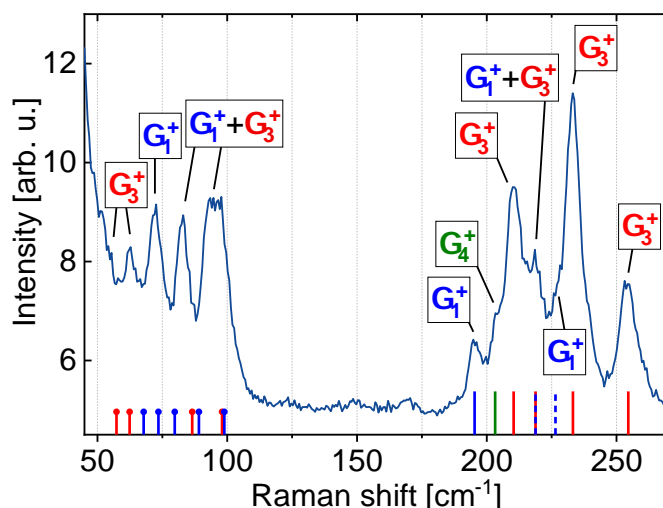
Figure A.2 – Raman spectrum of a nanosail acquired at 12 K in backscattering geometry. The incident laser light at 532 nm and at approx. 150 µW was linearly polarized along the main axis of the nanostructure while the scattered light was unpolarized.

Position	Mode Representation	Position in [424]
195.3	Γ_1^+	196.7
203.2	Γ_4^+	204.9
210.3	Γ_3^+	210.6
218.8	Γ_1^+ & Γ_3^+	215.4
226.5	Γ_1^+ (*)	225.7
233.2	Γ_3^+	232.4
254.5	Γ_3^+	252.1

Table A.2 – Deconvoluted peak positions of the high Raman shift stretching modes obtained by fitting with Lorentzians. The peak positions are matched with the corresponding peak and their symmetry determined by Pangilinan *et al.* [424].

Electrical Properties

Figure A.3a shows a nanosail device, with its four electrical contacts. The thickness of the characterized devices, determined with AFM, ranged from 80-160 nm.

We start by reporting on the temperature dependence of the electrical conductivity, between 4 K and 300 K. The measurements of three different nanosails obtained in the same batch are shown in Figure A.3b. The conductivity increases at lower temperatures. Such a behaviour is only expected in metals or in semiconductors with degenerate doping.

(a) Contacts
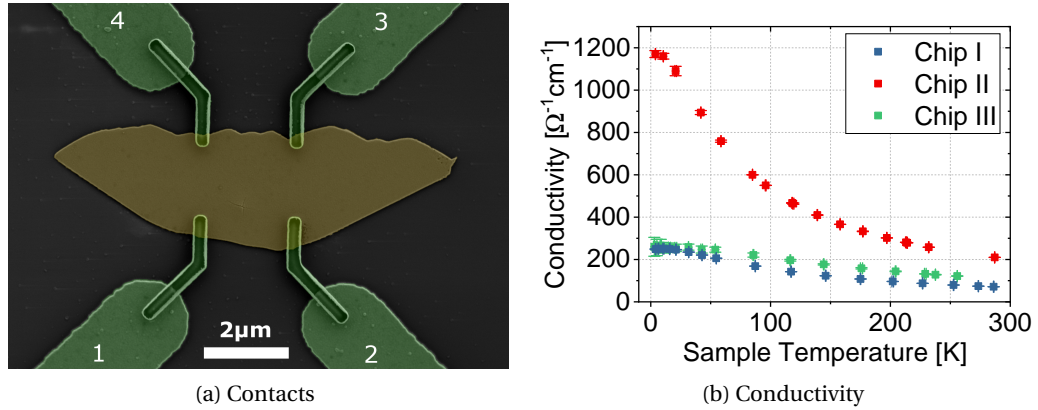
(b) Conductivity

Figure A.3 – (a) Top-view colourized SEM image of a Zn$_3$As$_2$ nanosail (yellow) and the four contacts used for electrical characterization (green). (b) Evolution of the conductivity of three nanosails with the temperature, measured with the van der Pauw method.

Figure A.4a shows an example of a typical relationship between the measured Hall voltage and the applied magnetic field. The positive slope of the curves indicates a positive Hall coefficient,

and hence confirms that the material is p-type, as reported extensively in the literature. The data follows the linear dependence of the Hall voltage as a function of the magnetic field: $V_H = IB/pte$ with a regression close to 1 ($\rho^2 = 0.9997$).

We use the conductivity measurements and the Hall voltage to determine the carrier concentration and mobility as a function of temperature. The concentration of free carriers and mobility is shown in Figure A.4b and Figure A.4c, respectively. The carrier concentration increases at high temperatures but does not freeze out at low temperatures, remaining above $4 \times 10^{18}\,\text{cm}^{-3}$.

(a) Hall Voltage

(b) Hole Concentration

(c) Hole Mobility
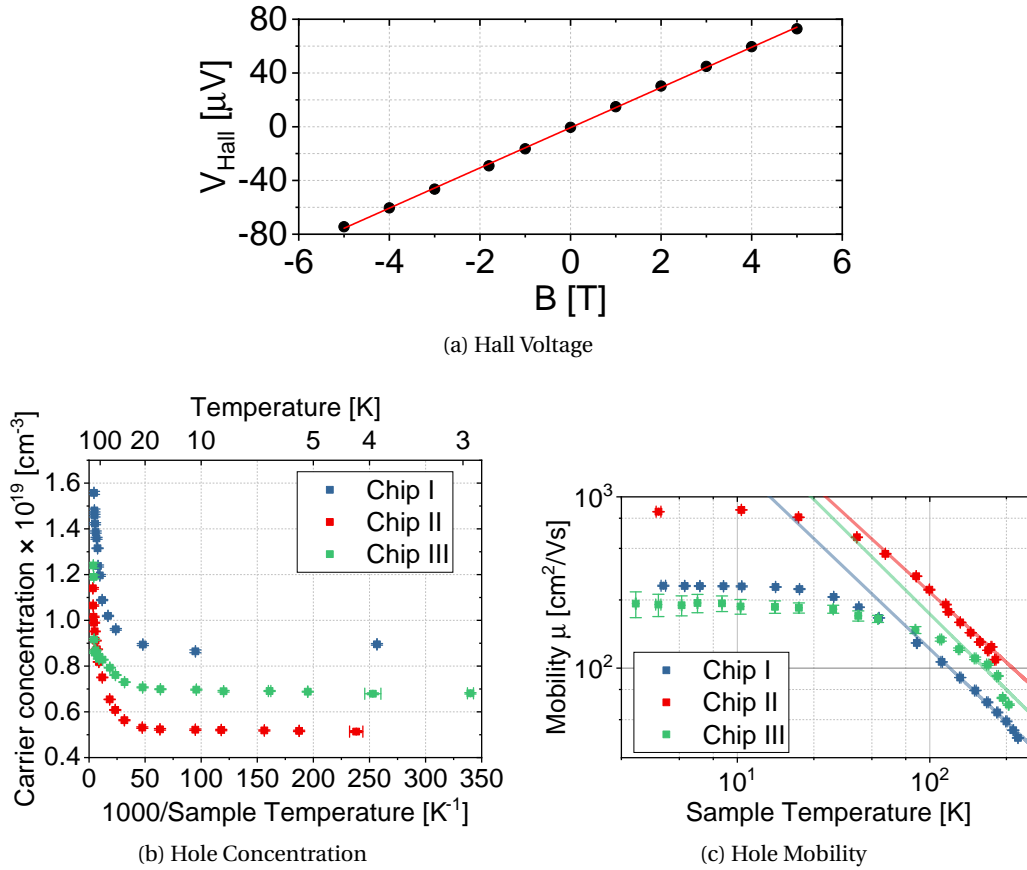
Figure A.4 – (a) Variation of the Hall voltage with the magnetic field applied on the nanosail and (in red) a linear fit to the data. (b) temperature dependence of the carrier concentration of three nanosails calculated using the measured Hall coefficients and (c) evolution of the hole mobility with the temperature (points). A fit to the linear high-temperature regime (full lines) provides the temperature dependence of lattice scattering in Zn_3As_2.

In all nanosails studied, the mobility of the carriers is constant below 10 K and decreases at higher temperatures. Linear fits to the high-energy parts of the curves reveal that the mobility is nearly proportional to the inverse of the temperature. This dependence is typical of metals and degenerate semiconductors, for which lattice vibrations are the dominant sources of

scattering above their Debye temperature.

The three nanosails characterized have qualitatively very similar properties. The most striking difference between the three is the approximately threefold increase in carrier mobility measured in Chip II compared to the other two. This, in turn, could explain most of the 4.5-fold increase in conductivity in that same nanosail. The reasons why this nanostructure exhibits increased mobility and conductivity with respect to the other two could be due to local differences of the growth conditions and environment during growth.

Overall, the electrical measurements indicate that the Zn_3As_2 nanosails are degenerately doped. Our results are consistent with some of the prior works on epitaxial Zn_3As_2 [405, 410, 428, 429]. The Zn_3As_2 material in this study is found to be unintentionally p-type. The unintentional p-doping is attributed to shallow[410] native defects [430]. Acceptor levels within a few dozen meV from the valence band maximum (VBM) have been detected in Zn_3As_2 by electrical, absorption [429], and photoluminescence [411, 431] spectroscopy measurements. Using the tight-binding method, Szatkowski and Sierański [432] calculated the energy levels of vacancies. They determined that zinc vacancies induce levels within 20 meV of the VBM. These findings are supported by density functional theory (DFT) computations of the point defect energy levels of Zn_3P_2 [433], which exhibits the same short-range order as Zn_3As_2. Finally, the presence of an impurity band (IB) in Zn_3As_2 due to the degenerate doping was proposed by Iwami *et al.* [428] and Sujak-Cyrul *et al.* [429].

The temperature dependence of the carrier concentration of our nanosails also shows two different regimes: below about 30 K, the concentration is nearly constant, and at higher temperatures, or only until about 80 K in Chip III, the concentration increases considerably. The transition temperature has been obtained by fitting the two regimes, as shown in Figure C.21 in the Appendix C.4. The constant low-temperature regime indicates that pure impurity band conduction occurs up to these temperatures, at which point thermal carrier generation initiates, leading to a further increase of the carrier concentration. The spacing between the VBM and the IB has been determined from the onset of thermal carrier generation to be 2.5 meV, a value consistent with previous observations. Whether the IB carrying the conduction carriers at the lowest temperature is degenerate with the top of the valence band or separated from it remains to be determined.

Based on the literature describing the low-temperature carrier properties of Zn_3As_2, the presence of an IB seems to be ubiquitous in this kind of material, whether synthesized by the Bridgman method[428], by resublimation [429] or pseudomorphically on InP by MBE [410].

Comparison of the conductivities measured in the different works shows striking differences. For example, Szatkowski and Sierański [432] obtained 7 S/cm at 5 K, Sujak-Cyrul *et al.* [429] 35 S/cm (calc.) at 5 K and Chelluri *et al.* [410] 220 S/cm (calc.) at 10 K. This is to be compared with our results of at least 250 S/cm at 5 K. Szatkowski and Sierański [432], reporting the lowest measured conductivity in single crystals at 5 K. This might be due to the presence of a higher density of defects associated with the growth method. Similarly, a reduction of the carrier

mobility in Zn_3As_2 thin films with decreasing material quality has been reported by [434].

Overall, the high values of mobility obtained by this work indicates the high potential of nanosails to bypass lattice and CTE mismatch challenges. In addition, we believe our results show Zn_3As_2 has excellent potential for photovoltaic applications. For this to be possible, junctions should be created by also growing n type regions or by heteroepitaxy of a second material yielding a type-II band alignment. Further work could also aim at optimizing the growth conditions to increase the yield of nanosails as in Refs. [435, 436].

In conclusion, we have shed light on the electrical properties of α''-Zn_3As_2 nanosails, whose crystalline structure has been demonstrated by polarized Raman spectroscopy. The temperature dependence of the conductivity, majority carrier concentration and carrier mobility between 4 K and 300 K are consistent with a high-quality degenerately doped p-type semiconductor. This work demonstrates the potential of Zn_3As_2 as an earth-abundant semiconductor for next generation energy harvesting or optoelectronic applications.

A.1.5   Acknowledgements

A.2   111A Nanowires by SAE

During the growth of GaAs nanomembranes (NMs) by selective-area epitaxy (SAE), it was observed that in certain cases, tilted nanowires (NWs) could be observed. Two SEM images are in given in Figure A.5.

(a) Top-view SEM   (b) Tilted SEM
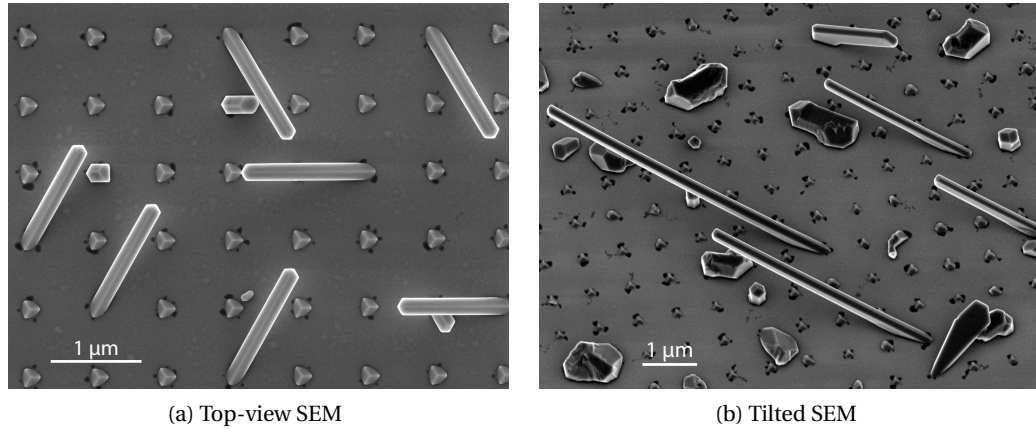
Figure A.5 – SEM images after a standard GaAs NM growth showing the appearance if (111)A oriented NWs.

The (111)A direction of the NWs was deduced by numerous measurements of the angle and faceting with respect to the growth substrate. Typically NWs prefer to grow in the (1 1 1)B direction and many studies have looked at how to encourage the growth of NWs in the (111)A direciton. The reason why this is so interesting is that while (111)B NWs often form twins, many have reported that (111)A NWs grow defect free.

transmission electron microscopy (TEM) analysis was also performed on these NWs and indeed they were also twin-free, as depicted in Figure A.6. When compared with a (1 1 1)B wire, we can clearly see that the crystal structure of the (111)A NWs have much less defects.
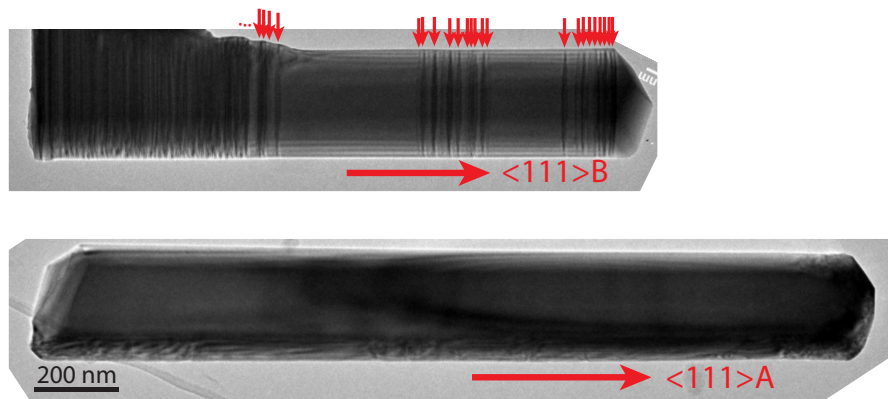
Figure A.6 – TEM image of two NWs grown by SAE on the same substrate. One was vertically-oriented and growing in the ⟨1 1 1⟩B direction (top) while the other grew tilted on the substrate in the ⟨1 1 1⟩A direction (bottom). Stacking faults are indicated by red arrows.

They were most often observed to grow by a vapour-solid growth mode, alongside the GaAs NMs, with no catalyst droplet. It was also noted that the NWs were only ever observed when

atomic layer deposition (ALD) SiO_2 masks were used instead of the typical plasma-enhanced chemical vapour deposition (PEVCD) SiO_2 masks. The reasons for this is unknown, possibly something in the way the GaAs nucleated in the ALD SiO_2 mask favoured the formation of these wires. However, significantly more investigations would be necessary to confirm this. Though this was an interesting result, despite multiple growth series and trials with different oxide patterns, the yield of the (111)A NWs could not be improved beyond a few percent. Special thanks to Eric Denervaud, Maxence Soria and Corentin Pignot who all had a role at one point or another in the pursuit to understand the formation of these NWs.

A.3 Etch Release of In(Ga)As NWs

One further experiment which was performed with In(Ga)As NWs grown on GaAs templates was to release the NWs by a selective etch of the GaAs. Selective wet chemical etching of InAs has been reported previously with good results [437–439]. Therefore, a similar approach was tried using a $NH_4OH/H_2O_2/H_2O$ etch, the results of which are shown in Figure A.7.

(a) Free etch release. (b) Etch release of contacted NWs.
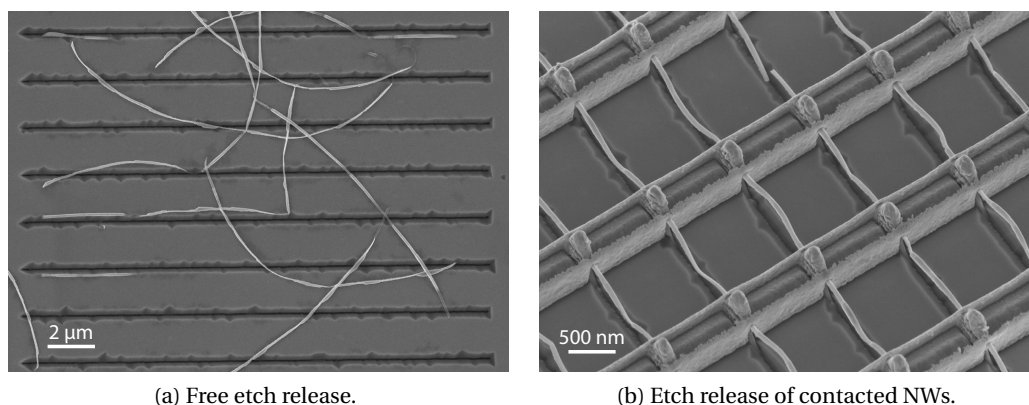
Figure A.7 – SEM images after etch release of InAs NWs grown on GaAs NMs using a selective wet etch to remove the GaAs templates below.

As seen in the SEM images, the selectivity is good enough to release multi-micron-long NWs and either deposit them on the substrate or suspend them between two contacts. In principle, this could be useful for applications requiring wrap-gating of the NWs. However, the variation in chemical composition along the length of the NW results in variable etch rates. The resulting released NWs are therefore undulating and non-uniform which is undesirable for electrical applications. Furthermore, when the template is removed, the elastic strain in the NW is removed which results in bending and bowing of the wires.

B Some Engineering

Once an engineer, always an engineer. In the hard sciences, I have experienced on more than one occasion the "that's just engineering" mindset that scientists sometimes adopt. It seems that for certain people things not directly related to scientific discovery can be seen as uninteresting or worse, as a distraction. For an engineer such as myself, such a mindset is, of course, a tremendous opportunity because it leaves many "just engineering" problems to be solved! I mean this a bit tongue-in-cheek, but in all seriousness, this PhD taught me that it is the engineering problems that keep me up at night (in a good way). I am therefore grateful for both being allowed to take the time to work on these kinds of problems and for being given free rein to poke around in the software/machinery of a system as complex as an MBE cluster.

This appendix is therefore dedicated to documenting the "just engineering" work that I did during the PhD. Though not directly scientifically-relevant to the results presented in this thesis, I felt the documentation of this work was important to both serve as a point of reference for future lab members who might make use of it and to acknowledge the significant amount of time spent on it.

B.1   Multiplexing Switch Box

When performing measurements on Zn_3P_2 nanoplatelets, described in Appendix A.1, Van der Pauw and Hall measurements were performed to measure the material's resistivity and carrier concentration, respectively. These were performed thanks to four metal contacts on each platelet. The inevitably imperfect sample and contact geometry meant that each measurement had to be repeated four consecutive times, each time permuting the contacts. The results were then processed to remove the effects of the sample/contact asymmetry to get an accurate value for the material.

These measurements were then performed as a function of temperature in a liquid helium cryostat equipped with a variable thermal insert (VTI). The measurement range was 4-300 K with a resolution of a few degrees. This meant hundreds of measurements needed to be

performed, each measurement requiring a different set of connections for the current source and nanovolt meters. Rather than do it manually, a digitally-controlled 5×5 multiplexer (MUX) box design was devised and fabricated to aid in the measurement.

In general, a grounding box serves the purpose of electrically protecting sensitive nanoscale samples whenever measurements are not being performed on them. This is achieved by grounding all the leads going to the sample. When a measurement is to be performed, the test equipment is initialized and then the grounding box serves to unground the sample and connects it to the test equipment so that the sample can be measured. The MUX, therefore, had to both multiplex the test equipment signals while also performing the task of a grounding box, all computer-controlled.

Mechanical switches such as relays are often a good bet for achieving low on-state resistances while isolating the high-frequency, high-voltage digital side of the circuit from the low-frequency, low-voltage side of the circuit. However, for sensitive samples, the possibility of switching transients due to the bouncing of mechanical contacts was to be avoided. Therefore I opted to use optocouplers instead, specifically the LBA120 and LCA120 from IXYS shown in Figure B.1.

(a) LBA120   (b) LCA120
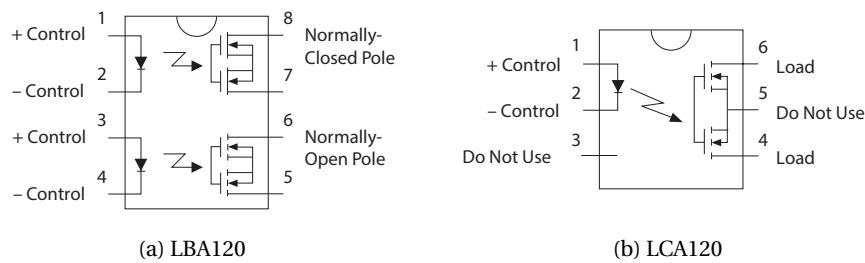
Figure B.1 – The two optocoupler chips used in the MUX box design.

Five LBA120 chips were used in place of a single pole double throw (SPDT) relay for the grounding of the sample through a $2\,\text{k}\Omega$ resistor, while 25 LCA120 chips were used as single pole single throw (SPST) switches to multiplex the signals. The control signal was to be supplied by an Arduino Mega 2560 microcontroller due to its large number of digital outputs and ease use when interfacing with a computer.

A schematic of the board is shown in Figure B.2.
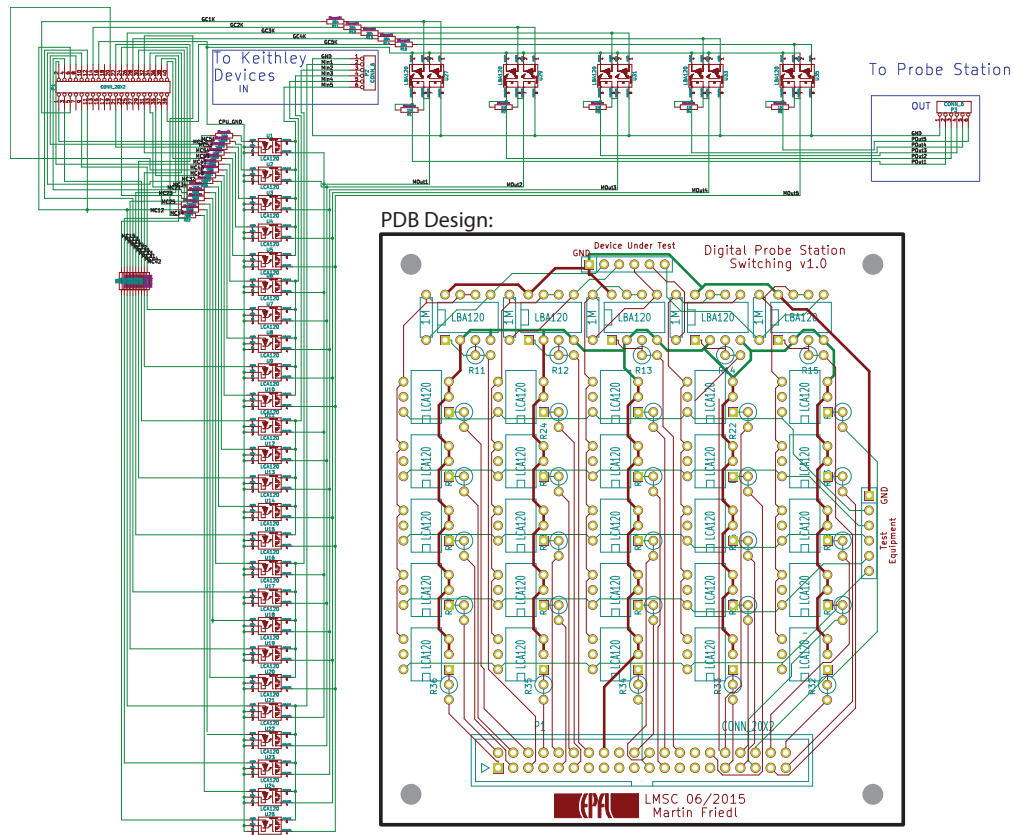
Figure B.2 – Printed circuit board (PCB) electrical schematic of the MUX circuit, with PCB layout shown in the inset.

The signal inputs and outputs were implemented via standard BNC connectors for compatibility with the rest of the lab equipment while the digital control signals were routed to the PCB via a 2x20-pin connector and ribbon cable.

In addition to the first board, a second board was designed and mounted directly on top of the first board. This one served as a light emitting diode (LED) control board which created a 25 × 25 LED matrix display, allowing the user to easily see which connections were currently active. The default state of the circuit is all LEDs off which means the sample is grounded and no MUX connections have been made. The schematic and PCB design of the second LED board are shown in Figure B.3.
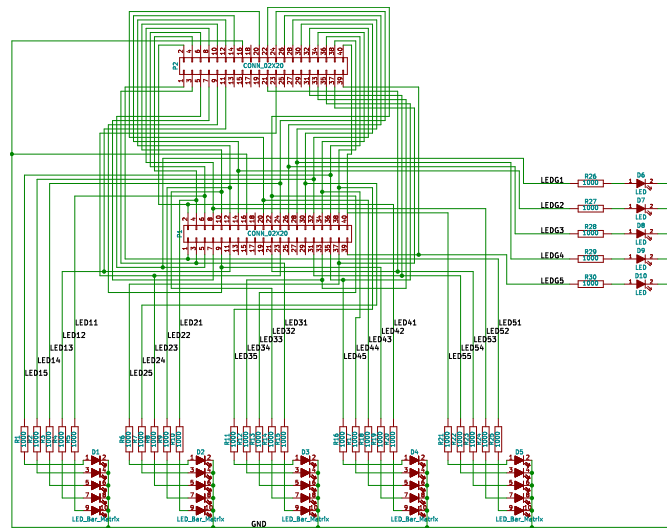
(a) Schematic
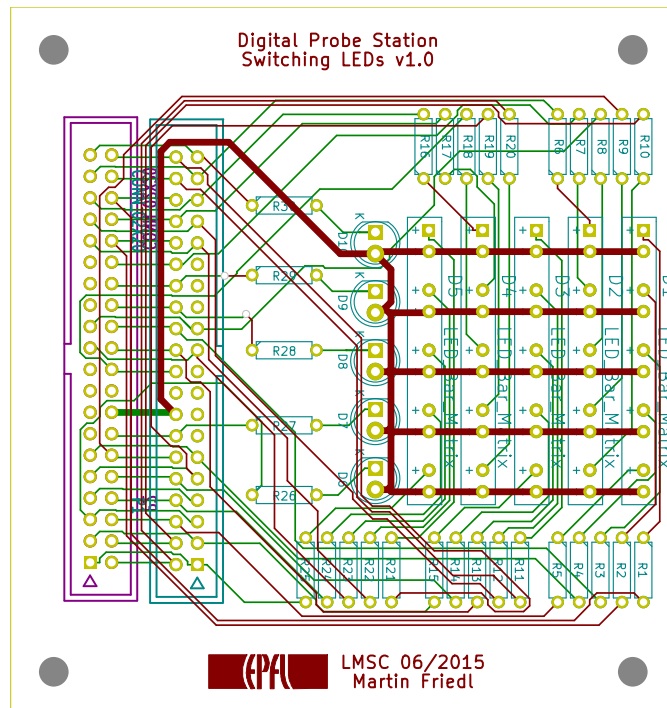
(b) PCB

Figure B.3 – Electrical schematic and PCB design of the LED portion of the MUX board.

The PCB was then mounted inside of a metal enclosure designed in SOLIDWORKS and machined to spec at the MX Workshop. The Arduino microcontroller was mounted on top of the metal case to reduce high-frequency noise on the signal lines. An image of the final resulting MUX box is shown in Figure B.4.

Figure B.4 – Image of the assembled MUX box with all connections activated.

The control of the Arduino is done by the Firmata[440] protocol and the PyFirmata library in Python. The commands are sent from Python to the Arduino simply over USB serial communication.

B.1.1 Future Improvements

A few design flaws have since been discovered in this prototype. The first issue is the fact that all BNC plugs have their shields connected to a common ground. To avoid the possibility of ground loops, one should implement the option to individually leave the shields floating if they are grounded on their other end. The second design flaw involved the connection with the Arduino Mega, hence the need for the tape in Figure B.4. As of now, it is simply done by using a ribbon cable soldered to a male pin header. However, this implementation isn't the most reliable because the pin header is quite short which means sometimes certain pins of the Arduino lose their connection to the MUX box. In the future, a more reliable connection at the Arduino should be devised, possibly by simply using longer male pins in the pin header.

B.2 MBE Web Server

The MBE is a machine that requires constant monitoring to not only diagnose potential problems quickly but also to maximize the number of samples that are grown in a day. Our

MBE has a fully-automated transfer arm and the machine itself is a 10 min walk away from the office. Therefore, most interaction with the machine for transferring samples and launching recipes is performed over remote desktop.

Though remote desktop is a very useful, full-featured interface allowing us to do everything we need as if we were in the lab, for getting information quickly it isn't the best. For getting a quick update on the current MBE status, one can imagine an improved solution which doesn't (necessarily) require user rights and is more visually appealing. An alternative was devised in the form of a web page which displays the current MBE status on the whole EPFL network.

Figure B.5 shows a diagram of the MBE room and how the computers are interconnected. For security reasons, there is an offline local network established between computer in the lab and only a single computer, called the Gateway PC, has access to both the EPFL network and the local network. Communication with the MBE control racks is performed by the MBE Server PC. Additionally, all MBE variables are logged once per second into a few uncompressed log files located on the MBE Server PC. All possible variables, including temperatures, pressures, shutters, gate-valve and interlock status are all logged.
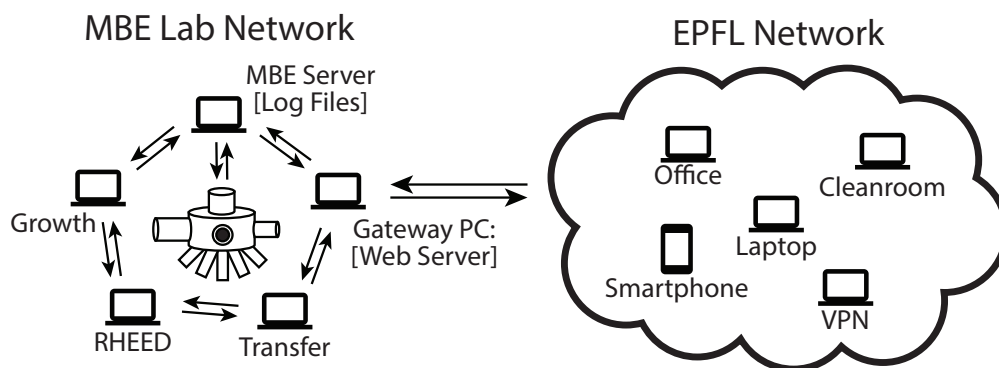
Figure B.5 – Network diagram of the MBE lab computers.

The hosting of the MBE Info web page is done on the MBE Gateway PC using Python and the Flask library. Whenever a client connects to the Gateway PC (located at http://lmscmbe) over the default HTTP port 80, the script fetches the latest data from the log file, parses it, injects it into a nicely-formatted HTML page and returns it to the client. An example of the info provided by this script is given in Figure B.6.

Remote	Power	Vacuum	Coolant	Motion	Process	Transfer Done	IGStatus
False	False	False	False	False	True	True	True

CTI-10:	Open	MBE Pressure:	1.20e-10 Torr
CTI-8	Open	BFM Pressure:	2.19e-01 Torr

Manip		SbCond		SUKO		SUSI		SbCracker		AsCracker		Al		As		Ga	
Shutter	OPEN	Shutter	CLOSED	Shutter	CLOSED	Shutter	CLOSED	Shutter		Shutter		Shutter	CLOSED	Shutter	CLOSED	Shutter	CLOSED
Temp	200.0	Temp	6.5	Temp	12.3	Temp	296.2	Temp	0.8	Temp	600.0	Temp	59.8	Temp	374.0	Temp	550.0
SetPoint	200.0	SetPoint	0.0	SetPoint	0.0	SetPoint	0.0	SetPoint	0.0	SetPoint	600.0	SetPoint	0.0	SetPoint	374.0	SetPoint	550.0
OperPoint	15.5	OperPoint	0.0	OperPoint	10.0	OperPoint	10.0	OperPoint	0.0	OperPoint	29.4	OperPoint	3.0	OperPoint	62.3	OperPoint	16.9
Mode	PID	Mode	Manual	Mode	Manual	Mode	Manual	Mode	Manual	Mode	Manual	Mode	Manual	Mode	PID	Mode	PID
Target		Target		Target		Target		Target		Target		Target		Target		Target	
T	200.0	T	0.0	T	0.0	T	0.0	T	0.0	T	600.0	T	374.0	T	374.0	T	550.0
OP	15.5	OP	0.0	OP	10.0	OP	10.0	OP	0.0	OP	29.9	OP	3.0	OP	62.7	OP	16.3
Rate		Rate		Rate		Rate		Rate		Rate		Rate		Rate		Rate	
T	100.0	T	10.0	T	0.0	T	0.0	T	0.0	T	10.0	T	0.0	T	2.0	T	40.0
OP	0.0	OP	0.0	OP	2.0	OP	2.0	OP	0.0	OP	0.0	OP	1.0	OP	0.0	OP	0.0

In		Sb	
Shutter	CLOSED	Shutter	CLOSED
Temp	515.0	Temp	15.7
SetPoint	515.0	SetPoint	0.0
OperPoint	27.3	OperPoint	3.0
Mode	PID	Mode	Manual
Target		Target	
T	515.0	T	0.0
OP	27.3	OP	3.0
Rate		Rate	
T	15.0	T	5.0
OP	0.0	OP	1.0

Pyrometer		Manipulator		Beam Flux Monitor		Viewport	
Shutter	CLOSED	RPM	0.0	Position	0.0	Shutter	CLOSED
Temp	nan° C						

As Valve	Sb Valve	Pressure Good At
0.0%	0.0%	Already good!

Timestamp: 2019-10-05 22:22:51.964847. Written by Martin Friedl. MBE Info Panel - CDC Info Panel - MBE Samples

Figure B.6 – Example of a web page served up by the MBE Info python webserver.

We can see that all essential information about the current MBE status is easily visible and colour-coded to draw attention to possible problems. This information is then accessible from any device on the EPFL campus, for our convenience. Since it serves to only monitor the equipment (and not control it), security is not considered to be a problem. Furthermore, it is important to mention that we do not consider the displayed information to be sensitive nor do we think it is useful to anybody but ourselves. Finally, this page is set to auto-refresh every 10 s making it possible to set it up on a Raspberry Pi as an always-on MBE dashboard in the office, which is how we have currently set up.

The last two features are accessed by the links at the bottom of the web page. The CDC Info link takes you to a page with all relevant information about the central distribution chamber and degassing chamber, as shown in Figure B.7.
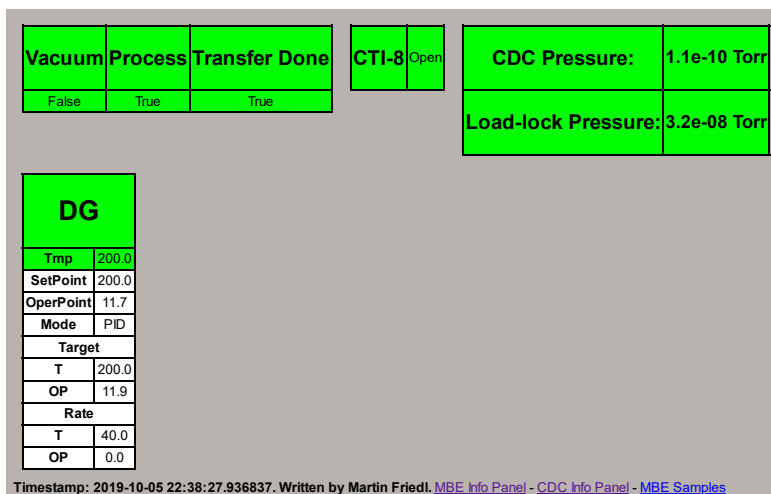
Figure B.7 – central distribution chamber (CDC) Info page for monitoring rest of MBE cluster.

The MBE Samples link displays a snapshot of the current samples loaded in the chambers of the MBE cluster and is shown in Figure B.8. A nice feature which isn't currently isn't available through any other interface (even through remote desktop) is the ability to see the list of "Today's Operations". This lets you know, at a glance, exactly what has been happening today and is very useful since we have six growers in our lab all sharing the machine.
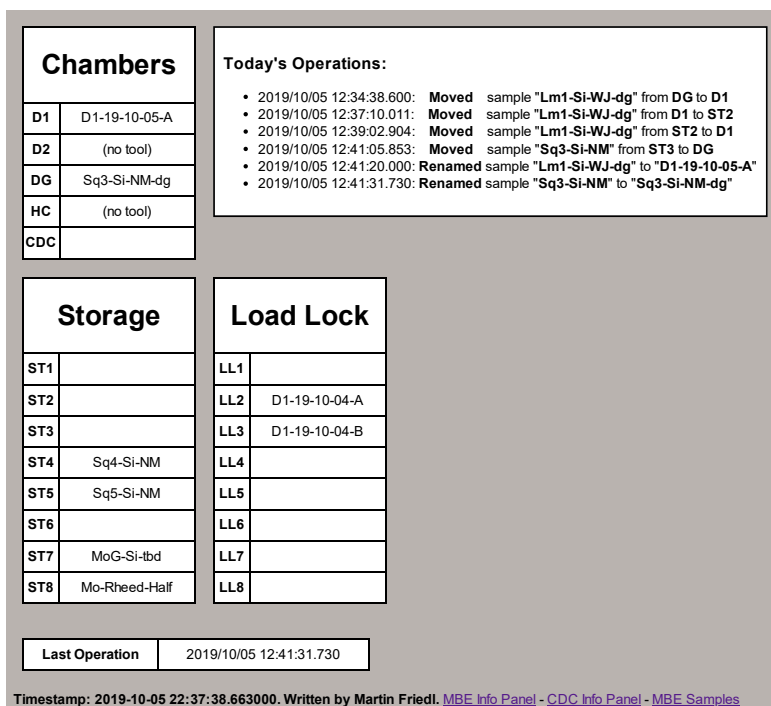
Figure B.8 – MBE Samples page for monitoring the status of samples in the machine.

B.3 Grafana Log File Viewer

Viewing and searching MBE machine logs is a tedious process. The log files are saved on a per-day basis as uncompressed ASCII files and end up being about 20 MB each. Though the PhD students that set up the system, Daniel Rüffer and Martin Heiss, did a fantastic job to make everything robust and functional, there was some room for improving user-friendliness and efficiency. I, therefore, implemented a web-based interface for viewing log file data using InfluxDB and Grafana.

InfluxDB is an open-source time-series database which is optimized for working with large amounts of data[441, 442]. It forms the back-end system which stores all of the log data, similar to an SQL database. However, unlike SQL, it is specifically meant for efficiently storing, accessing and working with time-series data.

Grafana is used as the front-end which serves as the link between the user and InfluxDB. It is an open-source analytics and monitoring software that runs on a local web server and can be interfaced with a multitude of database types[443]. It has an exhaustive list of features which include user authentication, data processing/filtering, alarms, dashboard creation, customization and integration with many external services. An example of our most frequently-used dashboard is given in Figure B.9 and credit goes to Lucas Güniat for having designed it. As an example, here we have MBE pressure in the top graph, with shaded-in portions that indicate various shutter openings. Below, another graph gives all the cell and manipulator temperatures.

The implementation of this log file interface is depicted in Figure B.10. A Grafana server is running on the Gateway PC, acting as a front end which is available to anyone on the EPFL network at http://lmscmbe:3000. Users need to authenticate themselves with a given username and password to access Grafana. When a user pulls up a dashboard, Grafana sends a query to InfluxDB to request the relevant data which then sends back the appropriate down-sampled data. Meanwhile, a Python script is running in the background and every minute it fetches, parses and uploads the last ten minutes (for redundancy) of MBE logging data. Any duplicate data is discarded and this way the InfluxDB is always kept up-to-date with the latest data.

One of the biggest advantages of using InfluxDB is that the database is continuous and transitions from one day to the next are seamless. Furthermore, where Grafana/InfluxDB excels is sampling data from a large time interval and displaying all the data effortlessly. In Figure B.11 we have an example where the MBE log data from the beginning of the year is being displayed all at once. This represents many gigabytes of data which have been down-sampled for display in the user's browser with nice navigation features like click and drag to zoom, etc. In this dataset we can easily see when the MBE was being used, when it was down for maintenance, when there were power cuts and we even see the base pressure slowly decreasing over the months after a major opening at the beginning of the year.
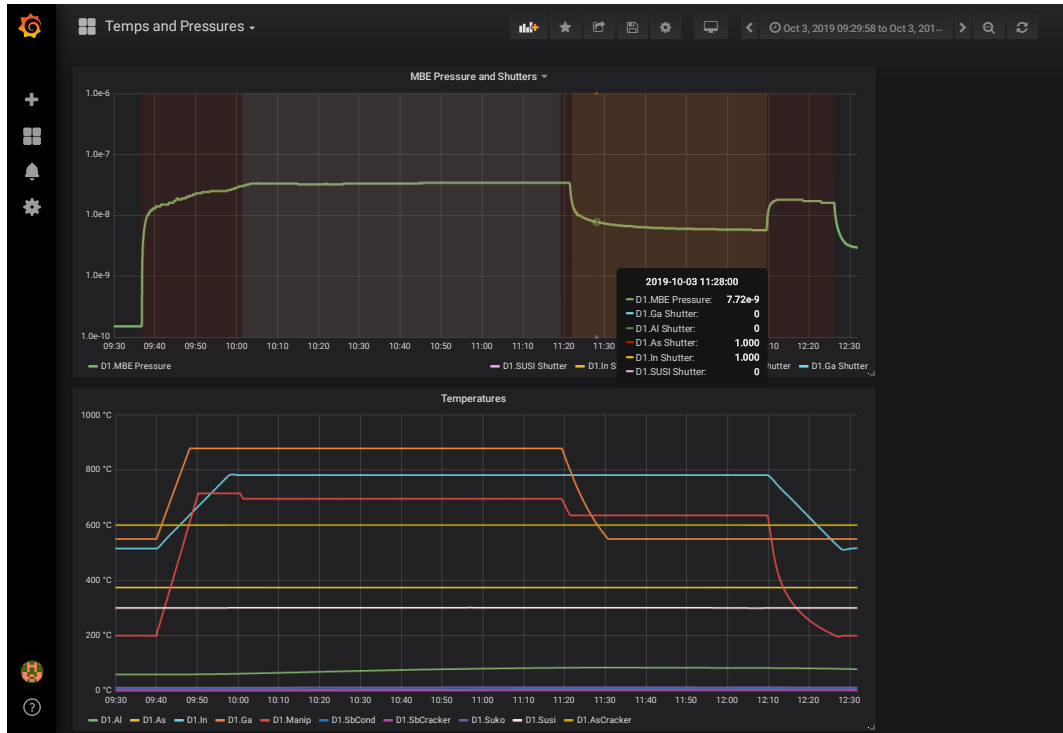
Figure B.9 – Example of a dashboard for viewing MBE log files in Grafana.
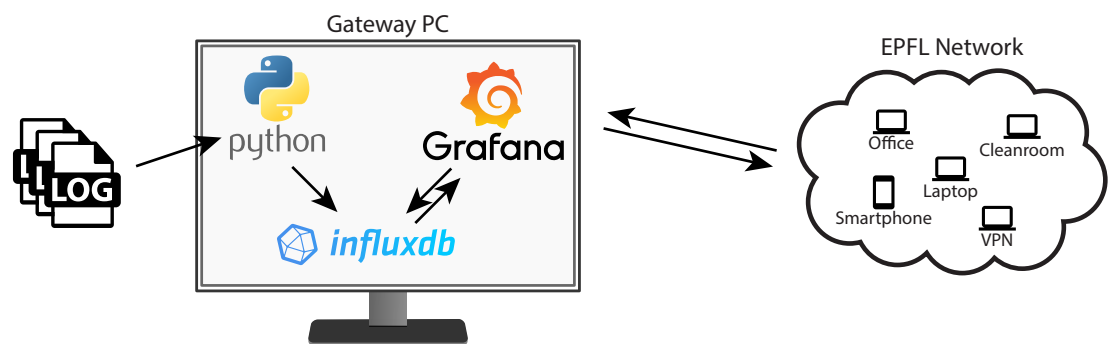
Figure B.10 – Diagram of how log files are loaded into an InfluxDB database and visualized using a Grafana-based web server.
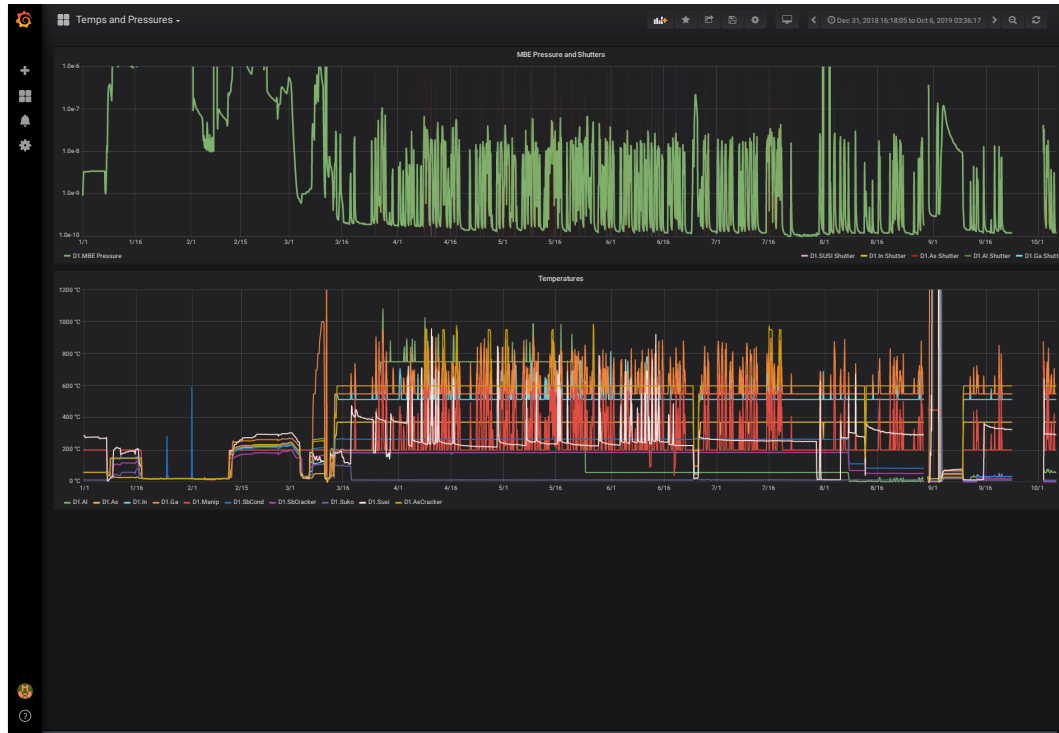
Figure B.11 – Grafana view of MBE log since the beginning of the year (2019).

Due to the sheer volume of features, there are many aspects of Grafana that I was not able to touch on, such as setting alarms and the integration with Slack or other services. However, if interested, the reader is highly recommended to read up on the many useful features of this open-source toolbox [443].

B.4 Python Scripts for MBE Growth and E-beam Pattern Generation

The last two projects I would like to document here are two Python-based projects that have been developed throughout my PhD. These were both born out of necessity for solving specific problems but in each case, they brought with them other, unforeseen advantages and benefits. This includes the benefits of getting a greater grasp of Python as a programming language. In the spirit of transparency and open-source software, both projects are made publicly available on Github at https://github.com/Martin09/E-BeamPatterns and https://github.com/Martin09/MBEToolbox under a GPL 3.0 license. A word of warning: though I did my best to document everything well, when deadlines were looming and stress was high, code readability inevitably suffered to some degree.

B.4.1 E-beam Pattern Generation

When first starting my work on (111)B GaAs growth I quickly realized that both high wafer cost and process variation could both be improved by being able to fit more growth chips on a single 2-inch GaAs wafer. To make matters worse, (111)B wafers have three-fold symmetry and therefore cleave at 60° angles. Most GDS pattern software is set up for (100) wafers which cleave at 90° angles and therefore making an optimal design for (111)B using a traditional layout editor such as L-Edit or CleWin was somewhat frustrating.

I, therefore, turned to Python and the GDSCad library with which I made all the patterns used in the PhD thesis. An example of such a pattern is shown in Figure B.12a. This meant a significant initial time investment to get things running, but it led to much better use of space on expensive GaAs wafers (costing 150 CHF each!) and smaller influence of process variation on growth because 24 chips could be obtained from a single 2-inch GaAs wafer, as shown in Figure B.12b. Also, once I started to accumulate hundreds of growth chips and was worried about potentially losing track of them, the flexibility of Python later allowed me to add unique identifiers on each fabricated chip. Now, each time a new wafer is generated, each chip is assigned a unique, 2-character, alphanumeric ID which is saved to a database. This database is linked to the parent wafer ID and thus the parent wafer of an orphaned chip can be unambiguously tracked down.

(a) E-beam Pattern   (b) Patterned Wafer
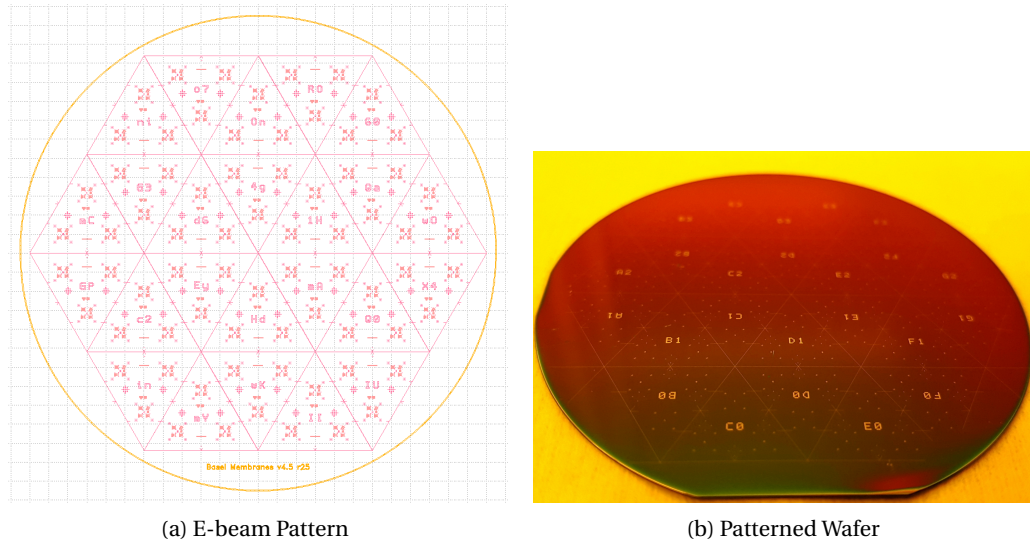
Figure B.12 – a) E-beam pattern generated using Python for a (111)B GaAs wafer. b) Example of a patterned (111)B GaAs wafer after evaporation of alignment marks.

B.4.2 MBE Recipe Toolbox

MBE growth is hard. In general, recipes can become quite complex and typically include things like flux calibrations, layer thickness calculations, unit conversions etc. Because of this complexity, I decided to forgo the established recipe client written in LabVIEW and instead built my own from scratch in Python. Again, Daniel Rüffer and Martin Heiss, did a great job writing the LabVIEW recipe client and most of the people in our lab still use it because it is user-friendly and robust. However, the desire for a more powerful recipe client led me to take another approach.

One of the main motivations for this switch was to be able to integrate calibrations automatically into a recipe. The reasoning being that, as long as the grower can specify a desired flux, then the exact temperature of a cell is irrelevant and can be handled in the background by the recipe environment. Thus, Python scripting enabled the implementation of a Calibration class which could auto-load the latest calibration file for a given cell and, when given a desired flux, automatically convert this to a cell set temperature. This simplified many recipes and allowed for easy comparison between recipes because set temperatures were not hard-coded.

A second big motivation behind moving to a Python environment was the ability to create a Virtual MBE for testing recipes. Python itself, being an interpreted language, has the disadvantage in this sort of application that if a syntax error is made 80% through a recipe, the script will crash only once it comes time to execute that line and will thus likely result in a failed growth. The virtual MBE feature was developed for this reason, and the more general reason which is that being able to perform a "dry run" and get feedback if a prototype recipe is working as expected is very valuable. Being able to run a recipe virtually means that samples

can be saved from potentially failed growths caused by untested recipes.

I, therefore, incorporated a virtual MBE server host which can be run in parallel with the real MBE server. When the user wants to test their recipe, they only need to change a variable from false to true and all of the commands get sent to the virtual MBE host server instead. After the growth is finished, the virtual MBE server outputs a log file and a PNG image summarizing the growth for the grower to consult. An example of the output from a virtual growth is given in Figure B.13.
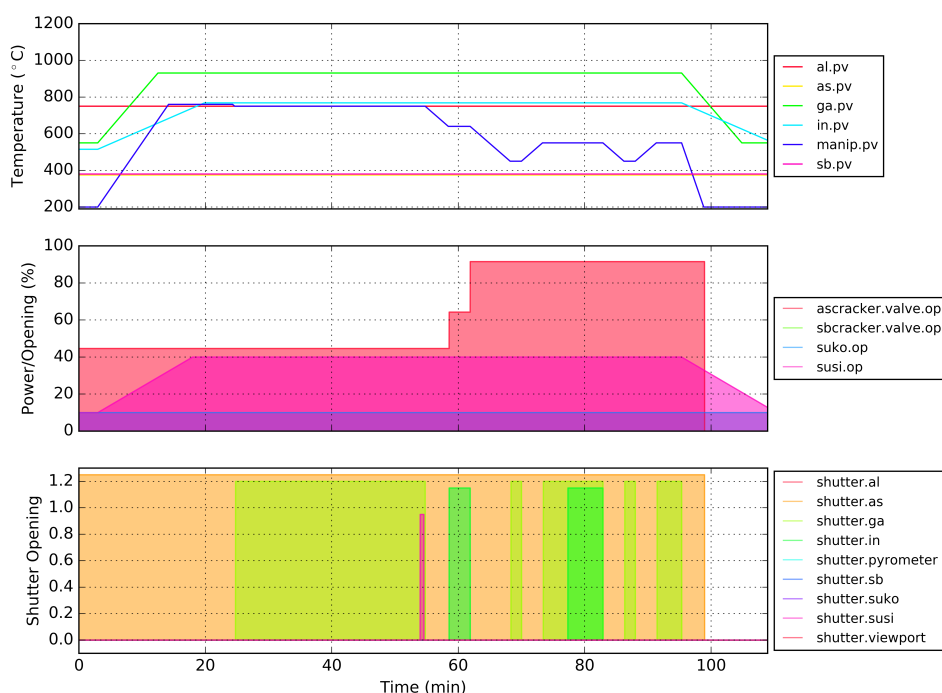
Figure B.13 – Example output from a virtual MBE growth for testing a relatively complex recipe. Credit for the recipe design goes to Didem Dede.

As mentioned previously, all the code, including all Python growth recipes used in my PhD, are made available on Github at https://github.com/Martin09/MBEToolbox.

C Paper Supplementaries

In this chapter, I have included all of the supplementary information sections to the papers included in the thesis. The formatting has been changed to match that of the current document, however, the content itself has not been modified in any way.

C.1 SI - Template-Assisted Scalable Nanowire Networks

C.1.1 Growth Details

The InAs NWs were grown by MBE on top of defect-free GaAs NMs. The growth of the NMs was performed according to an approach published previously using selective area epitaxy.1 Following the growth of the GaAs NMs at 630 °C, the substrate temperature was decreased to 540 °C and InAs was overgrown on top of the GaAs NMs. During the InAs growth, an arsenic flux of 8×10^{-6} Torr was used along with an indium rate of 0.2 Å/s. This was typically grown for 200 s, yielding a nominal deposited InAs thickness of 4 nm.

C.1.2 Temperature Dependence of InAs

As a first step during the growth optimization, two temperature series were performed. Some representative SEM images from these series are shown in Figure C.1. Here we see that at low temperatures the InAs grows as clusters on the sides/edges of the membrane rather than as a single coherent wire. This side growth is possibly due to the fact that at low temperatures the adatoms have shorter diffusion lengths and thus are not able to find the optimal (lowest energy) positions, i.e. on the vertex. As the temperature is increased, the InAs islands begin to merge and a coherent nanowire begins to form above ~530 °C.

In a second series, on a substrate with NM pitches of 1500 nm, the growth temperature was increased further to observe the limit of NW growth. At temperatures above about 550 °C, the InAs no longer grows on the NMs. The optimal growth temperature for achieving continuous coherent InAs NWs has therefore been found to be in the range of 540-550 °C.
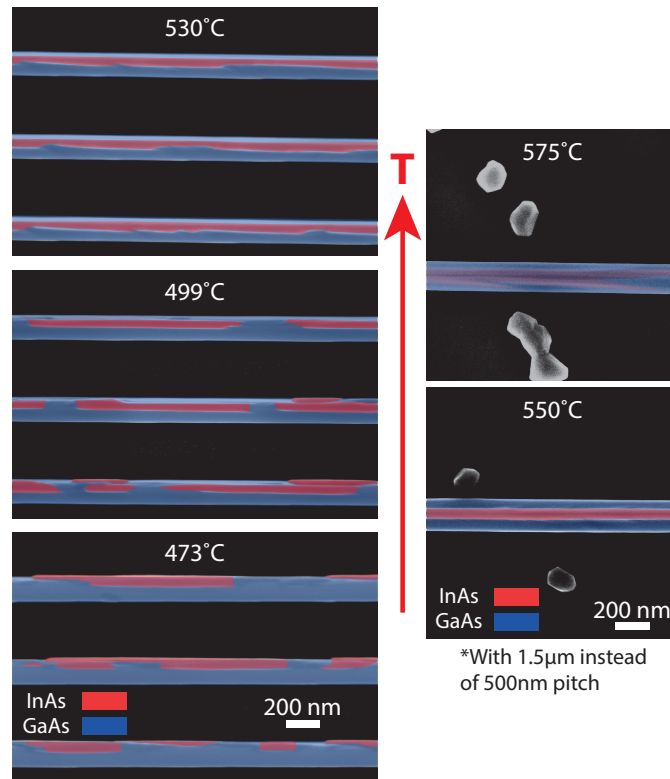
Figure C.1 – Top view SEM images showing temperature dependence of InAs growth on top of GaAs NMs. False coloured to show InAs islands as confirmed by energy-dispersive x-ray spectroscopy (EDS) measurements.

C.1.3 Width/Pitch Dependence of InAs

The influence of the GaAs NM geometry on the nanowire growth was also explored on a single substrate grown at 530 °C. This comparison is shown in Figure C.2. From this analysis we see that thinner membranes stabilize the nanowire, making it more uniform. Increasing the pitch also improves the uniformity of the InAs NWs, though this is likely due to the fact that the NMs are thinner at larger pitches. NMs at larger pitches, due to less efficient arsenic capture, grow more slowly in both height and width. The optimal NM geometry is therefore achieved at large pitches (> 1 μm) with mask openings as thin as possible in order to achieve very thin GaAs NMs. For sufficiently thin NMs, the InAs covers the whole top surface of the GaAs NM and grows as a single NW with uniform thickness.
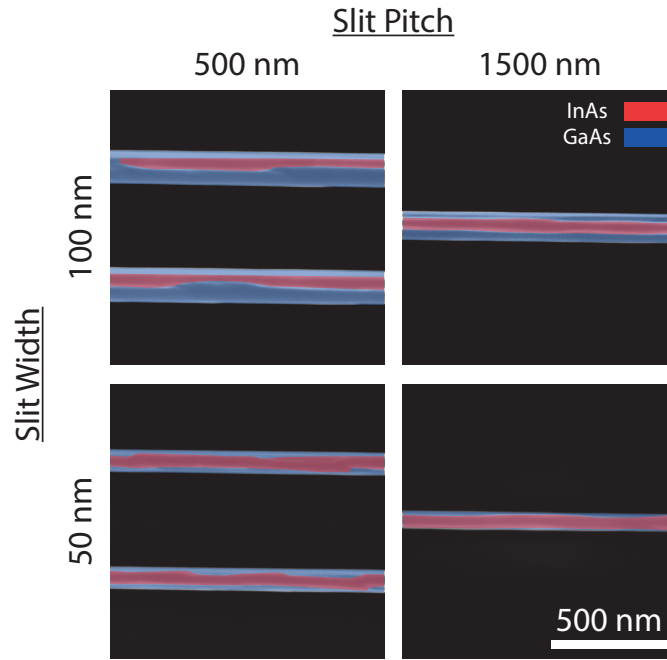
Figure C.2 – Top view, false coloured, SEM image comparison of InAs NW coverage of the GaAs NMs for various pitches and widths of the openings in the SiO$_2$ mask. The InAs/GaAs has been false coloured for visibility.

C.1.4 Raman Spectroscopy

Raman spectroscopy was performed on an InAs/GaAs device in order to measure strain. This was performed using 488 nm laser excitation at a power of 200 μW and ~1 μm spot size. A representative spectrum is shown in Figure C.3 where five main peaks can be distinguished and are summarized in Table C.1.

Here, the expected SO phonon peak was calculated assuming a cylindrical InAs nanowire with a diameter of 30 nm [444]. From Table C.1, it can be seen that most peaks are measured within ~4 cm^{-1} of the expected frequency. However, the InAs LO peak shows a significant shift
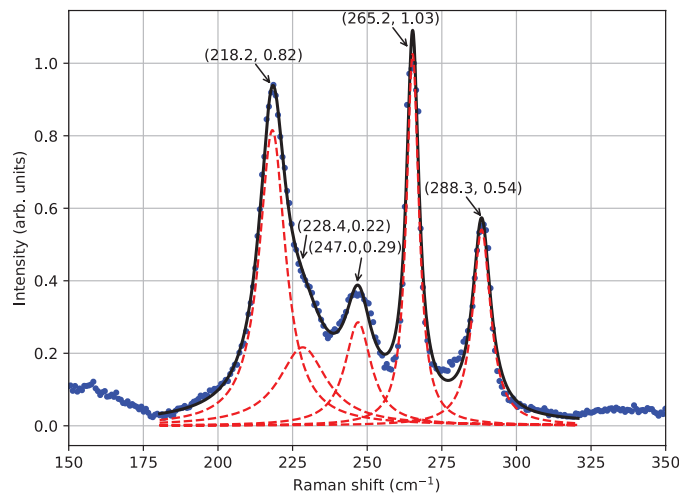
Figure C.3 – Raman spectrum of InAs NW on GaAs NM

Peak Name	Expected	Found
InAs TO	217.8/cm	218.2 cm^{-1}
InAs SO [444]	240.0 cm^{-1} (bulk) 226.6 cm^{-1} (60 nm NW)	228.4 cm^{-1}
InAs LO	233.9 cm^{-1} 240.2 cm^{-1} [445]	247.0/cm
GaAs TO	267.7 cm^{-1}	265.2 cm^{-1}
GaAs LO	291.2 cm^{-1}	288.3 cm^{-1}

Table C.1 – Table of expected and measured Raman peaks.

of ~7/cm due to strain [445]. Additionally, the shape of the LO phonon peak is broader than the expected Lorentzian fit, which we take as evidence of inhomogeneous broadening due to inhomogeneous strain that is as also seen in finite differences simulations (see Appendix C.1.5).

C.1.5 Strain Simulations

The strain and electrical properties of the InAs nanowires were simulated using nextnano[3] (v1.9.2), a Schrödinger-Poisson-current finite differences solver [446]. The simulation was set up allowing for relaxation of the structure into the air spaces around the NW/NM. An unstrained GaAs substrate was imposed on the system at the base of the simulation.

The resulting strain tensor maps are shown in Figure C.4. It can be seen that the strain in the InAs nanowire is about 2-3% on average. This agrees well with what was seen in scanning transmission electron microscopy (STEM) geometrical phase analysis (GPA) and Raman spectroscopy.

Note that, while the actual GaAs NMs are hundreds of nanometres tall, the simulations used a 50 nm-tall NM to reduce the computational expense. This approximation is justified because, as seen in the simulations, below about 30 nm from the top of the NM, there is little to no strain remaining in the GaAs NM.
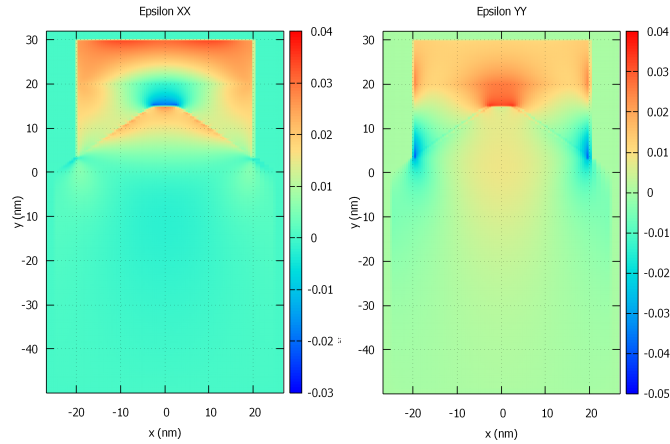
Figure C.4 – Simulations of strain tensor in x and y directions.

C.1.6 Growth Model

We provide a model to explain the preferential accumulation of InAs on the top ridge of the NW. Consider the NM/NW geometry shown in Figure C.5 in the cross-sectional view perpendicular to the NM.

We assume that the InAs NW facets are composed of vertical, horizontal and inclined facets of the (0 1 1), (1 1 1) and (1 1 3) families, respectively (see Figure C.5), and that the inclined

Appendix C. Paper Supplementaries
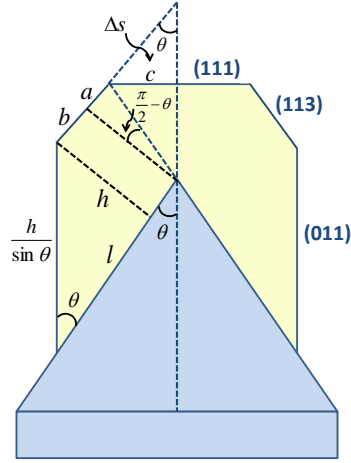
Figure C.5 – NW model geometry showing the geometrical parameters used in modelling the free energy of forming the InAs NW.

NW facets are replaced by the horizontal facets at the crossing point of the initial NM facets with the inclined NW facets, as suggested by Figure 3.2 of the main text. From geometrical considerations, we have $a = h\cot 2\theta$ and $b = l - h\cot\theta$, with θ as the taper angle of the NM, hence

$$b + a = l - h(\cot\theta - \cot 2\theta) \tag{C.1}$$

The $(1\,3\,1)$ facet of the InAs NW of width $b + a$ and surface energy $\gamma_{InAs}^{(131)}$ replaces the initial facet of the GaAs NM of width l and surface energy $\gamma_{GaAs}^{(131)}$. Additionally, the NW formation creates the InAs-GaAs interface of width l and interfacial energy $\gamma_{InAs-GaAs}^{(131)}$. We also create the vertical facet of height $h/\sin\theta$ having the surface energy $\gamma_{InAs}^{(011)}$, and the horizontal facet of width c and surface energy $\gamma_{InAs}^{(111)}$. From geometrical considerations,

$$c = h\frac{\sin\theta}{\sin 2\theta} \tag{C.2}$$

Summarizing all these surface energy terms and using $\cot 2\theta = (1/2)(\cot\theta - \tan\theta)$ and $\sin\theta = 2\sin\theta\cos\theta$ in Equation (C.1) and Equation (C.2), respectively, the surface energy change per the length $2d$ (where d is the length of the initial NM) equals,

$$\Delta F_{surf} = \left[\gamma_{InAs-GaAs}^{(131)} + \gamma_{InAs}^{(131)} - \gamma_{GaAs}^{(131)}\right] l + \left[\frac{\gamma_{InAs}^{(011)}}{\sin\theta} - \frac{1}{2}\gamma_{InAs}^{(131)}(\tan\theta + \cot\theta) + \frac{\gamma_{InAs}^{(111)}}{2\cos\theta}\right] h \quad (C.3)$$

Grouping the bracket into C_1 and C_2, we can write

$$F = C_1 l + C_2 h \tag{C.4}$$

Clearly, the C_1 term gives the surface energy change in the $\langle 1\,3\,1 \rangle$ direction and is positive in the non-wetting and negative in the wetting cases, respectively. The C_2 term should always be positive and is associated with the InAs facets in contact with the vapour. The surface area of half the NW cross-section s equals the area of the parallelogram lh minus the area of the upper triangle Δs. The latter is given by $h^2/(8\sin\theta\cos\theta)$, Therefore,

$$s = lh - \frac{h^2}{8\sin\theta\cos\theta} \tag{C.5}$$

where the second term is less than 10% of the first one in our geometry and can be neglected in the first approximation.

To account for the effect of the strain relaxation, we use the simplest formula [114, 447, 448],

$$\Delta G_{elastic} = \lambda \epsilon^2 V \frac{1}{1 + \alpha h/l} \tag{C.6}$$

showing that the elastic energy (for the reduced strain ϵ due to dislocations) rapidly decreases ($\alpha \gg 1$) with increasing the aspect ratio h/l with respect to the two-dimensional (2D) film of the same volume V. Using $V \approx 2dlh$ and dividing it to the facet length $2d$, we arrive at the equation expressing the free energy of forming the InAs NW of width l and height h on top of the GaAs NM,

$$\Delta F(l, h) = C_1 l + C_2 h + \frac{C_3 lh}{l + \alpha h/l} \tag{C.7}$$

This free energy is defined per unit length of the structure. The C_1 term gives the surface energy change upon covering the GaAs $(1\,3\,1)$ facets with InAs, and is proportional to the NW width l. The C_2 term ($C_2 > 0$) stands for the surface energy of all other InAs facets, and is proportional to the NW height h. The last term gives the elastic energy of the InAs NW, proportional to the NW cross-sectional area $s \approx lh$, with C_3 being the elastic energy per unit volume for the reduced mismatch [114], and α describing the stress relaxation with the aspect ratio h/l [114, 447, 448]. In fact, the NW cross-sectional area s equals $lh - \epsilon h^2$ due to the development of the horizontal $(1\,1\,1)$ InAs top facet seen in Figure 3.2 of the main text, but the ϵh^2 term is typically less than 10% and we omit it to simplify the analysis. We also assume that the term associated with the dislocation energy is roughly the same for any aspect ratio, which should be valid for large enough volumes of deposited InAs with the NW heights already well above the critical thickness for forming misfit dislocations (~1.2 nm) [447].
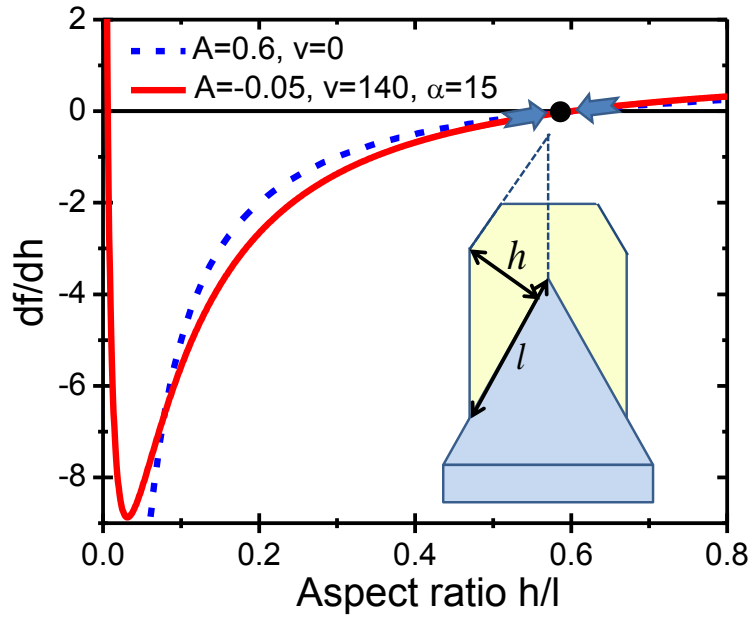
Figure C.6 – Change in free energy of formation with aspect ratio. Graphs of the df/dh versus the aspect ratio obtained in the non-wetting ($A > 0$) and wetting ($A < 0$) cases from Equation (C.8). The zero point at $h/l \approx 0.6$ corresponds to the minimum free energy of forming the NW, because its derivative is negative for smaller and positive for larger aspect ratios. The real curve is expected to be the one in the wetting case, where the system surpasses an energetic barrier at a small x as in the Stranski-Krastanow growth. The value of $v = 140$ corresponds to the parameters of InAs with the reduced mismatch $\epsilon = 0.03$. The insert shows the geometry, the approximation $s \approx lh$ used in the calculations neglects the truncation of the full parallelogram in the top part of the NW.

To access the preferred shape of InAs on top of GaAs, we minimize Equation (C.7) at a fixed $s = lh$, corresponding to a fixed volume of deposited InAs [449]. Introducing $f = \Delta F / b$ the result is given by

$$\frac{df}{dh} = 1 - \frac{A}{x} - \frac{v x^{1/2}}{(1 + \alpha x)^2} \tag{C.8}$$

with $A = C_1/C_2$ as the normalized surface energy change in the (1 3 1) plane, $v = 2\alpha C_3 s^{1/2}/b$ as the strain-induced factor that increases with the amount of deposited InAs and $x = l/h$ as the aspect ratio of the NW. The preferred aspect ratio is now defined by the stable zero point of df/dh corresponding to the minimum free energy.

Figure C.6 shows two possible cases with the preferred $x \approx 0.6$, as observed in Figure 3.2 of the main text. Of course, the three-dimensional (3D) geometry will occur in the non-wetting case with $A > 0$ even without any lattice mismatch, because the surface energy minimization leads to a reduction of the energetically-costly InAs-GaAs interface [448]. This is shown by the dashed curve in Figure C.6. We believe, however, that our GaAs/InAs system is initially wetting, that is, the surface energy favours 2D growth of InAs on GaAs, while 3D structures emerge only after the formation of a continuous wetting layer, as in the Stranski-Krastanow growth [448]. Therefore, the system is described by the solid line in Figure C.6. In this case, reaching a high aspect ratio on the order of 0.6, which is necessary to form the NWs on top of the NMs, can only be due to strain relaxation and requires a high value of the strain-induced v factor of about 140. The c coefficient equals $\lambda \epsilon^2$, with $\lambda = 1.22 \times 10^{11}$ J/m^3 as the elastic modulus of InAs and ϵ as the reduced lattice mismatch. With the experimentally-observed $\epsilon = 0.03$, this yields $v = 140$ at $\alpha = 15$ [447] for a plausible value of $C_2 = 0.091$ J/m^2.

C.1.7   TEM Compositional Line Scan

Looking at the electron energy loss spectroscopy (EELS) maps in more detail, a compositional map and line scan are shown in Figure C.8 and Figure C.7, respectively.
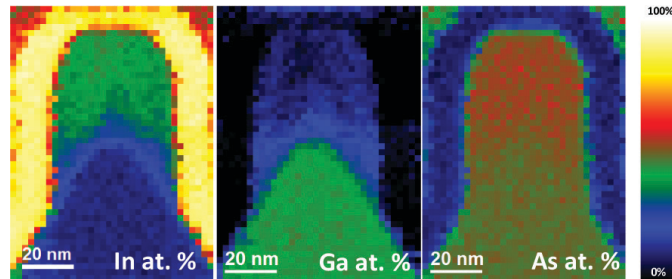
Figure C.7 – Compositional maps of InAs nanowire on GaAs NMs for In, Ga and As separately.

From the line scan, we first notice that the amount of indium in the GaAs region and gallium in the InAs region never goes below 10%. This is suspicious and is likely an artefact of the
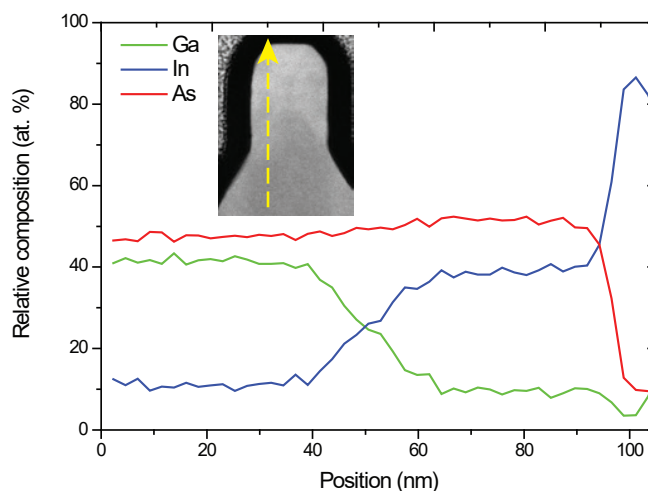
Figure C.8 – Compositional line scan from the GaAs NM into the InAs NW showing relative concentrations of Ga, In and As.

EELS measurement, possibly caused by indium/gallium adatom migration induced by the 200 keV electron beam. An additional contributor to the indium signal could be the titanium in the titanium dioxide capping layer. The two elements are difficult to differentiate as the titanium $L_{2,3}$ EELS edges overlap with the indium $M_{4,5}$ edges.

The scan also shows a region between about 40 nm and 60 nm where gallium is present in the InAs nanowire. atom probe tomography (APT) measurements have ruled out Ga cation diffusion during the focused ion beam (FIB) preparation process. Due to the 100 °C difference in growth temperature between the GaAs and InAs, and the necessary cool-down period between the two growths, we do not expect any free gallium adatoms on the surface to contribute to the formation of this InGaAs region. Rather, it is likely that stress drives diffusion of some gallium atoms from the NM into the InAs NW during NW growth to accommodate the high lattice mismatch. This observation suggests such strain might be used to overcome the miscibility gap that is present in unstrained $In_xGa_{(1-x)}As$ below about 800 K [450, 451].

C.1.8   InAs Crystal Quality

The crystal quality of the InAs NW was further assessed by TEM imaging from the side of a GaAs/InAs NM/NW structure. Figure C.9 (a) provides an example atomic resolution annular dark-field (ADF)-STEM analysis from a roughly 70×70 nm^2 region near the base of the InAs NW. GPA of $(\overline{1}\,\overline{1}\,\overline{1})$ dilatation (Figure C.9 (b)) reveals the presence of a double twin that appears to originate at the InAs/GaAs interface and propagates through the InAs layer.

The GPA structural map of the (-1-11) planes in Figure C.9 (c) allows us to identify misfit dislocations, highlighted in red. Figure C.9 (d) applies a rotation filter that further highlights these misfit dislocations. The appearance of misfit dislocations in the axial direction, along the

nanowire, is expected because the strain cannot be as easily relaxed as in the radial case. This is believed to be the reason that no misfit dislocations were observed in the transversal atomic resolution ADF-STEM cross sections. On the other hand, in the longitudinal cross section, one can count seven misfit dislocations in this roughly 70 nm-long region. Using this value as an initial guess, we estimate that this structure has on the order of 100 misfit dislocations per micrometre.
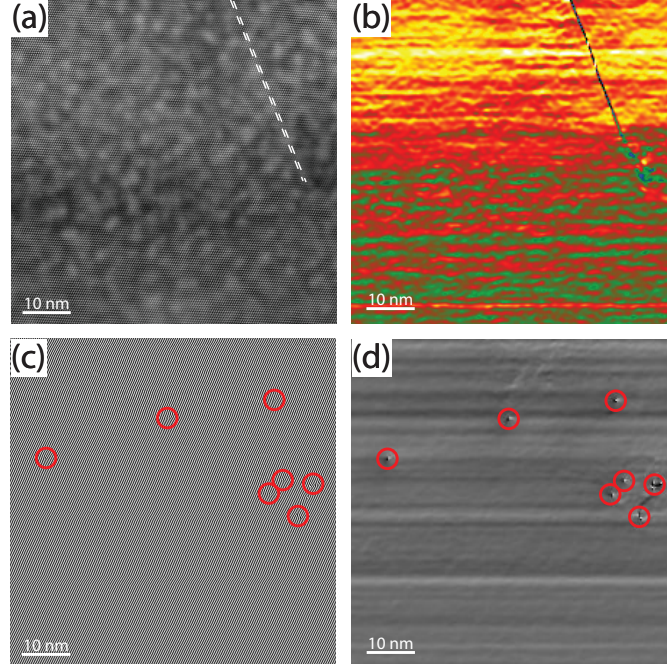
Figure C.9 – a) Atomic resolution ADF-STEM image taken from a ⟨011⟩ zone axis at the base of the InAs NW on a GaAs NM showing two twins originating at the heterojunction and propagating into the InAs nanowire. b) GPA analysis of image a looking at dilation of (111) planes. Here the twin is clearly visible and the colour contrast enables us to distinguish the InAs from the GaAs region. c) Structural map of (111) planes in image a allowing us to see the presence of misfit dislocations highlighted in red. d) Rotation filter of (111) planes from image a allowing us to better distinguish misfit dislocations.

C.1.9 Magnetotransport Model

The conductivity dependence on magnetic field was fit with the following weak localization model for the quantum correction to the classical conductivity in the quasi one-dimensional (1D) diffusive limit: [94, 237, 309]

$$\Delta G = \frac{2e^2}{hL} \left(\frac{1}{l_\phi^2} + \frac{1}{l_B^2} \right)^{-\frac{1}{2}}$$

where L is the length of the wire between contacts, l_ϕ the phase coherence length, and l_B the

magnetic dephasing length. l_B relates to the magnetic relaxation time τ_B as

$$l_B = \sqrt{D\tau_B},$$

with $D = v_F l_e$ for 1D wires. In our system, in the so-called diffusive limit, where $l_e << W$, with W the conducting channel width, and $W << l_\phi$, τ_B is given as

$$\tau_B = \frac{3l_m^4}{W^2 D},$$

where $l_m = \sqrt{\hbar/eB}$. This regime constrains l_e to maximally a few nanometres, which is in good agreement with the expected spacing between dopants. We estimate from a 3D doping concentration of 1×10^{27} m^{-3} a 1D concentration of 1×10^9/m, thus one dopant every couple of nanometres. The fits for the data yielded the values shown in the following table for l_ϕ in this limit.

Bias (mV)	l_ϕ (nm)	Error (nm)
0	134	4
5	97	2
10	84	2
15	73	2
20	66	2

The accuracy of the fits for l_ϕ in this diffusive limit need to be taken with a degree of caution. When spin-orbit length l_{so} and mean free path l_e are included into the formalism, one has [94]

$$\Delta G = -\frac{e^2}{hL}\left[3\left(\frac{1}{l_\phi^2} + \frac{4}{3l_{so}^2} + \frac{1}{l_B^2}\right)^{-\frac{1}{2}} - \left(\frac{1}{l_\phi^2} + \frac{1}{l_B^2}\right)^{-\frac{1}{2}} - 3\left(\frac{1}{l_\phi^2} + \frac{4}{3l_{so}^2} + \frac{1}{l_e^2} + \frac{1}{l_B^2}\right)^{-\frac{1}{2}} + \left(\frac{1}{l_\phi^2} + \frac{1}{l_e^2} + \frac{1}{l_B^2}\right)^{-\frac{1}{2}} \right]$$

The data was fit for a range of values for l_{so}, which result in slightly varying l_ϕ between 130 nm and 160 nm nm that quickly fall off with addition of voltage bias. When $l_{so} \to \infty$ the diffusive limit is recovered, as expected. The spin-orbit strength extracted from these fits is somewhat weaker, corresponding to larger spin-orbit lengths than otherwise known from InAs [90, 452]. This is likely due to the gallium content in the wires as well as could be due to motional narrowing in the diffusive limit with a mean free path of only a few nanometres. The complete lack of weak anti-localization in the data is consistent with very weak spin-orbit interaction, thus large l_{so}. A 2D conductance map is shown in Figure C.10 which shows the dependence of conductivity on both magnetic field and applied DC bias.
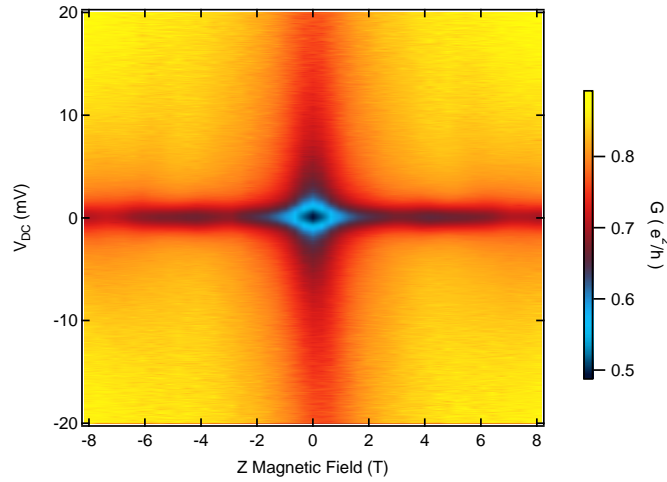
Figure C.10 – Conductivity map as a function of magnetic field and bias voltage. Colour scaling is differential conductance in units of e^2/h. The decrease in conductance around zero magnetic field is clearly manifested.

C.1.10 APT Mass Spectra
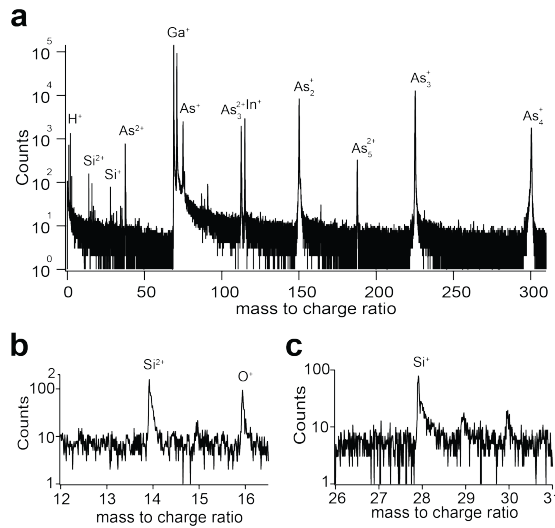
Figure C.11 – APT mass spectra. a) Mass spectrum of an InAs NW on a GaAs NM for the APT reconstruction shown in Figure 3.2 (g) and (h) in the main text. The acquisition conditions are described in the Methods section of the main text. b), c) Regions from the spectrum in a showing $^{14}Si^{2+}$ and $^{28}Si^+$ peaks, respectively. Peaks at m/q = 14, 14.5, 29 and 30, which include counts from Si isotopes, were not included in the reconstruction shown in Figure 3.2 (h) due to overlap with other unidentified species.

C.2 SI - Remote-Doping of Template-Assisted InGaAs Nanowire Networks

C.2.1 Finite Element Simulations of Doping

1D finite element simulations were performed using the nextnano software package [446] to simulate the band structure and carrier concentration of remote-doped template-assisted NW structures. A simulation of a GaAs NM with either a pure InAs NW or intermixed $In_{0.5}Ga_{0.5}As$ NW on top was performed, as shown in Figure C.12.

(a) Undoped InAs NW   (b) Undoped $In_{0.5}Ga_{0.5}As$ NW
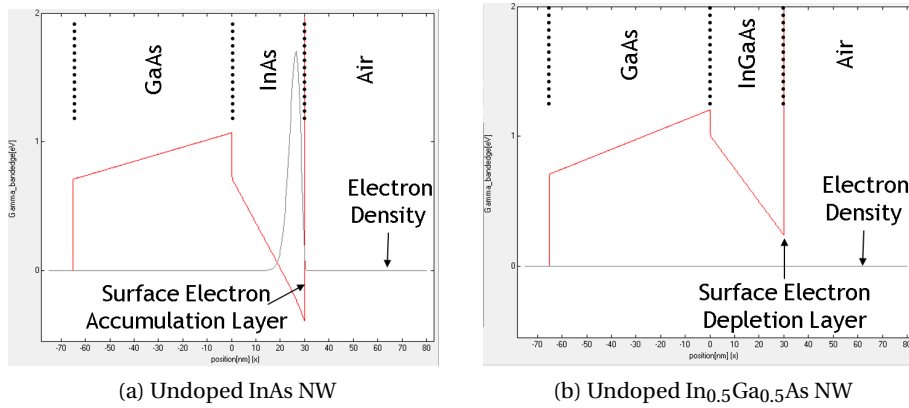
Figure C.12 – Finite element simulations showing the conduction band (red) and electron concentrations (grey) in undoped InAs (a) and $In_{0.5}Ga_{0.5}As$ (b) NWs.

Here, Fermi level pinning in the conduction band was assumed for the InAs NW, resulting in a large electron concentration near the surface of the NW. The Fermi level pinning was simulated by implementing a donor surface charge density of 2.5×10^{12} cm^{-2}. In contrast, the InGaAs NW has no free electrons in the conduction band due to the lack of Fermi level pinning.

A 10 nm-thick modulation-doped layer was then inserted into the structure 20 nm below the InGaAs NW. A dopant concentration of 1×10^{19} cm^{-3} was assumed. The result of this simulation is given in Figure C.13.
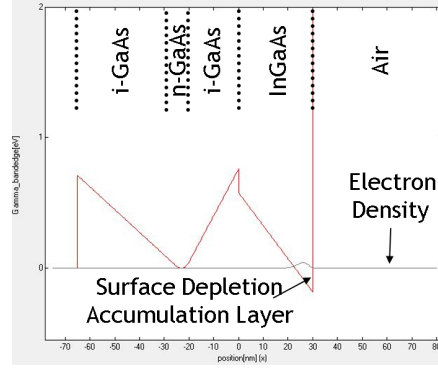
Figure C.13 – Finite element simulation of a modulation-doped $In_{0.5}Ga_{0.5}As$ NW showing the conduction band (red) and electron concentrations (grey). We see a maximum in the electron concentration now that appears in the InGaAs NW that appears due to the modulation-doped structure.

The addition of the remote doping layer does have an impact on the overall electron concentration in the NW. We now get a small peak in the electron density of 4×10^{16} cm^{-3}. This basic simulation is sufficient as a proof of concept, however, more in-depth studies will be performed in the future to more accurately model the electron concentration in the NW once the exact dopant profile in the structure is known.

C.2.2 X-ray Fluorescence Mapping

To get a better understanding of the uniformity of the NWs, specifically in the Y-junction devices, x-ray fluorescence (XRF) mapping was performed at the European Synchrotron Radiation Facility (ESRF) by Jaime Segura-Ruiz. Figure C.14 gives an example of two measurements performed on InGaAs Y-branch structures. We can see In K_α signal is relatively uniform across the junction for Figure C.14a. However, in the opposite orientation shown in Figure C.14a, both the SEM image and the In K_α signal show a large degree of non-uniformity across the junction.

(a) Good orientation
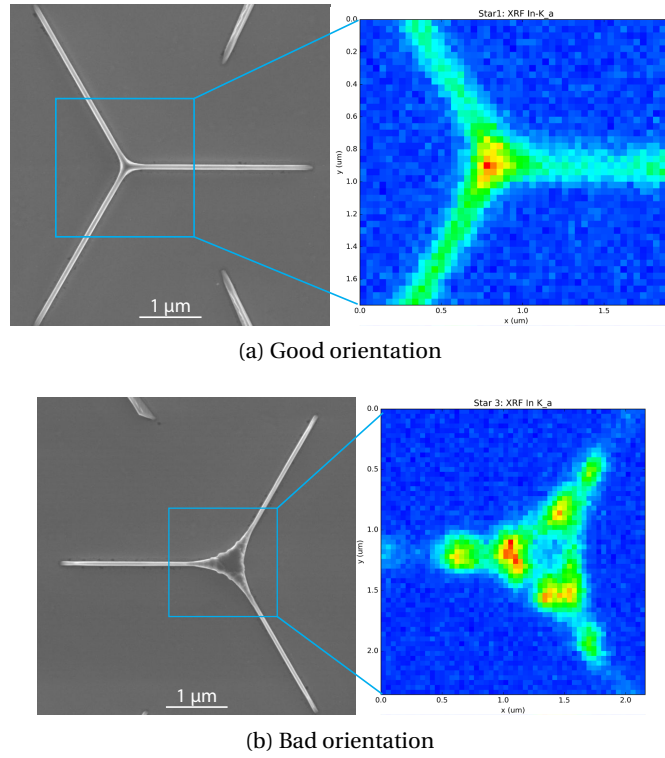
(b) Bad orientation

Figure C.14 – SEM images (left) combined with XRF maps of the In K_α signal (right) of InGaAs Y-branch structures in both the favourable intersection orientation (a) and unfavourable orientation (b).

There measurements were performed at the ID16B beamline at ESRF with a beam size of 52×56 nm and a beam energy of 29.8 keV.

C.3   SI - GaAs Nanoscale Membranes: Prospects for Seamless Integration of III-Vs on Silicon

C.3.1   EELS maps showing material diffusing on top of GaAs cap of passivated NMs

EELS spectrum images were acquired in a TECNAI F20 microscope operated at 200 kV with an energy resolution of 2 eV (full width at half maximum (FWHM)). Signal integration was performed after power law background extraction using Ga $L_{3,2}$, As $L_{3,2}$ Al K and Si K major edges.

Figure C.15 shows elemental composition mapping of main components in NM A. We observe a homogeneous elemental distribution of Ga and As along the NM and no Si diffusion into the membrane. We observe homogeneous distribution of Al in the NM from this view due to the presence of the {1 1 0} front and back facets. However, the areal density is not homogeneous at
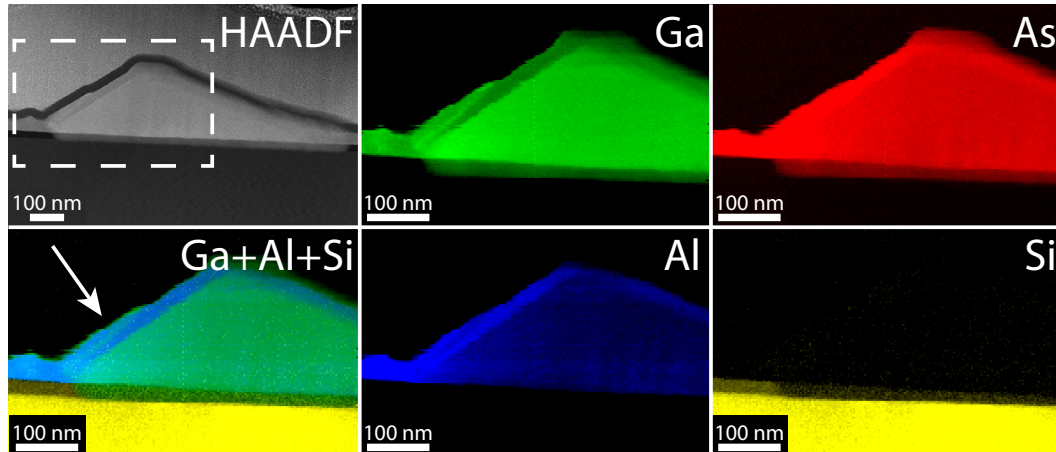
Figure C.15 – Elemental maps of Ga, As, Al and Si obtained through STEM EELS in the indicated area of the high-angle annular dark-field (HAADF) micrograph.

the edges of the membrane, instead getting higher on the short edge.

The AlGaAs shell is covered by a GaAs layer to prevent it from oxidizing. However, we can see that a thin AlGaAs layer is covering the most external GaAs layer in the region close to the intersection between the NM base and its back facet (marked by an arrow in the image). As this layer is formed once the flux of atoms (Ga and As) are closed, it indicates that there might be some diffusion of material from the irregular AlGaAs layer that covers the substrate to the NM itself.

C.3.2 HAADF/MAADF images on other defective areas

High-resolution medium-angle annular dark-field (MAADF) and HAADF images of defects are shown in Figure C.16.

The accumulation of strain is revealed by the higher intensity shown by these defects in the MAADF images. These defects are formed when twin boundaries in different directions match together.

C.3.3 Strain maps

We have performed strain maps from the HAADF high-resolution micrographs. By comparing the measured values of dilatation with the lattice mismatch between Si and relaxed GaAs we can evaluate strain relaxation in the membrane. An example of strain maps at the Si-GaAs interface close to vertices between the NM and the substrate are shown in Figure C.17. We observe a compression in GaAs lattice in the first 20 nm, which correspond to the region where the substrate is covered by the SiO_2 mask. Once the material is not constrained by the mask, it gets fully relaxed. Additionally, a slight rotation of the planes is observed (approx.
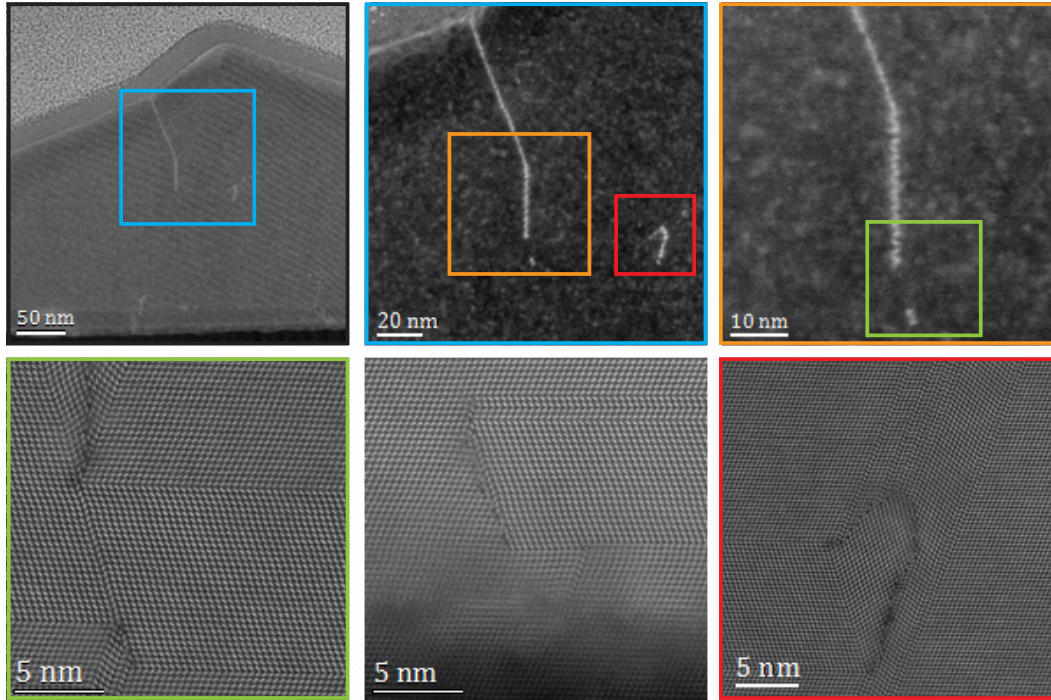
Figure C.16 – MAADF (top) and HAADF (bottom) micrographs obtained on defective areas of NM B where an accumulation of strain is detected

1.0-1.2°) in the region close to the origin of the inclined (($\bar{1}\bar{1}0$)) facet of the NM (green square). This phenomenon has been previously observed in other selective-area growth (SAG) 1D nanostructures [110].

C.3.4 Influence of different pre-growth treatments on the preferential orientation of the NMs

In order to check if we can favour a preferential orientation of the NMs, we tried different treatments of the substrate before NM growth. The additional steps considered include a short predeposition step of Ga or As_4 and the inclusion of an annealing time between the predeposition step and the NM growth. To perform the analysis, we obtained SEM images of regions where short NMs were grown (in 80 nm and 170 nm long slits). The preferential alignment is given by the number of NMs whose long axis points towards the [11$\bar{2}$] direction, divided by the total amount of NMs considered for the analysis. A minimum of 100 NMs per sample were checked for the quantification. The results obtained are summarized in Table C.2. As an example, two SEM micrographs of samples 1 and 4 are shown in Figure C.18.

We can see that when the substrate is not treated, the NMs are randomly oriented along the [11$\bar{2}$] or the [1$\bar{1}\bar{2}$]directions. However, whenever a pre-treatment of the substrate is applied, the NMs tend to orientate towards the [11$\bar{2}$] direction. The effect induced on the preferential orientation is enhanced when the duration of the predeposition time is increased or an
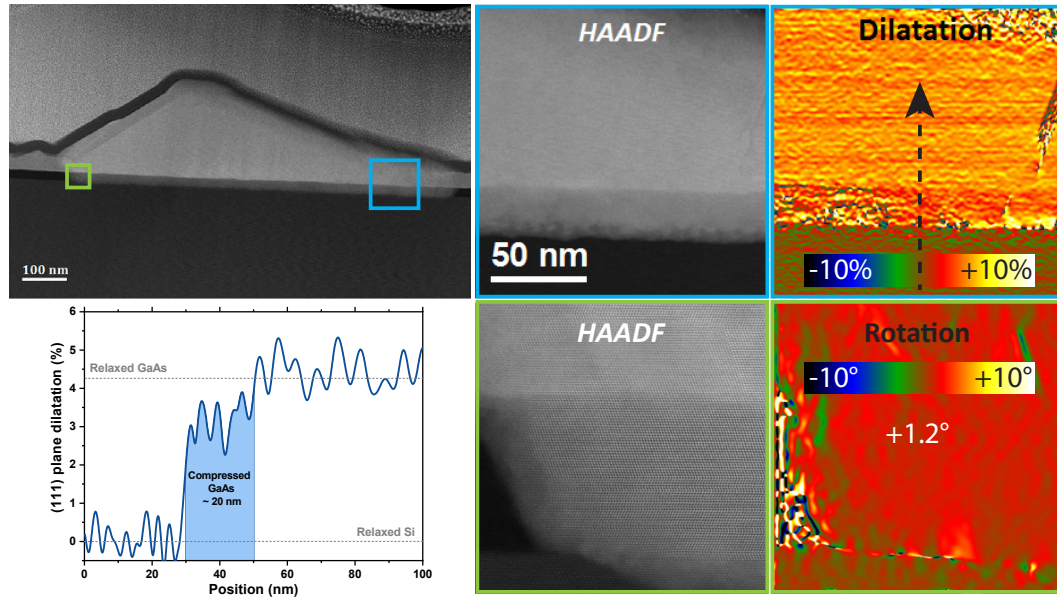
Figure C.17 – GPA applied to (1 1 1) horizontal planes for acquisition of dilatation and rotation of planes maps with Si lattice as reference value. A dilatation profile obtained through the arrow in the dilatation map is shown below.

annealing step is included just before the growth. Good results are obtained either via a Ga or an As_4 exposition of the substrate. By looking at the results, we believe that an improvement of the preferential alignment can be achieved by further increasing the predeposition time.

Sample #	Recipe	Pref. Alignment
1	NM Growth	54%
2	30s Ga Predep + NM Growth	67%
3	60s Ga Predep + NM Growth	77%
4	30s Ga Predep + 5min Anneal + NM Growth	87%
5	3min As Predep + 2min Anneal + NM Growth	88%

Table C.2 – Preferential alignment sample summary.

C.3.5   Gaussian fit of the PL emission of NM B

Figure C.19 shows the photoluminescence (PL) emission of NM B, which was previously represented by the green curve in Figure 5.3. The red curve in Figure C.19 corresponds to the experimental spectrum. This spectrum has been fitted by three Gaussian peaks, which are represented in the figure by the blue dotted curves. These three peaks are centred at 826 nm, 836 nm and 851 nm, respectively. The grey line is obtained as the sum of these components. The goodness of the fit is supported by the value of $R^2 = 0.9990$.
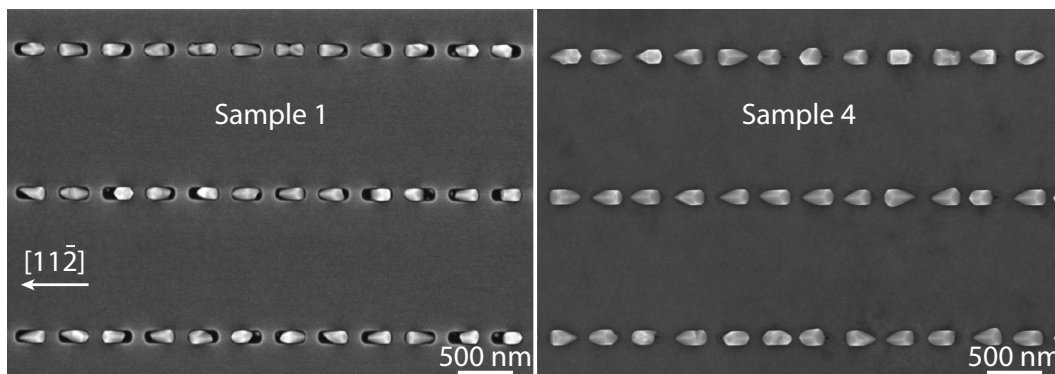
Figure C.18 – SEM images of Sample 1 (left) and Sample 4 (right), where an improvement of the preferential orientation of the NMs in Sample 4 is evident.
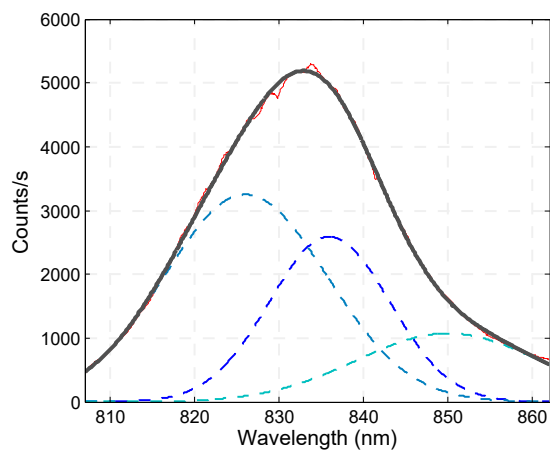
Figure C.19 – Gaussian fit of the PL emission of NM B (green curve in Figure 5.3).

C.3.6 Time-Resolved PL

time-resolved photoluminescence (TRPL) spectra were acquired for the highest-energy component of each NM. The experimental data has been fitted as the convolution of the instrument response function (IRF) with a double exponential function using an iterative reconvolution algorithm:

$$TRPL(t) = IRF \times \left(A_1 e^{-t/\tau_1} + A_2 e^{-t/\tau_2} \right)$$

The contribution of each lifetime component is given by its weight, which is calculated using the expression:

$$W_i = 100 \times \frac{A_i \tau_i}{A_1 \tau_1 + A_2 \tau_2}$$

Finally, the effective lifetime is given by:

$$\tau_m = \frac{(A_1 \tau_1 + A_2 \tau_2)}{100}$$

The results obtained are shown in Table C.3.

	A_1	τ_1 (ps)	A_2	τ_2 (ps)	W_1 (%)	W_2 (%)	$\langle \tau \rangle$ (ps)
NM A	0.029	1065	0.971	41	43.7	56.3	488
NM B	0.010	726	0.990	30	19	81.0	162

Table C.3 – TRPL fit results.

C.4 SI - Nanosails Showcasing Zn$_3$As$_2$ as an Optoelectronic-Grade Earth Abundant Semiconductor

C.4.1 Nanosail growth parameters

As stated in the main text, a horizontal flow metal-organic vapour phase epitaxy system (Aixtron 200/4) was used to grow the Zn$_3$As$_2$ nanostructures on (111)B GaAs substrates similarly to Burgess *et al.* [419]. The substrates were pre-treated with poly-l-lysine before the dispersion of 50 nm gold nanoparticles in colloidal solution. The growth was performed at 500 °C and 10 kPa under a total flow of 15 l/min using arsine and diethylzinc (DEZn) as precursors at molar fractions of 8.04×10^{-3} and 1.31×10^{-4}, respectively, giving a V/II ratio of approximately 60. The growth was carried out for 10 min.

C.4.2   Electrical contact fabrication and measurements

After growth, the nanoplatelets were detached by sonication in isopropanol and drop cast onto a silicon wafer with 200 nm of thermal oxide on it. The electrical contact pattern was written into a MMA/PMMA (400 nm/150 nm) bilayer exposed at 100 keV with a dose of $1000\,\mu C/cm^2$ in a Raith EBPG-5000+ e-beam tool. It was found that without any surface pre-treatment, Schottky barriers at the contacts yielded unreproducible electrical measurements. Therefore both wet and dry etching approaches were employed to achieve ohmic contacts. As a result, the three ohmic devices presented here were contacted with slightly different processes summarized in Table C.4.

	BHF Wet Etch	In-situ Ar Milling	Metallization
Chip I	10 s	-	20 nm/150 nm
Chip II	20 s	-	20 nm/150 nm
Chip III	15 s	30 s	20 nm/150 nm

Table C.4 – Details of contact preparation for electrical devices.

The last chip was additionally Ar milled *in-situ* to remove any oxide that may have re-grown before loading into the sputtering chamber, following a method known to work for InAs nanowires[89, 354]. The contacts were then deposited in the same Alliance-Concept DP-650 sputtering chamber. All of the electrical measurements were performed in a liquid helium cryostat from Cryogenic Ltd. equipped with a 9 T magnet and a VTI for temperature control. The connections to the sample were made through a home-made computer-controlled signal multiplexer and isolator in order to permute the sample connections during automated measurements.

Electrical properties were measured with a Keithley 6221 current source combined with a Keithley 2182A nanovoltmeter in a delta mode measurement configuration. The conductivity of the non-deterministic polynomials (NPs) was measured using the van der Pauw method. To reduce the measurement errors introduced by asymmetry of the platelet and the contacts, the resistances in the vertical and horizontal directions, R_v and R_h, respectively, were averaged between measurements in both polarities and flipped voltage/current contacts. The sheet resistance R_s was then obtained with the van der Pauw formula, $e^{-\pi R_v/R_s} + e^{-\pi R_h/R_s} = 1$. The conductivity σ of the NP was calculated using $\sigma = (R_s t)^{-1}$, where t is the thickness of the nanostructure determined by AFM. The mobility of the samples was measured using a standard Hall-effect measurement approach. In order to reduce the effects of sample and contact inhomogeneity, two measurements were performed using both possible contact configurations and averaged together. The resulting hall voltages obtained with this approach had the expected linear dependence of Hall voltage on magnetic field.

C.4.3   List of reported Raman peaks for α'-**Zn$_3$As$_2$**

Misiewicz [427] measured the Raman peak positions of a phase of Zn$_3$As$_2$. The space group used throughout that publication, C$_{4V}^{14}$, does not exist. Based on the author's previous publications and publications referenced in the article[453, 454], the space group was likely C$_{4V}^{12}$ (I4$_1$cd), which corresponds to the space group of α-Zn$_3$As$_2$. The room-temperature peak positions are listed in Table C.5.

63	97	139	186	210	230	255	303	327	352	392

Table C.5 – Observed room-temperature Raman frequencies of α-Zn$_3$As$_2$ reported by Misiewicz [427]. Units are cm^{-1}.

In our work, no other peak than the first-order silicon Raman peak was detected between the 270 cm^{-1} large Raman shift edge of the Raman spectrum shown in Figure A.2 in the main article and the 830/cm measurement limit.

C.4.4   Simulation of electron diffraction from the α''-**Zn$_3$As$_2$** phase

To the best of our knowledge, no crystal cell refinements have been carried out for α''-Zn$_3$As$_2$. It is known that the space group of this phase is P4$_2$/nmc, but the exact displacements of the atoms with respect to the ideal anti-fluorite structure are unknown. As a first approximation, we assume that the atomic positions of α''-Zn$_3$As$_2$ are the same as those of α/α'' Zn$_3$P$_2$. The lattice parameters of the tetragonal α''-Zn$_3$As$_2$ phase are approximately $a = 8.32$Å and $c = 11.82$Å[422]. Thermal lattice expansion was ignored because it is likely insignificant and the measurement temperature is not clearly stated by Zdanowicz *et al.* [422]. Equivalent zone axes need to be compared in the different structures. Zone axes $\langle 2\,2\,1 \rangle$, $\langle 2\,0\,1 \rangle$, $\langle 2\,4\,1 \rangle$ and $\langle 1\,1\,1 \rangle$ in α-Zn$_3$As$_2$ and α'-Zn$_3$As$_2$ are equivalent to $\langle 2\,0\,1 \rangle$, $\langle 1\,0\,0 \rangle$, $\langle 1\,0\,1 \rangle$ and $\langle 3\,1\,1 \rangle$, respectively, in α''-Zn$_3$As$_2$ and α/α''-Zn$_3$P$_2$. This is assuming that the four-fold axis also changes direction during the $\alpha' \rightleftarrows \alpha''$ phase transition as it does in Cd$_3$As$_2$[455].
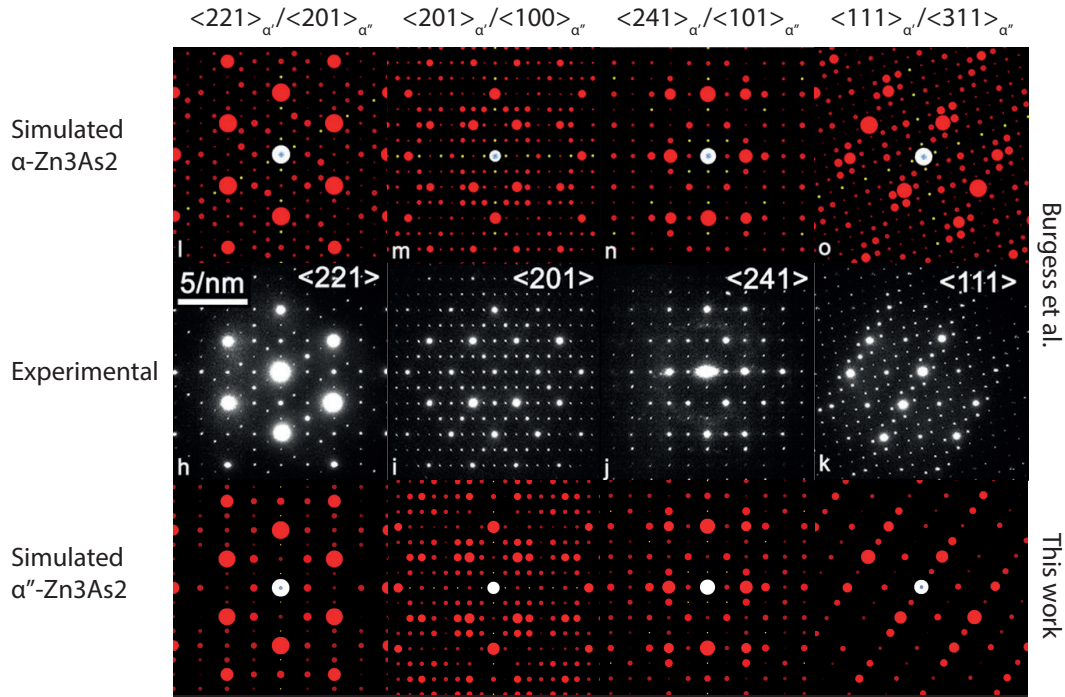
Figure C.20 – First and second rows: simulated α-Zn_3As_2 and experimental diffraction patterns, adapted with permission from [419]. Copyright 2015 American Chemical Society. Third row: simulated α''-Zn_3As_2 obtained by deriving the structure from α-Zn_3P_2 and by using the jems software (Pierre Stadelmann). The columns represent equivalent zone axes.

C.4.5 Fitting of the carrier concentration regime transition

The transition temperature between the nearly constant carrier concentration pure impurity band conduction regime and the thermal carrier generation regime has been determined by linear fitting of the two regimes in Log-vs-1/T plots. The transition temperatures are 31 K, 27 K and 27 K for chips I, II and III, respectively.

(a) Chip 1

(b) Chip 2

(c) Chip 3
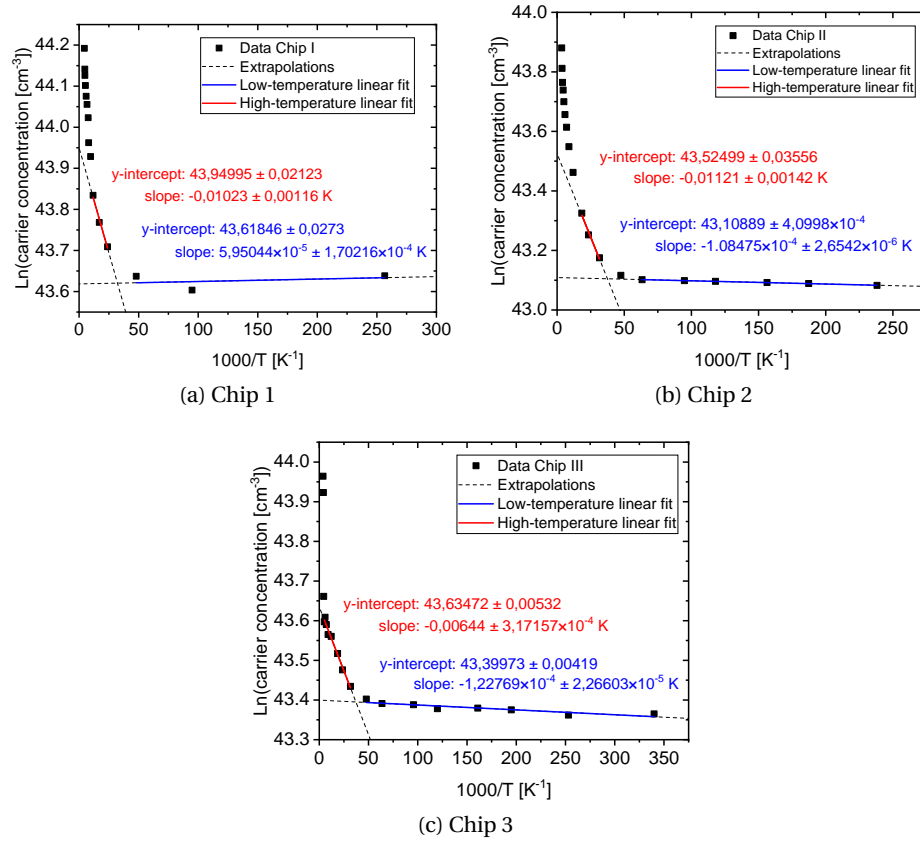
Figure C.21 – Arrhenius-type plots of the carrier concentration in the three studied nanosails. In each of them, the low-temperature and post-transition high-temperature linear parts are fitted. Dashed lines indicate extrapolations from the fitted range.

Bibliography

[1] M. T. Bohr and I. A. Young, "CMOS Scaling Trends and Beyond", *IEEE Micro*, vol. 37, no. 6, pp. 20–29, 2017. DOI: 10.1109/MM.2017.4241347.

[2] J. B. Chang, M. Guillorn, P. M. Solomon, C. H. Lin, S. U. Engelmann, A. Pyzyna, J. A. Ott, and W. E. Haensch, "Scaling of SOI FinFETs down to fin width of 4 nm for the 10nm technology node", *Digest of Technical Papers - Symposium on VLSI Technology*, pp. 12–13, 2011.

[3] K. Nakayama, C. Kodama, T. Kotani, S. Nojima, S. Mimotogi, and S. Miyamoto, "Self-aligned double and quadruple patterning layout principle", in *Design for Manufacturability through Design-Process Integration VI*, M. E. Mason, Ed., vol. 8327, SPIE, 2012, pp. 83270V–83270V–9. DOI: 10.1117/12.916678.

[4] J. R. Cantone, L. Jang, and R. R.-H. Kim, *Methods for fabricating integrated circuits using self-aligned quadruple patterning*, 2014. DOI: US9209038B2.

[5] R. Aitken, E. H. Cannon, M. Pant, and M. B. Tahoori, "Resiliency challenges in sub-10nm technologies", in *2015 IEEE 33rd VLSI Test Symposium (VTS)*, vol. 2015-Janua, IEEE, 2015, pp. 1–4. DOI: 10.1109/VTS.2015.7116281.

[6] T. Tanaka, K. Tomioka, S. Hara, J. Motohisa, E. Sano, and T. Fukui, "Vertical Surrounding Gate Transistors Using Single InAs Nanowires Grown on Si Substrates", *Applied Physics Express*, vol. 3, no. 2, p. 025 003, 2010. DOI: 10.1143/APEX.3.025003.

[7] R. Gandhi, Z. Chen, N. Singh, K. Banerjee, and S. Lee, "Vertical Si-Nanowire n-Type Tunneling FETs With Low Subthreshold Swing <50 mV/decade) at Room Temperature", *IEEE Electron Device Letters*, vol. 32, no. 4, pp. 437–439, 2011. DOI: 10.1109/LED.2011.2106757.

[8] G. Larrieu and X.-L. Han, "Vertical nanowire array-based field effect transistors for ultimate scaling", *Nanoscale*, vol. 5, no. 6, p. 2437, 2013. DOI: 10.1039/c3nr33738c.

[9] J. Ahopelto, G. Ardila, L. Baldi, F. Balestra, D. Belot, G. Fagas, S. De Gendt, D. Demarchi, M. Fernandez-Bolaños, D. Holden, A. Ionescu, G. Meneghesso, A. Mocuta, M. Pfeffer, R. Popp, E. Sangiorgi, and C. Sotomayor Torres, "NanoElectronics roadmap for Europe: From nanodevices and innovative materials to system integration", *Solid-State Electronics*, vol. 155, no. March, pp. 7–19, 2019. DOI: 10.1016/j.sse.2019.03.014.

Bibliography

[10] A. C. Seabaugh and Q. Zhang, "Low-Voltage Tunnel Transistors for Beyond CMOS Logic", *Proceedings of the IEEE*, vol. 98, no. 12, pp. 2095–2110, 2010. DOI: 10.1109/JPROC.2010.2070470.

[11] C. Convertino, C. B. Zota, H. Schmid, A. M. Ionescu, and K. E. Moselund, "III–V heterostructure tunnel field-effect transistor", *Journal of Physics: Condensed Matter*, vol. 30, no. 26, p. 264 005, 2018. DOI: 10.1088/1361-648X/aac5b4.

[12] M. Heyns and W. Tsai, "Ultimate Scaling of CMOS Logic Devices with Ge and III–V Materials", *MRS Bulletin*, vol. 34, no. 7, pp. 485–492, 2009. DOI: 10.1557/mrs2009.136.

[13] J. a. del Alamo, "Nanometre-scale electronics with III–V compound semiconductors", *Nature*, vol. 479, no. 7373, pp. 317–323, 2011. DOI: 10.1038/nature10677.

[14] A. Vardi and J. A. del Alamo, "Sub-10-nm Fin-Width Self-Aligned InGaAs FinFETs", *IEEE Electron Device Letters*, vol. 37, no. 9, pp. 1104–1107, 2016. DOI: 10.1109/LED.2016.2596764.

[15] B. Lambson, D. Carlton, and J. Bokor, "Exploring the thermodynamic limits of computation in integrated systems: Magnetic memory, nanomagnetic logic, and the landauer limit", *Physical Review Letters*, vol. 107, no. 1, pp. 1–4, 2011. DOI: 10.1103/PhysRevLett.107.010604.

[16] R. J. Lipton, "DNA solution of hard computational problems", *Science*, vol. 268, no. 5210, pp. 542–545, 1995. DOI: 10.1126/science.7725098.

[17] Z. Ezziane, "DNA computing: applications and challenges", *Nanotechnology*, vol. 17, no. 2, R27–R39, 2006. DOI: 10.1088/0957-4484/17/2/R01.

[18] N. Goldman, P. Bertone, S. Chen, C. Dessimoz, E. M. Leproust, B. Sipos, and E. Birney, "Towards practical, high-capacity, low-maintenance information storage in synthesized DNA", *Nature*, vol. 494, no. 7435, pp. 77–80, 2013. DOI: 10.1038/nature11875.

[19] R. P. Feynman, "Simulating physics with computers", *International Journal of Theoretical Physics*, vol. 21, no. 6-7, pp. 467–488, 1982. DOI: 10.1007/BF02650179.

[20] S. Lloyd, "Universal Quantum Simulators", *Science*, vol. 273, no. 5278, pp. 1073–1078, 1996. DOI: 10.1126/science.273.5278.1073.

[21] I. M. Georgescu, S. Ashhab, and F. Nori, "Quantum simulation", *Reviews of Modern Physics*, vol. 86, no. 1, pp. 153–185, 2014. DOI: 10.1103/RevModPhys.86.153.

[22] E. Pednault, J. A. Gunnels, G. Nannicini, L. Horesh, T. Magerlein, E. Solomonik, and R. Wisnieff, "Breaking the 49-Qubit Barrier in the Simulation of Quantum Circuits", no. 1, pp. 1–24, 2017.

[23]   C. Neill, P. Roushan, K. Kechedzhi, S. Boixo, S. V. Isakov, V. Smelyanskiy, A. Megrant, B. Chiaro, A. Dunsworth, K. Arya, R. Barends, B. Burkett, Y. Chen, Z. Chen, A. Fowler, B. Foxen, M. Giustina, R. Graff, E. Jeffrey, T. Huang, J. Kelly, P. Klimov, E. Lucero, J. Mutus, M. Neeley, C. Quintana, D. Sank, A. Vainsencher, J. Wenner, T. C. White, H. Neven, and J. M. Martinis, "A blueprint for demonstrating quantum supremacy with superconducting qubits", *Science*, vol. 360, no. 6385, pp. 195–199, 2018. DOI: 10.1126/science.aao4309.

[24]   E. G. Rieffel, "Quantum Supremacy Using a Programmable Superconducting Processor", no. August, 2019.

[25]   R. L. Rivest, A. Shamir, and L. Adleman, "A method for obtaining digital signatures and public-key cryptosystems", *Communications of the ACM*, vol. 21, no. 2, pp. 120–126, 1978. DOI: 10.1145/359340.359342.

[26]   S. Aaronson, "The limits of quantum computers.", *Scientific American*, vol. 298, no. 3, pp. 50–7, 2008. DOI: 10.1038/scientificamerican0308-62.

[27]   M. Vogel, "Quantum Computation and Quantum Information, by M.A. Nielsen and I.L. Chuang", *Contemporary Physics*, vol. 52, no. 6, pp. 604–605, 2011. DOI: 10.1080/00107514.2011.587535.

[28]   P. W. Shor, "Polynomial-Time Algorithms for Prime Factorization and Discrete Logarithms on a Quantum Computer", *SIAM Journal on Computing*, vol. 26, no. 5, pp. 1484–1509, 1997. DOI: 10.1137/S0097539795293172.

[29]   L. K. Grover, "Quantum Mechanics Helps in Searching for a Needle in a Haystack", *Physical Review Letters*, vol. 79, no. 2, pp. 325–328, 1997. DOI: 10.1103/PhysRevLett.79.325.

[30]   S. Jordan, *Quantum Algorithm Zoo*, 2018.

[31]   J. Biamonte, P. Wittek, N. Pancotti, P. Rebentrost, N. Wiebe, and S. Lloyd, "Quantum machine learning", *Nature*, vol. 549, no. 7671, pp. 195–202, 2017. DOI: 10.1038/nature23474.

[32]   E. Tang, "A quantum-inspired classical algorithm for recommendation systems", pp. 217–228, 2019. DOI: 10.1145/3313276.3316310.

[33]   J. Preskill, "Quantum Computing in the NISQ era and beyond", *Quantum*, vol. 2, no. July, p. 79, 2018. DOI: 10.22331/q-2018-08-06-79.

[34]   E. Merzbacher, "Decoherence and the Quantum-to-Classical Transition Decoherence and the Quantum-to-Classical Transition , Maximilian Schlosshauer , Springer, New York, 2007. $99.00 (416 pp.). ISBN 978-3-540-35773-5", *Physics Today*, vol. 61, no. 9, pp. 69–70, 2008. DOI: 10.1063/1.2982129.

[35]   M. H. Devoret and R. J. Schoelkopf, "Superconducting Circuits for Quantum Information: An Outlook", *Science*, vol. 339, no. 6124, pp. 1169–1174, 2013. DOI: 10.1126/science.1231930.

[36] C. Wang, J. Harrington, and J. Preskill, "Confinement-Higgs transition in a disordered gauge theory and the accuracy threshold for quantum memory", *Annals of Physics*, vol. 303, no. 1, pp. 31–58, 2003. DOI: 10.1016/S0003-4916(02)00019-2.

[37] A. G. Fowler, M. Mariantoni, J. M. Martinis, and A. N. Cleland, "Surface codes: Towards practical large-scale quantum computation", *Physical Review A*, vol. 86, no. 3, p. 032 324, 2012. DOI: 10.1103/PhysRevA.86.032324.

[38] J. M. Gambetta, J. M. Chow, and M. Steffen, "Building logical qubits in a superconducting quantum computing system", *npj Quantum Information*, vol. 3, no. 1, p. 2, 2017. DOI: 10.1038/s41534-016-0004-0.

[39] E. Jeffrey, D. Sank, J. Y. Mutus, T. C. White, J. Kelly, R. Barends, Y. Chen, Z. Chen, B. Chiaro, A. Dunsworth, A. Megrant, P. J. J. O'Malley, C. Neill, P. Roushan, A. Vainsencher, J. Wenner, A. N. Cleland, and J. M. Martinis, "Fast Accurate State Measurement with Superconducting Qubits", *Physical Review Letters*, vol. 112, no. 19, p. 190 504, 2014. DOI: 10.1103/PhysRevLett.112.190504.

[40] J. S. Otterbach, R. Manenti, N. Alidoust, A. Bestwick, M. Block, B. Bloom, S. Caldwell, N. Didier, E. S. Fried, S. Hong, P. Karalekas, C. B. Osborn, A. Papageorge, E. C. Peterson, G. Prawiroatmodjo, N. Rubin, C. A. Ryan, D. Scarabelli, M. Scheer, E. A. Sete, P. Sivarajah, R. S. Smith, A. Staley, N. Tezak, W. J. Zeng, A. Hudson, B. R. Johnson, M. Reagor, M. P. da Silva, and C. Rigetti, "Unsupervised Machine Learning on a Hybrid Quantum Computer", 2017.

[41] R. Barends, J. Kelly, A. Megrant, A. Veitia, D. Sank, E. Jeffrey, T. C. White, J. Mutus, A. G. Fowler, B. Campbell, Y. Chen, Z. Chen, B. Chiaro, A. Dunsworth, C. Neill, P. O'Malley, P. Roushan, A. Vainsencher, J. Wenner, A. N. Korotkov, A. N. Cleland, and J. M. Martinis, "Superconducting quantum circuits at the surface code threshold for fault tolerance", *Nature*, vol. 508, no. 7497, pp. 500–503, 2014. DOI: 10.1038/nature13171.

[42] J. Yoneda, K. Takeda, T. Otsuka, T. Nakajima, M. R. Delbecq, G. Allison, T. Honda, T. Kodera, S. Oda, Y. Hoshi, N. Usami, K. M. Itoh, and S. Tarucha, "A quantum-dot spin qubit with coherence limited by charge noise and fidelity higher than 99.9%", *Nature Nanotechnology*, vol. 13, no. 2, pp. 102–106, 2018. DOI: 10.1038/s41565-017-0014-x.

[43] R. Thalineau, S. Hermelin, A. D. Wieck, C. Bäuerle, L. Saminadayar, and T. Meunier, "A few-electron quadruple quantum dot in a closed loop", *Applied Physics Letters*, vol. 101, no. 10, 2012. DOI: 10.1063/1.4749811.

[44] T. A. Baart, N. Jovanovic, C. Reichl, W. Wegscheider, and L. M. K. Vandersypen, "Nanosecond-timescale spin transfer using individual electrons in a quadruple-quantum-dot device", *Applied Physics Letters*, vol. 109, no. 4, p. 043 101, 2016. DOI: 10.1063/1.4959183.

[45] T. Otsuka, T. Nakajima, M. R. Delbecq, S. Amaha, J. Yoneda, K. Takeda, G. Allison, T. Ito, R. Sugawara, A. Noiri, A. Ludwig, A. D. Wieck, and S. Tarucha, "Single-electron spin resonance in a quadruple quantum dot", *Scientific Reports*, vol. 6, no. 1, p. 31 820, 2016. DOI: 10.1038/srep31820.

[46] Y. Wang, M. Um, J. Zhang, S. An, M. Lyu, J.-N. Zhang, L.-M. Duan, D. Yum, and K. Kim, "Single-qubit quantum memory exceeding ten-minute coherence time", *Nature Photonics*, vol. 11, no. 10, pp. 646–650, 2017. DOI: 10.1038/s41566-017-0007-1.

[47] V. M. Schäfer, C. J. Ballance, K. Thirumalai, L. J. Stephenson, T. G. Ballance, A. M. Steane, and D. M. Lucas, "Fast quantum logic gates with trapped-ion qubits", *Nature*, vol. 555, no. 7694, pp. 75–78, 2018. DOI: 10.1038/nature25737.

[48] C. A. Riofrío, D. Gross, S. T. Flammia, T. Monz, D. Nigg, R. Blatt, and J. Eisert, "Experimental quantum compressed sensing for a seven-qubit system", *Nature Communications*, vol. 8, no. May, p. 15 305, 2017. DOI: 10.1038/ncomms15305.

[49] C. J. Ballance, T. P. Harty, N. M. Linke, M. A. Sepiol, and D. M. Lucas, "High-Fidelity Quantum Logic Gates Using Trapped-Ion Hyperfine Qubits", *Physical Review Letters*, vol. 117, no. 6, p. 060 504, 2016. DOI: 10.1103/PhysRevLett.117.060504.

[50] C. Knapp, T. Karzig, R. M. Lutchyn, and C. Nayak, "Dephasing of Majorana-based qubits", *Physical Review B*, vol. 97, no. 12, p. 125 404, 2018. DOI: 10.1103/PhysRevB.97.125404.

[51] D. Litinski, M. S. Kesselring, J. Eisert, and F. von Oppen, "Combining Topological Hardware and Topological Software: Color-Code Quantum Computing with Topological Superconductor Networks", *Physical Review X*, vol. 7, no. 3, p. 031 048, 2017. DOI: 10.1103/PhysRevX.7.031048.

[52] T. Karzig, C. Knapp, R. M. Lutchyn, P. Bonderson, M. B. Hastings, C. Nayak, J. Alicea, K. Flensberg, S. Plugge, Y. Oreg, C. M. Marcus, and M. H. Freedman, "Scalable designs for quasiparticle-poisoning-protected topological quantum computation with Majorana zero modes", *Physical Review B*, vol. 95, no. 23, p. 235 305, 2017. DOI: 10.1103/PhysRevB.95.235305.

[53] E. Majorana, "Teoria simmetrica dell'elettrone e del positrone", *Il Nuovo Cimento (1924-1942)*, vol. 14, no. 4, p. 171, 1937.

[54] N. Read and D. Green, "Paired states of fermions in two dimensions with breaking of parity and time-reversal symmetries and the fractional quantum Hall effect", *Physical Review B*, vol. 61, no. 15, pp. 10 267–10 297, 2000. DOI: 10.1103/PhysRevB.61.10267.

[55] A. Y. Kitaev, "Unpaired Majorana fermions in quantum wires", *Physics-Uspekhi*, vol. 44, no. 10S, pp. 131–136, 2001. DOI: 10.1070/1063-7869/44/10S/S29.

[56] L. Fu and C. L. Kane, "Superconducting proximity effect and majorana fermions at the surface of a topological insulator", *Physical Review Letters*, vol. 100, no. 9, pp. 1–4, 2008. DOI: 10.1103/PhysRevLett.100.096407.

[57] J. Alicea, "Majorana fermions in a tunable semiconductor device", *Physical Review B - Condensed Matter and Materials Physics*, vol. 81, no. 12, pp. 1–10, 2010. DOI: 10.1103/PhysRevB.81.125318.

Bibliography

[58] J. D. Sau, R. M. Lutchyn, S. Tewari, and S. Das Sarma, "Generic new platform for topological quantum computation using semiconductor heterostructures", *Physical Review Letters*, vol. 104, no. 4, pp. 1–4, 2010. DOI: 10.1103/PhysRevLett.104.040502.

[59] S. Plugge, A. Rasmussen, R. Egger, and K. Flensberg, "Majorana box qubits", *New Journal of Physics*, vol. 19, no. 1, p. 012 001, 2017. DOI: 10.1088/1367-2630/aa54e1.

[60] V. Lahtinen and J. Pachos, "A Short Introduction to Topological Quantum Computation", *SciPost Physics*, vol. 3, no. 3, p. 021, 2017. DOI: 10.21468/SciPostPhys.3.3.021.

[61] N. E. Bonesteel, L. Hormozi, G. Zikos, and S. H. Simon, "Braid topologies for quantum computation", *Physical Review Letters*, vol. 95, no. 14, pp. 1–4, 2005. DOI: 10.1103/PhysRevLett.95.140503.

[62] J. Alicea, Y. Oreg, G. Refael, F. von Oppen, and M. P. a. Fisher, "Non-Abelian statistics and topological quantum information processing in 1D wire networks", *Nature Physics*, vol. 7, no. 5, pp. 412–417, 2011. DOI: 10.1038/nphys1915.

[63] B. van Heck, A. R. Akhmerov, F. Hassler, M. Burrello, and C. W. J. Beenakker, "Coulomb-assisted braiding of Majorana fermions in a Josephson junction array", *New Journal of Physics*, vol. 14, no. 3, p. 035 019, 2012. DOI: 10.1088/1367-2630/14/3/035019.

[64] T. Hyart, B. Van Heck, I. C. Fulga, M. Burrello, A. R. Akhmerov, and C. W. J. Beenakker, "Flux-controlled quantum computation with Majorana fermions", *Physical Review B - Condensed Matter and Materials Physics*, vol. 88, no. 3, pp. 1–17, 2013. DOI: 10.1103/PhysRevB.88.035121.

[65] D. Aasen, M. Hell, R. V. Mishmash, A. Higginbotham, J. Danon, M. Leijnse, T. S. Jespersen, J. A. Folk, C. M. Marcus, K. Flensberg, and J. Alicea, "Milestones Toward Majorana-Based Quantum Computing", *Physical Review X*, vol. 6, no. 3, p. 031 016, 2016. DOI: 10.1103/PhysRevX.6.031016.

[66] F. L. Pedrocchi and D. P. DiVincenzo, "Majorana Braiding with Thermal Noise", *Physical Review Letters*, vol. 115, no. 12, pp. 1–6, 2015. DOI: 10.1103/PhysRevLett.115.120402.

[67] P. Bonderson, "Measurement-only topological quantum computation via tunable interactions", *Physical Review B*, vol. 87, no. 3, p. 035 113, 2013. DOI: 10.1103/PhysRevB.87.035113.

[68] M. Barkeshli and J. D. Sau, "Physical Architecture for a Universal Topological Quantum Computer based on a Network of Majorana Nanowires", 2015.

[69] P. Bonderson, M. Freedman, and C. Nayak, "Measurement-Only Topological Quantum Computation", *Physical Review Letters*, vol. 101, no. 1, p. 010 501, 2008. DOI: 10.1103/PhysRevLett.101.010501.

[70] P. Bonderson, M. Freedman, and C. Nayak, "Measurement-only topological quantum computation via anyonic interferometry", *Annals of Physics*, vol. 324, no. 4, pp. 787–826, 2009. DOI: 10.1016/j.aop.2008.09.009.

[71] B. I. Halperin, Y. Oreg, A. Stern, G. Refael, J. Alicea, and F. von Oppen, "Adiabatic manipulations of Majorana fermions in a three-dimensional network of quantum wires", *Physical Review B*, vol. 85, no. 14, p. 144 501, 2012. DOI: 10.1103/PhysRevB.85. 144501.

[72] K. Flensberg, "Non-Abelian Operations on Majorana Fermions via Single-Charge Control", *Physical Review Letters*, vol. 106, no. 9, p. 090 503, 2011. DOI: 10.1103/PhysRevLett. 106.090503.

[73] A. Vaezi and M. Barkeshli, "Fibonacci anyons from Abelian bilayer quantum hall states", *Physical Review Letters*, vol. 113, no. 23, pp. 1–5, 2014. DOI: 10.1103/PhysRevLett.113. 236804.

[74] E. M. Stoudenmire, D. J. Clarke, R. S. Mong, and J. Alicea, "Assembling Fibonacci anyons from a Z3 parafermion lattice model", *Physical Review B - Condensed Matter and Materials Physics*, vol. 91, no. 23, p. 235 112, 2015. DOI: 10.1103/PhysRevB.91.235112.

[75] J. Klinovaja and D. Loss, "Time-reversal invariant parafermions in interacting Rashba nanowires", *Physical Review B*, vol. 90, no. 4, p. 045 118, 2014. DOI: 10.1103/PhysRevB. 90.045118.

[76] J. Klinovaja and D. Loss, "Parafermions in an Interacting Nanowire Bundle", *Physical Review Letters*, vol. 112, no. 24, p. 246 403, 2014. DOI: 10.1103/PhysRevLett.112.246403.

[77] D. Rainis and D. Loss, "Majorana qubit decoherence by quasiparticle poisoning", *Physical Review B*, vol. 85, no. 17, p. 174 533, 2012. DOI: 10.1103/PhysRevB.85.174533.

[78] A. P. Higginbotham, S. M. Albrecht, G. Kiršanskas, W. Chang, F. Kuemmeth, P. Krogstrup, T. S. Jespersen, J. Nygård, K. Flensberg, and C. M. Marcus, "Parity lifetime of bound states in a proximitized semiconductor nanowire", *Nature Physics*, vol. 11, no. 12, pp. 1017–1021, 2015. DOI: 10.1038/nphys3461.

[79] V. Mourik, K. Zuo, S. M. Frolov, S. R. Plissard, E. P. A. M. Bakkers, and L. P. Kouwenhoven, "Signatures of Majorana Fermions in Hybrid Superconductor-Semiconductor Nanowire Devices", *Science*, vol. 336, no. 6084, pp. 1003–1007, 2012. DOI: 10.1126/science. 1222360.

[80] A. Das, Y. Ronen, Y. Most, Y. Oreg, M. Heiblum, and H. Shtrikman, "Zero-bias peaks and splitting in an Al-InAs nanowire topological superconductor as a signature of Majorana fermions", *Nature Physics*, vol. 8, no. 12, pp. 887–895, 2012. DOI: 10.1038/nphys2479.

[81] M. T. Deng, C. L. Yu, G. Y. Huang, M. Larsson, P. Caroff, and H. Q. Xu, "Anomalous Zero-Bias Conductance Peak in a Nb–InSb Nanowire–Nb Hybrid Device", *Nano Letters*, vol. 12, no. 12, pp. 6414–6419, 2012. DOI: 10.1021/nl303758w.

[82] R. M. Lutchyn, E. P. Bakkers, L. P. Kouwenhoven, P. Krogstrup, C. M. Marcus, and Y. Oreg, "Majorana zero modes in superconductor-semiconductor heterostructures", *Nature Reviews Materials*, vol. 3, no. 5, pp. 52–68, 2018. DOI: 10.1038/s41578-018-0003-1.

[83] R. S. Wagner, W. C. Ellis, K. A. Jackson, and S. M. Arnold, "Study of the Filamentary Growth of Silicon Crystals from the Vapor", *Journal of Applied Physics*, vol. 35, no. 10, p. 2993, 1964. DOI: 10.1063/1.1713143.

[84] P. Krogstrup, J. Yamasaki, C. B. Sørensen, E. Johnson, J. B. Wagner, R. Pennington, M. Aagesen, N. Tanaka, and J. Nygård, "Junctions in Axial III-V Heterostructure Nanowires Obtained via an Interchange of Group III Elements", *Nano Letters*, vol. 9, no. 11, pp. 3689–3693, 2009. DOI: 10.1021/nl901348d.

[85] K. A. Dick, C. Thelander, L. Samuelson, and P. Caroff, "Crystal phase engineering in single InAs nanowires", *Nano Letters*, vol. 10, no. 9, pp. 3494–3499, 2010. DOI: 10.1021/nl101632a.

[86] H. J. Joyce, J. Wong-Leung, Q. Gao, H. Hoe Tan, and C. Jagadish, *Phase perfection in zinc blende and wurtzite III- V nanowires using basic growth parameters*, 2010. DOI: 10.1021/nl903688v.

[87] S. R. Plissard, D. R. Slapak, M. A. Verheijen, M. Hocevar, G. W. G. Immink, I. van Weperen, S. Nadj-Perge, S. M. Frolov, L. P. Kouwenhoven, and E. P. A. M. Bakkers, "From InSb Nanowires to Nanocubes: Looking for the Sweet Spot", *Nano Letters*, vol. 12, no. 4, pp. 1794–1798, 2012. DOI: 10.1021/nl203846g.

[88] T. Xu, K. A. Dick, S. Plissard, T. H. Nguyen, Y. Makoudi, M. Berthe, J.-P. Nys, X. Wallart, B. Grandidier, and P. Caroff, "Faceting, composition and crystal phase evolution in III–V antimonide nanowire heterostructures revealed by combining microscopy techniques", *Nanotechnology*, vol. 23, no. 9, p. 095 702, 2012. DOI: 10.1088/0957-4484/23/9/095702.

[89] H. Potts, M. Friedl, F. Amaduzzi, K. Tang, G. Tütüncüoglu, F. Matteini, E. Alarcon Lladó, P. C. P. McIntyre, and A. Fontcuberta i Morral, "From Twinning to Pure Zincblende Catalyst-Free InAs(Sb) Nanowires", *Nano Letters*, vol. 16, no. 1, pp. 637–643, 2016. DOI: 10.1021/acs.nanolett.5b04367.

[90] A. E. Hansen, M. T. Björk, C. Fasth, C. Thelander, L. Samuelson, M. T. Bj??rk, C. Fasth, C. Thelander, and L. Samuelson, "Spin relaxation in InAs nanowires studied by tunable weak antilocalization", *Physical Review B*, vol. 71, no. 20, p. 205 328, 2005. DOI: 10.1103/PhysRevB.71.205328.

[91] S. A. Dayeh, D. P. R. Aplin, X. Zhou, P. K. L. Yu, E. T. Yu, and D. Wang, "High Electron Mobility InAs Nanowire Field-Effect Transistors", *Small*, vol. 3, no. 2, pp. 326–332, 2007. DOI: 10.1002/smll.200600379.

[92] M. D. Schroer and J. R. Petta, "Correlating the Nanostructure and Electronic Properties of InAs Nanowires", *Nano Letters*, vol. 10, no. 5, pp. 1618–1622, 2010. DOI: 10.1021/nl904053j.

[93] C. Thelander, P. Caroff, S. Plissard, A. W. Dey, and K. A. Dick, "Effects of crystal phase mixing on the electrical properties of InAs nanowires.", *Nano letters*, vol. 11, no. 6, pp. 2424–9, 2011. DOI: 10.1021/nl2008339.

[94] I. van Weperen, B. Tarasinski, D. Eeltink, V. S. Pribiag, S. R. Plissard, E. P. A. M. Bakkers, L. P. Kouwenhoven, and M. Wimmer, "Spin-orbit interaction in InSb nanowires", *Physical Review B*, vol. 91, no. 20, p. 201 413, 2015. DOI: 10.1103/PhysRevB.91.201413.

[95] P. Krogstrup, N. L. B. Ziino, W. Chang, S. M. Albrecht, M. H. Madsen, E. Johnson, J. Nygård, C. M. Marcus, and T. S. Jespersen, "Epitaxy of semiconductor–superconductor nanowires", *Nature Materials*, vol. 14, no. 4, pp. 400–406, 2015. DOI: 10.1038/nmat4176.

[96] C. Reeg, D. Loss, and J. Klinovaja, "Metallization of a Rashba wire by a superconducting layer in the strong-proximity regime", *Physical Review B*, vol. 97, no. 16, p. 165 425, 2018. DOI: 10.1103/PhysRevB.97.165425.

[97] W. Chang, S. M. Albrecht, T. S. Jespersen, F. Kuemmeth, P. Krogstrup, J. Nygård, and C. M. Marcus, "Hard gap in epitaxial semiconductor–superconductor nanowires", *Nature Nanotechnology*, vol. 10, no. 3, pp. 232–236, 2015. DOI: 10.1038/nnano.2014.306.

[98] S. R. Plissard, I. van Weperen, D. Car, M. a. Verheijen, G. W. G. Immink, J. Kammhuber, L. J. Cornelissen, D. B. Szombati, A. Geresdi, S. M. Frolov, L. P. Kouwenhoven, and E. P. a. M. Bakkers, "Formation and electronic properties of InSb nanocrosses", *Nature Nanotechnology*, vol. 8, no. 11, pp. 859–864, 2013. DOI: 10.1038/nnano.2013.198.

[99] D. Car, J. Wang, M. A. Verheijen, E. P. A. M. Bakkers, and S. R. Plissard, "Rationally Designed Single-Crystalline Nanowire Networks", *Advanced Materials*, vol. 26, no. 28, pp. 4875–4879, 2014. DOI: 10.1002/adma.201400924.

[100] S. Gazibegovic, D. Car, H. Zhang, S. C. Balk, J. A. Logan, M. W. A. de Moor, M. C. Cassidy, R. Schmits, D. Xu, G. Wang, P. Krogstrup, R. L. M. Op het Veld, K. Zuo, Y. Vos, J. Shen, D. Bouman, B. Shojaei, D. Pennachio, J. S. Lee, P. J. van Veldhoven, S. Koelling, M. A. Verheijen, L. P. Kouwenhoven, C. J. Palmstrøm, and E. P. A. M. Bakkers, "Epitaxy of advanced nanowire quantum devices", *Nature*, vol. 548, no. 7668, pp. 434–438, 2017. DOI: 10.1038/nature23468.

[101] J.-H. Kang, M. Galicka, P. Kacman, and H. Shtrikman, "Wurtzite/Zinc-Blende 'K'-shape InAs Nanowires with Embedded Two-Dimensional Wurtzite Plates", *Nano Letters*, vol. 17, no. 1, pp. 531–537, 2017. DOI: 10.1021/acs.nanolett.6b04598.

[102] J. Shabani, M. Kjaergaard, H. J. Suominen, Y. Kim, F. Nichele, K. Pakrouski, T. Stankevic, R. M. Lutchyn, P. Krogstrup, R. Feidenhans'L, S. Kraemer, C. Nayak, M. Troyer, C. M. Marcus, and C. J. Palmstrøm, "Two-dimensional epitaxial superconductor-semiconductor heterostructures: A platform for topological superconducting networks", *Physical Review B*, vol. 93, no. 15, pp. 1–6, 2016. DOI: 10.1103/PhysRevB.93.155402.

[103] M. Kjaergaard, F. Nichele, H. J. Suominen, M. P. Nowak, M. Wimmer, A. R. Akhmerov, J. A. Folk, K. Flensberg, J. Shabani, C. J. Palmstrøm, and C. M. Marcus, "Quantized conductance doubling and hard gap in a two-dimensional semiconductor–superconductor heterostructure", *Nature Communications*, vol. 7, no. 1, p. 12 841, 2016. DOI: 10.1038/ncomms12841.

Bibliography

[104] F. Nichele, A. C. Drachmann, A. M. Whiticar, E. C. O'Farrell, H. J. Suominen, A. Fornieri, T. Wang, G. C. Gardner, C. Thomas, A. T. Hatke, P. Krogstrup, M. J. Manfra, K. Flensberg, and C. M. Marcus, "Scaling of Majorana Zero-Bias Conductance Peaks", *Physical Review Letters*, vol. 119, no. 13, pp. 1–5, 2017. DOI: 10.1103/PhysRevLett.119.136803.

[105] H. J. Suominen, M. Kjaergaard, A. R. Hamilton, J. Shabani, C. J. Palmstrøm, C. M. Marcus, and F. Nichele, "Zero-Energy Modes from Coalescing Andreev States in a Two-Dimensional Semiconductor-Superconductor Hybrid Platform", *Physical Review Letters*, vol. 119, no. 17, p. 176 805, 2017. DOI: 10.1103/PhysRevLett.119.176805.

[106] M. Fahed, L. Desplanque, D. Troadec, G. Patriarche, and X. Wallart, "Selective area heteroepitaxy of GaSb on GaAs (001) for in-plane InAs nanowire achievement", *Nanotechnology*, vol. 27, no. 50, p. 505 301, 2016. DOI: 10.1088/0957-4484/27/50/505301.

[107] M. Fahed, L. Desplanque, D. Troadec, G. Patriarche, and X. Wallart, "Selective area heteroepitaxy of GaSb on GaAs (001) for in-plane InAs nanowire achievement", *Nanotechnology*, vol. 27, no. 50, p. 505 301, 2016. DOI: 10.1088/0957-4484/27/50/505301.

[108] M. Friedl, K. Cerveny, P. Weigele, G. Tütüncüoglu, S. Martí-Sánchez, C. Huang, T. Patlatiuk, H. Potts, Z. Sun, M. O. Hill, L. Güniat, W. Kim, M. Zamani, V. G. Dubrovskii, J. Arbiol, L. J. Lauhon, D. M. Zumbühl, and A. Fontcuberta i Morral, "Template-Assisted Scalable Nanowire Networks", *Nano Letters*, vol. 18, no. 4, pp. 2666–2671, 2018. DOI: 10.1021/acs.nanolett.8b00554.

[109] L. Desplanque, A. Bucamp, D. Troadec, G. Patriarche, and X. Wallart, "In-plane InSb nanowires grown by selective area molecular beam epitaxy on semi-insulating substrate", *Nanotechnology*, vol. 29, no. 30, p. 305 705, 2018. DOI: 10.1088/1361-6528/aac321.

[110] F. Krizek, J. E. Sestoft, P. Aseev, S. Marti-Sanchez, S. Vaitiekėnas, L. Casparis, S. A. Khan, Y. Liu, T. Stankevič, A. M. Whiticar, A. Fursina, F. Boekhout, R. Koops, E. Uccelli, L. P. Kouwenhoven, C. M. Marcus, J. Arbiol, and P. Krogstrup, "Field effect enhancement in buffered quantum nanowire networks", *Physical Review Materials*, vol. 2, no. 9, p. 093 401, 2018. DOI: 10.1103/PhysRevMaterials.2.093401.

[111] S. Vaitiekėnas, A. M. Whiticar, M. T. Deng, F. Krizek, J. E. Sestoft, C. J. Palmstrøm, S. Marti-Sanchez, J. Arbiol, P. Krogstrup, L. Casparis, and C. M. Marcus, "Selective Area Grown Semiconductor-Superconductor Hybrids: A Basis for Topological Networks", no. mV, 2018. DOI: arXiv:1802.04210v1.

[112] P. Aseev, A. Fursina, F. Boekhout, F. Krizek, J. E. Sestoft, F. Borsoi, S. Heedt, G. Wang, L. Binci, S. Martí-Sánchez, T. Swoboda, R. Koops, E. Uccelli, J. Arbiol, P. Krogstrup, L. P. Kouwenhoven, and P. Caroff, "Selectivity Map for Molecular Beam Epitaxy of Advanced III–V Quantum Nanowire Networks", *Nano Letters*, vol. 19, no. 1, pp. 218–227, 2019. DOI: 10.1021/acs.nanolett.8b03733.

[113] J. S. Lee, S. Choi, M. Pendharkar, D. J. Pennachio, B. Markman, M. Seas, S. Koelling, M. A. Verheijen, L. Casparis, K. D. Petersson, I. Petkovic, V. Schaller, M. J. W. Rodwell, C. M. Marcus, P. Krogstrup, L. P. Kouwenhoven, E. P. A. M. Bakkers, and C. J. Palmstrøm, "Selective-area chemical beam epitaxy of in-plane InAs one-dimensional channels grown on InP(001), InP(111)B, and InP(011) surfaces", *Physical Review Materials*, vol. 3, no. 8, p. 084 606, 2019. DOI: 10.1103/PhysRevMaterials.3.084606.

[114] F. Glas, "Critical dimensions for the plastic relaxation of strained axial heterostructures in free-standing nanowires", *Physical Review B*, vol. 74, no. 12, p. 121 302, 2006. DOI: 10.1103/PhysRevB.74.121302.

[115] J. Y. Tsao and J. P. Harbison, *Materials Fundamentals of Molecular Beam Epitaxy*. London: Academic Press Limited, 1993.

[116] T. Nishinaga, *Handbook of Crystal Growth Fundamentals : Thermodynamics Handbook of Crystal Growth Fundamentals : Transport and Stability*. 2015, vol. I, p. 1182.

[117] J. M. Moison, F. Houzay, F. Barthe, L. Leprince, E. André, and O. Vatel, "Self-organized growth of regular nanometer-scale InAs dots on GaAs", *Applied Physics Letters*, vol. 64, no. 2, pp. 196–198, 1994. DOI: 10.1063/1.111502.

[118] J.-Y. Marzin, J.-M. Gérard, A. Izraël, D. Barrier, and G. Bastard, "Photoluminescence of Single InAs Quantum Dots Obtained by Self-Organized Growth on GaAs", *Physical Review Letters*, vol. 73, no. 5, pp. 716–719, 1994. DOI: 10.1103/PhysRevLett.73.716.

[119] K. Yang and L. J. Schowalter, "Surface reconstruction phase diagram and growth on GaAs(111)B substrates by molecular beam epitaxy", *Applied Physics Letters*, vol. 60, no. 15, pp. 1851–1853, 1992. DOI: 10.1063/1.107188.

[120] P. Kratzer, C. G. Morgan, and M. Scheffler, "Density-functional theory studies on microscopic processes of gaas growth", *Progress in Surface Science*, vol. 59, no. 1-4, pp. 135–147, 1998. DOI: 10.1016/S0079-6816(98)00041-0.

[121] A. S. Bracker, M. J. Yang, B. R. Bennett, J. C. Culbertson, and W. J. Moore, "Surface reconstruction phase diagrams for InAs, AlSb, and GaSb", *Journal of Crystal Growth*, vol. 220, no. 4, pp. 384–392, 2000. DOI: 10.1016/S0022-0248(00)00871-X.

[122] E. D. Williams and N. C. Bartelt, "Surface faceting and the equilibrium crystal shape", *Ultramicroscopy*, vol. 31, no. 1, pp. 36–48, 1989. DOI: 10.1016/0304-3991(89)90032-6.

[123] N. Moll, A. Kley, E. Pehlke, and M. Scheffler, "GaAs equilibrium crystal shape from first principles", *Physical Review B*, vol. 54, no. 12, pp. 8844–8855, 1996. DOI: 10.1103/PhysRevB.54.8844.

[124] G. Wulff, "Zur Frage der Geschwindigkeit des Wachstums und der Aufliisung der Kristallfllchen", *Z. Krist. Miner*, vol. 34, pp. 499–530, 1901.

[125] C. Herring, "The use of classical macroscopic concepts in surface energy problems", in *Structure and properties of solid surfaces*, 1953, p. 5.

Bibliography

[126] W. Winterbottom, "Equilibrium shape of a small particle in contact with a foreign substrate", *Acta Metallurgica*, vol. 15, no. 2, pp. 303–310, 1967. DOI: 10.1016/0001-6160(67)90206-4.

[127] W. D. Kaplan, D. Chatain, P. Wynblatt, and W. C. Carter, "A review of wetting versus adsorption, complexions, and related phenomena: the rosetta stone of wetting", *Journal of Materials Science*, vol. 48, no. 17, pp. 5681–5717, 2013. DOI: 10.1007/s10853-013-7462-y.

[128] M. Albani, R. Bergamaschini, M. Salvalaglio, A. Voigt, L. Miglio, and F. Montalenti, "Competition Between Kinetics and Thermodynamics During the Growth of Faceted Crystal by Phase Field Modeling", *physica status solidi (b)*, vol. 256, no. 7, p. 1 800 518, 2019. DOI: 10.1002/pssb.201800518.

[129] T. Ujihara, Y. Yoshida, W. Sik Lee, and Y. Takeda, "Pattern size effect on source supply process for sub-micrometer scale selective area growth by organometallic vapor phase epitaxy", *Journal of Crystal Growth*, vol. 289, no. 1, pp. 89–95, 2006. DOI: 10.1016/j.jcrysgro.2005.11.088.

[130] M. Albani, L. Ghisalberti, R. Bergamaschini, M. Friedl, M. Salvalaglio, A. Voigt, F. Montalenti, G. Tütüncüoglu, A. Fontcuberta i Morral, and L. Miglio, "Growth kinetics and morphological analysis of homoepitaxial GaAs fins by theory and experiment", *Physical Review Materials*, vol. 2, no. 9, p. 093 404, 2018. DOI: 10.1103/PhysRevMaterials.2.093404.

[131] V. G. Dubrovskii and N. V. Sibirev, "Growth rate of a crystal facet of arbitrary size and growth kinetics of vertical nanowires", *Physical Review E - Statistical, Nonlinear, and Soft Matter Physics*, vol. 70, no. 3 1, pp. 1–7, 2004. DOI: 10.1103/PhysRevE.70.031604.

[132] A. Rätz, A. Ribalta, and A. Voigt, "Surface evolution of elastically stressed films under deposition by a diffuse interface model", *Journal of Computational Physics*, vol. 214, no. 1, pp. 187–208, 2006. DOI: 10.1016/j.jcp.2005.09.013.

[133] B. Li and J. Lowengrub, "Geometric evolution laws for thin crystalline films: modeling and numerics", *Commun. Comput. . . .*, vol. 6, no. 3, pp. 433–482, 2009.

[134] D. J. Smith, T. Aoki, J. K. Furdyna, X. Liu, M. R. McCartney, and Y.-H. Zhang, "Atomic-scale characterization of (mostly zincblende) compound semiconductor heterostructures", *Journal of Physics: Conference Series*, vol. 471, p. 012 005, 2013. DOI: 10.1088/1742-6596/471/1/012005.

[135] A. Rocher, "Interfacial Dislocations in the GaSb/GaAs (001) Heterostructure", *Solid State Phenomena*, vol. 19-20, pp. 563–572, 1991. DOI: 10.4028/www.scientific.net/SSP.19-20.563.

[136] M. Aindow, T. Cheng, N. Mason, T.-Y. Seong, and P. Walker, "Geometry and interface structure of island nuclei for GaSb buffer layers grown on (001) GaAs by metalorganic vapour phase epitaxy", *Journal of Crystal Growth*, vol. 133, no. 1-2, pp. 168–174, 1993. DOI: 10.1016/0022-0248(93)90117-F.

[137]   J. M. Kang, S. Min, and A. Rocher, "Asymmetric tilt interface induced by 60° misfit dislocation arrays in GaSb/GaAs(001)", *Applied Physics Letters*, vol. 65, no. 23, pp. 2954–2956, 1994. DOI: 10.1063/1.112502.

[138]   J. Kang, M. Nouaoura, L. Lassabatère, and A. Rocher, "Accommodation of lattice mismatch and threading of dislocations in GaSb films grown at different temperatures on GaAs (001)", *Journal of Crystal Growth*, vol. 143, no. 3-4, pp. 115–123, 1994. DOI: 10.1016/0022-0248(94)90045-0.

[139]   A. Trampert, E. Tournié, and K. H. Ploog, "Novel plastic strain-relaxation mode in highly mismatched III-V layers induced by two-dimensional epitaxial growth", *Applied Physics Letters*, vol. 66, no. 17, pp. 2265–2267, 1995. DOI: 10.1063/1.113187.

[140]   J. C. P. Chang, T. P. Chin, and J. M. Woodall, "Incoherent interface of InAs grown directly on GaP(001)", *Applied Physics Letters*, vol. 69, no. 7, pp. 981–983, 1996. DOI: 10.1063/1.117102.

[141]   A. Trampert, K. H. Ploog, and E. Tournié, "Anisotropic misfit dislocation nucleation in two-dimensional grown InAs/GaAs(001) heterostructures", *Applied Physics Letters*, vol. 73, no. 8, pp. 1074–1076, 1998. DOI: 10.1063/1.122088.

[142]   N. Y. Jin-Phillipp, W. Sigle, A. Black, D. Babic, J. E. Bowers, E. L. Hu, and M. Rühle, "Interface of directly bonded GaAs and InP", *Journal of Applied Physics*, vol. 89, no. 2, pp. 1017–1024, 2001. DOI: 10.1063/1.1331068.

[143]   A. Kuronen, K. Kaski, L. F. Perondi, and J. Rintala, "Atomistic modelling of interaction between dislocations and misfit interface", *Europhysics Letters (EPL)*, vol. 55, no. 1, pp. 19–25, 2001. DOI: 10.1209/epl/i2001-00375-2.

[144]   J. H. Van Der Merwe, "Misfit dislocations in epitaxy", *Metallurgical and Materials Transactions A*, vol. 33, no. 8, pp. 2475–2483, 2002. DOI: 10.1007/s11661-002-0369-x.

[145]   S. H. Huang, G. Balakrishnan, A. Khoshakhlagh, A. Jallipalli, L. R. Dawson, and D. L. Huffaker, "Strain relief by periodic misfit arrays for low defect density GaSb on GaAs", *Applied Physics Letters*, vol. 88, no. 13, p. 131 911, 2006. DOI: 10.1063/1.2172742.

[146]   A. Jallipalli, G. Balakrishnan, S. Huang, A. Khoshakhlagh, L. Dawson, and D. Huffaker, "Atomistic modeling of strain distribution in self-assembled interfacial misfit dislocation (IMF) arrays in highly mismatched III–V semiconductor materials", *Journal of Crystal Growth*, vol. 303, no. 2, pp. 449–455, 2007. DOI: 10.1016/j.jcrysgro.2006.12.032.

[147]   A. Jallipalli, G. Balakrishnan, S. H. Huang, T. J. Rotter, K. Nunna, B. L. Liang, L. R. Dawson, and D. L. Huffaker, "Structural Analysis of Highly Relaxed GaSb Grown on GaAs Substrates with Periodic Interfacial Array of 90° Misfit Dislocations", *Nanoscale Research Letters*, vol. 4, no. 12, pp. 1458–1462, 2009. DOI: 10.1007/s11671-009-9420-9.

[148]   C. Merckling, X. Sun, A. Alian, G. Brammertz, V. V. Afanas'ev, T. Y. Hoffmann, M. Heyns, M. Caymax, and J. Dekoster, "GaSb molecular beam epitaxial growth on p -InP(001) and passivation with in situ deposited Al 2 O 3 gate oxide", *Journal of Applied Physics*, vol. 109, no. 7, p. 073 719, 2011. DOI: 10.1063/1.3569618.

Bibliography

[149] D. Benyahia, L. Kubiszyn, K. Michalczewski, A. Keblowski, P. Martyniuk, J. Piotrowski, and A. Rogalski, "Low-temperature growth of GaSb epilayers on GaAs (001) by molecular beam epitaxy", *Opto-Electronics Review*, vol. 24, no. 1, pp. 40–45, 2016. DOI: 10.1515/oere-2016-0007.

[150] C.-J. Hsiao, M.-T.-H. Ha, C.-Y. Hsu, Y.-C. Lin, S.-P. Chang, S.-J. Chang, and E. Y. Chang, "Growth of ultrathin GaSb layer on GaAs using metal–organic chemical vapor deposition with Sb interfacial treatment", *Applied Physics Express*, vol. 9, no. 9, p. 095 502, 2016. DOI: 10.7567/APEX.9.095502.

[151] B. W. Jia, K. H. Tan, W. K. Loke, S. Wicaksono, and S. F. Yoon, "Formation of periodic interfacial misfit dislocation array at the InSb/GaAs interface via surface anion exchange", *Journal of Applied Physics*, vol. 120, no. 3, p. 035 301, 2016. DOI: 10.1063/1.4958863.

[152] C. J. Hsiao, R. K. Kakkerla, P. C. Chang, F. J. Lumbantoruan, T. T. Lee, Y. C. Lin, S. J. Chang, and E. Y. Chang, "Growth and characterization of high quality N-type GaSb/-GaAs heterostructure by IMF growth mode using MOCVD for low power application", *Applied Physics Letters*, vol. 111, no. 16, p. 162 108, 2017. DOI: 10.1063/1.5008737.

[153] B. W. Jia, K. H. Tan, W. K. Loke, S. Wicaksono, and S. F. Yoon, "Effects of surface reconstruction on the epitaxial growth of III-Sb on GaAs using interfacial misfit array", *Applied Surface Science*, vol. 399, pp. 220–228, 2017. DOI: 10.1016/j.apsusc.2016.12.051.

[154] G. T. Nelson, B.-C. Juang, M. A. Slocum, Z. S. Bittner, R. B. Laghumavarapu, D. L. Huffaker, and S. M. Hubbard, "GaSb solar cells grown on GaAs via interfacial misfit arrays for use in the III-Sb multi-junction cell", *Applied Physics Letters*, vol. 111, no. 23, p. 231 104, 2017. DOI: 10.1063/1.4991548.

[155] P.-N. Ni, J.-C. Tong, L. Y. Tobing, Z.-J. Xu, S. Qiu, X.-H. Tang, and D.-H. Zhang, "A buffer-free method for growth of InAsSb films on GaAs (001) substrates using MOCVD", *Journal of Crystal Growth*, vol. 468, pp. 252–257, 2017. DOI: 10.1016/j.jcrysgro.2016.11.124.

[156] W. L. Sarney, S. P. Svensson, Y. Xu, D. Donetsky, and G. Belenky, "Bulk InAsSb with 0.1 eV bandgap on GaAs", *Journal of Applied Physics*, vol. 122, no. 2, p. 025 705, 2017. DOI: 10.1063/1.4993454.

[157] D. Benyahia, L. Kubiszyn, K. Michalczewski, A. Kebłowski, P. Martyniuk, J. Piotrowski, and A. Rogalski, "Optimization of the interfacial misfit array growth mode of GaSb epilayers on GaAs substrate", *Journal of Crystal Growth*, vol. 483, pp. 26–30, 2018. DOI: 10.1016/j.jcrysgro.2017.11.015.

[158] T. Cerba, P. Hauchecorne, M. Martin, J. Moeyaert, R. Alcotte, B. Salem, E. Eustache, P. Bezard, X. Chevalier, G. Lombard, F. Bassani, S. David, G. Beainy, E. Tournié, G. Patriarche, H. Boutry, M. Bawedin, and T. Baron, "InAs/GaSb thin layers directly grown on nominal (0 0 1)-Si substrate by MOVPE for the fabrication of InAs FINFET", *Journal of Crystal Growth*, vol. 510, pp. 18–22, 2019. DOI: 10.1016/j.jcrysgro.2018.12.014.

[159]   A. Georgakilas, J. Stoemenos, K. Tsagaraki, P. Komninou, N. Flevaris, P. Panayotatos, and A. Christou, "Generation and annihilation of antiphase domain boundaries in GaAs on Si grown by molecular beam epitaxy", *Journal of Materials Research*, vol. 8, no. 8, pp. 1908–1921, 1993. DOI: 10.1557/JMR.1993.1908.

[160]   M. Heiß, E. Riedlberger, D. Spirkoska, M. Bichler, G. Abstreiter, and A. F. i. Morral, "Growth mechanisms and optical properties of GaAs-based semiconductor microstructures by selective area epitaxy", *Journal of Crystal Growth*, vol. 310, no. 6, pp. 1049–1056, 2008. DOI: 10.1016/j.jcrysgro.2007.12.061.

[161]   B. D. Joyce and J. A. Baldrey, "Selective Epitaxial Deposition of Silicon", *Nature*, vol. 195, no. 4840, pp. 485–486, 1962. DOI: 10.1038/195485a0.

[162]   F. W. Tausch and A. G. Lapierre, "A Novel Crystal Growth Phenomenon: Single Crystal GaAs Overgrowth onto Silicon Dioxide", *Journal of The Electrochemical Society*, vol. 112, no. 7, p. 706, 1965. DOI: 10.1149/1.2423670.

[163]   D. W. Shaw, "Selective Epitaxial Deposition of Gallium Arsenide in Holes", *Journal of The Electrochemical Society*, vol. 113, no. 9, p. 904, 1966. DOI: 10.1149/1.2424153.

[164]   L. Jastrzebski, "SOI by CVD: Epitaxial Lateral Overgrowth (ELO) process—Review", *Journal of Crystal Growth*, vol. 63, no. 3, pp. 493–526, 1983. DOI: 10.1016/0022-0248(83)90164-1.

[165]   R. W. McClelland, C. O. Bozler, and J. C. C. Fan, "A technique for producing epitaxial films on reuseable substrates", *Applied Physics Letters*, vol. 37, no. 6, pp. 560–562, 1980. DOI: 10.1063/1.91987.

[166]   H. Asai, S. Yamada, and T. Fukui, "Narrow two-dimensional electron gas channels in GaAs/AlGaAs sidewall interfaces by selective growth", *Applied Physics Letters*, vol. 51, no. 19, pp. 1518–1520, 1987. DOI: 10.1063/1.98621.

[167]   T. Fukui and S. Ando, "New GaAs quantum wires on {111}B facets by selective MOCVD", *Electronics Letters*, vol. 25, no. 6, p. 410, 1989. DOI: 10.1049/el:19890282.

[168]   T. Fukui, S. Ando, and Y. K. Fukai, "Lateral quantum well wires fabricated by selective metalorganic chemical vapor deposition", *Applied Physics Letters*, vol. 57, no. 12, pp. 1209–1211, 1990. DOI: 10.1063/1.103487.

[169]   A. Okamoto and K. Ohata, "Selective epitaxial growth of gallium arsenide by molecular beam epitaxy", *Applied Physics Letters*, vol. 51, no. 19, pp. 1512–1514, 1987. DOI: 10.1063/1.98619.

[170]   N. Yamamoto, N. Kondo, and Y. Nanishi, "Selective area growth of GaAs by Electron-Cyclotron Resonance plasma-excited Molecular-Beam Epitaxy (ECR-MBE)", *Journal of Crystal Growth*, vol. 96, no. 3, pp. 705–707, 1989. DOI: 10.1016/0022-0248(89)90072-9.

[171]   S. Yokoyama, J. Oogi, D. Yui, and M. Kawabe, "Low-temperature selective growth of GaAs by alternately supplying molecular beam epitaxy", *Journal of Crystal Growth*, vol. 95, no. 1-4, pp. 32–34, 1989. DOI: 10.1016/0022-0248(89)90344-8.

Bibliography

[172] T. Sugaya, Y. Okada, and M. Kawabe, "Selective Growth of GaAs by Molecular Beam Epitaxy", *Japanese Journal of Applied Physics*, vol. 31, no. Part 2, No. 6A, pp. L713–L716, 1992. DOI: 10.1143/JJAP.31.L713.

[173] N. Kuroda, S. Sugou, T. Sasaki, and M. Kitamura, "Selective Growth of InGaAs/InP Layers by Gas Source Molecular Beam Epitaxy with Atomic Hydrogen Irradiation", *Japanese Journal of Applied Physics*, vol. 32, no. Part 2, No. 11A, pp. L1627–L1630, 1993. DOI: 10.1143/JJAP.32.L1627.

[174] K. Tomioka, T. Tanaka, S. Hara, K. Hiruma, and T. Fukui, "III–V Nanowires on Si Substrate: Selective-Area Growth and Device Applications", *IEEE Journal of Selected Topics in Quantum Electronics*, vol. 17, no. 4, pp. 1112–1129, 2011. DOI: 10.1109/JSTQE.2010.2068280.

[175] S. C. Lee, L. R. Dawson, and S. R. Brueck, "Epitaxial growth of a nanoscale, vertically faceted, one-dimensional, high-aspect ratio grating in III-V materials for integrated photonics", *Applied Physics Letters*, vol. 87, no. 7, pp. 2–4, 2005. DOI: 10.1063/1.1984085.

[176] Z. Zhao, K. Yadavalli, Z. Hao, and K. L. Wang, "Direct integration of III-V compound semiconductor nanostructures on silicon by selective epitaxy", *Nanotechnology*, vol. 20, no. 3, 2009. DOI: 10.1088/0957-4484/20/3/035304.

[177] G. Tutuncuoglu, M. de la Mata, D. Deiana, H. Potts, F. Matteini, J. Arbiol, and A. Fontcuberta i Morral, "Towards defect-free 1-D GaAs/AlGaAs heterostructures based on GaAs nanomembranes", *Nanoscale*, vol. 7, no. 46, pp. 19 453–19 460, 2015. DOI: 10.1039/C5NR04821D.

[178] L. Güniat, S. Martí-Sánchez, O. Garcia, M. Boscardin, D. Vindice, N. Tappy, M. Friedl, W. Kim, M. Zamani, L. Francaviglia, A. Balgarkashi, J.-B. Leran, J. Arbiol, and A. Fontcuberta i Morral, "III–V Integration on Si(100): Vertical Nanospades", *ACS Nano*, vol. 13, no. 5, pp. 5833–5840, 2019. DOI: 10.1021/acsnano.9b01546.

[179] C.-Y. Chi, C.-C. Chang, S. Hu, T.-W. Yeh, S. B. Cronin, and P. D. Dapkus, "Twin-Free GaAs Nanosheets by Selective Area Growth: Implications for Defect-Free Nanostructures", *Nano Letters*, vol. 13, no. 6, pp. 2506–2515, 2013. DOI: 10.1021/nl400561j.

[180] C.-C. Chang, C.-Y. Chi, C.-C. Chen, N. Huang, S. Arab, J. Qiu, M. L. Povinelli, P. D. Dapkus, and S. B. Cronin, "Carrier dynamics and doping profiles in GaAs nanosheets", *Nano Research*, vol. 7, no. 2, pp. 163–170, 2014. DOI: 10.1007/s12274-013-0383-x.

[181] S. Arab, C.-y. Chi, T. Shi, Y. Wang, D. P. Dapkus, H. E. Jackson, L. M. Smith, and S. B. Cronin, "Effects of Surface Passivation on Twin-Free GaAs Nanosheets", *ACS Nano*, vol. 9, no. 2, pp. 1336–1340, 2015. DOI: 10.1021/nn505227q.

[182] Y. Kato, S. Kitamura, K. Hiramatsu, and N. Sawaki, "Selective growth of wurtzite GaN and AlxGa1-xN on GaN/sapphire substrates by metalorganic vapor phase epitaxy", *Journal of Crystal Growth*, vol. 144, no. 3-4, pp. 133–140, 1994. DOI: 10.1016/0022-0248(94)90448-0.

[183] P. Gibart, "Metal organic vapour phase epitaxy of GaN and lateral overgrowth", *Reports on Progress in Physics*, vol. 67, no. 5, pp. 667–715, 2004. DOI: 10.1088/0034-4885/67/5/R02.

[184] T.-W. Yeh, Y.-T. Lin, B. Ahn, L. S. Stewart, P. Daniel Dapkus, and S. R. Nutt, "Vertical nonpolar growth templates for light emitting diodes formed with GaN nanosheets", *Applied Physics Letters*, vol. 100, no. 3, p. 033 119, 2012. DOI: 10.1063/1.3671182.

[185] H. Heinecke, B. Baur, A. Miklis, R. Matz, C. Cremer, and R. Höger, "Evidence for vertical superlattices grown by surface selective growth in MOMBE (CBE)", *Journal of Crystal Growth*, vol. 124, no. 1-4, pp. 186–191, 1992. DOI: 10.1016/0022-0248(92)90458-U.

[186] M. Wachter and H. Heinecke, "Beam geometrical effects on planar selective area epitaxy of heterostructures", *Journal of Crystal Growth*, vol. 164, no. 1-4, pp. 302–307, 1996. DOI: 10.1016/0022-0248(96)00002-4.

[187] M. Fahed, L. Desplanque, C. Coinon, D. Troadec, and X. Wallart, "Impact of P/In flux ratio and epilayer thickness on faceting for nanoscale selective area growth of InP by molecular beam epitaxy", *Nanotechnology*, vol. 26, no. 29, p. 295 301, 2015. DOI: 10.1088/0957-4484/26/29/295301.

[188] R. Oga, S. Yamamoto, I. Ohzawa, Y. Fujiwara, and Y. Takeda, "Droplet Hetero-Epitaxy of InAs Quantum Structures on InP Nanopyramids Formed by Selective-Area Flow Rate Modulation Epitaxy", *Japanese Journal of Applied Physics*, vol. 41, no. Part 1, No. 2B, pp. 1026–1029, 2002. DOI: 10.1143/JJAP.41.1026.

[189] R. Oga, S. Yamamoto, I. Ohzawa, Y. Fujiwara, and Y. Takeda, "Improved size control of InP nanopyramids by selective-area flow rate modulation epitaxy", *Journal of Crystal Growth*, vol. 237-239, no. 1-4 I, pp. 239–243, 2002. DOI: 10.1016/S0022-0248(01)01882-6.

[190] Y. Yoshida, R. Oga, W. S. Lee, Y. Fujiwara, and Y. Takeda, "Fabrication of InAs quantum dots by droplet heteroepitaxy on periodic arrays of InP nanopyramids", *Thin Solid Films*, vol. 464-465, pp. 240–243, 2004. DOI: 10.1016/j.tsf.2004.06.044.

[191] J. Yuan, H. Wang, P. J. van Veldhoven, and R. Nötzel, "Impact of base size and shape on formation control of multifaceted InP nanopyramids by selective area metal organic vapor phase epitaxy", *Journal of Applied Physics*, vol. 106, no. 12, p. 124 304, 2009. DOI: 10.1063/1.3267856.

[192] S. Conesa-Boj, E. Russo-Averchi, A. Dalmau-Mallorqui, J. Trevino, E. F. Pecora, C. Forestiere, A. Handin, M. Ek, L. Zweifel, L. R. Wallenberg, D. Rüffer, M. Heiss, D. Troadec, L. Dal Negro, P. Caroff, and A. Fontcuberta i Morral, "Vertical "III–V" V-Shaped Nanomembranes Epitaxially Grown on a Patterned Si[001] Substrate and Their Enhanced Light Scattering", *ACS Nano*, vol. 6, no. 12, pp. 10 982–10 991, 2012. DOI: 10.1021/nn304526k.

[193] J. Seidl, J. G. Gluschke, X. Yuan, S. Naureen, N. Shahid, H. H. Tan, C. Jagadish, A. P. Micolich, and P. Caroff, "Regaining a spatial dimension: mechanically-transferrable 2D InAs nanofins grown by selective area epitaxy", *Nano Letters*, acs.nanolett.9b01703, 2019. DOI: 10.1021/acs.nanolett.9b01703.

Bibliography

[194]   J. Treu, M. Speckbacher, K. Saller, S. Morkötter, M. Döblinger, X. Xu, H. Riedl, G. Abstreiter, J. J. Finley, and G. Koblmüller, "Widely tunable alloy composition and crystal structure in catalyst-free InGaAs nanowire arrays grown by selective area molecular beam epitaxy", *Applied Physics Letters*, vol. 108, no. 5, 2016. DOI: 10.1063/1.4941407.

[195]   J. Vukajlovic-Plestina, W. Kim, V. G. Dubrovski, G. Tütüncüoğlu, M. Lagier, H. Potts, M. Friedl, and A. Fontcuberta i Morral, "Engineering the Size Distributions of Ordered GaAs Nanowires on Silicon", *Nano Letters*, vol. 17, no. 7, pp. 4101–4108, 2017. DOI: 10.1021/acs.nanolett.7b00842.

[196]   K. Ikejiri, T. Sato, H. Yoshida, K. Hiruma, J. Motohisa, S. Hara, and T. Fukui, "Growth characteristics of GaAs nanowires obtained by selective area metal-organic vapour-phase epitaxy", *Nanotechnology*, vol. 19, no. 26, p. 265 604, 2008. DOI: 10.1088/0957-4484/19/26/265604.

[197]   M. Cantoro, G. Brammertz, O. Richard, H. Bender, F. Clemente, M. Leys, S. Degroote, M. Caymax, M. Heyns, and S. De Gendt, "Controlled III/V Nanowire Growth by Selective-Area Vapor-Phase Epitaxy", *Journal of The Electrochemical Society*, vol. 156, no. 11, H860, 2009. DOI: 10.1149/1.3222852.

[198]   K. Tomioka, Y. Kobayashi, J. Motohisa, S. Hara, and T. Fukui, "Selective-area growth of vertically aligned GaAs and GaAs/AlGaAs core–shell nanowires on Si(111) substrate", *Nanotechnology*, vol. 20, no. 14, p. 145 302, 2009. DOI: 10.1088/0957-4484/20/14/145302.

[199]   K. Tomioka, J. Motohisa, S. Hara, K. Hiruma, and T. Fukui, "GaAs/AlGaAs core multishell nanowire-based light-emitting diodes on Si", *Nano Letters*, vol. 10, no. 5, pp. 1639–1644, 2010. DOI: 10.1021/nl9041774.

[200]   J. N. Shapiro, A. Lin, P. S. Wong, A. C. Scofield, C. Tu, P. N. Senanayake, G. Mariani, B. L. Liang, and D. L. Huffaker, "InGaAs heterostructure formation in catalyst-free GaAs nanopillars by selective-area metal-organic vapor phase epitaxy", *Applied Physics Letters*, vol. 97, no. 24, p. 243 102, 2010. DOI: 10.1063/1.3526734.

[201]   G. Mariani, A. C. Scofield, C.-H. Hung, and D. L. Huffaker, "GaAs nanopillar-array solar cells employing in situ surface passivation", *Nature Communications*, vol. 4, no. 1, p. 1497, 2013. DOI: 10.1038/ncomms2509.

[202]   J. P. P. Kakko, T. Haggrén, V. Dhaka, T. Huhtio, A. Peltonen, H. Jiang, E. Kauppinen, and H. Lipsanen, "Fabrication of dual-type nanowire arrays on a single substrate", *Nano Letters*, vol. 15, no. 3, pp. 1679–1683, 2015. DOI: 10.1021/nl504308x.

[203]   M. Yao, C. Sheng, M. Ge, C.-Y. Chi, S. Cong, A. Nakano, P. D. Dapkus, and C. Zhou, "Facile Five-Step Heteroepitaxial Growth of GaAs Nanowires on Silicon Substrates and the Twin Formation Mechanism", *ACS Nano*, vol. 10, no. 2, pp. 2424–2435, 2016. DOI: 10.1021/acsnano.5b07232.

[204]   S. D. Hersee, X. Sun, and X. Wang, "The controlled growth of GaN nanowires", *Nano Letters*, vol. 6, no. 8, pp. 1808–1811, 2006. DOI: 10.1021/nl060553t.

[205] D. Saxena, F. Wang, Q. Gao, S. Mokkapati, H. H. Tan, and C. Jagadish, "Mode Profiling of Semiconductor Nanowire Lasers", *Nano Letters*, vol. 15, no. 8, pp. 5342–5348, 2015. DOI: 10.1021/acs.nanolett.5b01713.

[206] Q. Gao, V. G. Dubrovskii, P. Caroff, J. Wong-Leung, L. Li, Y. Guo, L. Fu, H. H. Tan, and C. Jagadish, "Simultaneous Selective-Area and Vapor–Liquid–Solid Growth of InP Nanowire Arrays", *Nano Letters*, vol. 16, no. 7, pp. 4361–4367, 2016. DOI: 10.1021/acs.nanolett.6b01461.

[207] M. T. Robson, V. G. Dubrovskii, and R. R. LaPierre, "Conditions for high yield of selective-area epitaxy InAs nanowires on SiOx /Si(111) substrates", *Nanotechnology*, vol. 26, no. 46, p. 465 301, 2015. DOI: 10.1088/0957-4484/26/46/465301.

[208] M. Robson and R. LaPierre, "InAs nanowire growth modes on Si (111) by gas source molecular beam epitaxy", *Journal of Crystal Growth*, vol. 436, pp. 1–11, 2016. DOI: 10.1016/j.jcrysgro.2015.11.035.

[209] K. Tomioka, J. Motohisa, S. Hara, and T. Fukui, "Control of InAs nanowire growth directions on Si.", *Nano letters*, vol. 8, no. 10, pp. 3475–80, 2008. DOI: 10.1021/nl802398j.

[210] X. Ji, X. Yang, W. Du, H. Pan, and T. Yang, "Selective-Area MOCVD Growth and Carrier-Transport-Type Control of InAs(Sb)/GaSb Core–Shell Nanowires", *Nano Letters*, vol. 16, no. 12, pp. 7580–7587, 2016. DOI: 10.1021/acs.nanolett.6b03429.

[211] M. Hata, A. Watanabe, and T. Isu, "Surface diffusion length observed by in situ scanning microprobe reflection high-energy electron diffraction", *Journal of Crystal Growth*, vol. 111, no. 1-4, pp. 83–87, 1991. DOI: 10.1016/0022-0248(91)90951-Z.

[212] X.-Q. Shen, D. Kishimoto, and T. Nishinaga, "Arsenic Pressure Dependence of Surface Diffusion of Ga on Nonplanar GaAs Substrates", *Japanese Journal of Applied Physics*, vol. 33, no. Part 1, No.1A, pp. 11–17, 1994. DOI: 10.1143/JJAP.33.11.

[213] V. G. Dubrovskii, G. E. Cirlin, I. P. Soshnikov, A. A. Tonkikh, N. V. Sibirev, Y. B. Samso-nenko, and V. M. Ustinov, "Diffusion-induced growth of GaAs nanowhiskers during molecular beam epitaxy: Theory and experiment", *Physical Review B*, vol. 71, no. 20, p. 205 325, 2005. DOI: 10.1103/PhysRevB.71.205325.

[214] T. Sugaya, T. Nakagawa, Y. Sugiyama, Y. Tanuma, and K. Yonei, "Difference in Diffusion Length of Ga Atoms under As 2 and As 4 Flux in Molecular Beam Epitaxy", *Japanese Journal of Applied Physics*, vol. 36, no. Part 1, No. 9A, pp. 5670–5673, 1997. DOI: 10.1143/JJAP.36.5670.

[215] H. Schmid, M. Borg, K. Moselund, L. Gignac, C. M. Breslin, J. Bruley, D. Cutaia, and H. Riel, "Template-assisted selective epitaxy of III–V nanoscale devices for co-planar heterogeneous integration with Si", *Applied Physics Letters*, vol. 106, no. 23, p. 233 101, 2015. DOI: 10.1063/1.4921962.

[216] M. Borg, H. Schmid, K. E. Moselund, D. Cutaia, and H. Riel, "Mechanisms of template-assisted selective epitaxy of InAs nanowires on Si", *Journal of Applied Physics*, vol. 117, no. 14, p. 144 303, 2015. DOI: 10.1063/1.4916984.

Bibliography

[217]   J. Gooth, M. Borg, H. Schmid, V. Schaller, S. Wirths, K. Moselund, M. Luisier, S. Karg, and H. Riel, "Ballistic One-Dimensional InAs Nanowire Cross-Junction Interconnects", *Nano Letters*, vol. 17, no. 4, pp. 2596–2602, 2017. DOI: 10.1021/acs.nanolett.7b00400.

[218]   J. Vukajlovic-Plestina, W. Kim, L. Ghisalberti, G. Varnavides, G. Tütüncuoglu, H. Potts, M. Friedl, L. Güniat, W. C. Carter, V. G. Dubrovskii, and A. Fontcuberta i Morral, "Fundamental aspects to localize self-catalyzed III-V nanowires on silicon", *Nature Communications*, vol. 10, no. 1, p. 869, 2019. DOI: 10.1038/s41467-019-08807-9.

[219]   D. Dalacu, A. Kam, D. G. Austing, and P. J. Poole, "Droplet Dynamics in Controlled InAs Nanowire Interconnections", *Nano Letters*, vol. 13, no. 6, pp. 2676–2681, 2013. DOI: 10.1021/nl400820w.

[220]   C. Kittel, *Introduction to Solid State Physics*, 8th ed. John Wiley & Sons, Inc, 2005, pp. 1–681. DOI: 10.1119/1.1974177.

[221]   S. Sze and K. K. Ng, *Physics of Semiconductor Devices*. Hoboken, NJ, USA: John Wiley & Sons, Inc., 2006, pp. 1–815. DOI: 10.1002/0470068329.

[222]   S. Sze and J. Irvin, "Resistivity, mobility and impurity levels in GaAs, Ge, and Si at 300K", *Solid-State Electronics*, vol. 11, no. 6, pp. 599–602, 1968. DOI: 10.1016/0038-1101(68)90012-9.

[223]   W. G. Spitzer and M. B. Panish, "Silicon-Doped Gallium Arsenide Grown from Gallium Solution: Silicon Site Distribution", *Journal of Applied Physics*, vol. 40, no. 10, pp. 4200–4202, 1969. DOI: 10.1063/1.1657165.

[224]   C. Domke, P. Ebert, M. Heinrich, and K. Urban, "Microscopic identification of the compensation mechanisms in Si-doped GaAs", *Physical Review B*, vol. 54, no. 15, pp. 10 288–10 291, 1996. DOI: 10.1103/PhysRevB.54.10288.

[225]   J. E. Northrup and S. B. Zhang, "Dopant and defect energetics: Si in GaAs", *Physical Review B*, vol. 47, no. 11, pp. 6791–6794, 1993. DOI: 10.1103/PhysRevB.47.6791.

[226]   D. Long, "Scattering of Conduction Electrons by Lattice Vibrations in Silicon", *Physical Review*, vol. 120, no. 6, pp. 2024–2032, 1960. DOI: 10.1103/PhysRev.120.2024.

[227]   H. Ehrenreich, "Band structure and electron transport of GaAs", *Physical Review*, vol. 120, no. 6, pp. 1951–1963, 1960. DOI: 10.1103/PhysRev.120.1951.

[228]   A. Fortini, D. Diguet, and J. Lugand, "Analysis of Polar Optical Scattering of Electrons in GaAs", *Journal of Applied Physics*, vol. 41, no. 7, pp. 3121–3127, 1970. DOI: 10.1063/1.1659373.

[229]   C. M. Wolfe, G. E. Stillman, and W. T. Lindley, "Electron mobility in high-purity GaAs", *Journal of Applied Physics*, vol. 41, no. 7, pp. 3088–3091, 1970. DOI: 10.1063/1.1659368.

[230]   E. Conwell and V. F. Weisskopf, "Theory of Impurity Scattering in Semiconductors", *Physical Review*, vol. 77, no. 3, pp. 388–390, 1950. DOI: 10.1103/PhysRev.77.388.

[231]   C. Erginsoy, "Neutral Impurity Scattering in Semiconductors", *Physical Review*, vol. 79, no. 6, pp. 1013–1014, 1950. DOI: 10.1103/PhysRev.79.1013.

[232] C. Sah, T. Ning, and L. Tschopp, "The scattering of electrons by surface oxide charges and by lattice vibrations at the silicon-silicon dioxide interface", *Surface Science*, vol. 32, no. 3, pp. 561–575, 1972. DOI: 10.1016/0039-6028(72)90183-5.

[233] R. Gottinger, A. Gold, G. Abstreiter, G. Weimann, and W. Schlapp, "Interface Roughness Scattering and Electron Mobilities in Thin GaAs Quantum Wells", *Europhysics Letters (EPL)*, vol. 6, no. 2, pp. 183–188, 1988. DOI: 10.1209/0295-5075/6/2/015.

[234] C. R. Bolognesi, H. Kroemer, and J. H. English, "Interface roughness scattering in InAs/AlSb quantum wells", *Applied Physics Letters*, vol. 61, no. 2, pp. 213–215, 1992. DOI: 10.1063/1.108221.

[235] T. Ihn, *Semiconductor Nanostructures*. Oxford University Press, 2009, p. 580. DOI: 10.1093/acprof:oso/9780199534425.001.0001.

[236] G. Bergmann, "Weak localization in thin films", *Physics Reports*, vol. 107, no. 1, pp. 1–58, 1984. DOI: 10.1016/0370-1573(84)90103-0.

[237] S. Chakravarty and A. Schmid, "Weak localization: The quasiclassical theory of electrons in a random potential", *Physics Reports*, vol. 140, no. 4, pp. 193–236, 1986. DOI: 10.1016/0370-1573(86)90027-X.

[238] W. Knap, C. Skierbiszewski, A. Zduniak, E. Litwin-Staszewska, D. Bertho, F. Kobbi, J. L. Robert, G. E. Pikus, F. G. Pikus, S. V. Iordanskii, V. Mosser, K. Zekentes, and Y. B. Lyanda-Geller, "Weak antilocalization and spin precession in quantum wells", *Physical Review B*, vol. 53, no. 7, pp. 3912–3924, 1996. DOI: 10.1103/PhysRevB.53.3912.

[239] G. Dresselhaus, "Spin-Orbit Coupling Effects in Zinc Blende Structures", *Physical Review*, vol. 100, no. 2, pp. 580–586, 1955. DOI: 10.1103/PhysRev.100.580.

[240] E. Rashba and I. Boiko, "Properties of semiconductors with an extremum loop: III. Behavior in a magnetic field parallel to the plane of the loop", *Sov. Phys. Solid State*, vol. 2, pp. 1109–1122, 1960.

[241] A. Manchon, H. C. Koo, J. Nitta, S. M. Frolov, and R. A. Duine, "New perspectives for Rashba spin–orbit coupling", *Nature Materials*, vol. 14, no. 9, pp. 871–882, 2015. DOI: 10.1038/nmat4360.

[242] T. Koga, J. Nitta, T. Akazaki, and H. Takayanagi, "Rashba Spin-Orbit Coupling Probed by the Weak Antilocalization Analysis in InAlAs/InGaAs/InAlAs Quantum Wells as a Function of Quantum Well Asymmetry", *Physical Review Letters*, vol. 89, no. 4, p. 046801, 2002. DOI: 10.1103/PhysRevLett.89.046801.

[243] J. Nitta and T. Koga, *Rashba spin-orbit interaction and its applications to spin-interference effect and spin-filter device*, 2003. DOI: 10.1023/A:1025309805995.

[244] S. Dhara, H. S. Solanki, V. Singh, A. Narayanan, P. Chaudhari, M. Gokhale, A. Bhattacharya, and M. M. Deshmukh, "Magnetotransport properties of individual InAs nanowires", *Physical Review B*, vol. 79, no. 12, p. 121311, 2009. DOI: 10.1103/PhysRevB.79.121311.

Bibliography

[245]   A. Iorio, M. Rocci, L. Bours, M. Carrega, V. Zannier, L. Sorba, S. Roddaro, F. Giazotto, and E. Strambini, "Vectorial Control of the Spin-Orbit Interaction in Suspended InAs Nanowires", *Nano Letters*, vol. 19, no. 2, pp. 652–657, 2019. DOI: 10.1021/acs.nanolett.8b02828.

[246]   F. G. Allen and G. W. Gobeli, "Work Function, Photoelectric Threshold, and Surface States of Atomically Clean Silicon", *Physical Review*, vol. 127, no. 1, pp. 150–158, 1962. DOI: 10.1103/PhysRev.127.150.

[247]   L. F. Wagner and W. E. Spicer, "Photoemission study of the effect of bulk doping and oxygen exposure on silicon surface states", *Physical Review B*, vol. 9, no. 4, pp. 1512–1515, 1974. DOI: 10.1103/PhysRevB.9.1512.

[248]   W. E. Spicer, I. Lindau, J. N. Miller, D. T. Ling, P. Pianetta, P. W. Chye, and C. M. Garner, "Studies of Surface Electronic Structure and Surface Chemistry Using Synchrotron Radiation", *Physica Scripta*, vol. 16, no. 5-6, pp. 388–397, 1977. DOI: 10.1088/0031-8949/16/5-6/037.

[249]   W. Spicer, P. Chye, C. Garner, I. Lindau, and P. Pianetta, "The surface electronic structure of 3-5 compounds and the mechanism of Fermi level pinning by oxygen (passivation) and metals (Schottky barriers)", *Surface Science*, vol. 86, pp. 763–788, 1979. DOI: 10.1016/0039-6028(79)90458-8.

[250]   S. Kawaji and H. C. Gatos, "Electric field effect on the magnetoresistance of indium arsenide surfaces in high magnetic fields", *Surface Science*, vol. 7, no. 2, pp. 215–228, 1967. DOI: 10.1016/0039-6028(67)90128-8.

[251]   D. C. Tsui, "Observation of Surface Bound State and Two-Dimensional Energy Band by Electron Tunneling", *Physical Review Letters*, vol. 24, no. 7, pp. 303–306, 1970. DOI: 10.1103/PhysRevLett.24.303.

[252]   M. Noguchi, K. Hirakawa, and T. Ikoma, "Intrinsic electron accumulation layers on reconstructed clean InAs(100) surfaces", *Physical Review Letters*, vol. 66, no. 17, pp. 2243–2246, 1991. DOI: 10.1103/PhysRevLett.66.2243.

[253]   L. Olsson, C. Andersson, M. Håkansson, J. Kanski, L. Ilver, and U. Karlsson, "Charge accumulation at InAs surfaces.", *Physical review letters*, vol. 76, no. 19, pp. 3626–3629, 1996.

[254]   H. S. Karlsson, R. Viselga, and U. O. Karlsson, "Electron accumulation at the InAs(110) cleavage surface", *Surface Science*, vol. 402-404, no. August 1997, pp. 590–594, 1998. DOI: 10.1016/S0039-6028(98)00002-8.

[255]   H. Carstensen, R. Claessen, R. Manzke, and M. Skibowski, "Direct determination of III-V semiconductor surface band gaps", *Physical Review B*, vol. 41, no. 14, pp. 9880–9885, 1990. DOI: 10.1103/PhysRevB.41.9880.

[256]   S. Abe, T. Inaoka, and M. Hasegawa, "Evolution of electron states at a narrow-gap semiconductor surface in an accumulation-layer formation process", *Physical Review B*, vol. 66, no. 20, p. 205 309, 2002. DOI: 10.1103/PhysRevB.66.205309.

[257] Y. Chen, J. C. Hermanson, and G. J. Lapeyre, "Coupled plasmon and phonon in the accumulation layer of InAs(110) cleaved surfaces", *Physical Review B*, vol. 39, no. 17, pp. 12 682–12 687, 1989. DOI: 10.1103/PhysRevB.39.12682.

[258] J. R. Weber, A. Janotti, and C. G. Van De Walle, "Intrinsic and extrinsic causes of electron accumulation layers on InAs surfaces", *Applied Physics Letters*, vol. 97, no. 19, 2010. DOI: 10.1063/1.3518061.

[259] H.-U. Baier, L. Koenders, and W. Mönch, "Oxidation of cleaved InAs(1 1 0) surfaces at room temperature: Surface band-bending and ionization energy", *Solid State Communications*, vol. 58, no. 5, pp. 327–331, 1986. DOI: 10.1016/0038-1098(86)90094-3.

[260] K. Smit, "Adsorption of chlorine and oxygen on cleaved InAs(110) surfaces: Raman spectroscopy, photoemission spectroscopy, and Kelvin probe measurements", *Journal of Vacuum Science & Technology B: Microelectronics and Nanometer Structures*, vol. 7, no. 4, p. 888, 1989. DOI: 10.1116/1.584619.

[261] V. Y. Aristov, G. Le Lay, L. T. Vinh, K. Hricovini, and J. E. Bonnet, "Giant band bending induced by Ag on InAs(110) surfaces at low temperature", *Physical Review B*, vol. 47, no. 4, pp. 2138–2145, 1993. DOI: 10.1103/PhysRevB.47.2138.

[262] T. van Gemmeren, S. Salmagne, and W. Mönch, "Atomic nitrogen on InAs(110) surfaces at room temperature", *Applied Surface Science*, vol. 65-66, no. C, pp. 625–631, 1993. DOI: 10.1016/0169-4332(93)90730-Y.

[263] C. Nowak, J. Krujatz, A. Märkl, C. Meyne, A. Chassé, W. Braun, W. Richter, and D. Zahn, "The adsorption of Sb on InAs(110) studied by photoemission and photoelectron diffraction", *Surface Science*, vol. 331-333, no. PART A, pp. 619–624, 1995. DOI: 10.1016/0039-6028(95)00329-0.

[264] J. Tersoff, "Schottky barriers and semiconductor band structures", *Physical Review B*, vol. 32, no. 10, pp. 6968–6971, 1985. DOI: 10.1103/PhysRevB.32.6968.

[265] L. F. Piper, T. D. Veal, M. J. Lowe, and C. F. McConville, "Electron depletion at InAs free surfaces: Doping-induced acceptorlike gap states", *Physical Review B - Condensed Matter and Materials Physics*, vol. 73, no. 19, pp. 1–7, 2006. DOI: 10.1103/PhysRevB.73.195321.

[266] W. Zhou and Z. L. Wang, *Scanning Microscopy for Nanotechnology*, W. Zhou and Z. L. Wang, Eds. New York, NY: Springer New York, 2007. DOI: 10.1007/978-0-387-39620-0.

[267] M. Goulding, "The selective epitaxial growth of silicon", *Materials Science and Engineering: B*, vol. 17, no. 1, pp. 47–67, 1993. DOI: 10.1016/0921-5107(93)90080-7.

[268] A. Y. Cho and W. C. Ballamy, "GaAs planar technology by molecular beam epitaxy (MBE)", *Journal of Applied Physics*, vol. 46, no. 2, pp. 783–785, 1975. DOI: 10.1063/1.321645.

[269]   T. S. Cheng, A. Davies, A. Summerfield, Y. Cho, I. Cebula, R. J. A. Hill, C. J. Mellor, A. N. Khlobystov, T. Taniguchi, K. Watanabe, P. H. Beton, C. T. Foxon, L. Eaves, and S. V. Novikov, "High temperature MBE of graphene on sapphire and hexagonal boron nitride flakes on sapphire", *Journal of Vacuum Science & Technology B, Nanotechnology and Microelectronics: Materials, Processing, Measurement, and Phenomena*, vol. 34, no. 2, p. 02L101, 2016. DOI: 10.1116/1.4938157.

[270]   V. Umansky, M. Heiblum, Y. Levinson, J. Smet, J. Nübler, and M. Dolev, "MBE growth of ultra-low disorder 2DEG with mobility exceeding 35×106 cm2/V s", *Journal of Crystal Growth*, vol. 311, no. 7, pp. 1658–1661, 2009. DOI: 10.1016/j.jcrysgro.2008.09.151.

[271]   R. L. Samaraweera, H. C. Liu, B. Gunawardana, A. Kriisa, C. Reichl, W. Wegscheider, and R. G. Mani, "Coherent backscattering in quasi-ballistic ultra-high mobility GaAs/Al-GaAs 2DES", *Scientific Reports*, vol. 8, no. 1, pp. 1–8, 2018. DOI: 10.1038/s41598-018-28359-0.

[272]   V. G. Dubrovskii, G. E. Cirlin, I. P. Soshnikov, a. a. Tonkikh, N. V. Sibirev, Y. B. Samsonenko, and V. M. Ustinov, "Diffusion-induced growth of GaAs nanowhiskers during molecular beam epitaxy: Theory and experiment", *Physical Review B*, vol. 71, no. 20, p. 205 325, 2005. DOI: 10.1103/PhysRevB.71.205325.

[273]   B. Inkson, "Scanning electron microscopy (SEM) and transmission electron microscopy (TEM) for materials characterization", in *Materials Characterization Using Nondestructive Evaluation (NDE) Methods*, Elsevier, 2016, pp. 17–43. DOI: 10.1016/B978-0-08-100040-3.00002-X.

[274]   D. W. Aitken and R. S. Frankel, "High-resolution, energy-dispersive microcalorimeter spectrometer for X-ray microanalysis", *Applied Spectroscopy, Vol. 24, Issue 6, pp. 557-566*, vol. 24, no. 6, pp. 557–566, 1970.

[275]   D. B. Williams, A. J. Papworth, and M. Watanabe, "High resolution X-ray mapping in the STEM", in *Journal of Electron Microscopy*, vol. 51, 2002, S113–S126. DOI: 10.1093/jmicro/51.Supplement.S113.

[276]   D. I. Enache, J. K. Edwards, P. Landon, B. Solsona-Espriu, A. F. Carley, A. A. Herzing, M. Watanabe, C. J. Kiely, D. W. Knight, and G. J. Hutchings, "Solvent-free oxidation of primary alcohols to aldehydes using Au-Pd/TiO2 catalyst", *Science*, vol. 311, no. 5759, pp. 362–365, 2006. DOI: 10.1126/science.1120560.

[277]   A. A. Herzing, M. Watanabe, J. K. Edwards, M. Conte, Z.-R. Tang, G. J. Hutchings, and C. J. Kiely, "Energy dispersive X-ray spectroscopy of bimetallic nanoparticles in an aberration corrected scanning transmission electron microscope", *Faraday Discuss.*, vol. 138, pp. 337–351, 2008. DOI: 10.1039/B706293C.

[278]   A. J. D'Alfonso, B. Freitag, D. Klenov, and L. J. Allen, "Atomic-resolution chemical mapping using energy-dispersive x-ray spectroscopy", *Physical Review B*, vol. 81, no. 10, p. 100 101, 2010. DOI: 10.1103/PhysRevB.81.100101.

[279]   H. A. Potts, "Gold-free Growth of InAs Nanowires: Growth , Structural & Electrical Properties", PhD thesis, EPFL, 2017. DOI: 10.5075/epfl-thesis-7939.

[280] D. Loss and D. P. DiVincenzo, "Quantum Computation with Quantum Dots", *Physical Review A*, vol. 57, no. 1, p. 12, 1998. DOI: 10.1103/PhysRevA.57.120.

[281] D. Kielpinski, C. Monroe, and D. J. Wineland, "Architecture for a large-scale ion-trap quantum computer", *Nature*, vol. 417, no. 6890, pp. 709–711, 2002. DOI: 10.1038/nature00784.

[282] D. Gottesman, "An introduction to quantum error correction and fault-tolerant quantum computation", in *Proceedings of Symposia in Applied Mathematics*, vol. 0000, 2010, pp. 13–58. DOI: 10.1090/psapm/068/2762145.

[283] D. J. Reilly, "Engineering the quantum-classical interface of solid-state qubits", *npj Quantum Information*, vol. 1, no. April, p. 15 011, 2015. DOI: 10.1038/npjqi.2015.11.

[284] S. Takahashi, I. S. Tupitsyn, J. van Tol, C. C. Beedle, D. N. Hendrickson, and P. C. E. Stamp, "Decoherence in crystals of quantum molecular magnets", *Nature*, vol. 476, no. 7358, pp. 76–79, 2011. DOI: 10.1038/nature10314.

[285] J. Goetz, F. Deppe, P. Eder, M. Fischer, M. Müting, J. P. Martínez, S. Pogorzalek, F. Wulschner, E. Xie, K. G. Fedorov, A. Marx, and R. Gross, "Second-order decoherence mechanisms of a transmon qubit probed with thermal microwave states", *Quantum Science and Technology*, vol. 2, no. 2, p. 025 002, 2017. DOI: 10.1088/2058-9565/aa66e7.

[286] A. Kitaev, "Fault-tolerant quantum computation by anyons", *Annals of Physics*, vol. 303, no. 1, pp. 2–30, 2003. DOI: 10.1016/S0003-4916(02)00018-0.

[287] A. Stern and N. H. Lindner, "Topological Quantum Computation–From Basic Concepts to First Experiments", *Science*, vol. 339, no. 6124, pp. 1179–1184, 2013. DOI: 10.1126/science.1231473.

[288] S. M. Albrecht, A. P. Higginbotham, M. Madsen, F. Kuemmeth, T. S. Jespersen, J. Nygård, P. Krogstrup, and C. M. Marcus, "Exponential protection of zero modes in Majorana islands", *Nature*, vol. 531, no. 7593, pp. 206–209, 2016. DOI: 10.1038/nature17162.

[289] E. J. H. Lee, X. Jiang, R. Aguado, G. Katsaros, C. M. Lieber, and S. De Franceschi, "Zero-Bias Anomaly in a Nanowire Quantum Dot Coupled to Superconductors", *Physical Review Letters*, vol. 109, no. 18, p. 186 802, 2012. DOI: 10.1103/PhysRevLett.109.186802.

[290] E. J. Lee, X. Jiang, M. Houzet, R. Aguado, C. M. Lieber, and S. De Franceschi, "Spin-resolved Andreev levels and parity crossings in hybrid superconductor-semiconductor nanostructures", *Nature Nanotechnology*, vol. 9, no. 1, pp. 79–84, 2014. DOI: 10.1038/nnano.2013.267.

[291] R. M. Lutchyn, E. P. A. M. Bakkers, L. P. Kouwenhoven, P. Krogstrup, C. M. Marcus, and Y. Oreg, "Majorana zero modes in superconductor–semiconductor heterostructures", *Nature Reviews Materials*, vol. 3, no. 5, pp. 52–68, 2018. DOI: 10.1038/s41578-018-0003-1.

[292] Y. Huang, "Logic Gates and Computation from Assembled Nanowire Building Blocks", *Science*, vol. 294, no. 5545, pp. 1313–1317, 2001. DOI: 10.1126/science.1066192.

Bibliography

[293] Y. Huang, X. Duan, Q. Wei, and C. M. Lieber, "Directed assembly of one-dimensional nanostructures into functional networks", *Science*, vol. 291, no. 5504, pp. 630–633, 2001. DOI: 10.1126/science.291.5504.630.

[294] N. A. Melosh, A. Boukai, F. Diana, B. Gerardot, A. Badolato, P. M. Petroff, and J. R. Heath, "Ultrahigh-density nanowire lattices and circuits", *Science*, vol. 300, no. 5616, pp. 112–115, 2003. DOI: 10.1126/science.1081940.

[295] Ö. Gül, D. J. V. Woerkom, I. V. Weperen, D. Car, S. R. Plissard, E. P. a. M. Bakkers, and L. P. Kouwenhoven, "Towards high mobility InSb nanowire devices", *Nanotechnology*, vol. 26, no. 21, p. 215 202, 2015. DOI: 10.1088/0957-4484/26/21/215202.

[296] T. Rieger, D. Rosenbach, D. Vakulov, S. Heedt, T. Schäpers, D. Grützmacher, and M. I. Lepsa, "Crystal Phase Transformation in Self-Assembled InAs Nanowire Junctions on Patterned Si Substrates", *Nano Letters*, vol. 16, no. 3, pp. 1933–1941, 2016. DOI: 10.1021/acs.nanolett.5b05157.

[297] J. H. Kang, Y. Cohen, Y. Ronen, M. Heiblum, R. Buczko, P. Kacman, R. Popovitz-Biro, and H. Shtrikman, "Crystal structure and transport in merged InAs nanowires MBE grown on (001) InAs", *Nano Letters*, vol. 13, no. 11, pp. 5190–5196, 2013. DOI: 10.1021/nl402571s.

[298] C. B. Collins, R. O. Carlson, and C. J. Gallagher, "Properties of gold-doped silicon", *Physical Review*, vol. 105, no. 4, pp. 1168–1173, 1957. DOI: 10.1103/PhysRev.105.1168.

[299] Z. Yang, A. Surrente, G. Tutuncuoglu, K. Galkowski, M. Cazaban-Carrazé, F. Amaduzzi, P. Leroux, D. K. Maude, A. Fontcuberta i Morral, and P. Plochocka, "Revealing Large-Scale Homogeneity and Trace Impurity Sensitivity of GaAs Nanoscale Membranes", *Nano Letters*, vol. 17, no. 5, pp. 2979–2984, 2017. DOI: 10.1021/acs.nanolett.7b00257.

[300] C.-Y. Chi, C.-C. Chang, S. Hu, T.-W. Yeh, S. B. Cronin, and P. D. Dapkus, "Twin-Free GaAs Nanosheets by Selective Area Growth: Implications for Defect-Free Nanostructures", *Nano Letters*, vol. 13, no. 6, pp. 2506–2515, 2013. DOI: 10.1021/nl400561j.

[301] M. de la Mata, C. Magén, P. Caroff, and J. Arbiol, "Atomic Scale Strain Relaxation in Axial Semiconductor III–V Nanowire Heterostructures", *Nano Letters*, vol. 14, no. 11, pp. 6614–6620, 2014. DOI: 10.1021/nl503273j.

[302] M. de la Mata, R. Leturcq, S. R. Plissard, C. Rolland, C. Magén, J. Arbiol, and P. Caroff, "Twin-Induced InSb Nanosails: A Convenient High Mobility Quantum System", *Nano Letters*, vol. 16, no. 2, pp. 825–833, 2016. DOI: 10.1021/acs.nanolett.5b05125.

[303] M. O. Lipinski, H. Schuler, O. G. Schmidt, K. Eberl, and N. Y. Jin-Phillipp, "Strain-induced material intermixing of InAs quantum dots in GaAs", *Applied Physics Letters*, vol. 77, no. 12, p. 1789, 2000. DOI: 10.1063/1.1311314.

[304] E. Pehlke, N. Moll, and M. Scheffler, "The Equilibrium Shape of Quantum Dots", *Quantum*, p. 10, 1996.

[305]   N. Moll, M. Scheffler, and E. Pehlke, "Influence of surface stress on the equilibrium shape of strained quantum dots", *Physical Review B*, vol. 58, no. 8, pp. 4566–4571, 1998. DOI: 10.1103/PhysRevB.58.4566.

[306]   J. G. Belk, D. W. Pashley, C. F. McConville, J. L. Sudijono, B. A. Joyce, and T. S. Jones, "Surface atomic configurations due to dislocation activity in InAs/GaAs(110) heteroepitaxy", *Physical Review B*, vol. 56, no. 16, pp. 10 289–10 296, 1997. DOI: 10.1103/PhysRevB.56.10289.

[307]   B. Z. Nosho, L. A. Zepeda-Ruiz, R. I. Pelzel, W. H. Weinberg, and D. Maroudas, "Surface morphology in InAs/GaAs(111)A heteroepitaxy: Experimental measurements and computer simulations", *Applied Physics Letters*, vol. 75, no. 6, pp. 829–831, 1999. DOI: 10.1063/1.124527.

[308]   J. M. Garcia, G. Medeiros-Ribeiro, K. Schmidt, T. Ngo, J. L. Feng, A. Lorke, J. Kotthaus, and P. M. Petroff, "Intermixing and shape changes during the formation of InAs self-assembled quantum dots", *Applied Physics Letters*, vol. 71, no. 14, pp. 2014–2016, 1997. DOI: 10.1063/1.119772.

[309]   C. W. J. Beenakker and H. van Houten, "Boundary scattering and weak localization of electrons in a magnetic field", *Physical Review B*, vol. 38, no. 5, pp. 3232–3240, 1988. DOI: 10.1103/PhysRevB.38.3232.

[310]   A. Trampert, E. Tournie, and K. H. Ploog, "Influence of the Growth Mode on the Microstructure of Highly Mismatched InAs/GaAs Heterostructures", *Physica Status Solidi (a)*, vol. 145, no. 2, pp. 481–489, 1994. DOI: 10.1002/pssa.2211450231.

[311]   L. E. Ocola and A. Stein, "Effect of cold development on improvement in electron-beam nanopatterning resolution and line roughness", *Journal of Vacuum Science & Technology B: Microelectronics and Nanometer Structures*, vol. 24, no. 6, p. 3061, 2006. DOI: 10.1116/1.2366698.

[312]   D. B. Suyatin, C. Thelander, M. T. Björk, I. Maximov, and L. Samuelson, "Sulfur passivation for ohmic contact formation to InAs nanowires", *Nanotechnology*, vol. 18, no. 10, p. 105 307, 2007. DOI: 10.1088/0957-4484/18/10/105307.

[313]   S. Hikami, A. I. Larkin, and Y. Nagaoka, "Spin-Orbit Interaction and Magnetoresistance in the Two Dimensional Random System", *Progress of Theoretical Physics*, vol. 63, no. 2, pp. 707–710, 1980. DOI: 10.1143/ptp.63.707.

[314]   B. Al'Tshuler and A. Aronov, "Magnetoresistance of thin films and of wires in a longitudinal magnetic field", *Soviet Journal of Experimental and Theoretical Physics Letters*, vol. 33, no. 10, p. 499, 1981.

[315]   Z. Sun, O. Hazut, R. Yerushalmi, L. J. Lauhon, and D. N. Seidman, "Criteria and considerations for preparing atom-probe tomography specimens of nanomaterials utilizing an encapsulation methodology", *Ultramicroscopy*, vol. 184, pp. 225–233, 2018. DOI: 10.1016/j.ultramic.2017.09.007.

Bibliography

[316]   K. Thompson, D. Lawrence, D. Larson, J. Olson, T. Kelly, and B. Gorman, "In situ site-specific specimen preparation for atom probe tomography", *Ultramicroscopy*, vol. 107, no. 2-3, pp. 131–139, 2007. DOI: 10.1016/j.ultramic.2006.06.008.

[317]   D. C. Tsui, H. L. Stormer, and A. C. Gossard, "Two-Dimensional Magnetotransport in the Extreme Quantum Limit", *Physical Review Letters*, vol. 48, no. 22, pp. 1559–1562, 1982. DOI: 10.1103/PhysRevLett.48.1559.

[318]   K. von Klitzing, "The quantized Hall effect", *Reviews of Modern Physics*, vol. 58, no. 3, pp. 519–531, 1986. DOI: 10.1103/RevModPhys.58.519.

[319]   H. L. Stormer, "Nobel Lecture: The fractional quantum Hall effect", *Reviews of Modern Physics*, vol. 71, no. 4, pp. 875–889, 1999. DOI: 10.1103/RevModPhys.71.875.

[320]   M. Gonschorek, J.-F. Carlin, E. Feltin, M. A. Py, and N. Grandjean, "High electron mobility lattice-matched AlInN/GaN field-effect transistor heterostructures", *Applied Physics Letters*, vol. 89, no. 6, p. 062 106, 2006. DOI: 10.1063/1.2335390.

[321]   J. A. Del Alamo, "The high-electron mobility transistor at 30: Impressive accomplishments and exciting prospects", in *2011 International Conference on Compound Semiconductor Manufacturing Technology, CS MANTECH 2011*, 2011.

[322]   M. J. Manfra, "Molecular Beam Epitaxy of Ultra-High-Quality AlGaAs/GaAs Heterostructures: Enabling Physics in Low-Dimensional Electronic Systems", *Annual Review of Condensed Matter Physics*, vol. 5, no. 1, pp. 347–373, 2014. DOI: 10.1146/annurev-conmatphys-031113-133905.

[323]   J. V. Holm, H. I. Jørgensen, P. Krogstrup, J. Nygard, H. Liu, M. Aagesen, J. Nygård, H. Liu, and M. Aagesen, "Surface-passivated GaAsP single-nanowire solar cells exceeding 10% efficiency grown on silicon", *Nature communications*, vol. 4, p. 1498, 2013. DOI: 10.1038/ncomms2510.

[324]   P. Krogstrup, H. I. Jørgensen, M. Heiss, O. Demichel, J. V. Holm, M. Aagesen, J. Nygard, and A. Fontcuberta i Morral, "Single-nanowire solar cells beyond the Shockley-Queisser limit", *Nature Photonics*, vol. 7, no. 4, pp. 306–310, 2013. DOI: 10.1038/nphoton.2013.32.

[325]   R. R. LaPierre, A. C. E. Chia, S. J. Gibson, C. M. Haapamaki, J. Boulanger, R. Yee, P. Kuyanov, J. Zhang, N. Tajik, N. Jewell, and K. M. A. Rahman, "III-V nanowire photovoltaics: Review of design for high efficiency", *physica status solidi (RRL) - Rapid Research Letters*, vol. 7, no. 10, pp. 815–830, 2013. DOI: 10.1002/pssr.201307109.

[326]   A. D. Mallorquí, E. Alarcón-Lladó, E. Russo-Averchi, G. Tütüncüoglu, F. Matteini, D. Rüffer, and A. F. I. Morral, "Characterization and analysis of InAs/p–Si heterojunction nanowire-based solar cell", *Journal of Physics D: Applied Physics*, vol. 47, no. 39, p. 394 017, 2014. DOI: 10.1088/0022-3727/47/39/394017.

[327]   A. D. Mallorquí, E. Alarcón-Lladó, I. C. Mundet, A. Kiani, B. Demaurex, S. De Wolf, A. Menzel, M. Zacharias, and A. Fontcuberta i Morral, "Field-effect passivation on silicon nanowire solar cells", *Nano Research*, vol. 8, no. 2, pp. 673–681, 2014. DOI: 10.1007/s12274-014-0551-7.

[328] J. Svensson, N. Anttu, N. Vainorius, B. M. Borg, and L. E. Wernersson, "Diameter-dependent photocurrent in InAsSb nanowire infrared photodetectors", *Nano Letters*, vol. 13, no. 4, pp. 1380–1385, 2013. DOI: 10.1021/nl303751d.

[329] T. Burgess, P. Caroff, Y. Wang, B. H. Badada, H. E. Jackson, L. M. Smith, Y. Guo, H. H. Tan, and C. Jagadish, "Zn 3 As 2 Nanowires and Nanoplatelets: Highly Efficient Infrared Emission and Photodetection by an Earth Abundant Material", *Nano Letters*, vol. 15, no. 1, pp. 378–385, 2015. DOI: 10.1021/nl5036918.

[330] M. Robson, K. M. Azizur-Rahman, D. Parent, P. Wojdylo, D. A. Thompson, and R. R. LaPierre, "Multispectral absorptance from large-diameter InAsSb nanowire arrays in a single epitaxial growth on silicon", *Nano Futures*, vol. 1, no. 3, p. 035 001, 2017. DOI: 10.1088/2399-1984/aa9015.

[331] R. R. LaPierre, M. Robson, K. M. Azizur-Rahman, and P. Kuyanov, "A review of III–V nanowire infrared photodetectors and sensors", *Journal of Physics D: Applied Physics*, vol. 50, no. 12, p. 123 001, 2017. DOI: 10.1088/1361-6463/aa5ab3.

[332] D. Saxena, S. Mokkapati, P. Parkinson, N. Jiang, Q. Gao, H. H. Tan, and C. Jagadish, "Optically pumped room-temperature GaAs nanowire lasers", *Nature Photonics*, vol. 7, no. 12, pp. 963–968, 2013. DOI: 10.1038/nphoton.2013.303.

[333] B. Mayer, D. Rudolph, J. Schnell, S. Morkötter, J. Winnerl, J. Treu, K. Müller, G. Bracher, G. Abstreiter, G. Koblmüller, and J. J. Finley, "Lasing from individual GaAs-AlGaAs core-shell nanowires up to room temperature", *Nature Communications*, vol. 4, no. 1, p. 2931, 2013. DOI: 10.1038/ncomms3931.

[334] J. Tatebayashi, S. Kako, J. Ho, Y. Ota, S. Iwamoto, and Y. Arakawa, "Room-temperature lasing in a single nanowire with quantum dots", *Nature Photonics*, vol. advance on, no. June, pp. 4–6, 2015. DOI: 10.1038/nphoton.2015.111.

[335] T. Burgess, D. Saxena, S. Mokkapati, Z. Li, C. R. Hall, J. A. Davis, Y. Wang, L. M. Smith, L. Fu, P. Caroff, H. H. Tan, and C. Jagadish, "Doping-enhanced radiative efficiency enables lasing in unpassivated GaAs nanowires", *Nature Communications*, vol. 7, no. 1, p. 11 927, 2016. DOI: 10.1038/ncomms11927.

[336] E. Bermúdez-Ureña, G. Tutuncuoglu, J. Cuerda, C. L. C. Smith, J. Bravo-Abad, S. I. Bozhevolnyi, A. Fontcuberta i Morral, F. J. García-Vidal, and R. Quidant, "Plasmonic Waveguide-Integrated Nanowire Laser", *Nano Letters*, vol. 17, no. 2, pp. 747–754, 2017. DOI: 10.1021/acs.nanolett.6b03879.

[337] J. Claudon, J. Bleuse, N. S. Malik, M. Bazin, P. Jaffrennou, N. Gregersen, C. Sauvan, P. Lalanne, and J.-M. Gérard, "A highly efficient single-photon source based on a quantum dot in a photonic nanowire", *Nature Photonics*, vol. 3, no. 2, pp. 116–116, 2010. DOI: 10.1038/nphoton.2009.287.

Bibliography

[338] M. Heiss, Y. Fontana, a. Gustafsson, G. Wüst, C. Magen, D. D. O'Regan, J. W. Luo, B. Ketterer, S. Conesa-Boj, a. V. Kuhlmann, J. Houel, E. Russo-Averchi, J. R. Morante, M. Cantoni, N. Marzari, J. Arbiol, a. Zunger, R. J. Warburton, and a. Fontcuberta i Morral, "Self-assembled quantum dots in a nanowire system for quantum photonics.", *Nature materials*, vol. 12, no. 5, pp. 439–44, 2013. DOI: 10.1038/nmat3557.

[339] T. Bryllert, L.-E. Wernersson, L. Froberg, and L. Samuelson, "Vertical high-mobility wrap-gated InAs nanowire transistor", *IEEE Electron Device Letters*, vol. 27, no. 5, pp. 323–325, 2006. DOI: 10.1109/LED.2006.873371.

[340] C. Blömers, T. Grap, M. I. Lepsa, J. Moers, S. Trellenkamp, D. Grützmacher, H. Lüth, and T. Schäpers, "Hall effect measurements on InAs nanowires", *Applied Physics Letters*, vol. 101, no. 15, 2012. DOI: 10.1063/1.4759124.

[341] A. Konar, J. Mathew, K. Nayak, M. Bajaj, R. K. Pandey, S. Dhara, K. V. R. M. Murali, and M. M. Deshmukh, "Carrier Transport in High Mobility InAs Nanowire Junctionless Transistors", *Nano Letters*, vol. 15, no. 3, pp. 1684–1690, 2015. DOI: 10.1021/nl5043165.

[342] H. J. Joyce, C. J. Docherty, Q. Gao, H. H. Tan, C. Jagadish, J. Lloyd-Hughes, L. M. Herz, and M. B. Johnston, "Electronic properties of GaAs, InAs and InP nanowires studied by terahertz spectroscopy.", *Nanotechnology*, vol. 24, no. 21, p. 214 006, 2013. DOI: 10.1088/0957-4484/24/21/214006.

[343] J. L. Boland, F. Amaduzzi, S. Sterzl, H. Potts, L. M. Herz, A. Fontcuberta i Morral, and M. B. Johnston, "High Electron Mobility and Insights into Temperature-Dependent Scattering Mechanisms in InAsSb Nanowires", *Nano Letters*, vol. 18, no. 6, pp. 3703–3710, 2018. DOI: 10.1021/acs.nanolett.8b00842.

[344] T. C. Harman, H. L. Goering, and A. C. Beer, "Electrical properties of n-type InAs", *Physical Review*, vol. 104, no. 6, pp. 1562–1564, 1956. DOI: 10.1103/PhysRev.104.1562.

[345] J. L. Boland, S. Conesa-Boj, P. Parkinson, G. Tütüncüoglu, F. Matteini, D. Rüffer, A. Casadei, F. Amaduzzi, F. Jabeen, C. L. Davies, H. J. Joyce, L. M. Herz, A. Fontcuberta i Morral, and M. B. Johnston, "Modulation Doping of GaAs/AlGaAs Core–Shell Nanowires With Effective Defect Passivation and High Electron Mobility", *Nano Letters*, vol. 15, no. 2, pp. 1336–1342, 2015. DOI: 10.1021/nl504566t.

[346] J. L. Boland, G. Tütüncüoglu, J. Q. Gong, S. Conesa-Boj, C. L. Davies, L. M. Herz, A. Fontcuberta i Morral, and M. B. Johnston, "Towards higher electron mobility in modulation doped GaAs/AlGaAs core shell nanowires", *Nanoscale*, vol. 9, no. 23, pp. 7839–7846, 2017. DOI: 10.1039/C7NR00680B.

[347] S. Funk, M. Royo, I. Zardo, D. Rudolph, S. Morkötter, B. Mayer, J. Becker, A. Bechtold, S. Matich, M. Döblinger, M. Bichler, G. Koblmüller, J. J. Finley, A. Bertoni, G. Goldoni, and G. Abstreiter, "High mobility one- and two-dimensional electron systems in nanowire-based quantum heterostructures", *Nano Letters*, vol. 13, no. 12, pp. 6189–6196, 2013. DOI: 10.1021/nl403561w.

[348] K. Tomioka, M. Yoshimura, and T. Fukui, "A III-V nanowire channel on silicon for high-performance vertical transistors.", *Nature*, vol. 488, no. 7410, pp. 189–92, 2012. DOI: 10.1038/nature11293.

[349] W. P. Gillin, K. P. Homewood, L. K. Howard, and M. T. Emeny, "Thermal interdiffusion in InGaAs/GaAs strained quantum wells as a function of doping density", *Superlattices and Microstructures*, vol. 9, no. 1, pp. 39–42, 1991. DOI: 10.1016/0749-6036(91)90089-A.

[350] O. M. Khreis, K. P. Homewood, W. P. Gillin, and K. E. Singer, "Intermixing in GaAsSb/-GaAs single quantum wells", *Journal of Applied Physics*, vol. 84, no. 7, pp. 4017–4019, 1998. DOI: 10.1063/1.368583.

[351] O. M. Khreis, K. P. Homewood, and W. P. Gillin, "Interdiffusion in InGaAs/GaAs: The effect of growth conditions", *Journal of Applied Physics*, vol. 84, no. 1, pp. 232–236, 1998. DOI: 10.1063/1.368079.

[352] F. Dettwiler, J. Fu, S. Mack, P. J. Weigele, J. C. Egues, D. D. Awschalom, and D. M. Zumbühl, "Stretchable Persistent Spin Helices in GaAs Quantum Wells", *Physical Review X*, vol. 7, no. 3, p. 031 010, 2017. DOI: 10.1103/PhysRevX.7.031010.

[353] M. J. Carballido, C. Kloeffel, D. M. Zumbühl, and D. Loss, "Low-symmetry nanowire cross-sections for enhanced Dresselhaus spin-orbit interaction", 2019.

[354] M. J. L. Sourribes, I. Isakov, M. Panfilova, and P. a. Warburton, "Minimization of the contact resistance between InAs nanowires and metallic contacts", *Nanotechnology*, vol. 24, no. 4, p. 045 703, 2013. DOI: 10.1088/0957-4484/24/4/045703.

[355] J. Gao, G. He, S. Liang, D. Wang, and B. Yang, "Comparative study on in situ surface cleaning effect of intrinsic oxide-covering GaAs surface using TMA precursor and Al 2 O 3 buffer layer for HfGdO gate dielectrics", *Journal of Materials Chemistry C*, vol. 6, no. 10, pp. 2546–2555, 2018. DOI: 10.1039/C8TC00070K.

[356] R. Timm, A. R. Head, S. Yngman, J. V. Knutsson, M. Hjort, S. R. McKibbin, A. Troian, O. Persson, S. Urpelainen, J. Knudsen, J. Schnadt, and A. Mikkelsen, "Self-cleaning and surface chemical reactions during hafnium dioxide atomic layer deposition on indium arsenide", *Nature Communications*, vol. 9, no. 1, p. 1412, 2018. DOI: 10.1038/s41467-018-03855-z.

[357] J. Miao, W. Hu, N. Guo, Z. Lu, X. Liu, L. Liao, P. Chen, T. Jiang, S. Wu, J. C. Ho, L. Wang, X. Chen, and W. Lu, "High-Responsivity Graphene/InAs Nanowire Heterojunction Near-Infrared Photodetectors with Distinct Photocurrent On/Off Ratios", *Small*, vol. 11, no. 8, pp. 936–942, 2015. DOI: 10.1002/smll.201402312.

[358] R. Yan, D. Gargas, and P. Yang, "Nanowire photonics", *Nature Photonics*, vol. 3, no. 10, pp. 569–576, 2009. DOI: 10.1038/nphoton.2009.184.

[359] Y. Ma, X. Guo, X. Wu, L. Dai, and L. Tong, "Semiconductor nanowire lasers", *Advances in Optics and Photonics*, vol. 5, no. 3, p. 216, 2013. DOI: 10.1364/AOP.5.000216.

Bibliography

[360] Z. Zhang, Z.-Y. Lu, P.-P. Chen, W. Lu, and J. Zou, "Defect-Free Zinc-Blende Structured InAs Nanowires Realized by in-situ Two-V/III-Ratio Growth in Molecular Beam Epitaxy", *Nanoscale*, pp. 12 592–12 597, 2015. DOI: 10.1039/C5NR03503A.

[361] S. Yazji, E. A. Hoffman, D. Ercolani, F. Rossella, A. Pitanti, A. Cavalli, S. Roddaro, G. Abstreiter, L. Sorba, and I. Zardo, "Complete thermoelectric benchmarking of individual InSb nanowires using combined micro-Raman and electric transport analysis", *Nano Research*, vol. 8, no. 12, pp. 4048–4060, 2015. DOI: 10.1007/s12274-015-0906-8.

[362] G. Otnes and M. T. Borgström, "Towards high efficiency nanowire solar cells", *Nano Today*, vol. 12, pp. 31–45, 2017. DOI: 10.1016/j.nantod.2016.10.007.

[363] S. F. Fang, K. Adomi, S. Iyer, H. Morkoç, H. Zabel, C. Choi, and N. Otsuka, "Gallium arsenide and other compound semiconductors on silicon", *Journal of Applied Physics*, vol. 68, no. 7, R31–R58, 1990. DOI: 10.1063/1.346284.

[364] B. Kunert, W. Guo, Y. Mols, B. Tian, Z. Wang, Y. Shi, D. Van Thourhout, M. Pantouvaki, J. Van Campenhout, R. Langer, and K. Barla, "III/V nano ridge structures for optical applications on patterned 300 mm silicon substrate", *Applied Physics Letters*, vol. 109, no. 9, p. 091 101, 2016. DOI: 10.1063/1.4961936.

[365] E. Uccelli, J. Arbiol, C. Magen, P. Krogstrup, E. Russo-Averchi, M. Heiss, G. Mugny, F. Morier-Genoud, J. Nygård, J. R. Morante, and A. Fontcuberta i Morral, "Three-Dimensional Multiple-Order Twinning of Self-Catalyzed GaAs Nanowires on Si Substrates", *Nano Letters*, vol. 11, no. 9, pp. 3827–3832, 2011. DOI: 10.1021/nl201902w.

[366] R. Alcotte, M. Martin, J. Moeyaert, R. Cipro, S. David, F. Bassani, F. Ducroquet, Y. Bogumilowicz, E. Sanchez, Z. Ye, X. Y. Bao, J. B. Pin, and T. Baron, "Epitaxial growth of antiphase boundary free GaAs layer on 300 mm Si(001) substrate by metalorganic chemical vapour deposition with high mobility", *APL Materials*, vol. 4, no. 4, p. 046 101, 2016. DOI: 10.1063/1.4945586.

[367] Y. Takagi, H. Yonezu, T. Kawai, K. Hayashida, K. Samonji, N. Ohshima, and K. Pak, "Suppression of threading dislocation generation in GaAs-on-Si with strained short-period superlattices", *Journal of Crystal Growth*, vol. 150, no. 1 -4 pt 1, pp. 677–680, 1995. DOI: 10.1016/0022-0248(95)80294-M.

[368] E. Y. Chang, T. H. Yang, G. Luo, and C. Y. Chang, "A GeSi-buffer structure for growth of high-quality GaAs epitaxial layers on a Si substrate", *Journal of Electronic Materials*, vol. 34, no. 1, pp. 23–26, 2005. DOI: 10.1007/s11664-005-0175-5.

[369] J. A. Carlin, S. A. Ringel, E. A. Fitzgerald, M. Bulsara, and B. M. Keyes, "Impact of GaAs buffer thickness on electronic quality of GaAs grown on graded Ge/GeSi/Si substrates", *Applied Physics Letters*, vol. 76, no. 14, pp. 1884–1886, 2000. DOI: 10.1063/1.126200.

[370] J. W. Lee, H. Shichijo, H. L. Tsai, and R. J. Matyi, "Defect reduction by thermal annealing of GaAs layers grown by molecular beam epitaxy on Si substrates", *Applied Physics Letters*, vol. 50, no. 1, pp. 31–33, 1987. DOI: 10.1063/1.98117.

[371] H. Yamaguchi, M. Kawashima, and Y. Horikoshi, "Migration-enhanced epitaxy", *Applied Surface Science*, vol. 33-34, no. C, pp. 406–412, 1988. DOI: 10.1016/0169-4332(88) 90333-9.

[372] A. Krost, R. F. Schnabel, F. Heinrichsdorff, U. Rossow, D. Bimberg, and H. Cerva, "Defect reduction in GaAs and InP grown on planar Si(111) and on patterned Si(001) substrates", *Journal of Crystal Growth*, vol. 145, no. 1-4, pp. 314–320, 1994. DOI: 10.1016/ 0022-0248(94)91069-3.

[373] Y. Li, Y. Liu, L. Zhu, X. Qin, Q. Wu, W. Huang, Z. Niu, W. Xiang, H. Hao, and Y. Chen, "Observation of interface dependent spin polarized photocurrents in InAs/GaSb superlattice", *Applied Physics Letters*, vol. 106, no. 19, p. 192 402, 2015. DOI: 10.1063/1.4919894.

[374] S. Plissard, K. A. Dick, G. Larrieu, S. Godey, A. Addad, X. Wallart, and P. Caroff, "Gold-free growth of GaAs nanowires on silicon: Arrays and polytypism", *Nanotechnology*, vol. 21, no. 38, p. 385 602, 2010. DOI: 10.1088/0957-4484/21/38/385602.

[375] F. Furtmayr, M. Vielemeyer, M. Stutzmann, J. Arbiol, S. Estradé, F. Peiró, J. R. Morante, and M. Eickhoff, "Nucleation and growth of GaN nanorods on Si (111) surfaces by plasma-assisted molecular beam epitaxy - The influence of Si- and Mg-doping", *Journal of Applied Physics*, vol. 104, no. 3, p. 034 309, 2008. DOI: 10.1063/1.2953087.

[376] J. Vukajlovic-Plestina, W. Kim, L. Ghisalberti, G. Varnavides, G. Tütüncuoglu, H. Potts, M. Friedl, L. Güniat, W. C. Carter, V. G. Dubrovskii, and A. Fontcuberta i Morral, "Fundamental aspects to localize self-catalyzed III-V nanowires on silicon", *Nature Communications*, vol. 10, no. 1, p. 869, 2019. DOI: 10.1038/s41467-019-08807-9.

[377] H. Y. Li, O. Wunnicke, M. T. Borgström, W. G. G. Immink, M. H. M. Van Weert, M. A. Verheijen, and E. P. A. M. Bakkers, "Remote p-doping of InAs nanowires", *Nano Letters*, vol. 7, no. 5, pp. 1144–1148, 2007. DOI: 10.1021/nl0627487.

[378] J. G. Fiorenza, J. S. Park, J. M. Hydrick, J. Li, J. Z. Li, M. Curtin, M. Carroll, and A. Lochtefeld, "Aspect ratio trapping: A unique technology for integrating Ge and III-Vs with silicon CMOS", in *ECS Transactions*, vol. 33, 2010, pp. 963–976. DOI: 10.1149/1. 3487628.

[379] W. Guo, L. Date, V. Pena, X. Bao, C. Merckling, N. Waldron, N. Collaert, M. Caymax, E. Sanchez, E. Vancoille, K. Barla, A. Thean, P. Eyben, and W. Vandervorst, "Selective metal-organic chemical vapor deposition growth of high quality GaAs on Si(001)", *Applied Physics Letters*, vol. 105, no. 6, p. 062 101, 2014. DOI: 10.1063/1.4892468.

[380] J. Motohisa, J. Noborisaka, J. Takeda, M. Inari, and T. Fukui, "Catalyst-free selective-area MOVPE of semiconductor nanowires on (111)B oriented substrates", *Journal of Crystal Growth*, vol. 272, no. 1-4, pp. 180–185, 2004. DOI: 10.1016/j.jcrysgro.2004.08.118.

[381] F. Schuster, M. Hetzl, S. Weiszer, J. A. Garrido, M. de la Mata, C. Magen, J. Arbiol, and M. Stutzmann, "Position-Controlled Growth of GaN Nanowires and Nanotubes on Diamond by Molecular Beam Epitaxy", *Nano Letters*, vol. 15, no. 3, pp. 1773–1779, 2015. DOI: 10.1021/nl504446r.

Bibliography

[382] E. Russo-Averchi, G. Tütüncüoglu, A. Dalmau-Mallorqui, I. Canales Mundet, M. de la Mata, D. Rüffer, J. Arbiol, S. Conesa-Boj, and A. Fontcuberta i Morral, "Bottom-up engineering of InAs at the nanoscale: From V-shaped nanomembranes to nanowires", *Journal of Crystal Growth*, vol. 420, pp. 47–56, 2015. DOI: 10.1016/j.jcrysgro.2015.01.040.

[383] A. M. Raya, D. Fuster, and J. M. Llorens, "Numerical Study on Mie Resonances in Single GaAs Nanomembranes", *Nanomaterials*, vol. 9, no. 6, p. 856, 2019. DOI: 10.3390/nano9060856.

[384] G. Tütüncüoglu, "The growth and optical properties of III-V nanostructures grown by Molecular Beam Epitaxy", *PhD Thesis*, vol. 7393, 2017. DOI: 10.5075/EPFL-THESIS-7393.

[385] H. Yoshida, K. Ikejiri, T. Sato, S. Hara, K. Hiruma, J. Motohisa, and T. Fukui, "Analysis of twin defects in GaAs nanowires and tetrahedra and their correlation to GaAs(111)B surface reconstructions in selective-area metal organic vapour-phase epitaxy", *Journal of Crystal Growth*, vol. 312, no. 1, pp. 52–57, 2009. DOI: 10.1016/j.jcrysgro.2009.10.006.

[386] V. G. Dubrovskii and Y. S. Berdnikov, "Natural scaling of size distributions in homogeneous and heterogeneous rate equations with size-linear capture rates", *The Journal of Chemical Physics*, vol. 142, no. 12, p. 124 110, 2015. DOI: 10.1063/1.4916323.

[387] F. Matteini, V. G. Dubrovskii, D. Rüffer, G. Tütüncüoğlu, Y. Fontana, and A. F. I. Morral, "Tailoring the diameter and density of self-catalyzed GaAs nanowires on silicon", *Nanotechnology*, vol. 26, no. 10, p. 105 603, 2015. DOI: 10.1088/0957-4484/26/10/105603.

[388] V. G. Dubrovskii, "Theory of VLS Growth of Compound Semiconductors", in *Semiconductors and Semimetals*, vol. 93, Elsevier, 2015, pp. 1–78. DOI: 10.1016/bs.semsem.2015.09.002.

[389] V. G. Dubrovskii, Y. Berdnikov, J. Schmidtbauer, M. Borg, K. Storm, K. Deppert, and J. Johansson, "Length Distributions of Nanowires Growing by Surface Diffusion", *Crystal Growth and Design*, vol. 16, no. 4, pp. 2167–2172, 2016. DOI: 10.1021/acs.cgd.5b01832.

[390] V. G. Dubrovskii, "Analytic form of the size distribution in irreversible growth of nanoparticles", *Physical Review E*, vol. 99, no. 1, p. 012 105, 2019. DOI: 10.1103/PhysRevE.99.012105.

[391] M. Heigoldt, J. Arbiol, D. Spirkoska, J. M. Rebled, S. Conesa-Boj, G. Abstreiter, F. Peiró, J. R. Morante, and A. Fontcuberta I Morral, "Long range epitaxial growth of prismatic heterostructures on the facets of catalyst-free GaAs nanowires", *Journal of Materials Chemistry*, vol. 19, no. 7, pp. 840–848, 2009. DOI: 10.1039/b816585h.

[392] M. Hetzl, M. Kraut, J. Winnerl, L. Francaviglia, M. Döblinger, S. Matich, A. FontcubertaMorral, and M. Stutzmann, "Strain-Induced Band Gap Engineering in Selectively Grown GaN-(Al,Ga)N Core-Shell Nanowire Heterostructures", *Nano Letters*, vol. 16, no. 11, pp. 7098–7106, 2016. DOI: 10.1021/acs.nanolett.6b03354.

[393] J. Arbiol, S. Estradé, J. D. Prades, A. Cirera, F. Furtmayr, C. Stark, A. Laufer, M. Stutzmann, M. Eickhoff, M. H. Gass, A. L. Bleloch, F. Peiró, and J. R. Morante, "Triple-twin domains in Mg doped GaN wurtzite nanowires: structural and electronic properties of this zinc-blende-like stacking", *Nanotechnology*, vol. 20, no. 14, p. 145 704, 2009. DOI: 10.1088/0957-4484/20/14/145704.

[394] D. Spirkoska, J. Arbiol, A. Gustafsson, S. Conesa-Boj, F. Glas, I. Zardo, M. Heigoldt, M. H. Gass, A. L. Bleloch, S. Estrade, M. Kaniber, J. Rossler, F. Peiro, J. R. Morante, G. Abstreiter, L. Samuelson, and A. Fontcuberta i Morral, "Structural and optical properties of high quality zinc-blende/wurtzite GaAs nanowire heterostructures", *Physical Review B*, vol. 80, no. 24, p. 245 325, 2009. DOI: 10.1103/PhysRevB.80.245325.

[395] M. Heiss, B. Ketterer, E. Uccelli, J. R. Morante, J. Arbiol, and A. Fontcuberta i Morral, "In(Ga)As quantum dot formation on group-III assisted catalyst-free InGaAs nanowires.", *Nanotechnology*, vol. 22, no. 19, p. 195 601, 2011. DOI: 10.1088/0957-4484/22/19/195601.

[396] M. de la Mata, C. Magen, J. Gazquez, M. I. B. Utama, M. Heiss, S. Lopatin, F. Furtmayr, C. J. Fernández-Rojas, B. Peng, J. R. Morante, R. Rurali, M. Eickhoff, A. Fontcuberta i Morral, Q. Xiong, and J. Arbiol, "Polarity Assignment in ZnTe, GaAs, ZnO, and GaN-AlN Nanowires from Direct Dumbbell Analysis", *Nano Letters*, vol. 12, no. 5, pp. 2579–2586, 2012. DOI: 10.1021/nl300840q.

[397] M. de la Mata, R. R. Zamani, S. Martí-Sánchez, M. Eickhoff, Q. Xiong, A. Fontcuberta i Morral, P. Caroff, and J. Arbiol, "The Role of Polarity in Nonplanar Semiconductor Nanostructures", *Nano Letters*, vol. 19, no. 6, pp. 3396–3408, 2019. DOI: 10.1021/acs.nanolett.9b00459.

[398] M. Zamani, G. Tütüncüoglu, S. Martí-Sánchez, L. Francaviglia, L. Güniat, L. Ghisalberti, H. Potts, M. Friedl, E. Markov, W. Kim, J.-B. Leran, V. G. Dubrovskii, J. Arbiol, and A. Fontcuberta i Morral, "Optimizing the yield of A-polar GaAs nanowires to achieve defect-free zinc blende structure and enhanced optical functionality", *Nanoscale*, vol. 10, no. 36, pp. 17 080–17 091, 2018. DOI: 10.1039/C8NR05787G.

[399] M. J. Hÿtch, E. Snoeck, and R. Kilaas, "Quantitative measurement of displacement and strain fields from HREM micrographs", *Ultramicroscopy*, vol. 74, no. 3, pp. 131–146, 1998. DOI: 10.1016/S0304-3991(98)00035-7.

[400] R. R. Zamani, F. S. Hage, S. Lehmann, Q. M. Ramasse, and K. A. Dick, "Atomic-Resolution Spectrum Imaging of Semiconductor Nanowires", *Nano Letters*, vol. 18, no. 3, pp. 1557–1563, 2018. DOI: 10.1021/acs.nanolett.7b03929.

[401] F. Krizek, J. E. Sestoft, P. Aseev, S. Marti-Sanchez, S. Vaitiekėnas, L. Casparis, S. A. Khan, Y. Liu, T. Stankevič, A. M. Whiticar, A. Fursina, F. Boekhout, R. Koops, E. Uccelli, L. P. Kouwenhoven, C. M. Marcus, J. Arbiol, and P. Krogstrup, "Field effect enhancement in buffered quantum nanowire networks", *Physical Review Materials*, vol. 2, no. 9, p. 093 401, 2018. DOI: 10.1103/PhysRevMaterials.2.093401.

[402] C. A. Lehner, T. Tschirky, T. Ihn, W. Dietsche, J. Keller, S. Fält, and W. Wegscheider, "Limiting scattering processes in high-mobility InSb quantum wells grown on GaSb buffer systems", *Physical Review Materials*, vol. 2, no. 5, p. 054 601, 2018. DOI: 10.1103/PhysRevMaterials.2.054601.

[403] H. Kroemer, "Polar-on-nonpolar epitaxy", *Journal of Crystal Growth*, vol. 81, no. 1-4, pp. 193–204, 1987. DOI: 10.1016/0022-0248(87)90391-5.

[404] L. Lazzarini, L. Nasi, G. Salviati, C. Fregonara, Y. Li, L. Giling, C. Hardingham, and D. Holt, "Antiphase disorder in GaAs/Ge heterostructures for solar cells", *Micron*, vol. 31, no. 3, pp. 217–222, 2000. DOI: 10.1016/S0968-4328(99)00086-4.

[405] J. Szatkowski and K. Sierański, "Electrical conductivity of Zn3As2", *Journal of Physics and Chemistry of Solids*, vol. 51, no. 3, pp. 249–251, 1990. DOI: 10.1016/0022-3697(90)90053-I.

[406] G. Chen, Z. Liu, B. Liang, G. Yu, Z. Xie, H. Huang, B. Liu, X. Wang, D. Chen, M.-Q. Zhu, and G. Shen, "Single-Crystalline p-Type Zn 3 As 2 Nanowires for Field-Effect Transistors and Visible-Light Photodetectors on Rigid and Flexible Substrates", *Advanced Functional Materials*, vol. 23, no. 21, pp. 2681–2690, 2013. DOI: 10.1002/adfm.201202739.

[407] G. A. Castellion and L. C. Beegle, "The preparation and properties of Cd3As2-Zn3As2 alloys", *Journal of Physics and Chemistry of Solids*, vol. 26, no. 4, pp. 767–773, 1965. DOI: 10.1016/0022-3697(65)90031-4.

[408] H. S. Im, K. Park, D. M. Jang, C. S. Jung, J. Park, S. J. Yoo, and J. G. Kim, "Zn3P2-Zn3As2 solid solution nanowires", *Nano Letters*, vol. 15, no. 2, pp. 990–997, 2015. DOI: 10.1021/nl5037897.

[409] H. Lu, X. Zhang, Y. Bian, and S. Jia, "Topological Phase Transition in Single Crystals of (Cd1-xZnx)3As2", *Scientific Reports*, vol. 7, no. 1, p. 3148, 2017. DOI: 10.1038/s41598-017-03559-2.

[410] B. Chelluri, T. Y. Chang, A. Ourmazd, a. H. Dayem, J. L. Zyskind, and A. Srivastava, "Molecular beam epitaxial growth of the II-V semiconductor compound Zn3As2", *Applied Physics Letters*, vol. 49, no. 24, pp. 1665–1667, 1986. DOI: 10.1063/1.97261.

[411] J. R. Botha, G. J. Scriven, J. A. A. Engelbrecht, and A. W. R. Leitch, "Photoluminescence properties of metalorganic vapor phase epitaxial Zn3As2", *Journal of Applied Physics*, vol. 86, no. 10, pp. 5614–5618, 1999. DOI: 10.1063/1.371569.

[412] S. Sudhakar, V. Ganesh, I. Sulania, P. K. Kulriya, and K. Baskar, "Liquid phase epitaxial growth of II–V semiconductor compound Zn 3 As 2", *Journal of Physics D: Applied Physics*, vol. 40, no. 17, pp. 5071–5074, 2007. DOI: 10.1088/0022-3727/40/17/011.

[413] J. Engelbrecht, G. Scriven, J. Neethling, and M. Wagener, "Crack formation in Zn3As2 epilayers grown by MOVPE", *Journal of Crystal Growth*, vol. 216, no. 1-4, pp. 235–244, 2000. DOI: 10.1016/S0022-0248(00)00453-X.

[414] M. T. Björk, B. J. Ohlsson, T. Sass, A. I. Persson, C. Thelander, M. H. Magnusson, K. Deppert, L. R. Wallenberg, and L. Samuelson, "One-dimensional heterostructures in semiconductor nanowhiskers", *Applied Physics Letters*, vol. 80, no. 6, pp. 1058–1060, 2002. DOI: 10.1063/1.1447312.

[415] M. Glaser, A. Kitzler, A. Johannes, S. Prucnal, H. Potts, S. Conesa-Boj, L. Filipovic, H. Kosina, W. Skorupa, E. Bertagnolli, C. Ronning, A. Fontcuberta i Morral, and A. Lugstein, "Synthesis, Morphological, and Electro-optical Characterizations of Metal/Semiconductor Nanowire Heterostructures", *Nano Letters*, vol. 16, no. 6, pp. 3507–3513, 2016. DOI: 10.1021/acs.nanolett.6b00315.

[416] K.-W. Kwon and M. Shim, "γ-Fe 2 O 3 /II-VI Sulfide Nanocrystal Heterojunctions", *Journal of the American Chemical Society*, vol. 127, no. 29, pp. 10 269–10 275, 2005. DOI: 10.1021/ja051713q.

[417] N. Kouklin, S. Sen, and M. Gajdardziska-Josifovska, "Self-driven formation and structure of single crystal platelets of Zn3As2", *Applied Physics Letters*, vol. 89, no. 7, p. 071 901, 2006. DOI: 10.1063/1.2335682.

[418] J. Li, L.-S. Wang, D. B. Buchholz, and R. P. H. Chang, "Simultaneous Growth of Pure Hyperbranched Zn 3 As 2 Structures and Long Ga 2 O 3 Nanowires", *Nano Letters*, vol. 9, no. 5, pp. 1764–1769, 2009. DOI: 10.1021/nl8035228.

[419] T. Burgess, P. Caroff, Y. Wang, B. H. Badada, H. E. Jackson, L. M. Smith, Y. Guo, H. H. Tan, and C. Jagadish, "Zn3As2 Nanowires and Nanoplatelets: Highly Efficient Infrared Emission and Photodetection by an Earth Abundant Material", *Nano Letters*, vol. 15, pp. 378–385, 2015. DOI: 10.1021/nl5036918.

[420] P. Blanc, M. Heiss, C. Colombo, A. D. Mallorquì, T. S. Safaei, P. Krogstrup, J. Nygård, and A. F. i. Morral, "Electrical contacts to single nanowires: a scalable method allowing multiple devices on a chip. Application to a single nanowire radial p-i-n junction", *International Journal of Nanotechnology*, vol. 10, no. 5/6/7, p. 419, 2013. DOI: 10.1504/IJNT.2013.053513.

[421] L. J. van der Pauw, "A method of measuring specific resistivity and Hall effect of discs of aribtrary shape", *Philips Research Reports*, vol. 13, pp. 1–11, 1958.

[422] W. Zdanowicz, K. Lukaszewicz, and W. Trzebiatowski, "Crystal Structure of the Semiconducting System Cd3As2-Zn3As2", *Bulletin de l'Académie Polonaise des Sciences: Série des sciences chimiques*, vol. 12, no. 3, pp. 169–176, 1964.

[423] V. N. Yakimovich, V. A. Rubtsov, and V. M. Trukhan, "Phase equilibria in Zn-P-As-Cd system", *Neorganicheskie Materialy*, vol. 32, no. 7, pp. 799–803, 1996.

[424] G. Pangilinan, R. Sooryakumar, B. Chelluri, and T. Y. Chang, "New long-range atomic order and heteroepitaxy of single-crystal Zn3As2", *Physical Review Letters*, vol. 62, no. 5, pp. 551–554, 1989. DOI: 10.1103/PhysRevLett.62.551.

Bibliography

[425] J. Hanuza, A. Lemiec, and J. Misiewicz, "Molecular model of lattice vibrations in Zn3P2", *Vibrational Spectroscopy*, vol. 17, no. 1, pp. 93–103, 1998. DOI: 10.1016/S0924-2031(98)00022-8.

[426] G. Pangilinan, R. Sooryakumar, and J. Misiewicz, "Raman activity of Zn3P2", *Physical Review B*, vol. 44, no. 6, pp. 2582–2588, 1991. DOI: 10.1103/PhysRevB.44.2582.

[427] J. Misiewicz, "The Raman scattering of Zn3As2", *Infrared Physics & Technology*, vol. 35, no. 6, pp. 781–783, 1994. DOI: 10.1016/1350-4495(94)90005-1.

[428] M. Iwami, K. Fujishima, and K. Kawabe, "Magnetoresistance Effect in p -Zn3As2 Single Crystals", *Journal of the Physical Society of Japan*, vol. 41, no. 2, pp. 521–525, 1976. DOI: 10.1143/JPSJ.41.521.

[429] B. Sujak-Cyrul, B. Kolodka, and J. Misiewicz, *Intraband and interband optical transitions in Zn3As2*, 1982. DOI: 10.1016/0038-1098(82)90913-9.

[430] G. Scriven, A. Leitch, J. Neethling, V. Kozyrkov, and V. Watters, "The growth of Zn3As2 on InP by atmospheric pressure MOVPE", *Journal of Crystal Growth*, vol. 170, no. 1-4, pp. 813–816, 1997. DOI: 10.1016/S0022-0248(96)00558-1.

[431] S. F. Marenkin, N. S. Zhalilov, A. V. Mudryi, A. I. Patuk, and I. A. Shakin, "Optical Properties of Single Crystals and Films of Semiconducting Compound Zn3As2", *Inorganic Materials*, vol. 28, no. 10-11, pp. 1659–1661, 1992.

[432] J. Szatkowski and K. Sierański, "Electronic energy levels of an ideal vacancy in II3–V2 compounds", *Solid State Communications*, vol. 93, no. 7, pp. 595–598, 1995. DOI: 10.1016/0038-1098(94)00682-3.

[433] W.-J. Yin and Y. Yan, "The electronic properties of point defects in earth-abundant photovoltaic material Zn 3 P 2 : A hybrid functional method study", *Journal of Applied Physics*, vol. 113, no. 1, p. 013 708, 2013. DOI: 10.1063/1.4772708.

[434] B. Kolodka, J. Misiewicz, and J. M. Pawlikowski, "Optical Transitions in Zn3As2 Thin Films and Single Crystals", *Acta Physica Polonica A*, vol. 62, no. 1-2, pp. 63–81, 1982.

[435] I. Aberg, G. Vescovi, D. Asoli, U. Naseem, J. P. Gilboy, C. Sundvall, A. Dahlgren, K. E. Svensson, N. Anttu, M. T. Bjork, and L. Samuelson, "A GaAs Nanowire Array Solar Cell With 15.3% Efficiency at 1 Sun", *IEEE Journal of Photovoltaics*, vol. 6, no. 1, pp. 185–190, 2016. DOI: 10.1109/JPHOTOV.2015.2484967.

[436] S. Gazibegovic, G. Badawy, T. L. J. Buckers, P. Leubner, J. Shen, F. K. de Vries, S. Koelling, L. P. Kouwenhoven, M. A. Verheijen, and E. P. A. M. Bakkers, "Bottom-Up Grown 2D InSb Nanostructures", *Advanced Materials*, vol. 31, no. 14, p. 1 808 181, 2019. DOI: 10.1002/adma.201808181.

[437] H. Yamaguchi, R. Dreyfus, Y. Hirayama, and S. Miyashita, "Excellent electric properties of free-standing InAs membranes", *Applied Physics Letters*, vol. 78, no. 16, pp. 2372–2374, 2001. DOI: 10.1063/1.1365946.

[438]   S. J. Paik, J. Kim, S. Park, S. Kim, C. Koo, S. K. Lee, and D. D. Cho, "A novel microma-chining technique to fabricate released GaAs microstructures with a rectangular cross section", *Japanese Journal of Applied Physics, Part 1: Regular Papers and Short Notes and Review Papers*, vol. 42, no. 1, pp. 326–332, 2003. DOI: 10.1143/JJAP.42.326.

[439]   T. Rieger, M. Luysberg, T. Schäpers, D. Grützmacher, and M. I. Lepsa, "Molecular Beam Epitaxy Growth of GaAs/InAs Core–Shell Nanowires and Fabrication of InAs Nanotubes", *Nano Letters*, vol. 12, no. 11, pp. 5559–5564, 2012. DOI: 10.1021/nl302502b.

[440]   H.-C. Steiner, "Firmata: Towards making microcontrollers act like extensions of the computer", in *New Interfaces for Musical Expression*, 2009, pp. 125–130.

[441]   D. McKay and R. Savage, *Open Source Time Series Database: InfluxDB*, 2019.

[442]   S. N. Z. Naqvi, S. Yfantidou, and E. Zimányi, "Time Series Databases and InfluxDB", *Studienarbeit, Université Libre de Bruxelles*, no. 000455274, 2017.

[443]   T. Ödegaard, "Grafana: The Open Observability Platform", 2019.

[444]   M. Cantoro, A. V. Klekachev, A. Nourbakhsh, B. Sorée, M. M. Heyns, and S. De Gendt, "Long-wavelength, confined optical phonons in InAs nanowires probed by Raman spectroscopy", *The European Physical Journal B*, vol. 79, no. 4, pp. 423–428, 2011. DOI: 10.1140/epjb/e2011-10705-2.

[445]   L. Pavesi, G. Mariotto, J. Carlin, A. Rudra, and R. Houdré, "Raman study of a single InP/InAs/InP strained quantum well", *Solid State Communications*, vol. 84, no. 7, pp. 705–709, 1992. DOI: 10.1016/0038-1098(92)90463-J.

[446]   S. Birner, T. Zibold, T. Andlauer, T. Kubis, M. Sabathil, A. Trellakis, and P. Vogl, "nextnano: General Purpose 3-D Simulations", *IEEE Transactions on Electron Devices*, vol. 54, no. 9, pp. 2137–2142, 2007. DOI: 10.1109/TED.2007.902871.

[447]   X. Zhang, V. G. Dubrovskii, N. V. Sibirev, and X. Ren, "Analytical study of elastic relax-ation and plastic deformation in nanostructures on lattice mismatched substrates", *Crystal Growth and Design*, vol. 11, no. 12, pp. 5441–5448, 2011. DOI: 10.1021/cg201029x.

[448]   V. G. Dubrovskii, N. V. Sibirev, X. Zhang, and R. A. Suris, "Stress-driven nucleation of three-dimensional crystal islands: From quantum dots to nanoneedles", *Crystal Growth and Design*, vol. 10, no. 9, pp. 3949–3955, 2010. DOI: 10.1021/cg100495b.

[449]   V. G. Dubrovskii, V. Consonni, A. Trampert, L. Geelhaar, and H. Riechert, "Scaling thermodynamic model for the self-induced nucleation of GaN nanowires", *Physical Review B - Condensed Matter and Materials Physics*, vol. 85, no. 16, pp. 1–6, 2012. DOI: 10.1103/PhysRevB.85.165317.

[450]   J. Y. Shen, C. Chatillon, I. Ansara, A. Watson, B. Rugg, and T. Chart, "Optimisation of the thermodynamic and phase diagram data in the ternary As-Ga-In system", *Calphad*, vol. 19, no. 2, pp. 215–226, 1995. DOI: 10.1016/0364-5916(95)00022-7.

[451]   D. Schlenker, T. Miyamoto, Z. Pan, F. Koyama, and K. Iga, "Miscibility gap calculation for Ga1-xInxNyAs1-y including strain effects", *Journal of Crystal Growth*, vol. 196, no. 1, pp. 67–70, 1999. DOI: 10.1016/S0022-0248(98)00787-8.

Bibliography

[452]   D. Liang and X. P. a. Gao, "Strong Tuning of Rashba Spin-Orbit Interaction in Single InAs Nanowires", 2012.

[453]   J. Misiewicz, J. Wróbel, and K. Jezierski, "Interband transitions in Zn3As2", *Solid State Communications*, vol. 86, no. 8, pp. 509–511, 1993. DOI: 10.1016/0038-1098(93)90098-8.

[454]   J. Misiewicz, J. Wrobel, and K. Jezierski, "Optical constants and band transitions of Zn 3 P 2 and Zn 3 As 2", *Journal of Physics C: Solid State Physics*, vol. 17, no. 17, pp. 3091–3099, 1984. DOI: 10.1088/0022-3719/17/17/018.

[455]   A. Pietraszko and K. Łukaszewicz, "Thermal expansion and phase transitions of Cd3As2 and Zn3As2", *Physica Status Solidi (a)*, vol. 18, no. 2, pp. 723–730, 1973. DOI: 10.1002/pssa.2210180234.

Acronyms

1D one-dimensional.

2D two-dimensional.

2DEG two-dimensional electron gas.

3D three-dimensional.

ADF annular dark-field.

AFM atomic force microscopy.

ALD atomic layer deposition.

APB anti-phase boundary.

APD avalanche photodiode.

APT atom probe tomography.

BEP beam equivalent pressure.

BF bright-field.

BFM beam flux monitor.

CBM conduction band minimum.

CCD charge-coupled device.

CDC central distribution chamber.

CL cathodoluminescence.

CMOS complementary metal-oxide-semiconductor.

CPU central processing unit.

CTE coefficient of thermal expansion.

Acronyms

CVD chemical vapour deposition.

CZTS copper zinc tin sulfide.

DFT density functional theory.

ECR-MBE electron-cyclotron resonance plasma-excited molecular beam epitaxy.

ECS equilibrium crystal shape.

EDS energy-dispersive x-ray spectroscopy.

EELS electron energy loss spectroscopy.

ELO epitaxial lateral overgrowth.

ESRF European Synchrotron Radiation Facility.

FEG field emission gun.

FET field-effect transistor.

FFT fast Fourier transform.

FIB focused ion beam.

FWHM full width at half maximum.

GIS gas injection system.

GPA geometrical phase analysis.

H-MBE hydrogen-assisted molecular beam epitaxy.

HAADF high-angle annular dark-field.

HEMT high electron mobility transistor.

HR-TEM high-resolution transmission electron microscopy.

IB impurity band.

IMF interfacial misfit.

IRF instrument response function.

KCS kinetic crystal shape.

LEAP local-electrode atom-probe.

LED light emitting diode.

MAADF medium-angle annular dark-field.

MBE molecular beam epitaxy.

MCE microchannel epitaxy.

MEE migration-enhanced epitaxy.

MF Majorana fermion.

MOCVD metalorganic chemical vapour deposition.

MOVPE metal-organic vapour phase epitaxy.

MPF Majorana parafermion.

MUX multiplexer.

MZM Majorana zero mode.

NA numerical aperture.

NISQ noisy intermediate-scale quantum.

NM nanomembrane.

NP non-deterministic polynomial.

NW nanowire.

PCB printed circuit board.

PEVCD plasma-enhanced chemical vapour deposition.

PID proportional–integral–derivative.

PL photoluminescence.

PV photovoltaic.

QD quantum dot.

QEC quantum error correction.

QPP quasiparticle poisoning.

RHEED reflectance high-energy electron diffraction.

RSA Rivest–Shamir–Adleman.

Acronyms

SA selective-area.

SAE selective-area epitaxy.

SAG selective-area growth.

SAQP self-aligned quadruple patterning.

SC superconducting circuit.

SDD silicon drift detector.

SEM scanning electron microscopy.

SI supplementary information.

SIMS secondary ion mass spectrometry.

SOI spin-orbit interaction.

SPDT single pole double throw.

SPST single pole single throw.

STEM scanning transmission electron microscopy.

TASE template-assisted selective epitaxy.

TCSPC time correlated single photon counting.

TEM transmission electron microscopy.

TFET tunnel field-effect transistor.

TRPL time-resolved photoluminescence.

UHV ultra-high vacuum.

VBM valence band maximum.

VLS vapour–liquid–solid.

VTI variable thermal insert.

WAL weak anti-localization.

WL weak localization.

XRF x-ray fluorescence.

ZB zincblende.

Martin George Friedl

Rue du Sablon 1
1110 Morges, Switzerland
martingf9@yahoo.com
+41 78 760 42 19
linkedin.com/in/martinfriedl

PERSONAL INFORMATION

<u>Age</u>: 28
<u>Marital Status</u>: Single
<u>Citizenship</u>: Canadian & Czech
<u>Residence</u>: Swiss B Permit

EDUCATION

École Polytechnique Fédérale de Lausanne, Switzerland	June 2015 - Present

PhD in Materials Science and Engineering (In Progress)
- Supervisor: Anna Fontcuberta i Morral
- Laboratory of Semiconductor Materials (LMSC)

École Polytechnique Fédérale de Lausanne, Switzerland	September 2013 – February 2015

Master in Materials Science and Engineering
- Cumulative GPA: 5.8/6.0 (96.7%)

Carleton University, Ottawa, Canada	September 2009 – April 2013

Bachelor of Engineering Physics
- Cumulative GPA: 5.8/6.0 (96.7%)

AWARDS & HONORS

NSP 2018 Best Poster Award (St. Petersburg, Russia)	May 2018
IUMRS-ICAM 2017 Best Poster Award (Kyoto, Japan)	Sept. 2017
NSERC Postgraduate Scholarship (Ottawa, Canada)	Sept. 2013 – Sept. 2014
IPP CERN Summer Undergraduate Student Award (Geneva, Switzerland)	July 2012 – Aug. 2012
NSERC Undergraduate Student Research Award (Ottawa, Canada)	May 2011 – Aug. 2012

RESEARCH AND WORK EXPERIENCE

<u>Laboratory of Semiconductor Materials - EPFL</u>, Lausanne, Switzerland	June 2015 – Present

PhD Candidate, Supervised by Prof. Anna Fontcuberta i Morral
- Working on catalyst-free growth of III-V heterostructures
- Maintaining and operating a molecular beam epitaxy chamber
- Fabricating growth substrates in cleanroom using atomic layer deposition, e-beam lithography and reactive ion etching
- Characterizing grown samples using focused ion beam sample prep. and transmission/scanning electron microscopy
- Further fabricating electrical contacts and performing electrical characterization of grown samples at liquid helium temperatures

<u>European Space Agency - ESTEC</u>, Noordwijk, The Netherlands	May 2013 – August 2013

Trainee, Supervised by Dr. Andreas Tesch
- Mechanical testing of titanium, aluminum and state-of-the art metal-matrix composite materials

<u>CERN - ATLAS Group</u>, Geneva, Switzerland	July 2012 – August 2012

CERN Summer Student, Supervised by Prof. Thomas Koffas
- Used 2012 particle collision data from the LHC to assist in the calibration of ATLAS detector

SKILLS AND EXPERIENCE

Cleanroom Skills
- Well-versed in optical, SEM and TEM imaging
- Experience in contact design, photolithography and e-beam lithography
- Knowledgeable in CVD, evaporation and sputtering deposition techniques

Computer Skills
- Advanced proficiency in Python, C++, Java, and MATLAB
- Basic experience coding in LabVIEW, BASIC, HTML5 and ROOT
- Experience with Linux-based OSes and use of Photoshop, ImageJ, Blender, SOLIDWORKS

TEACHING

Advanced Semiconductor Materials (Master, Spring Semester, English)   Feb. 2015 – June 2018
- Exercise/lab question preparation and tutorial assistance
- Give lectures to replace professor when needed

Algèbre Linéaire (Bachelor, Fall Semester, French)   Sept. 2013, Sept. 2015 – Dec. 2017
- Exercise/tutorial assistance
- Exam supervision and correction

CONFERENCES & SCHOOLS

Laterally-oriented In(Ga)As nanowires grown on GaAs nanomembranes (Talk)   June 2018
Nanowire Week 2018, Hamilton, Canada

InGaAs Nanowires grown on GaAs Nanomembranes by MBE (Poster)   May 2018
NSP 2018, St. Petersburg, Russia

Bottom-up engineered nanostructures for quantum applications (Talk)   Feb. 2018
NCCR QSIT General Meeting, Arosa, Switzerland

Horizontally-Oriented InAs Nanowires Grown by MBE on GaAs (Poster)   Sept. 2017
IUMRS-ICAM, Kyoto, Japan

Quantum Heterostructures Based on GaAs Nanomembranes (Talk)   Sept. 2016
19th International Conference on MBE, Montpellier, France

KEY PUBLICATIONS

Remote-Doping of Template-Assisted InGaAs Nanowire Networks
M. Friedl*, K. Cerveny*, *et al.,* [In Preparation]

GaAs Nanoscale Membranes: Prospects for a Seamless Integration of III-Vs on Silicon
A. M. Raya*, M. Friedl*, S. Marti-Sanchez*, *et al.,* Nanoscale, (2019) [Submitted]

Nanosails Showcasing Zn_3As_2 as an Optoelectronic-Grade Earth Abundant Semiconductor.
E. Z. Stutz*, M. Friedl*, *et al.,* Physica Status Solidi – Rapid Research Letter, 1900084 (2019)

Template-Assisted Scalable Nanowire Networks
M. Friedl, *et al.,* Nano Letters 18, 2666 (2018)

*Equal contribution

LANGUAGES

English	Native Proficiency	**Italian**	Working Proficiency
French	Native Proficiency	**German**	Elementary Proficiency
Czech	Native Proficiency		